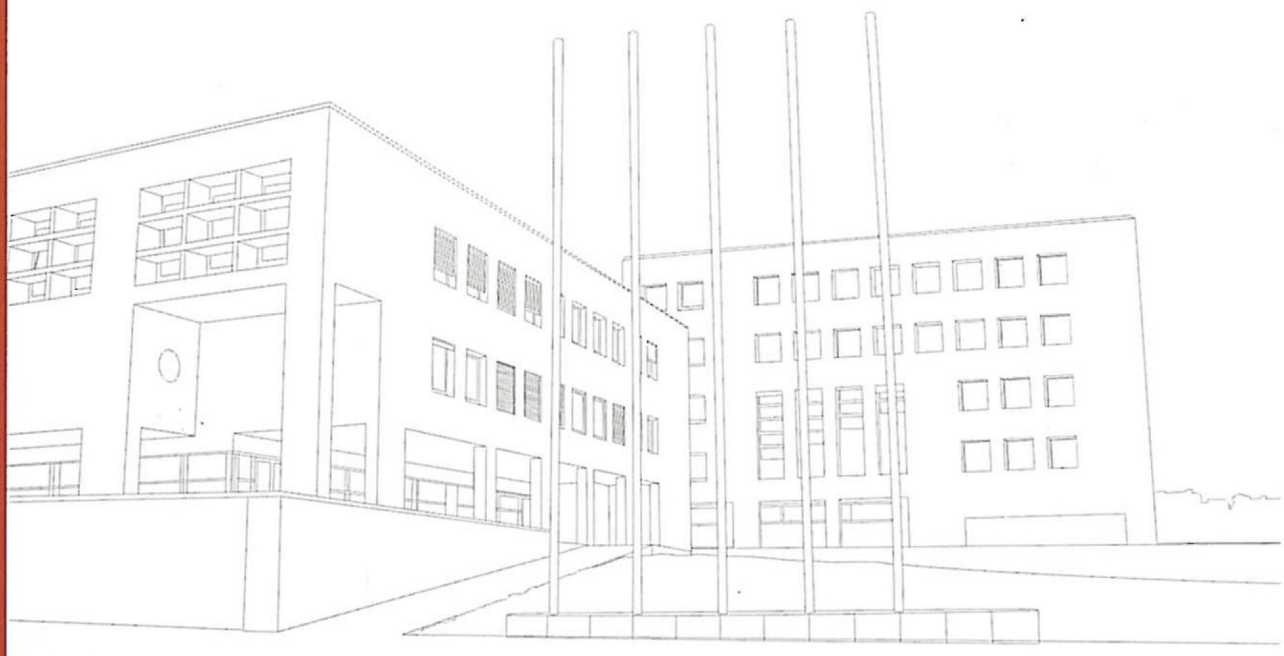
FEUP FACULDADE DE ENGENHARIA
UNIVERSIDADE DO PORTO





Separation of Light Naphtha for the Octane Upgrading of Gasoline

Adsorption and Membrane Technologies and New Adsorbents

Patrick da Silva Bárcia
DEQB 2010

U.PORTO

Separation of Light Naphtha for the Octane Upgrading of Gasoline
Adsorption and Membrane Technologies and New Adsorbents

A dissertation presented to the
Faculdade de Engenharia da Universidade do Porto
For the degree of Doctor in Chemical
and Biological Engineering

by

Patrick da Silva Bárcia

Supervisor: Prof. Alírio E. Rodrigues
Co-supervisor: Prof. José A.C. Silva
LSRE – Laboratory of Separation and Reaction Engineering
Department of Chemical Engineering
University of Porto

March 2010

Agradecimentos
Akcnowledgements

Aos meus orientadores, Professor Alírio Rodrigues e Professor José Silva, pela oportunidade concedida, acompanhamento científico, dedicação, sabedoria e amizade demonstrada ao longo deste trabalho.

Ao LSRE (*Laboratory of Separation and Reaction Engineering*), na pessoa do Professor Alírio Rodrigues, e à direcção da Escola Superior de Tecnologia e de Gestão do Instituto Politécnico de Bragança, pelas condições técnicas disponibilizadas.

A todos os colegas do LSRE pela amizade e espírito de camaradagem demonstrada ao longo destes anos. Um agradecimento especial à Patricia, ao Miguel, à Carolina, ao Nuno, à Inês, ao Laurent, ao Carlos Grande, à Carla, e ao Granato.

Ao meus pais, Abílio e Maria Isabel, por tudo, e principalmente pelo apoio que tive e sempre terei. Agradeço também ao meu irmão, aos familiares e amigos, que estiveram sempre do meu lado.

To Professor Sofia Calero and Elena from Universidad Pablo de Olavide (Seville), for their collaboration in the preliminary molecular simulation studies.

To Professor Banglin Chen, from the University of Texas (USA), Professor Gérard Férey and Professor Christian Serre, from Université de Versaille (France), for their collaboration in the synthesis of MOFs.

To Professor Freek Kapteijn and his team, Jorge, Alexandre, and Sonia, for receiving me during my stay at DelftChemTech, and for their cooperation in making possible the introduction at LSRE of technical expertise in the synthesis of zeolite materials and zeolite membranes. Thanks to Johan van den Bergh for the help with the membrane setup. Thank you also to Pedro, Chieh-Chao, Joana, Asun, Ana Rita, Alvaro, Alexandro, Loli… I enjoyed the time I spent in The Netherlands. Thank you guys!

À Fundação para a Ciência e a Tecnologia e ao Fundo Social Europeu, pelo apoio financeiro através da bolsa SFRH/BD/30994/2006. Ao governo Português e ao FEDER pelos projectos POCI/EQU/60828/2004 e PTDC/EQU-EQU/69731/2006.

A uma mulher muito especial,

à Susana.

"There is a driving force more powerful than that of vapour, electricity or atomic energy: the will" Albert Einstein (1879-1955)

Abstract

The aim of this work is to contribute for the development of adsorption based separation processes with considerable potential for commercial application on the refining industry, namely, in the separation of high research octane number (HRON) paraffins from light naphtha fractions. The development of an adsorption process requires first a detailed knowledge of equilibria and kinetics of adsorption and their impact on the dynamic response of an adsorption column. Accordingly, we start collecting single and mixture adsorption equilibrium isotherms of C_6 isomers, *n*-hexane (*n*HEX), 3-methylpentane (3MP), 2,3-dimethylbutane (23DMB), and 2,2-dimethylbutane (22DMB), from breakthrough experiments in zeolite beta. This adsorbent was selected because its pore system posses interesting characteristics for the separation of HRON dibranched C_6 from their low research octane number (LRON) monobranched isomers. It was found that the sorption hierarchy in zeolite beta was most favourable towards the linear isomer and least favourable towards the di-branched ones. Zeolite beta demonstrated significant selectivity to discriminate between mono and dibranched C_6 isomers, especially at low coverage. Based on an analysis of sorption events at the molecular level, a Tri-Site Langmuir model (TSL) was developed to interpret the equilibrium data with good accuracy.

Sorption kinetics studied by zero-length chromatography technique allowed us to find the nature of controlling diffusion mechanism; for *n*HEX and 3MP macropore diffusion is controlling. For 23DMB and 22DMB, the system is governed apparently by both macropore and micropore diffusion.

The dynamics of equimolar C_5/C_6 paraffin fractions in a fixed bed of zeolite beta was studied. Breakthrough experiments demonstrate that the sorption hierarchy is temperature-dependent. At 583 K, an enriched HRON fraction of 22DMB, iso-pentane (iPEN) and 23DMB can be selectively separated from the isomerate feed. For the case of feed mixtures with the typical composition of the hydroisomerization reactor product, the enriched fraction contains LRON *n*-pentane (*n*PEN) which decreases the octane quality of the product obtained. However, the use of a layered bed with zeolite 5A and zeolite beta can displace the *n*PEN from the enriched fraction, resulting in a maximum octane number of about 92.5 points. Aspen Adsim was used to simulate the dynamic behaviour of the C_5/C_6 fraction in a non-isothermal and non-adiabatic bed giving a good description of the set of experimental data. An optimal design of a mono/dibranched separation process can be achieved by properly tuning the operating temperature and the zeolite 5A/zeolite beta ratio on a layered fixed bed.

The performance of a layered pressure swing adsorption (PSA) process for the separation of HRON paraffins from a C_5/C_6 light naphtha fraction is simulated using a detailed, adiabatic single column PSA model. A zeolite 5A layer is used for selective adsorption of LRON *n*-paraffins while a zeolite beta layer is used to reduce the concentration of the LRON 3MP in the HRON fraction. The effects of various independent process variables (zeolite 5A-to-zeolite beta ratio, purge-to-feed ratio, cycle time, depressurization mode and operating temperature) on the process performance (product RON, HRON molecules recovery, HRON purity, and process productivity) are evaluated. It is demonstrated that an optimal zeolite 5A-to-zeolite beta ratio can improve the product average RON of up to 1.0 point comparatively to existing processes using zeolite 5A only. Moreover, process simulations demonstrated that an increase of 20 K in the operating temperature results in octane gain of 0.2 RON.

The study and development of membrane technologies was also included in this work as an alternative to PSA processes. The preparation of supported zeolite beta membranes was successfully achieved by exploring several combinations of seeding techniques and synthesis methods. The surface of the membranes was completely covered by well intergrown crystals. The quality of the membranes was tested by means of pervaporation of ethanol/1,3,5-triisopropylbenzene mixtures together with permporometry experiments. The performance in the vapour separation of quaternary equimolar mixtures of C_6 isomers showed that permeate flux decreases as the branching degree increases following the order: *n*HEX>>3MP>23DMB>22DMB. In the retentate, the fractions of 3MP and *n*HEX decrease while the concentration of dibranched isomers is increased compared to the feed composition. The RON of the quaternary mixture was enhanced up to 5 points with the best synthesized membrane.

The potential application of the novel metal-organic frameworks (MOFs) as an alternative to zeolites was also addressed. A screening study for mixtures of C_6 isomers was performed in three different MOFs.The first is a rigid zirconium terephthalate UiO-66, which possesses two types of cages of diameter 12 Å and 9 Å; the second is a chromium trimesate MIL-100(Cr), which possesses a rigid structure with giant cages accessible through 5-9 Å microporous windows; and the third is the flexible $Zn_2(BDC)_2(H_2O)_2\cdot(DMF)$ (MOF-2), in which the pore system contains 1-D large channels. Multicomponent equimolar experiments show that UiO-66 exhibits inverse shape selectivity for C_6 isomers, being the retention governed by the rotational freedom of the molecules in the small cages. In the MIL-100(Cr), the sorption hierarchy is similar to the one found in zeolite beta. Finally, MOF-2 exhibits extraordinary *n*/iso selectivity, by making use of an unusual guest-dependent dynamic behaviour to exclusively take up nHEX, while hindering the access of branched C_6 isomers to the pore system.

Resumo

O objectivo deste trabalho consistiu no desenvolvimento de processos adsorptivos com potencial para a aplicação na indústria de refinação, nomeadamente, na separação de parafinas com elevado índice de octanas (parafinas HRON) a partir de fracções de nafta leve. O desenvolvimento de um processo adsorptivo requer em primeiro lugar o conhecimento detalhado do equilíbrio e da cinética de adsorção e do seu impacto na resposta dinâmica de um leito de partículas de adsorvente. Procedeu-se numa primeira fase, à medição de isotérmicas de equilíbrio de adsorção dos isómeros de C_6, *n*-hexano (*n*HEX), 3-metilpentano (3MP), 2,3-dimetilbutano (23DMB), e 2,2-dimetilbutano (22DMB), e correspondente misturas, a partir da medição de curvas de ruptura em zeólito beta. Este adsorvente é produzido em larga escala para processos catalíticos e foi seleccionado porque o seu sistema de poros possui características interessantes para a separação entre os hexanos bi-ramificados e os seus isómeros mono-ramificados de baixo índice de octanas (parafinas LRON). Observou-se que a hierarquia de adsorção no zeólito beta é ditada pelo grau de ramificação dos isómeros, sendo o composto mais adsorvido o *n*HEX. O zeólito beta mostra um grau de selectividade significativo entre isómeros mono- e bi-ramificados, especialmente na gama de baixa pressão parcial. Foi desenvolvido um modelo denominado Tri-site Langmuir para interpretar com rigor os dados de equilíbrio.

A cinética de sorção, estudada através da técnica cromatográfica ZLC, permitiu encontrar a natureza do mecanismo de difusão controlante. Para *n*HEX e 3MP, a cinética é governada pela difusão nos macroporos, enquanto que, para 23DMB e 22DMB, o controlo da cinética é aparentemente repartido entre macroporos e microporos.

O estudo da dinâmica de fracções equimolares C_5/C_6 num leito fixo de zeólito beta monstra que a hierarquia de sorção varia com a temperatura. À temperatura de 583 K, uma fracção enriquecida com 22DMB, *i*PEN (isopentano) e 23DMB, pode ser selectivamente separada do isomerado. No caso em que a alimentação tem a composição típica do produto resultante da hidroisomerização, obtém-se uma fracção enriquecida com uma percentagem significativa de *n*PEN (*n*-pentano), o que reduz o índice de octano do produto final. No entanto, a utilização de um leito em camadas, com zeólito 5A e zeolito beta, contribui para a retenção do *n*PEN, evitando a contaminação da fracção enriquecida. Obtém-se assim, no produto acumulado, um índice de octanas máximo de 92.5 pontos. O comportamento dinâmico da fracção C_5/C_6 num leito não-isotérmico e não-adiabático foi simulado com o Aspen Adsim. As simulações oferecem uma boa descrição do conjunto de dados experimentais.

O desempenho de um processo de adsorção cíclico, baseado no conceito “Pressure Swing Adsorption” (PSA), para a produção de parafinas HRON a partir de fracções de nafta leve na gama C_5/C_6, foi simulado utilizando um modelo detalhado. A camada de zeólito 5A adsorve selectivamente *n*-parafinas LRON, enquanto que a camada de zeólito beta reduz a concentração do LRON 3MP na fracção enriquecida com compostos HRON. Foi estudado o efeito de diferentes variáveis independentes (razão zeólito 5A/zeólito beta, razão purga/alimentação, tempo de ciclo, modo de despressurização, e temperatura de operação) no desempenho do processo (RON do produto, recuperação de compostos HRON, pureza dos compostos HRON, e produtividade do adsorvente). Demonstrou-se que uma relação óptima entre as quantidades de zeólito 5A e de zeólito beta, permite melhorar o RON do produto até 1.0 ponto, comparativamente ao processo que utiliza exclusivamente zeólito 5A. Além disso, as simulações mostram que um aumento de 20 K na temperatura de operação, resulta num ganho adicional de 0.2 RON.

O estudo e o desenvolvimento de tecnologias de membranas foram também incluídos neste trabalho, como uma alternativa aos processos PSA. A preparação de membranas de zeólito beta foi levada a cabo combinando diferentes técnicas de “seeding and secondary growth”. O desempenho das membranas na separação de vapor de misturas quaternárias equimolares de isómeros C_6 mostrou que o fluxo de permeado diminui com o aumento do grau de ramificação na seguinte ordem: nHEX>> 3MP> 23DMB> 22DMB. No retido, a fracção de isómeros bi-ramificados aumenta relativamente à composição da alimentação. O RON da mistura quaternária foi reforçado até 5 pontos, com a melhor membrana.

A potencial aplicação dos “metal-organic frameworks” (MOFs) como alternativa aos zeólitos foi também abordada neste trabalho. Foi estudada a performance de três diferentes MOFs para a separação de misturas de isómeros C_6. O UiO-66, é uma estrutura rígida constituída por dois tipos de jaulas de diâmetro 12 Å e 9 Å. O MIL-100(Cr), possui uma estrutura rígida com jaulas gigantes, acessível através de janelas com diâmetro entre 5 e 9 Å. O MOF-2, apresenta uma estrutura flexível e um sistema de canais largos 1D. As experiências com misturas equimolares mostram que o UiO-66 exibe selectividade inversa para isómeros C_6, sendo a retenção ditada pela liberdade de rotação das moléculas nas jaulas de 9 Å. No MIL-100(Cr), a hierarquia de adsorção é similar aquela encontrada no zeólito beta. Finalmente, o MOF-2 exibe um mecanismo dinâmico de contracção dos poros, induzido pela presença de adsorbato. Essa contracção resulta na adsorção selectiva de *n*-parafinas, e na consequente exclusão dos compostos ramificados.

Sommaire

L'objectif de cette thèse est de développer des procédés de séparation par adsorption, avec grand potentiel d'applications sur l'industrie du raffinage, à savoir, pour la séparation des paraffines à indice d'octane élevé (paraffines HRON) à partir des fractions de naphta légère. Le développement d'un processus d'adsorption requiert d'abord une connaissance détaillée des paramètres cinétiques et des équilibres d'adsorption, et de leur impact sur la réponse dynamique d'une colonne d'adsorption. Nous avons commencé par mesurer les isothermes d'équilibre d'adsorption des isomères de C_6 purs, *n*-hexane (*n*HEX), 3-methylpentane (3MP), 2,3-dimethylbutane (23DMB), et 2,2-dimethylbutane (22DMB), et de ces mélanges, à partir des courbes de perçage dans la zéolithe bêta. Cet adsorbant a été sélectionné car son système de pores possède des caractéristiques intéressantes pour la séparation des HRON C_6 di-branchés, de leurs isomères mono-branchés de faible indice d'octane (paraffines LRON). Il a été constaté que la hiérarchie d'adsorption dans la zéolithe bêta était plus favorable à l'adsorption des isomères peu ramifiés. La zéolithe bêta présente une sélectivité considérable pour la séparation mono-/di-branchés, surtout dans la gamme de basse pression partielle. L'analyse des événements de sorption au niveau moléculaire a servi de support pour le développement d'un modèle Tri-site Langmuir, qui a été utilisé pour interpréter les données d'équilibre avec une bonne précision.

La cinétique de sorption, étudiée par la technique ZLC, nous a permis de trouver la nature du mécanisme de contrôle de la diffusion. Pour *n*HEX et 3MP, la diffusion dans les macropores est dominante, alors que pour 23DMB et 22DMB, le système est apparemment régi par la diffusion à la fois dans les macropores et les micropores.

La dynamique des fractions équimolaire de paraffines C_5/C_6 dans un lit fixe de zéolithe bêta a été étudiée. Les courbes de perçage des mélanges montrent que la hiérarchie de sorption est dépendante de la température. À 583 K, une fraction HRON enrichi de 22DMB, *i*PEN et 23DMB peut être sélectivement séparée d'un flux d'alimentation d'isomérat. Pour le cas des flux d'alimentation avec la composition typique du produit de l'hydroisomérisation, la fraction enrichie contient du LRON nPEN, ce qui diminue l'indice d'octane du produit final. Néanmoins, l'utilisation d'un lit d'adsorbant avec des couches de zéolite 5A et zéolithe bêta, peut être employée pour déplacer le *n*PEN de la fraction enrichie. En résultat, on peut obtenir a la sortie de la colonne un isomérat avec un indice d'octane maximum d'environ 92.5 points. Aspen Adsim a été utilisé pour simuler le comportement dynamique d'une fraction C_5/C_6 dans

un lit fixe non-isotherme et non-adiabatique, donnant une bonne description de l'ensemble des données expérimentales.

La performance d'un procédé cyclique d'adsorption, basé sur le concept "Pressure Swing Adsorption" (PSA), pour la production de paraffines HRON à partir d'une fraction de naphta légère C_5/C_6, a été simulé utilisant un modèle détaillé. Une couche de zéolithe 5A a été utilisée pour l'adsorption sélective des *n*-paraffines, tandis qu'une couche de zéolithe bêta a permit de réduire la concentration du LRON 3MP dans le produit enrichie. On a évalué l'effet de diverses variables indépendante (ratio zéolite 5A/zéolithe bêta, ratio purge/alimentation, le temps de cycle, le mode de dépressurisation, et la température d'opération) sur la performance du processus (RON du produit, récupération des composées HRON, pureté des composées HRON, et productivité de l'adsorbant). Il a été montré qu'un ratio optimal zéolithe 5A/zéolithe bêta, peut augmenter le RON du produit jusqu'à 1.0 point, comparativement aux processus traditionnels qui utilisent uniquement la zéolithe 5A. En outre, les simulations montrent que l'augmentation de 20 K sur la température opération, contribue à un gain additionnel de 0.2 points dans l'indice d'octane de la fraction enrichie.

L'étude et le développement des technologies membranaires ont été également inclus dans ce travail, comme une alternative aux procédés PSA. Des membranes de zéolithe bêta ont été synthétisées sur des supports céramiques, en utilisant la technique «seeding and secondary growth». Leur performance pour la séparation des mélanges de vapeur équimolaire d'isomères C_6 a montré que le flux de perméat diminue avec le degré de ramification suivant l'ordre. Dans le rétentat, la concentration de composé di-branchées augmente par rapport à la composition de l'alimentation. Le RON du mélange a été amélioré jusqu'à 5 points avec la meilleure membrane.

Le potentiel des « metal-organique frameworks » (MOFs) a aussi été abordé comme une alternative aux zéolithes. Trois différents MOFs ont été étudiés pour la séparation de mélanges d'isomères C_6: la structure rigide, UiO-66, qui possède deux types de cages de 9 Å et 12 Å ; le MIL-100(Cr), rigide, avec des cages géantes accessible par des fenêtres entre 5 Å et 9 Å ; et le MOF-2, une structure flexible qui contient des canaux larges 1D. Les courbes de perçage des mélanges équimolaires montrent que l'UiO-66 présente une sélectivité inverse pour les isomères C_6. La rétention dans la maille du UiO-66 est régie par la liberté rotationnelle des molécules dans les cages 9 Å. Dans le MIL-100(Cr), la hiérarchie de sorption est similaire à celle observée dans la zéolithe bêta. Enfin, le MOF-2 a démontré une extraordinaire sélectivité *n*/iso-alcanes, en faisant usage d'un mécanisme dynamique de contraction des pores, qui est induit par la présence d'adsorbat. Cette contraction a comme résultat l'adsorption sélective de *n*-paraffines, et la conséquente exclusion des paraffines branchées.

Table of Contents

LIST OF FIGURES **VII**

LIST OF TABLES **XVII**

LIST OF SYMBOLS **XX**

INTRODUCTION **1-1**

1.1 Relevance and Motivation **1-1**
1.1.1 The Development of Light Naphtha Isomerization Processes 1-2
1.1.2 Zeolites as Separating Media for Recycling Technologies 1-10
1.1.3 The Zeolite Membrane Alternative 1-13
1.1.4 Metal-Organic Frameworks as an Alternative to Zeolites 1-15

1.2 Objectives and Outline **1-16**

1.3 References **1-24**

SINGLE ADSORPTION EQUILIBRIUM AND KINETICS OF C_6 ISOMERS IN ZEOLITE BETA **2-1**

2.1 Introduction **2-2**

2.2 Adsorption Equilibria **2-2**
2.2.1 Langmuir Model 2-3
2.2.2 Nitta Model 2-4
2.2.3 Dual-site Langmuir Model 2-5
2.2.4 Toth Model 2-6

2.3 Sorption Kinetics **2-6**
2.3.1 Modelling ZLC Experiments 2-7

2.4 Hexane Isomers Configuration **2-9**

2.5 Zeolite Beta Structure 2-10

2.6 Experimental Section 2-10
2.6.1 Adsorbent Characterization 2-10
2.6.2 Adsorption Equilibrium and ZLC Apparatus 2-15
2.6.3 Experimental Procedure 2-17

2.7 Results and Discussion 2-19
2.7.1 Pure component Breakthrough Curves 2-19
2.7.2 Pure component Equilibrium Data 2-21
2.7.3 Modelling of Pure Component Isotherms 2-28
2.7.4 Kinetics of Sorption 2-32

2.8 Conclusions 2-41

2.9 References 2-42

MULTICOMPONENT ADSORPTION OF C_6 ISOMERS IN ZEOLITE BETA 3-1

3.1 Introduction 3-2

3.2 Theoretical Analysis 3-2
3.2.1 Equilibrium Data from Multicomponent Breakthrough Curves 3-2
3.2.2 Tri-site Langmuir Model 3-3
3.2.3 Support to TSL model Theory from Molecular Simulation 3-6

3.3 Modeling of Breakthrough Experiments 3-10

3.4 Experimental Section 3-15
3.4.1 Experimental Set-up 3-15
3.4.2 Experimental Procedure 3-18

3.5 Results and Discussion 3-20
3.5.1 TSL Model Applied to the Adsorption of C_6 Isomers in Zeolite Beta 3-20
3.5.2 Binary Adsorption Isotherms 3-23
3.5.3 Ternary Adsorption Isotherms 3-23
3.5.4 Quaternary Adsorption Isotherms 3-26

3.6 Multicomponent Breakthrough Curves 3-30
3.6.1 Influence of Temperature on Binary Breakthrough Curves of C_6 Isomers 3-30
3.6.2 Influence of Temperature on Ternary Breakthrough Curves of C_6 Isomers 3-33
3.6.3 Influence of Temperature on Quaternary Breakthrough Curves of C_6 Isomers 3-35

3.7 Conclusions 3-37

3.8 References 3-38

ADSORPTION DYNAMICS OF C_5/C_6 FRACTIONS IN A LAYERED BED OF ZEOLITE BETA AND ZEOLITE 5A 4-1

4.1 Introduction 4-2

4.2 Migration to Aspen Adsim Simulator 4-4

4.3 Model Development 4-6
4.3.1 Feed Model 4-7
4.3.2 Product Model 4-7
4.3.3 Bed Model 4-8

4.4 Experimental Section 4-17
4.4.1 Adsorbent and Adsorbates 4-17
4.4.2 Experimental Equipment and Procedure 4-17

4.5 Results and Discussion 4-17
4.5.1 Adsorption Equilibrium of C_5/C_6 Isomers in Zeolite Beta 4-17
4.5.2 Equimolar C_5/C_6 Six-Component Breakthrough Curves 4-22
4.5.3 Analysis of Heat Effects in Adsorption Column Dynamics 4-25
4.5.4 C_5/C_6 Six-Component Breakthrough Curve of the Typical Hydroisomerization Reactor Product 4-27
4.5.5 Simulation of C_5/C_6 Six-Component Breakthrough Curves on a Layered Bed 4-30

4.6 Conclusions 4-32

4.7 References 4-33

SEPARATION OF C_5/C_6 LIGHT NAPHTHA BY LAYERED PRESSURE SWING ADSORPTION 5-1

5.1 Introduction 5-2

5.2 Study of a Single Column Layered PSA Cycle 5-5
5.2.1 PSA Process Description 5-5
5.2.2 Definition of the Parametric Study 5-10
5.2.3 Process Performance Criteria 5-11

5.3 Model Development 5-12
5.3.1 Feed Model 5-13
5.3.2 Valve Model 5-13
5.3.3 Tank Void Model 5-14
5.3.4 Product Model 5-14
5.3.5 Bed Model 5-14
5.3.6 Cycle Organizer 5-16
5.3.7 Numerical Methods 5-18

5.4 Results and Discussion 5-19

5.4.1 Layered PSA –General Dynamics 5-19
5.4.2 Concentration Profiles in the Layered Bed at Cyclic Steady State 5-24
5.4.3 Effect of the P/F Ratio for Different Values of L_{5A}/L_B 5-29
5.4.4 Effect of the Cycle Time for Different Values of L_{5A}/L_B 5-34
5.4.5 Effect of the Temperature for Different Values of L_{5A}/L_B 5-34
5.4.6 Effect of the Depressurization Mode 5-36
5.4.7 General Performance of the Layered PSA Process 5-37

5.5 Conclusions 5-40

5.6 References 5-41

ZEOLITE BETA MEMBRANES FOR THE SEPARATION OF C_6 ISOMERS 6-1

6.1 Introduction 6-2

6.2 Experimental 6-5
6.2.1 Preparation of α-Alumina Supported Zeolite Beta Membranes 6-5
6.2.2 Static Characterization of Membranes and Materials 6-8
6.2.3 Dynamic Characterization of Supported Membranes 6-10

6.3 Results and Discussion 6-18
6.3.1 XRD Patterns 6-18
6.3.2 N_2 Permeation 6-19
6.3.3 Morphology 6-20
6.3.4 TIPB Pervaporation 6-21
6.3.5 Permporometry 6-26
6.3.6 Mixture Separation Measurements 6-27

6.4 Conclusions 6-33

6.5 References 6-34

SEPARATION OF C_6 ISOMERS IN METAL-ORGANIC FRAMEWORKS 7-1

7.1 Introduction 7-2

7.2 Activation of the MOFs and Preparation of the Adsorption Column 7-3

7.3 Separation of C_6 Isomers in the Rigid MOF UiO-66 7-4
7.3.1 Experimental Procedure 7-4
7.3.2 Adsorption of Quaternary Mixtures 7-6

7.4 Separation of C_6 Isomers in the Rigid MOF MIL-100(Cr) 7-13
7.4.1 Experimental Procedure 7-14

7.4.2 Influence of the Coordinated Water in the Adsorption of C_6 Isomers in MIL-100(Cr) 7-15
7.4.3 Effect of the Pressing/Shaping on the Adsorption of C_6 Isomers in the MIL-100(Cr) 7-18

7.5 Separation of C_6 Isomers in the Flexible MOF-2 7-20
7.5.1 Experimental Procedure 7-20
7.5.2 Pure Component Adsorption 7-22
7.5.3 Binary and Ternary Adsorption 7-29

7.6 Conclusions 7-33

7.7 References 7-34

CONCLUSIONS AND SUGGESTIONS FOR FUTURE WORK 8-1

LIST OF PUBLICATIONS I

APPENDICES V

Single Sorption Data for *n*PEN and *i*PEN in Zeolite Beta Pellets vi

Derivation of the Isosteric Heat of Adsorption for TSL Model viii

List of Figures

INTRODUCTION 1-1

Figure 1.1. World trends in the refining product demand. Numbers are the percentage of total demand. Source: IFP (Benazzi and Cameron, 2005). 1-2

Figure 1.2. Equilibrium composition of pentane and hexane isomers as a function of the isomerization temperature. Solid line represents the liquid phase and dashed line gas phase equilibrium (Vermeiren and Gilson, 2009). 1-4

Figure 1.3. Simplified scheme of the conventional Total Isomerization Process (TIP): (I) isomerization reactor; (S) hydrogen separator; (C) compressor; (A) adsorption stage; (D) desorption stage. Adapted from Cusher (2004a). 1-5

Figure 1.4. Typical composition of streams in Figure 1, according to Cusher (2004a). 1-6

Figure 1.5. Variations of the conventional isomerization process: a) post-separation isomerization process with dual-layer PSA unit (Volles, 1992) and b) basic *Ipsorb* process with deisopentanizer column, DIP (Minkkinen et al., 1993). 1-7

Figure 1.6. View of a 10,500 BPSD *Ipsorb* unit (taken from Watripont and Domergue, 2003). 1-9

Figure 1.7. Deisohexanizer column: height = 57 m, diameter = 7 m, weight = 221 tons. 1-9

Figure 1.8. Schematic illustration of the molecular sieving effect for normal and branched paraffins in zeolite 5A. 1-12

Figure 1.9. Commercial application of zeolite membranes: *a)* Mitsui bio-ethanol pilot plant in Brazil (3.000 l/d); *b)* Multichannel 4A Smart zeolite membranes produced by Inocermic GmbH; *c)* Module with 5.8 m^2 4A Smart zeolite membranes. 1-13

Figure 1.10. Pore size tuning exemplified with the IRMOF family (Eddaoudi, 2002). 1-15

Figure 1.11. Hexane isomers: research octane number (RON); boiling point (T_b) and kinetic diameter (d_k). 1-17

Figure 1.12. Zeolite beta framework and maximum free spheres fitting inside the channels. 1-19

Figure 1.13. Flowchart for the development of an adsorption process. 1-21

Figure 1.14. Thesis organization. 1-23

SINGLE ADSORPTION EQUILIBRIUM AND KINETICS OF C_6 ISOMERS IN ZEOLITE BETA 2-1

Figure 2.1. Porosity levels within an adsorbent particle and associated diffusion mechanisms. (Adapted from Bárcia, 2006) 2-7

Figure 2.2. Tree-dimensional view, research octane number (RON), boiling point (T_b) and kinetic diameter (d_k) of hexane isomers. 2-9

Figure 2.3. Stereographic drawings and perspectives views of zeolite beta viewed along axis (a) [010], (b) [100] and (c) [001]. The 12-MR pores of straight and zigzag channels were also shown for a good visualization of its structure. 2-11

Figure 2.4. (A) Zeolite beta pellets provided by Süd-Chemie AG (Si/Al=75). Scaning electron micrographs (SEM): (B) top view of the pellet (50×); (C) and (D) different view of transversal cut (15.000×). 2-12

Figure 2.5. XRD pattern of the commercial zeolite beta powder compared with the reference simulated pattern. 2-13

Figure 2.6. Pore size distribution obtained from the N_2 desorption data using the BJH formalism, in the Süd-Chemie AG zeolite beta sample. 2-14

Figure 2.7. Front view of the adsorption equilibrium and ZLC apparatus. 2-15

Figure 2.8. Schematic diagram of the ZLC experiment apparatus used to measure adsorption equilibibrium and ZLC data. 2-16

Figure 2.9. Schematic diagram showing the method used to calculate the amount adsorbed from single breakthrough curve experiments. 2-18

Figure 2.10. Single component breakthrough curves at partial pressure near to 12 kPa, for 22DMB, 23DMB, 3MP and *n*HEX at 423 K, 473 K and 523 K. 2-20

Figure 2.11. Adsorption equilibrium isotherms of hexane isomers on zeolite beta. (a) 22DMB, (b) 23DMB, (c) 3MP and (d) *n*HEX on pellets of zeolite beta at 423K, 473K and 523K. 2-25

Figure 2.12. Semilog plot of p/q vs. q for analysis of virial isotherm of (a) 22DMB, (b) 23DMB, (c) 3MP, (d) *n*HEX. 2-26

Figure 2.13. Coverage dependence of isosteric heat of adsorption. 2-28

Figure 2.14. Adsorption equilibrium isotherm models fitted to experimental data of (a) 22DMB, (b) 23DMB, (c) 3MP and (d) *n*HEX on pellets of zeolite beta. The represented models are Langmuir, dual-site Langmuir (DSL), Toth and Nitta *et al*. 2-30

Figure 2.15. Effect of temperature on ZLC desorption curves: (a) 22DMB, (b) 23DMB, (c) 3MP and (d) *n*HEX. Semilog plot of c/c_0 *vs* time. 2-37

Figure 2.16. Arrhenius plot of τ_{dif} for the hexane isomers. 2-39

MULTICOMPONENT ADSORPTION OF C_6 ISOMERS IN ZEOLITE BETA 3-1

Figure 3.1. Schematic diagram showing the method used to calculate the amount adsorbed from experimental binary breakthrough curves. 3-3

Figure 3.2. Ternary sorption data (22DMB/23DMB/3MP at T = 423K) cannot be predicted using the DSL model parameters from the fitting of the pure component isotherms (Table 2.5). 3-4

Figure 3.3. Schematic representation of the hypothetical distribution of the sorption sites in the zeolite beta framework. 3-5

Figure 3.4. Energy profiles for the BEA framework and schematic representation of the adsorption sites: S, straight channels; I, intersection and Z, zigzag channels. 3-7

Figure 3.5. Snapshots obtained at 100 MPa and at 423 K for a) 22DMB and b) 23DMB. 3-8

Figure 3.6. Snapshot obtained at 100 MPa and at 423 K for c) 3MP and d) *n*HEX. 3-9

Figure 3.7. Porosity levels in the fixed-bed and corresponding resistance to mass transfer. 3-10

Figure 3.8. Schematic diagram of the multicomponent breakthrough experimental apparatus. 3-16

Figure 3.9. View of the multicomponent breakthrough apparatus (a), detailed view of the independent ventilated ovens with adsorbent column (*left*) and chromatographic column (*right*) (b), and 10-loops sample collector (c). 3-17

Figure 3.10. Schematic representation of the experimental procedure used for the determination of the multicomponent breakthrough curves (e.g., ternary mixture experiment). 3-18

Figure 3.11. FID chromatogram of a C_6 isomers equimolar mixture analyzed in a 60m MTX-1 capillary column at 313 K and 20 psi helium pressure (FID temp = 523 K). 3-19

Figure 3.12. Pure component adsorption equilibrium isotherm fitted with the TSL model. 3-21

Figure 3.13. Binary adsorption equilibrium isotherms for an equimolar mixture of (a) 22DMB/3MP and (b) 23DMB/3MP. 3-24

Figure 3.14. Ternary adsorption equilibrium isotherms for an equimolar mixture of 22DMB/23DMB/3MP on pellets of zeolite beta. 3-25

Figure 3.15. Quaternary adsorption equilibrium isotherms for an equimolar mixture of 22DMB/23DMB/3MP/nHEX on pellets of zeolite beta. 3-27

Figure 3.16. Effect of temperature in the sorption selectivity for an equimolar quaternary mixture 22DMB/23DMB/3MP/*n*HEX as a function of a) total hydrocarbon pressure and b) total hydrocarbon loading. 3-28

Figure 3.17. Effect of temperature on binary breakthrough curves of equimolar mixtures a) 22DMB/3MP and b) 23DMB/3MP at 1) 423 K, 2) 473 K and 3) 523 K and hydrocarbon pressure near to 14 kPa. 3-31

Figure 3.18. Effect of temperature on ternary breakthrough curves of equimolar mixtures 22DMB/23DMB/3MP at a) 423 K, b) 473 K and c) 523 K and hydrocarbon pressure near to 16 kPa. 3-34

Figure 3.19. Effect of temperature on quaternary breakthrough curves of equimolar mixtures 22DMB/23DMB/3MP/*n*HEX at a) 423 K, b) 473 K and c) 523 K and hydrocarbon pressure near to 9 kPa. 3-36

ADSORPTION DYNAMICS OF C_5/C_6 FRACTIONS IN A LAYERED BED OF ZEOLITE BETA AND ZEOLITE 5A 4-1

Figure 4.1. a) Simplified scheme of a conventional Total Isomerization Process. b) Typical composition of streams in Figure 4.1a according to Holcombe et al. (1990). 4-2

Figure 4.2. RON *versus* kinetic diameter for C_5/C_6 alkanes. 4-3

Figure 4.3. Aspen Adsim flowsheeting environment. 4-5

Figure 4.4. Breakthrough curve simulated with the FORTRAN code used in chapter 3 (dashed line) and with Aspen Adsim (solid line), using the model parameters of Table 3.1 and Table 3.3. 4-6

Figure 4.5. Simple flowsheet with three blocks: feed (F1), bed (B1), and product (P1). 4-7

Figure 4.6. Heat of adsorption predicted from TSL isotherm model as a function of the loading. 4-19

Figure 4.7. Experimental and fitted adsorption equilibrium isotherm for a C_5/C_6 six-component equimolar mixture of 22DMB/23DMB/3MP/*n*HEX/*i*PEN/*n*PEN on pellets of zeolite beta at: a) *T* = 423K; b) *T* = 473K and c) *T* = 523K. 4-21

Figure 4.8. Effect of the temperature on the six-component breakthrough curves of the equimolar feed mixtures *i*PEN/*n*PEN/22DMB/23DMB/3MP/*n*HEX at p_{mix} = 9.8 kPa and *a) T* = 423 K (Run *Eq6_3*), *b) T* = 473 K (Run *Eq6_7*) and *c) T* = 523 K (Run *Eq6_10*). 4-23

Figure 4.9. Six-component breakthrough curves for an equimolar feed mixture containing *i*PEN/*n*PEN/22DMB/23DMB/ 3MP/*n*HEX at *T* = 583 K and p_{mix} = 9.7 kPa (Run *Eq6_12*). 4-24

Figure 4.10. Isothermal adsorption (dashed lines) *versus* non-isothermal and non-adiabatic adsorption (solid lines). 4-26

Figure 4.11. Six-component breakthrough curve and RON history of the accumulated product for a feed mixture *i*PEN/*n*PEN/22DMB/23DMB/3MP/*n*HEX at *T* = 473 K and p_{mix} = 10.2 kPa (Run *Iso6_2*). 4-26

Figure 4.12. Simulation of the six-component breakthrough curve and RON history of the accumulated product for a feed mixture *i*PEN/*n*PEN/22DMB/ 23DMB/3MP/*n*HEX in a layered bed of zeolite 5A and zeolite beta at p_{mix} = 10.2 kPa: a) at *T* = 473 K (Run *Lay6_1*); b) at *T* = 523 K (Run *Lay6_2*). 4-31

SEPARATION OF C_5/C_6 LIGHT NAPHTHA BY LAYERED PRESSURE SWING ADSORPTION 5-1

Figure 5.1. Schematic diagram and details of the product obtained through the process disclosed by a) Minkkinen et al (1993), and b) Volles (1992). 5-3

Figure 5.2. Proposed scheme: *TIP* process incorporating a dual-layer PSA unit. 5-5

Figure 5.3. Sequence of the 4-steps PSA cycle with (a) countercurrent and (b) co-current depressurization mode. 5-9

Figure 5.4. Schematic diagram of the single layered bed PSA with input/output streams and *gas_model* blocks used for the Aspen Adsim simulations. 5-12

Figure 5.5. Cycle organizer: Steps and cycle description. 5-17

Figure 5.6. Cycle organizer: Manipulated variables. Example given for step 2 (feed). 5-18

Figure 5.7. Historical of the pressure and molar flow obtained at the column outlet at CSS (*Run_32*). 5-19

Figure 5.8. Transient variation of the gas phase temperature at the column outlet and average RON of the accumulated product (*Run_32*). 5-21

Figure 5.9. Evolution of the gas phase temperature profile at the end of the feed step with the cycle number (*Run_32*). 5-22

Figure 5.10. Evolution of the gas velocity profile at the end of the feed step with the cycle number (*Run_32*). 5-22

Figure 5.11. Evolution of the gas phase velocity profile obtained along the bed at CSS (*Run_32*): a) pressurization with feed; b) adsorption; c) co-current depressurization and d) counter-current purge with pure H_2. 5-23

Figure 5.12. Gas phase concentration profile obtained along the bed at the end of each step at CSS (*Run_32*): a) pressurization with feed; b) adsorption; c) co-current depressurization and d) counter-current purge with pure H_2. 5-25

Figure 5.13. Solid phase concentration profile obtained along the bed at the end of each step at CSS (*Run_32*): a) pressurization with feed; b) adsorption; c) co-current depressurization and d) counter-current purge with pure H_2. 5-26

Figure 5.14. Molar composition of the product stream as a function of the total cycle time at CSS. 5-27

Figure 5.15. Evolution of the gas phase molar fraction and temperature profiles during the adsorption step at CSS (*Run_32*): a) t_{feed} = 0 s, b) t_{feed} = 20 s, c) t_{feed} = 40 s and d) t_{feed} = 60 s. 5-28

Figure 5.16. Effect of the *P*/*F* ratio on the (a) product average RON and (b) adsorbent productivity, at CSS (*T* = 423K, t_{feed}= t_{purge}= 80 s). 5-30

Figure 5.17. Effect of the *P*/*F* ratio on the composition of a) isomerate product, and b) recycle stream, and corresponding accumulated RON. 5-32

Figure 5.18. Effect of the cycle time on the composition of a) isomerate product, and b) recycle stream, and corresponding accumulated RON. 5-33

Figure 5.19. Effect of the operating temperature on the composition of a) isomerate product, and b) recycle stream, and corresponding accumulated product RON. 5-35

Figure 5.20. Product average RON as a function of the zeolite 5A layer length and purge-to-feed ratio at *T* = 523 K and t_{press}/t_{feed} = 20/80 s (*Run 1-21*). 5-38

Figure 5.21. HRON purity as a function of the zeolite 5A layer length and purge-to-feed ratio at *T* = 523 K and t_{press}/t_{feed} = 20/80 s (*Run 1-21*). 5-38

Figure 5.22. Recovery of HRON molecules as a function of the zeolite 5A layer length and purge-to-feed ratio at *T* = 523 K and t_{press}/t_{feed} = 20/80 s (*Run 1-21*). 5-39

Figure 5.23. Adsorbent productivity as a function of the zeolite 5A layer length and purge-to-feed ratio at T = 523 K and t_{press}/t_{feed} = 20/80 s (*Run 1-21*). 5-39

ZEOLITE BETA MEMBRANES FOR THE SEPARATION OF C_6 ISOMERS 6-1

Figure 6.1. Conceptual design of a novel ZMR process. 6-3

Figure 6.2. Tubular α-Al_2O_3 support from Inocermic GmbH, and application of glaze (a); SEM observation of the support cross-section showing the asymmetric structure (b). 6-6

Figure 6.3. View of the autoclave used for hydrothermal synthesis, with PTFE liner. 6-7

Figure 6.4. Flowchart for the preparation of zeolite membranes. 6-8

Figure 6.5. Views of the membrane module developed at LSRE: (a) cut view; (b) disassembled module with rings and flange screws; (c) assembled module; (d) ZMR with catalyst packed in the shell side (vol. = 10 cm^3); (e) connection to the 8-way crossover valve of the ZEOPERM unit. 6-11

Figure 6.6. Schematic representation of the ZEOPERM setup operating in the N_2 permeance mode. 6-12

Figure 6.7. Schematic representation of the ZEOPERM setup operating in the pervaporation mode. 6-12

Figure 6.8. Schematic representation of the nano-permporometry setup: BPC – back pressure controller. 6-14

Figure 6.9. Schematic representation of the ZEOPERM setup operating in the vapour separation mode: a) before permeation (feed analysis); b) during permeation (permeate and retentate analysis). 6-16

Figure 6.10. Details of the ZEOPERM setup: a1) valves and manometers lateral panel; a2) close-up of the evaporator; a3) close-up of the microprocessor controlled temperature regulator for heat tracing. 6-17

Figure 6.11. XRD patterns of uncalcined powder collected from the beta membranes synthesis compared with the (calcined) reference commercial zeolite beta. 6-19

Figure 6.12. SEM micrographs of non-calcined beta membrane MB_1: (a) cross section view; (b) top view. 6-22

Figure 6.13. SEM micrographs of non-calcined beta membrane MB_3: (a) cross section view; (b) top view. 6-23

Figure 6.14. SEM micrographs of non-calcined beta membrane MB_10: (a) cross section view; (b) top view. 6-24

Figure 6.15. SEM micrographs of non-calcined beta membrane MB_16: (a) cross section view; (b) top view. 6-25

Figure 6.16. Permporometry characterization of the different zeolite beta membranes showing the residual Helium permeance as a measure of the defect concentration. 6-26

Figure 6.17. Permeate fluxes of 22DMB, 23DMB, 3MP and nHEX equimolar mixture at T = 373 K and p_{mix} = 1 kPa through α-Al_2O_3 supported zeolite beta membranes. 6-28

Figure 6.18. Composition of the retentate 22DMB, 23DMB, 3MP and nHEX equimolar mixture at T = 373 K and p_{mix} = 1 kPa through α-Al_2O_3 supported zeolite beta membranes. 6-30

Figure 6.19. Composition of the retentate stream and octane enhancement as a function of the temperature for an equimolar mixture 22DMB, 23DMB, 3MP and nHEX through membrane MB_5. 6-32

SEPARATION OF C_6 ISOMERS IN METAL-ORGANIC FRAMEWORKS 7-1

Figure 7.1. Cages in MOF UiO-66. Adapted from Chevreau (2009). 7-5

Figure 7.2. Preparation of agglomerates from a UiO-66 powder sample. 7-5

Figure 7.3. Quaternary breakthrough curves of C_6 isomers in UiO-66. 7-8

Figure 7.4. Effect of the temperature in the sorption selectivity in MOF UiO-66 at a) 0.6 kPa, and b) 6.3 kPa. 7-9

Figure 7.5. Van der Waals volume of C_6 isomers. 7-10

Figure 7.6. Schematic representations: a) length entropy effect during adsorption of *n*HEX, 3MP, 22DMB and 23DMB in the cylindrical channels of AFI (adapted from Smit and Krishna, 2003); b) MWW supercage (taken from Huang et al. (2009)). 7-11

Figure 7.7. Cages of MIL-100(Cr) (Illustration taken from Llewellyn et al. (2008)). 7-13

Figure 7.8. MOF MIL-100(Cr) a) in powder form, and b) in agglomerate form. 7-14

Figure 7.9. Equimolar quaternary breakthrough curves of C_6 isomers in agglomerates of MIL-100(Cr), at T = 323 K and p_{isom}= 10 kPa: a) with coordinated water (Act_1); b) without coordinated water (Act_2). 7-16

Figure 7.10. Influence of the coordinated water on the adsorption capacity of MIL-100(Cr) for an equimolar quaternary mixture. 7-17

Figure 7.11. Influence of the pressing/shaping procedure on the equimolar quaternary breakthrough curves at T = 323 K and p_{isom} = 4.0 kPa: a) powder form; b) agglomerate form. 7-19

Figure 7.12. Reversible framework transformation from a) MOF-1 to b) MOF-2, and corresponding topologies c) and d), respectively (taken from Chen et al. (2009)). 7-21

Figure 7.13. Perspective view of the channels in MOF-2. The structure was generated in CrystalMaker version 2.2.3, using the crystallographic information file (cif) given in the literature (Chen et al., 2009). 7-21

Figure 7.14. MOF-2 powder packed with glass wool. 7-22

Figure 7.15. Pure component breakthrough curves for 22DMB, 3MP, and *n*HEX at *T* = 313 K and a) 6 kPa, and b) 28 kPa. 7-23

Figure 7.16. Pure component adsorption isotherms of 22DMB, 3MP, and *n*HEX at a) 313 K, and b) 343 K. Lines in *n*HEX isotherms are to aid the eyes. 7-24

Figure 7.17. Effect of the partial pressure on the single breakthrough curves of a) 3MP, and b) *n*HEX, at 313 K. 7-26

Figure 7.18. Effect of the partial pressure on the single breakthrough curves of *n*HEX at 343 K. 7-27

Figure 7.19. Schematic illustration of the ‘‘breathing’’ effect in MOF-2. 7-28

Figure 7.20. Wavefront propagation through a fixed bed packed with MOF exhibiting “breathing” effect. 7-29

Figure 7.21. Binary breakthrough curves for equimolar mixtures of 22DMB-3MP at *T* = 313 K: a) p_{isom}= 0.7 kPa (run_ *MOF2_1*); b) p_{isom}= 4.8 kPa (run_ *MOF2_2*); c) p_{isom}= 24.0 kPa (run_ *MOF2_3*). 7-30

Figure 7.22. Binary breakthrough curves for equimolar mixtures of a) 22DMB-*n*HEX (run_ *MOF2_4*), and b) 3MP-*n*HEX (run_ *MOF2_5*) at *T* = 313 K, and p_{isom}= 4.8 kPa. 7-31

Figure 7.23. Ternary breakthrough curves for equimolar mixture of 22DMB-3MP-*n*HEX (run_ *MOF2_6*) at *T* = 313 K, and p_{isom}= 24.3 kPa. 7-32

CONCLUSIONS AND SUGGESTIONS FOR FUTURE WORK 8-1

Figure 8.1. Novel concept for PSA processes with flexible MOFs: the rapid purge step. 8-8

List of Tables

INTRODUCTION 1-1

Table 1.1. Typical LSR naphtha composition and components properties (Cusher, 2004a). 1-3

Table 1.2. Zeolite structures with industrial application. 1-11

SINGLE ADSORPTION EQUILIBRIUM AND KINETICS OF C_6 ISOMERS IN ZEOLITE BETA 2-1

Table 2.1. Physical properties of zeolite beta crystals, mercury porosimetry data and N_2 adsorption data of pellets. 2-14

Table 2.2. Experimental conditions for breakthrough curves and amount adsorbed. 2-21

Table 2.3. Adsorption enthalpy's at zero coverage ($-\Delta H_0$) and Henry constants (H) on beta zeolite at 423 K, 473 K and 523 K for hexane isomers. 2-27

Table 2.4. Selectivities based on Henry's constant between hexane isomers on zeolite beta at 423 K, 473 K and 523 K 2-27

Table 2.5. Isotherm models parameters for hexane isomers on pellets of zeolite beta and average deviation between predicted values and experimental data. 2-31

Table 2.6 Diffusivity and thermodynamic data reported in the literature for C_6 isomers in silicalite and zeolite beta. 2-34

Table 2.7. Experimental conditions and model parameters for ZLC experiments. 2-36

Table 2.8. Diffusional time constants and activation energies obtained from ZLC experimental data. 2-38

Table 2.9. Importance of the diffusion mechanisms, measured by, $\gamma = \frac{D_c / r_c^2 (1+K)}{D_p / R_p^2}$. 2-39

Table 2.10. Experimental and predicted pore diffusivities of hexane isomers in zeolite beta. 2-40

MULTICOMPONENT ADSORPTION OF C_6 ISOMERS IN ZEOLITE BETA 3-1

Table 3.1. TSL model parameters and deviations between model and experiments. 3-22

Table 3.2. Experimental conditions for multicomponent breakthrough curves, and mean absolute deviation between the TSL predictions and the experimental equilibrium data. 3-29

Table 3.3. Dynamic model parameters for the simulation of multicomponent breakthrough curves. 3-32

ADSORPTION DYNAMICS OF C_5/C_6 FRACTIONS IN A LAYERED BED OF ZEOLITE BETA AND ZEOLITE 5A 4-1

Table 4.1. Operating parameters for fixed bed adsorption and properties of zeolite beta and zeolite 5A. 4-16

Table 4.2. TSL model parameters for the adsorption equilibrium of C_5/C_6 isomers in pellets of zeolite beta. Overall saturation loading and enthalpy at zero coverage are also represented. 4-18

Table 4.3. Experimental conditions of the six-component breakthrough curves and amount adsorbed of each component in the mixture† 4-28

Table 4.4. Axial dispersion, macropore diffusion, mass and heat transfer coefficients. 4-29

SEPARATION OF C_5/C_6 LIGHT NAPHTHA BY LAYERED PRESSURE SWING ADSORPTION 5-1

Table 5.1. Operating parameters common to all simulations for the layered PSA, and properties of zeolite 5A (Silva, 1998), and zeolite beta (this work). 5-6

Table 5.2. Map of the parametric study for the optimization of the process. 5-10

Table 5.3. Mathematical model for the study of the layered bed PSA cycle. 5-15

Table 5.4. Boundary conditions associated with the 4-steps of the PSA cycle. 5-16

Table 5.5. Operating conditions and process performance of the PSA cycles simulated. *(Pressurization with feed, time of pressurization and depressurization step = 20 s)* 5-20

Table 5.6. Process performance: comparison between COD and CTD step. 5-36

ZEOLITE BETA MEMBRANES FOR THE SEPARATION OF C_6 ISOMERS 6-1

Table 6.1. N_2 permeance of the zeolite beta membranes after second synthesis and after calcination. Transmembrane pressure difference of 200 kPa. Room temperature. Si/Al ratio calculated from the composition of the synthesis mixture. 6-9

Table 6.2. Pervaporation experiments at room temperature with a 10 wt% TIPB mixture in ethanol. 6-21

Table 6.3. Vapour separation experiments of an equimolar mixture nHEX/3MP/23DMB /22DMB in He as carrier gas 50 ml/min; He sweep gas 50 ml/min; p_{mix} = 1 kPa. 6-29

SEPARATION OF C_6 ISOMERS IN METAL-ORGANIC FRAMEWORKS 7-1

Table 7.1. Experimental conditions of the multicomponent breakthrough curves in UiO-66. 7-6

Table 7.2. Experimental conditions for the equimolar quaternary breakthrough curves, and partial loadings (T = 323 K; p_{isom}= 10.0 kPa). 7-15

Table 7.3. Sorption selectivity obtained from the equimolar quaternary breakthrough curves shown in Figure 7.9. 7-17

Table 7.4. Experimental conditions for the equimolar quaternary breakthrough curves shown in Figure 7.11, and partial loadings (T = 323 K; p_{isom}= 4.0 kPa). 7-19

Table 7.5. Experimental conditions of the single breakthrough curves in MOF-2. 7-25

Table 7.6. Experimental conditions of the multicomponent breakthrough curves in MOF-2, and amount adsorbed for each run. 7-32

APPENDICES

Table A.1. Experimental conditions for single component breakthrough curves and amount adsorbed for each run. vii

List of Symbols

a_p	specific particle surface per unit volume of bed ($m^2_{particle}/m^3_{bed}$)
b	adsorption affinity constant (kPa^{-1})
b^0	frequency factor of the affinity constant (kPa^{-1})
c_i	concentration of solute *i* in fluid ($kmol/m^3$)
c_0	saturation concentration of the ZLC cell ($kmol/m^3$)
c_{out}	outlet concentration of the ZLC ($kmol/m^3$)
C_{ps}	specific heat capacity of adsorbent (kJ/kg/K)
C_{pg}	specific gas phase heat capacity at constant pressure (kJ/kmol/K)
C_{pw}	specific heat capacity of column wall (kJ/kg/K)
C_V	linear valve constant (kmol/kPa/s)
C_{vg}	specific gas phase heat capacity at constant volume (kJ/kmol/K)
d_p	pellet diameter (m)
d_k	molecular kinetic diameter (m)
d_B	internal bed diameter (m)
d_p	particle diameter (m)
D_{ax}	axial dispersion coefficient (m^2/s)
$D_{i/o}$	internal/external diameter of tubular supports (m)
D_K	Knudsen diffusion coefficient (m^2/s)
D_m	molecular diffusion coefficient (m^2/s)
D_p	macropore diffusion coefficient (m^2/s)
$E_{i,j}$	interaction energy of component *i*, in site *j* (kJ/kmol)
F_0	total molar rate of adsorptive species in the feed (mol/s)

F_i	molar rate of adsorptive species at the column outlet (mol/s)
$F_{i,0}$	molar rate of adsorptive species in the feed (mol/s)
h_p	gas-solid heat transfer coefficient (W/m^2/K)
h_w	gas-wall heat transfer coefficient (W/m^2/K)
H	Henry's constant (kg/kg$_{ads}$/kPa)
H_{ad}	dimensionless Henry's constant $\left(= \rho_p RTH / M_W\right)$
ΔH	heat of adsorption (kJ/kmol)
ΔH_0	heat of adsorption at zero coverage (kJ/kmol)
$J_0(\beta_1)$	Bessel functions of first kind and zero order (-)
$J_1(\beta_1)$	Bessel functions of first kind and first order (-)
k_f	film mass transfer coefficient (s^{-1})
k_{gz}	effective axial gas phase thermal conductivity (W/m/K)
k_{MTC}	effective mass transfer coefficient (s^{-1})
k_{sz}	effective axial solid phase thermal conductivity (W/m/K)
k_w	thermal conductivity of the column wall (W/m/K)
K	capacity factor $\left(= (1-\varepsilon_p) H_{ad} / \varepsilon_p\right)$
$\overline{K}_K$	dimensionless Henry's coefficient $\left(= RT\rho_b / \varepsilon_b (\partial q_i^* / \partial p_i)\right)$
L	ZLC operating parameter (-)
L_{5A}	length of the zeolite 5A layer (m)
L_{beta}	length of the zeolite beta layer (m)
L_B	total bed length (m)
m_{ads}	mass of adsorbent (kg)
M	number of experimental measurements for fitting procedure (-)
M_W	molecular weight (kg/kmol)
n	number of actives sites for multisite Langmuir model (-)
N	number of paraffins in the mixture (-)
Nu_w	Nusselt number for gas-wall heat transfer ($= h_w x_{char} / k_g$)

p	partial pressure (kPa)
p_{HC}	total hydrocarbon pressure (kPa)
p_{isom}	total isomers pressure (kPa)
P	total system pressure (kPa)
P_H	high feed pressure (kPa)
P_L	low purge pressure (kPa)
Pr	Prandl number ($=\mu C_{pg} / k_g M_W$)
P_s	saturated vapour pressure (kPa)
ΔP	transmembrane pressure difference (kPa)
q	adsorbed concentration of sorbate in the adsorbent (kmol/kg$_{ads}$)
q_i^*	equilibrium amount adsorbed of solute *i* (kmol/kg$_{ads}$)
$\overline{q}_i$	average amount of solute *i* adsorbed (kmol/kg$_{ads}$)
q^m	saturation loading capacity of sorbate in the adsorbent (kmol/kg$_{ads}$)
q_{mix}	total mixture loading (kmol/kg$_{ads}$)
q_{st}	isosteric heat of sorption (kJ/kmol)
$\overline{\Delta q}$	mean absolute deviation between model and experimental loading (kmol/kg$_{ads}$)
r_c	crystal radius (m)
r_{pore}	pore radius (m)
R_p	pellet radius (m)
R	universal gas constant (kPa·m^3/kmol/K)
Re	particle Reynolds number ($=d_p M_W \rho_g v_g / \mu$)
RON	research octane number (-)
s	heterogeneity parameter for Toth model (-)
S_{BET}	adsorbent BET surface area (m^2/kg)
Sc	component Schmid number ($=\mu / D_m \rho_g M_W$)
Sh	component Sherwood number ($=k_f d_p / D_m$)
$S_{i/j}$	sorption selectivity; separation factor (-)
t	time (s)

t_{st} stoichiometric time (s)

t_{cycle} total cycle time (s)

t_{dpress} time of depressurization step (s)

t_{feed} time of feed step (s)

t_{press} time of pressurization step (s)

t_{purge} time of purge step (s)

T_g gas-phase temperature (K)

T_s solid-phase temperature (K)

T_w internal wall temperature (K)

T_∞ oven temperature (K)

U_∞ wall-oven heat transfer coefficient (W/m^2/K)

v_g gas phase superficial velocity (m/s)

V_B effective volume of the bed (m^3)

V_m molar volume (m^3/mol)

x molar fraction (-)

x_{char} characteristic length (m)

y_i mol fraction of component *i* in the gas phase (-)

$y_{i,0}$ mol fraction of component *i* in the hydrocarbon feed (-)

z axial coordinate (m)

Greek Symbols

α_w ratio of the internal surface area to the volume of the column wall (m^{-1})

α'_w ratio of the log mean surface area to the volume of the column wall (m^{-1})

β radial dispersion factor for packed beds (-)

γ ratio of macropore and micropore diffusional time constants $\left(= \frac{D_c / r_c^{\,2}(1+K)}{D_p / R_p^{\,2}} \right)$

Γ_{ax} axial tortuosity factor for packed beds (-)

Γ_p	tortuosity factor (-)
δ_w	column wall thickness (m)
ε_b	interparticle voidage (m^3_{void}/m^3_{bed})
ε_p	intraparticle voidage ($m^3_{pore}/m^3_{particle}$)
ε_t	total bed voidage ($m^3_{void + pore}/m^3_{bed}$)
θ	fractional coverage of the adsorbent (-); contact angle in the Kelvin equation (°)
μ	dynamic viscosity (kg/m/s)
Π	permeance ($mol/m^2/s/Pa$)
ρ_b	adsorbent bulk density (kg/m^3)
ρ_g	gas phase molar density ($kmol/m^3$)
ρ_p	apparent pellet density (kg/m^3_{pellet})
ρ_s	solid density of pellet ($kg/m^3_{(pellet - pore)}$)
ρ_w	wall density (kg/m^3)
σ	surface tension in the Kelvin equation (N/m)
τ_{dif}	reciprocal time constant of diffusion (s^{-1})

Subscripts and Superscripts

ads	adsorbent
C5	pentane isomers
C6	hexane isomers
HC	hydrocarbon
I	sorption site located at the intersection between the channels
S	sorption site located at the straight channels
Z	sorption site located at the zigzag channels

List of Abbreviations

BPD	barrels per day (1 BPD ≈ 0.159 m^3/day)
BPSD	barrels per stream day
COD	co-current depressurization
CSS	cyclic steady state

CTD	countercurrent depressurization
DIH	deisohexanizer column
DIP	deisopentanizer column
DPR	depressurization mode
DSL	dual-site Langmuir
HRON	high research octane number
*i*PEN	2-metylbutane (also isopentane)
LDF	linear driving force
LRON	low research octane number
LSR	light straight-run naphtha
MOF	metal-organic framework
*n*HEX	*n*-hexane
*n*PEN	*n*-pentane
PR	pressurization mode
PSA	pressure swing adsorption
TEAOH	tetraethylammonium hydroxide
TIP	total isomerization process
TIPB	1,3,5-triisopropylbenzene
TSL	tri-site Langmuir
ZLC	zero-length column
ZMR	zeolite membrane reactor
22DMB	2,2-dimethylbutane
23DMB	2,3-dimethylbutane
2MP	2-methylpentane
3MP	3-methylpentane

1

Introduction

This chapter provides a general survey and critical evaluation of the technological processes and adsorbent materials currently used in the refining industry for the production of high-octane gasoline. The potential of novel alternative materials and technologies are also introduced. The objectives for the Ph.D. work are established.

1.1 Relevance and Motivation

In a world aware of the environmental concerns, it is time to research for solutions that can provide maximum energy efficiency, fulfilling at the same time the environmental standards imposed. The end of cheap oil will drive the refining industry to optimize even more the performances of their fuels, increasing the efficiency of the vehicle motors. Despite the move towards diesel in Western Europe, the global gasoline demand is forecast to slightly increase in the next decade (see Figure 1.1).

In the case of gasoline, the combustion quality is measured by the research octane number (RON). When the RON is high, the combustion occurs like a smooth explosion instead of a detonation and the performances of the motor are improved. At present,

cracking, alkylation, isomerization and other processes can be used to increase the RON of gasoline to about 90. An extra boost of the RON quality is commonly obtained by the addition of high-octane oxygenates such as the methyl tertiary butyl ether (MTBE) which has been used in the last twenty years in gasoline to replace lead as an octane enhancer. However, controversy has surrounded its use and by extension all ethers, because of concern over contamination of drinking water supplies, leading to calls for restrictions on its use (McCarthy and Tiemann, 2006). The switch to MTBE-free gasoline will require an extra effort to produce more high RON compounds from the gasoline feedstock to maintain or even further increase the quality of gasoline.

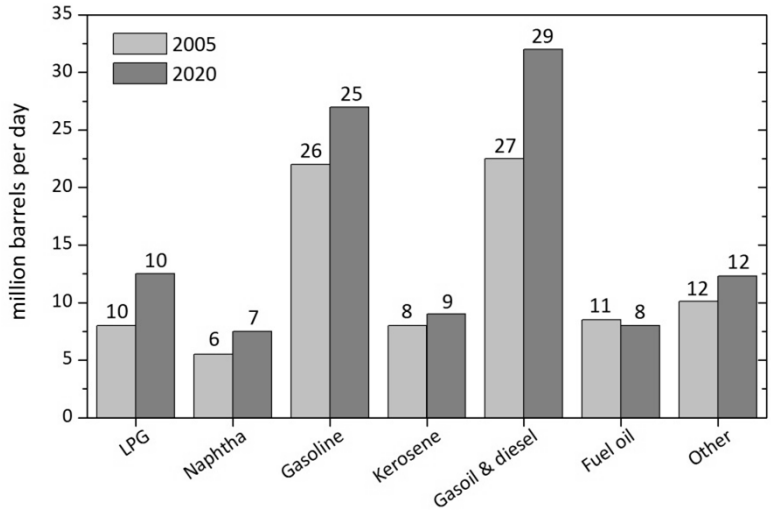


Figure 1.1. World trends in the refining product demand. Numbers are the percentage of total demand. Source: IFP (Benazzi and Cameron, 2005).

1.1.1 The Development of Light Naphtha Isomerization Processes

The light straight-run (LSR) naphtha fraction produced by fractional distillation is one of the feedstock used for the production of gasoline. The main constituents of typical LSR naphtha are listed in Table 1.1. This gasoline blending pool is about 90 percent paraffinic, clear of sulphur and aromatics, and has low benzene content. Its major constituents include C_5 and C_6 normal paraffins which have relatively low RON

compared to their branched isomers. Therefore, octane upgrading commonly uses isomerization to rearrange the structure of the linear paraffins into branched components. The first light naphtha isomerization process – the *Hysomer* process – using a zeolite-based catalyst for the conversion of linear alkanes, was started up by Shell in 1970 in La Spezia, Italy (Cusher, 1986b). Since then, other processes have been commercialized such as the CEPSA's *CKS ISOM* process with the Sud-Chemie *HYSOPAR* catalyst (Schmidt and Köhler, 2002). The paraffin isomerization is performed in a hydrogen atmosphere at moderated pressures (12–20 bar) using a bi-functional catalyst, having a (de)hydrogenation function and an acid function. Nowadays the most commonly used catalysts are platinum loaded mordenite (Pt/H-MOR), platinum on chlorinated alumina (Pt/Al_2O_3-Cl) and more recently platinum-impregnated sulphated zirconia (Pt/ZrO_2-SO_4^{2-}) (Weyda and Köhler, 2003).

Table 1.1. Typical LSR naphtha composition and components properties (Cusher, 2004a).

Component	Molecular weight, g/mol	Boiling point, ºC	LSR naphtha, mol%	RON
Isobutane	58.1	-11.7	0.1	100+
n-butane	58.1	-0.5	0.7	93.6
Isopentane	72.1	27.9	17.5	92.3
n-pentane	72.1	36.1	30.5	61.7
Cyclopentane	70.0	49.3	2.2	100.0
2,2-dimethylbutane	86.2	49.7	0.5	91.8
2,3-dimethylbutane	86.2	58.0	1.8	101.7
2-methylpentane	86.2	60.3	11.2	73.4
3-methylpentane	86.2	63.3	8.0	74.5
n-hexane	86.2	68.7	17.7	24.8
Methylcyclopentane	84.2	71.8	2.1	91.3
Cyclohexane	84.2	80.7	3.8	83.0
Benzene	78.1	80.1	2.4	100+
Heptanes	100.2	98.4	1.6	0.0

The hydroisomerization of linear C_5/C_6 paraffins are equilibrium-limited reactions generally favoured by low temperatures, this trend is shown in Figure 1.2. The more active the catalyst, the lower the reaction temperature: 130-150ºC for Pt/Al_2O_3-Cl, 160-210ºC for Pt/ZrO_2-SO_4^{2-} and 250-280ºC for Pt/H-MOR (Weyda and Köhler, 2003). Despite their higher activity, alumina-based catalysts require a special feed pre-

treatment since they are susceptible to be deactivated by the presence of sulphur and water.

Depending on the feedstock composition and operating conditions, a 10 to 12 RON increase for the light naphtha can be achieved with the *Hysomer* process resulting in a product RON of about 78–82 points. However, the equilibrium mixture from the hydroisomerization reactor still contains about 30 wt% of low RON molecules such as *n*-pentane (*n*PEN) and *n*-hexane (*n*HEX).

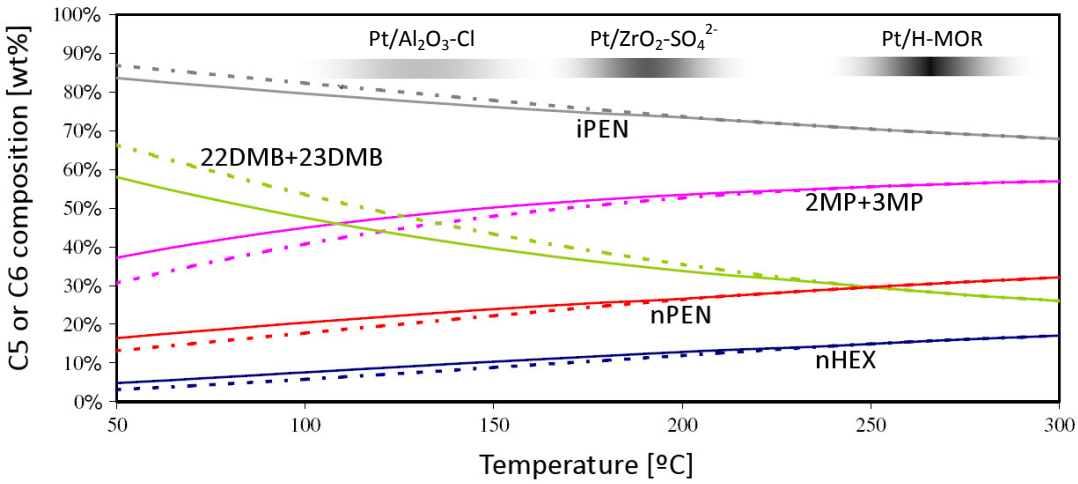


Figure 1.2. Equilibrium composition of pentane and hexane isomers as a function of the isomerization temperature. Solid line represents the liquid phase and dashed line gas phase equilibrium (Vermeiren and Gilson, 2009).

The performances of the *Hysomer* process was substantially enhanced in 1975 with the integration of a UOP (Universal Oil Products) molecular sieve separation process – the *IsoSiv* process – in a refinery in Kawasaki, Japan (Cusher, 1986a). This unit was one of the earliest applications of a combined catalytic-adsorptive integrated process in the refining industry being marketed as the Total Isomerization Process (TIP). TIP uses zeolite 5A to separate and recycle the normal paraffins to the hydroisomerization reactor (Holcombe, 1980; Cusher 2004b). The conventional TIP is sketched in Figure 1.3 where the integration of reaction and separation units can be seen. The reactor effluent is cooled and flashed in a hydrogen separator drum. The liquid containing

some unconverted linear paraffins is vaporized and passed to the *IsoSiv* unit. Typically the process has two or four adsorption columns packed with zeolite 5A. The continuous processing is accomplished through cyclic operation, using a system of valves actuated in a predetermined sequence. The basic process consists of two essential steps:

Adsorption – The isomerate light naphtha in the vapour phase is fed upward through a column where the *n*-paraffins are selectively adsorbed in the bed. The non-adsorbed molecules are obtained as a product at the column outlet. The adsorption step finish when the wavefront of the *n*-paraffins penetrates into about 75% of the bed;

Desorption – The bed saturated with normal paraffins is counter currently purged with non-adsorbable gas. This counter current purge cleans the bed from normal paraffins and recycles them to the hydroisomerization reactor.

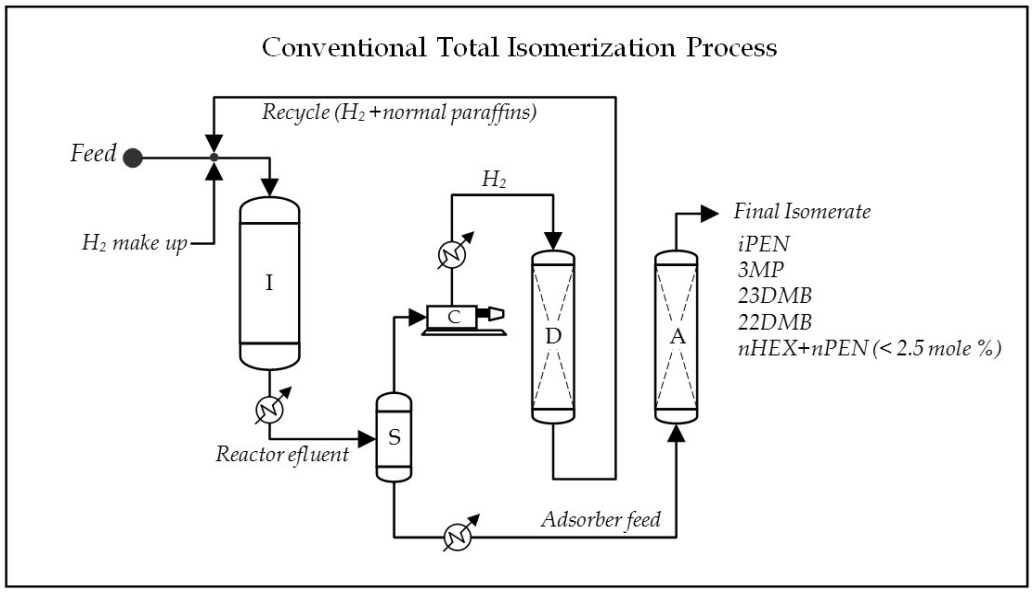


Figure 1.3. Simplified scheme of the conventional Total Isomerization Process (TIP): (I) isomerization reactor; (S) hydrogen separator; (C) compressor; (A) adsorption stage; (D) desorption stage. Adapted from Cusher (2004a).

Typically, the TIP operates in isobaric mode, i.e., *IsoSiv* unit operates at the same pressure than the *Hysomer* reactor, 13 to 34 bar range and in the temperature range of 518 K to 543 K (Holcombe, 1980). Therefore, the hydrogen separated from the reactor effluent must be recompressed before the desorption stage. Both the compression and vaporization stages are important operation cost in this process. Several variations of the basic TIP are commercially available (e.g., *Ipsorb* or *Hexsorb*, from Axens). Some of these schemes will be discussed further; however, the intermediate stages previously mentioned are common to all of them.

In terms of performance, the TIP can produce a final isomerate with 87–90 RON, i.e. an improvement of approximately 20 points comparatively to the LSR naphtha. Figure 1.4 shows the typical composition of linear and branched C_5/C_6 in the fresh feed, reactor effluent and final isomerate in a TIP. From this Figure it is observed a clear reduction on the composition of the low RON (LRON) molecules *n*HEX and *n*PEN – being *n*HEX practically extinct – and an increase of the high RON (HRON) *i*PEN, 22DMB and 23DMB and the LRON 3MP. In sum, the LRON molecules represent about 18 wt% of the final product. It must be noted that despite the significant amount of the LRON 2-methylpentane in the LSR naphtha (see Table 1.1) this component was not included in this present study for reasons that will be discussed further.

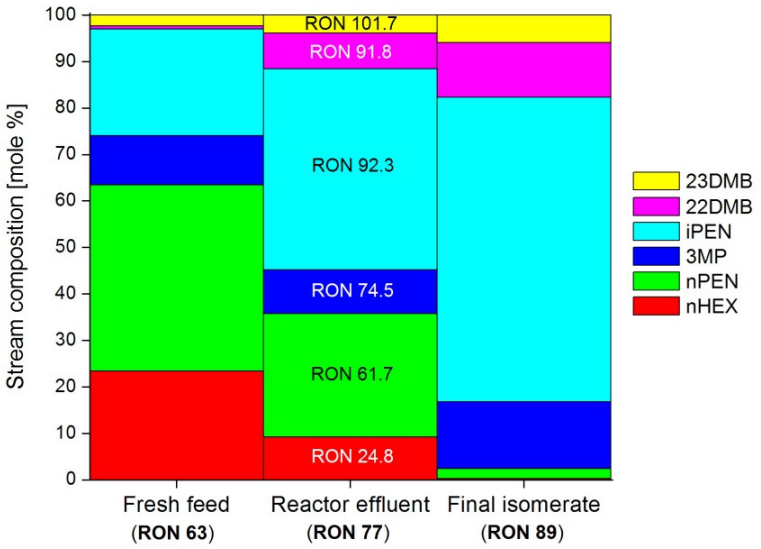


Figure 1.4. Typical composition of streams in Figure 1.3, according to Cusher (2004a).

As previously mentioned, during the last decades alternative schemes and improvements have been developed for the recycling of LRON paraffins (Jensen, 2002). Some includes the adsorption zone before the isomerization one (Volles, 1992), as shown in Figure 1.5a. This patented UOP post-separation isomerization scheme has four layered-beds packed with zeolite 5A and MFI. The second adsorbent is used to separate part of the LRON methylpentanes. Nevertheless, the main drawback of this scheme is the significant amount of HRON *i*PEN recycled to the reaction section, due to its strong adsorption in zeolite MFI. In addition, the high final product RON* (93) is essentially due to a low adsorbent productivity, 79 mmol/(min·kg_{ads})†.

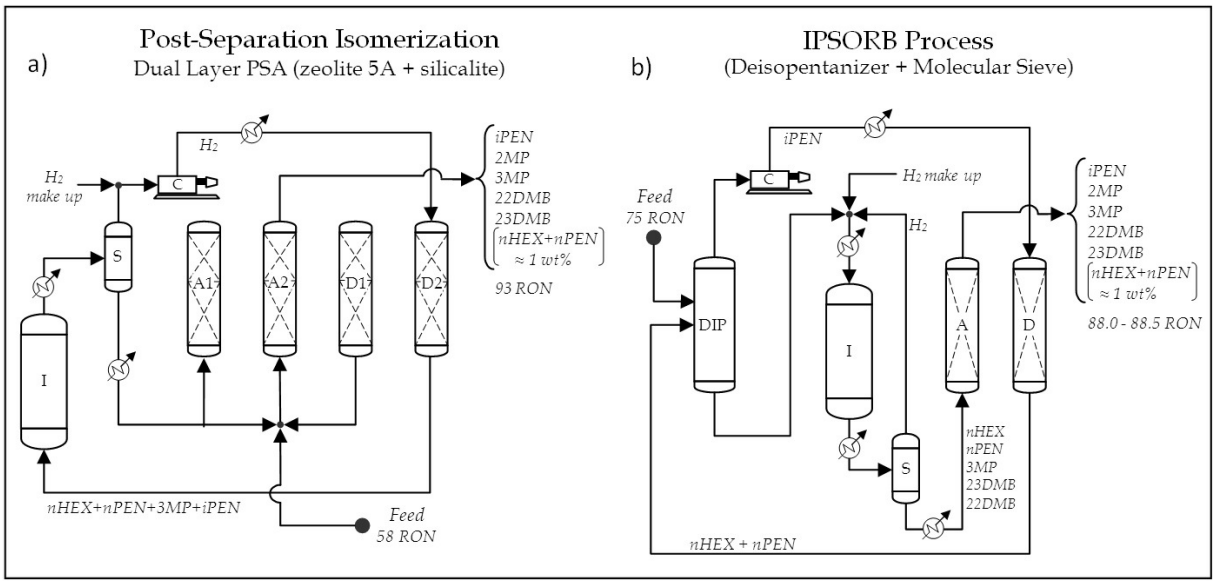


Figure 1.5. Variations of the conventional isomerization process: a) post-separation isomerization process with dual-layer PSA unit (Volles, 1992) and b) basic *Ipsorb* process with deisopentanizer column, DIP (Minkkinen et al., 1993).

The *Ipsorb* and *Hexsorb* processes are two advanced recycle technologies for C_5/C_6 isomerization which are commercialized by Axens – a commercial branch of Institut Français du Pétrole (IFP). These processes combine molecular sieve adsorption technology and fractionation to separate and recycle LRON C_5 and C_6 paraffins

* RON considering only the contribution of 22DMB, 23DMB, 3MP, *n*HEX, *i*PEN, and *n*PEN.
† Productivity considering only the production of 22DMB, 23DMB, 3MP, *n*HEX, *i*PEN, and *n*PEN.

(Domergue and Watripont, 2005). In the *Ipsorb* process – schematized in Figure 1.5b – the adsorption section is located downstream of the isomerate stabilizer. Normal paraffins are separated from isoparaffins using zeolite 5A and vapour phase *i*PEN, which is then recycled to an upstream deisopentanizer column. This column generates an overhead *i*PEN stream which is used as the desorbent for the molecular sieve section and a net isopentane isomerate product and generates a normal paraffin rich feed for the reactor section (Domergue and Watripont, 2005). In an IFP patent (Minkkinen et al., 1993) the superior productivity of this process, approximately 323 mmol/(min·kg_{ads})[‡], is achieved to the detriment of the RON gain in the final product, only 13 RON[§]. The first *Ipsorb* unit was commissioned in Italy, in 1994. By 2003, two *Ipsorb* units were operating with capacities up to 10.500 BPSD[**] (Figure 1.6) (Watripont and Domergue, 2003).

A higher product RON can be achieved when using a variation of the *Ipsorb* process called *Hexsorb* (Graeme and Ross, 2004; Domergue and Watripont, 2005). The desorbent in this case is a side cut stream rich in methylpentane from a downstream deisohexanizer (DIH) column. As result, an increased methylpentane conversion into dimethylbutane is obtained, thereby raising the RON of the final product. This patented process provides isomerate having typically 91–92 RON. Despite the highest performance announced for this technology, none unit had been installed up to 2003, in part due to the higher investment cost associated – about 35 % more than for *Ipsorb* (Domergue and Watripont, 2005). One of the main drawbacks of deisopentanizers and deisohexanizers is that high reflux ratios and consequently substantial reboiling rates are required to separate closely boiling compounds having significantly different RON such as monobranched and dibranched C_6 isomers. Add to this, a large number of theoretical plates are required to achieve the separation – e.g., about 60 trays for a deisohexanizer (Kruse, 1989) – resulting in a very tall column and consequently a large amount of equipment consumed (Figure 1.7). On the other hand, molecular sieve-

[‡] Productivity considering only the production of 22DMB, 23DMB, 3MP, *n*HEX, *i*PEN, and *n*PEN.
[§] RON_{final} - RON_{feed}, considering only the contribution of 22DMB, 23DMB, 3MP, *n*HEX, *i*PEN, and *n*PEN.
[**] BPSD: barrels per stream day

based separation processes are cleaner technologies which have proven to be less energy-intensive than distillation. Indeed, the economy of energy can reach up to 80% comparatively to distillation.



Figure 1.6. View of a 10,500 BPSD *Ipsorb* unit (taken from Watripont and Domergue, 2003).



Figure 1.7. Deisohexanizer column: height = 57 m, diameter = 7 m, weight = 221 tons. (ESSAR Oil, www.essar.com)

The processes previously described differ from the basic TIP also in the method by which the adsorbent is regenerated during desorption stage. While in the TIP the basic method for regeneration is the purge gas stripping, the processes described in Figure 1.5 use the pressure-swing adsorption (PSA) technique to clean the bed. In the first method, the bed is regenerated at essentially constant pressure and temperature by purging with a non-adsorbing inert gas. In a PSA process, desorption is accomplished by reducing the pressure total pressure in the bed at essentially constant temperature and then purging the bed at low pressure. Some versions of the *IsoSiv* process uses vacuum desorption which can be considered as a special case of PSA.

The first commercial application of PSA processes was the separation of air (Skarstrom, 1960). Nowadays, this technique is also used for hydrogen purification, air drying and *n*/iso-paraffins separation (Ruthven, 1984; Yang, 1987; Crittenden and Thomas, 1998; Silva, 1998). Since the 60's, UOP has licensed all over the world more than 700 PSA units in different industrial fields such as refining, petrochemical, polymer, steel and power generation (Hydrocarbon Processing, 2006).

1.1.2 Zeolites as Separating Media for Recycling Technologies

The molecular sieve-based separation processes use zeolites as separating media. Zeolites are porous crystals with a three-dimensional framework of SiO_4 and AlO_4 tetrahedra linked to each other by sharing oxygen atoms. The structural arrangement of the tetrahedra gives rise to a uniform pores system of molecular dimensions. The first zeolite mineral (stilbite) was discovered in 1756. Since then, 179 unique zeolite frameworks have been identified (International Zeolite Association, http://www.iza-online.org). Of these zeolites, about 40 occur in nature. However, zeolites did not find any significant commercial use until synthetic zeolites were discovered and developed. The pioneer in this field was Barrer (1948) with the synthesis of mordenite. In 1953, the Linde division of the Union Carbide Corporation, USA, started the

commercialization of the Linde Type A (LTA), also known as zeolite A. The most commercially important synthetic zeolites are LTA, faujasite (FAU) and ZSM-5 (MFI).

Table 1.2. Zeolite structures with industrial application.
(Tanabe and Höelderich, 1999; Guisnet, 2002 and Vermeiren and Gilson, 2009)

IZA code[a]	Name	Channel dimensions (Å)[b]	Applications
AEL	$AlPO_4$-11	4.0 x 6.5*	Cat
*BEA	Beta	6.6 x 6.7** ↔ 5.6 x 5.6*	Cat
CHA	Chabazite	⊥ 3.8 x 3.8***	Ads
EDI	Edingtonite	2.8 x 3.8** ↔ 2.0 x 3.1*	Ads
ERI	Erionite	⊥ 3.6 x 5.1***	Cat
EUO	EU-1	4.1 x 5.4*	Cat
FAU	Faujasite	7.4 x 7.4***	Cat / Ads
FER	Ferrierite	4.2 x 5.4* ↔ 3.5 x 4.8*	Cat
GIS	Gismondine	{3.1 x 4.5 ↔ 2.8 x 4.8}***	IEx / Ads
HEU	Heulandite	{3.1 x 7.5* + 3.6 x 4.6*} ↔ 2.8 x 4.7*	Ads
LTA	Linde Type A	4.1 x 4.1***	IEx / Dry / Ads
LTL	Linde Type L	7.1 x 7.1*	Cat
MER	Merlinoite	3.1 x 3.5* ↔ 2.7 x 3.6* ↔ {3.4 x 5.1* + 3.3 x 3.3*}	Ads
MFI	ZSM-5	{5.1 x 5.5 ↔ 5.3 x 5.6}***	Cat / Ads
MOR	Mordenite	6.5 x 7.0* ↔ {3.4 x 4.8 ↔ 2.6 x 5.7}*	Cat
MTW	ZSM-12	5.6 x 6.0*	Cat
MWW	MCM-22	⊥ 4.0 x 5.5** | ⊥ 4.1 x 5.1**	Cat
RHO	Rho	3.6 x 3.6*** | 3.6 x 3.6***	Cat

[a] IZA code based on IUPAC rules;

[b] Source, Baerlocher et al. (2007): (*) 1-, (**) 2- or (***) 3-D channel system; (↔) interconnecting channel systems; (|) no direct access from one channel system to the other; (⊥) channels interconnected at right angles. Applications: (Ads) adsorption/separation; (Cat) catalysis; (Dry) drying; (IEx) ion exchange.

The current world production of synthetic zeolites is estimated to be about 1.4 million tons per year (Virta, 2008). Zeolites have widespread applications in the refining and petrochemical industry because of their unique adsorption, catalytic, ion exchange, and molecular sieve properties (Ribeiro et al., 1984). Among the 179 known zeolite

structures, only 18 are being used in different types of commercial processes (see Table 1.2). In the refining area, these microporous materials are mainly used as:

- *Catalysts for the production of fuels* (e.g., naphtha and olefin isomerization, catalytic cracking, hydrocraking, catalytic dewaxing and hydro-dearomatization);

- *Molecular sieve for separation and purification process* (e.g., separation of normal paraffins from naphtha and kerosene, removal of impurities detrimental to downstream processing such as sulfur and corrosive agents, H_2 production and drying in natural gas production).

The separation of *n*-paraffins and *iso*-paraffins was one of the first applications of zeolites in the refinery (Flanigen, 1980). This process commonly uses zeolite 5A (LTA ion-exchanged with Ca^{2+}) which possess a uniform 3-dimensional structure consisting of cavities of minimum free diameter 11.4 Å interconnected by windows with free aperture 5 Å (see Figure 1.8). Branched paraffins have larger molecular diameters and are therefore excluded from accessing the crystal cavity through the pore opening. Examples of its application are the UOP TIP and the Axens *Ipsorb* processes described in the previous section.

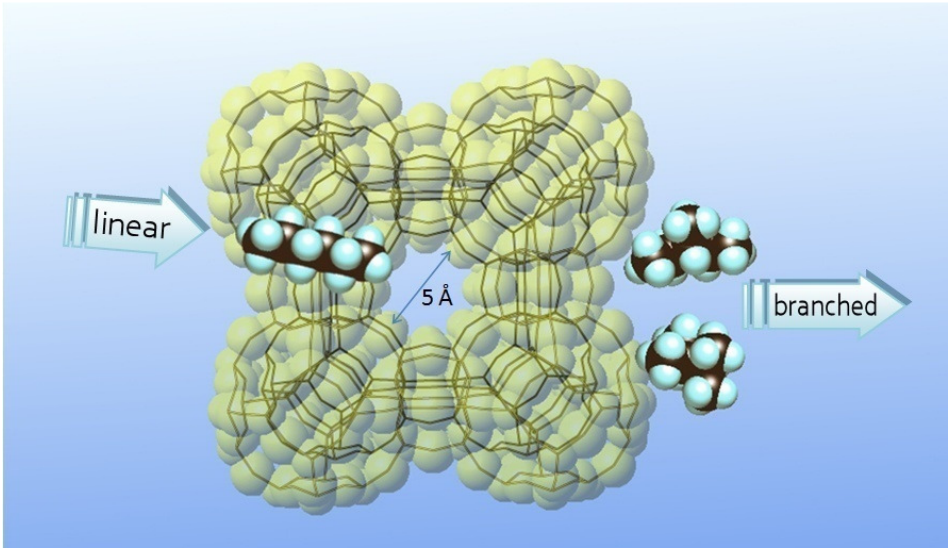


Figure 1.8. Schematic illustration of the molecular sieving effect for normal and branched paraffins in zeolite 5A.

1.1.3 The Zeolite Membrane Alternative

During the last decade, interest in zeolite membranes has been growing rapidly in both the scientific and industrial field due to their capability to separate compounds in continuous operation. Zeolites membranes are also very attractive because they are more resistant against high temperatures and pressures, fouling, aggressive feeds, and regeneration treatments than the widespread organic membranes (Ebner and Ritter, 2009). Many types of zeolites have been prepared as membrane and already tested for gas separation (Caro et al., 2000; Muraza and Jansen, 2004), for instance, small pores (LTA), medium pores (MFI, MEL, FER), and large pores (MOR, FAU). Many efforts have been accumulated in MFI structure (Burggraaf et al., 1998; Flanders et al., 2000; Krishna et al., 2000a, 2000b; Matsufuji et al., 2000; Zhu et al., 2003).

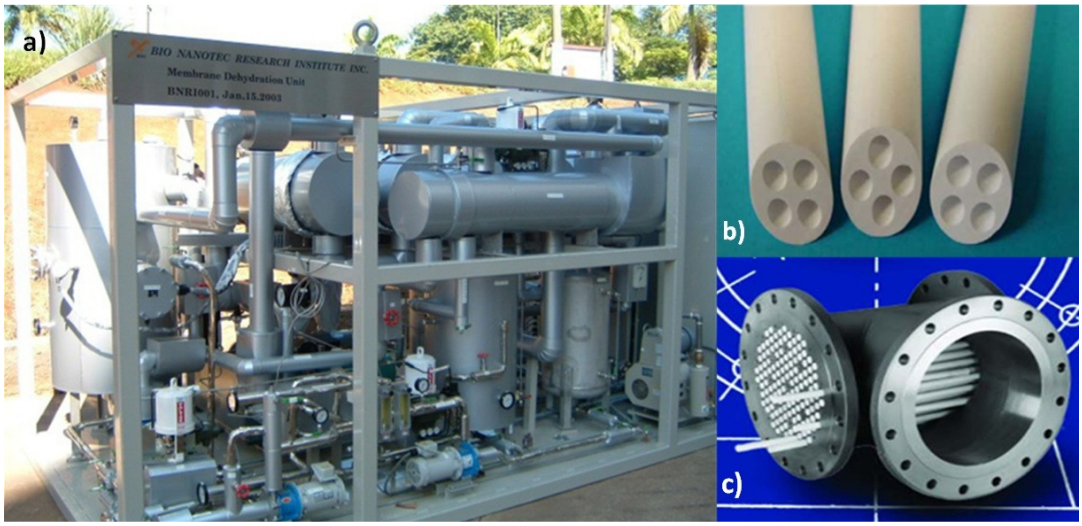


Figure 1.9. Commercial application of zeolite membranes: *a)* Mitsui bio-ethanol pilot plant in Brazil (3.000 l/d); *b)* Multichannel 4A Smart zeolite membranes produced by Inocermic GmbH; *c)* Module with 5.8 m^2 4A Smart zeolite membranes.

Some industrial applications of zeolite membranes are already being operated (Morigami et al., 2001), such as the dehydration systems for bioethanol plants built by *Mitsui & Co*. (Figure 1.9a) and *The Smart Chemical Company Ltd.* (disappeared) which use zeolite 4A (LTA in the Na^+ form) membranes developed by *Bussan Nanotech Research Institute Inc*. (van Hoof et al., 2006) and *Inocermic GmbH* (Figure 1.9b),

respectively. Membrane devices usually operate under continuous steady-state conditions with three streams (Figure 1.9c). The feed stream – a high-pressure gas mixture – passes along one side of the membrane. The molecules that permeate the membrane are swept using a gas (or vacuum) on the other side of the membrane in the so-called permeate stream. The non-permeating molecules that remain on the feed-stream side exit the membrane as the retentate stream. A pressure difference across the membrane drives the permeation process.

Recently, the use of zeolite membranes has been suggested as an alternative for the recycle of linear paraffins (Haag and Tsikoyiannis, 1991; Verduijn et al., 2000; Ragil et al., 2000, 2002; Muraza and Jansen, 2004). Medium pore MFI zeolite membranes for the separation of linear and branched paraffins have been already provided by *NGK Insulators, Ltd.*, Japan (Matsufuji et al., 2000). However, the permeation flux for linear paraffins under operating conditions so far are too low to be competitive with respect to current adsorption separation systems or even distillation process such as DIH. Alternatively, the use of a zeolite membrane contactor in the bottoms stream of a DIH column has been disclosed to reduce the energy consumption of the distillation unit by providing a normal hexane-containing permeate suitable for recycle to the isomerisation (Rice, 2009).

Hybrid units combining the reaction and separation operations in a single membrane reactor unit were suggested for the process intensification of the C_5/C_6 hydroisomerization (Sie, 1997). Unlike the TIP, the use of membranes as the separation phase will allow a continuous process avoiding adsorption and desorption cycles. The membrane reactor concept, combining reactor and membrane separator, into a single unit, is a natural design evolution that follows, with numerous benefits such as energy and cost savings (van de Graaf et al., 1999; Maloncy, 2006; McLeary 2007). The most serious challenge for the industrial application of zeolite membrane-based separation processes is on the preparation of large surface area membrane capable to balance selectivity and permeability features.

1.1.4 Metal-Organic Frameworks as an Alternative to Zeolites

Porous metal-organic frameworks (MOFs), which are new types of zeolite analogues, have been of major interest during the last decade because of their potential applications in gas storage, separation, heterogeneous catalysis, and sensing (Férey, 2007). Their framework consists of a network of transition metal ions linked by bridging organic ligands. MOFs are attractive for adsorptive application because the pores can be systematically varied by the judicious choice of the metal ion and/or bridging organic linkers. An example of this tunability is shown in Figure 1.10 where different pore sizes are obtained just by changing the organic linker (Eddaoudi et al., 2002). This remarkable attribute is quite different from that of traditional zeolites whose pores are confined by rigid tetrahedral oxide skeleton that are usually difficult to alter. This superior feature is significantly important to develop novel functional materials for gas separation, which are based on their selective sorption behaviours and mainly determined by size exclusive effect in which smaller molecules can go through the microporous channels while larger molecules are blocked.

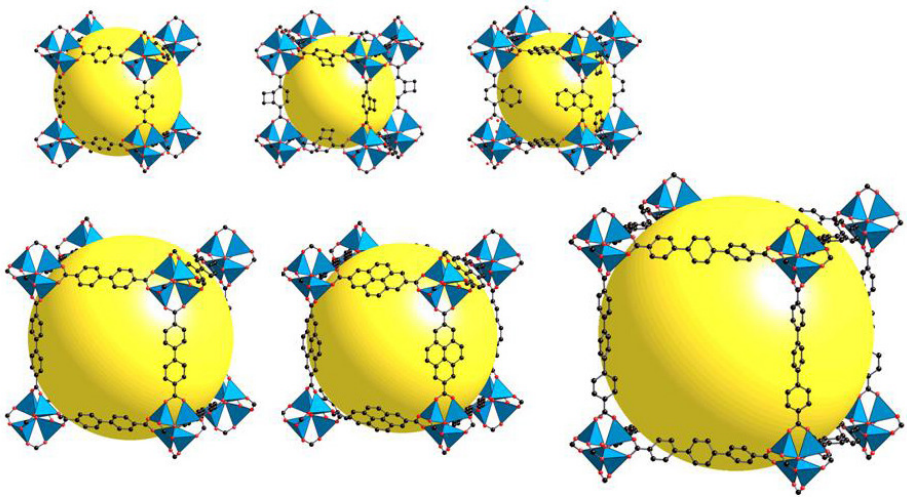


Figure 1.10. Pore size tuning exemplified with the IRMOF[††] family (Eddaoudi, 2002).

[††] IRMOF = Iso-Reticular Metal-Organic Framework

MOFs can be made with exceptionally high porosity and are synthesised by a simple self-assembly reaction between metals ions and organic linkers under mild conditions. For that reason, MOFs are ideal for laboratory studies and practical applications, such as gas and vapour separation or purification as adsorbents (Mueller et al., 2006; Britt et al., 2008). Another interesting feature of this new class of adsorbents is the flexibility of the pores observed in some MOFs. These dynamic frameworks respond to external stimuli such as pressure, temperature and guest molecules (Yaghi et al., 1998; Fletcher et al., 2005; Kitagawa and Uemura, 2005, Trung et al., 2008). This particular behaviour can be explored for the process intensification of the current cyclic adsorptive processes.

Currently, the research of MOFs as adsorbents in gas and vapour separation processes is in its early stage. Most of the literature is focused on selective adsorption studies based on the measurement of sorption isotherms which provide the basic information for adsorbent screening. Nevertheless, four MOFs manufactured by BASF – and essentially orientated to gas storage and catalysis applications – are already available in the market under the trade name *Basolite* (http://www.basf-futurebusiness.com). This is a clear evidence of the great interest around these materials. Presently, about 100 kg/day batches are being produced in a BASF pilot plant in Ludwigshafen (Germany), but it is expected a significant production growth for the next years (Jacoby, 2008).

1.2 Objectives and Outline

To maximize the effectiveness of LSR naphtha isomerization processes it is also desirable to separate di- from monobranched isomers. For example, the RON of 3-methylpentane is 74.5 compared with 101.7 for 2,3-dimethylbutane (Figure 1.11). These isomers are the major constituents of the output of the isomerisation processes and their molecular kinetic diameter is similar, which makes the separation very challenging. The complete separation of monobranched and dibranched C_6 from a

typical refinery gasoline pool would result in an octane gain of 2 points considering the final product resulting from the TIP or *Ipsorb* processes. For a 10,000 BPSD hydroisomerization unit, the added value will be close to 2,000,000 US$ per year (Schmidt and Köhler, 2002; Albemarle Corporation, 2009).

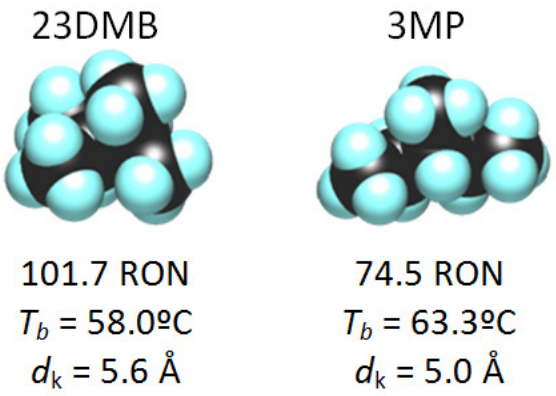


Figure 1.11. Hexane isomers: research octane number (RON); boiling point (T_b) and kinetic diameter (d_k).

Most studies published in literature regarding the separation of hexane isomers use MFI type zeolites as adsorbents. This is due to the fact that MFI has a three dimensional micropore system with straight channels interconnected by sinusoidal channels (http://www.iza-online.org) with dimensions of pores similar to the kinetic diameter of the hexane isomers. These characteristics have been explored by several researchers to understand sorption equilibrium and kinetics based on computer molecular simulation (Krishna et al., 1999, 2000a; Vlugt, 2000; Smit and Krishna, 2003; Fox et al., 2004). Smith and Krishna (2003) investigate entropy effects during sorption of mixtures of alkanes in MFI zeolite, concluding that for a mixture of mono-methyl and di-methyl alkanes with the same number of carbon atoms, configurational effects favour the single branched isomers leading to the following hierarchy of sorption strengths: linear alkanes >> mono-methyl alkanes >> di-methyl alkanes. In other computational study (Krishna et al., 1999) it is shown that the influence of isotherm inflection can change the selectivity between isomers on silicalite when mixtures are in contact with the zeolite structure, and this effect can be explored to separate the hexane isomers. Experimentally, work has been performed both in fixed bed and in

membranes, using novel techniques to measure adsorption equilibrium and diffusion of hexane isomers. In membranes, Talu et al. (1998) developed the single-crystal membrane technique to measure diffusivities of alkanes, including n-hexane. Recently, a study of Sommer et al. (2003) for transport of hexane isomers through ZSM-5 zeolite membranes, show selectivities between *n*HEX, 3MP and 22DMB based on permeation rates of the hydrocarbons across the membrane, that can reach values in the order of 1000. However, Funke et al. (1997) found no selectivity between 3MP and 22DMB at 362 K and 443 K on binary mixtures of these compounds in permeation studies performed through silicalite membranes. Jolimaitre et al. (1999, and 2002) studied experimentally in a fixed bed adsorber the separation of the mono and dibranched paraffins of hexane in silicalite concluding that the separation is feasible.

Several data can be found regarding the diffusion of hexane isomers in silicalite; Zhu et al. (2001) using the novel Tapered Element Oscillating Microbalance (TEOM) found that the mobility of the isomers decreases as the degree of branching increases, being critical for 22DMB. The Zero-length Column (ZLC) technique has already been used to measure diffusivities by Voogd et al. (1991) and Shavit et al. (1992). Cavalcante and Ruthven (1995a, 1995b) have also measured equilibrium and kinetics of hexane isomers in silicalite using gravimetric techniques.

In a study of adsorption equilibrium on several types of zeolites, including ZSM-5, beta, Y and ZSM-22, Denayer et al. (1998) found that ZSM-22 gives the best selectivities for separating hexane isomers. Also, these authors demonstrated that pentane and hexane isomers might be separated by chromatography according to their branching degree using columns of ZSM-22 and zeolite beta. Some years before, Huddersman and Klimczyk (1996a, 1996b) indicated that zeolite beta in cation form (H,Ba) is an effective adsorbent for the separation of branched hexane isomers, and even better than silicalite.

Zeolite beta was first synthesized by Mobil in 1967. However, the structure of this zeolite was determined only in 1988 (Treacy, 1988) due to its complexity. It is reported

that in zeolite beta structure, the ordered and disordered framework coexist. Zeolite beta possesses a three-dimensional pore structure consisting of perpendicular straight channels 6.6 × 6.7 Å which interconnections create narrow helicoidal channels of effective pore diameter 5.6 × 5.6 Å (Figure 1.12).

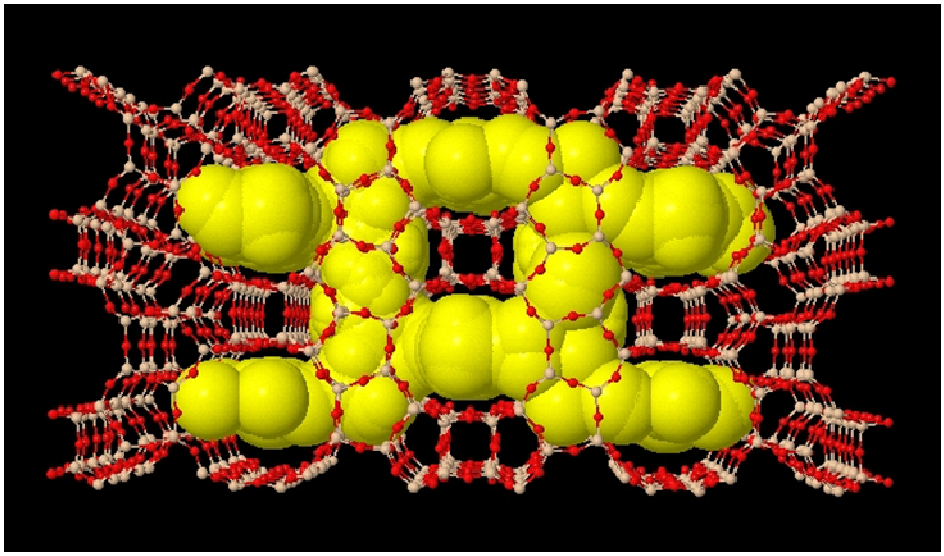


Figure 1.12. Zeolite beta framework and maximum free spheres fitting inside the channels.

Zeolite beta is produced in large scale for commercial applications such as catalyst and catalyst support (alkylation of aromatics, Friedel Crafts reactions, isomerization of waxes) and as a sorbent in separation of aromatics and reduction of exhaust gas emission (Guisnet and Ribeiro, 2004). The potential application of zeolite beta for the separation of branched C_6 might benefit from its commercial availability (Table 1.2). However, there are very few published data concerning the adsorption and diffusion of alkanes in this structure, especially in commercial pellets important to set-up adsorption processes. For example, Karger and Ruthven (1994) in one of the reference books for diffusion in zeolites available on literature has no reference for diffusion of any compound on zeolite beta despite the importance of this zeolite in catalysis nowadays. There is also a lack of experimental data respecting the behaviour of alkanes mixtures in this material. Such information is essential for the design and

development of a cyclic separation process like the PSA used in the TIP and *Ipsorb* processes.

One of the goals of this work is to contribute to a better understanding of the adsorption of alkanes in this large pore zeolite, using linear and branched C_5 and C_6 isomers with considerable potential for commercial application on petroleum industry, especially in isomerization schemes. To reach the objective the adsorptive process is developed by selecting a proper commercial sample of zeolite beta, measuring equilibria and kinetic data in single and multicomponent systems. The adsorption of mixtures containing both pentane and hexane isomers are also addressed to obtain reliable experimental data representative of the real process. All these data are used in the development of a detailed mathematical model capable to predict the adsorption dynamic of the C_5/C_6 paraffins in zeolite beta.

The flowchart in Figure 1.13 describes the basic steps in the development of an adsorption process. The final goal is the design and optimization of a cyclic adsorption process.

Cooperation with the Materials Computational Group of the University Pablo de Olavide (Seville, Spain) is carried out to give insight into the behaviour of the hexane isomers in the zeolite beta structure.

Additionally, the potential of both zeolite beta membranes and novel MOF materials is investigated through cooperation with international leading groups on zeolite membranes synthesis (The Pore, TUDelft, The Netherland) and MOFs synthesis (University of Texas-Pan American, USA; Institut Lavoisier de Versailles, France).

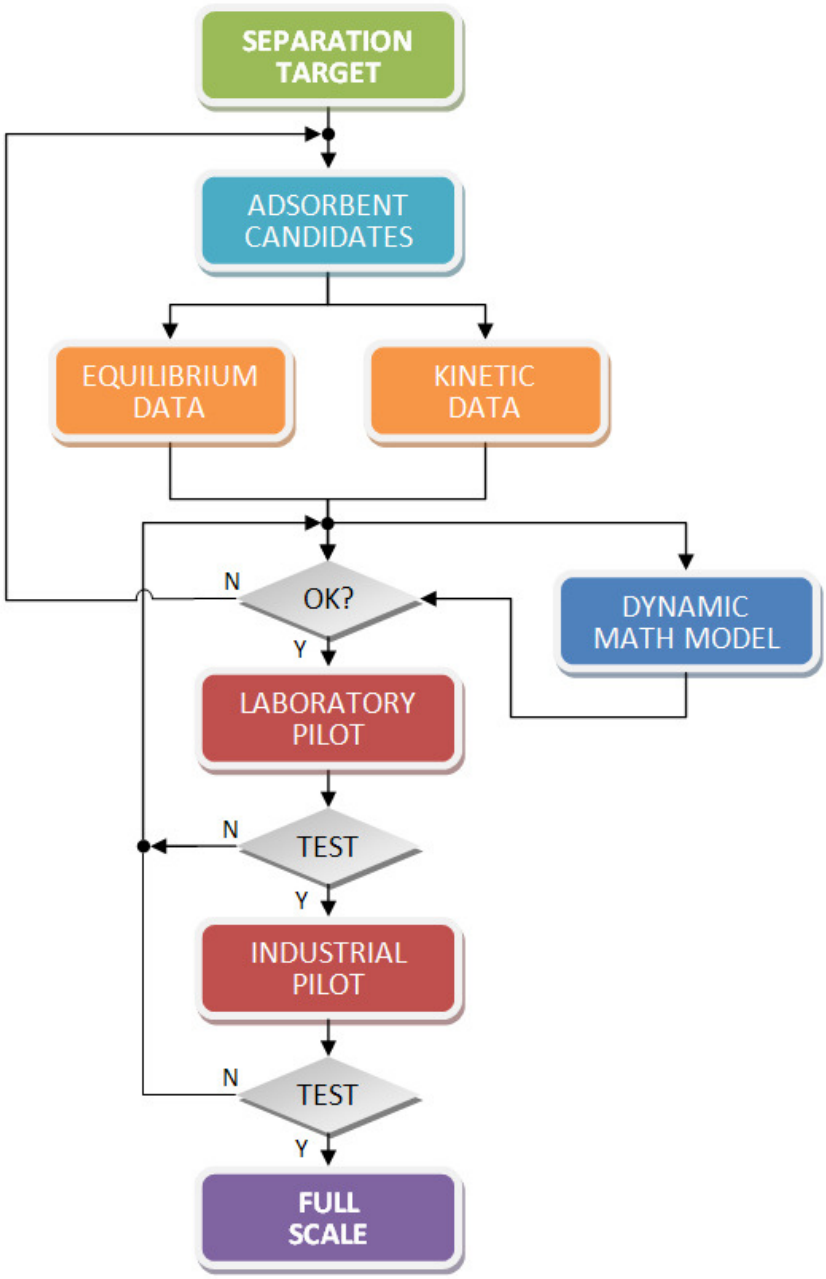


Figure 1.13. Flowchart for the development of an adsorption process.
Adapted from Adsorption Research Inc. homepage (http://www.adsorption.com)

In summary, the aim of the thesis is the development of an adsorptive process to separate branched hexane isomers in order to improve the octane quality of gasoline pool. Alternative solutions are explored in parallel to the main investigation as illustrated in Figure 1.14.

Chapter 2 deals with single component adsorption equilibrium and kinetic on a commercial sample of zeolite beta measured by the fixed bed adsorption and zero-length column (ZLC) techniques, respectively.

Chapter 3 shows the results of adsorption equilibrium measurements of binary, ternary and quaternary mixtures of hexane isomers in zeolite beta.

Chapter 4 is focused on the study of the adsorption dynamics of C_5/C_6 fractions in a fixed bed of zeolite beta. The application of a layered bed containing zeolite 5A and zeolite beta is also addressed.

In *Chapter 5* the principles of the PSA technique are described. The simulation results of a layered PSA process for the separation of HRON paraffins from a C_5/C_6 light naphtha fraction are shown. A parametric study of the effect of different variables on the process performance is addressed.

In *Chapter 6* methods for manufacturing zeolite beta membranes have been explored and their performance in the vapour phase separation of hexane isomer mixtures has been studied.

Chapter 7 demonstrates the potential of MOFs materials for the separation of hexane isomers in a fixed bed column.

Chapter 8 has the conclusions of this work and some suggestion for future work.

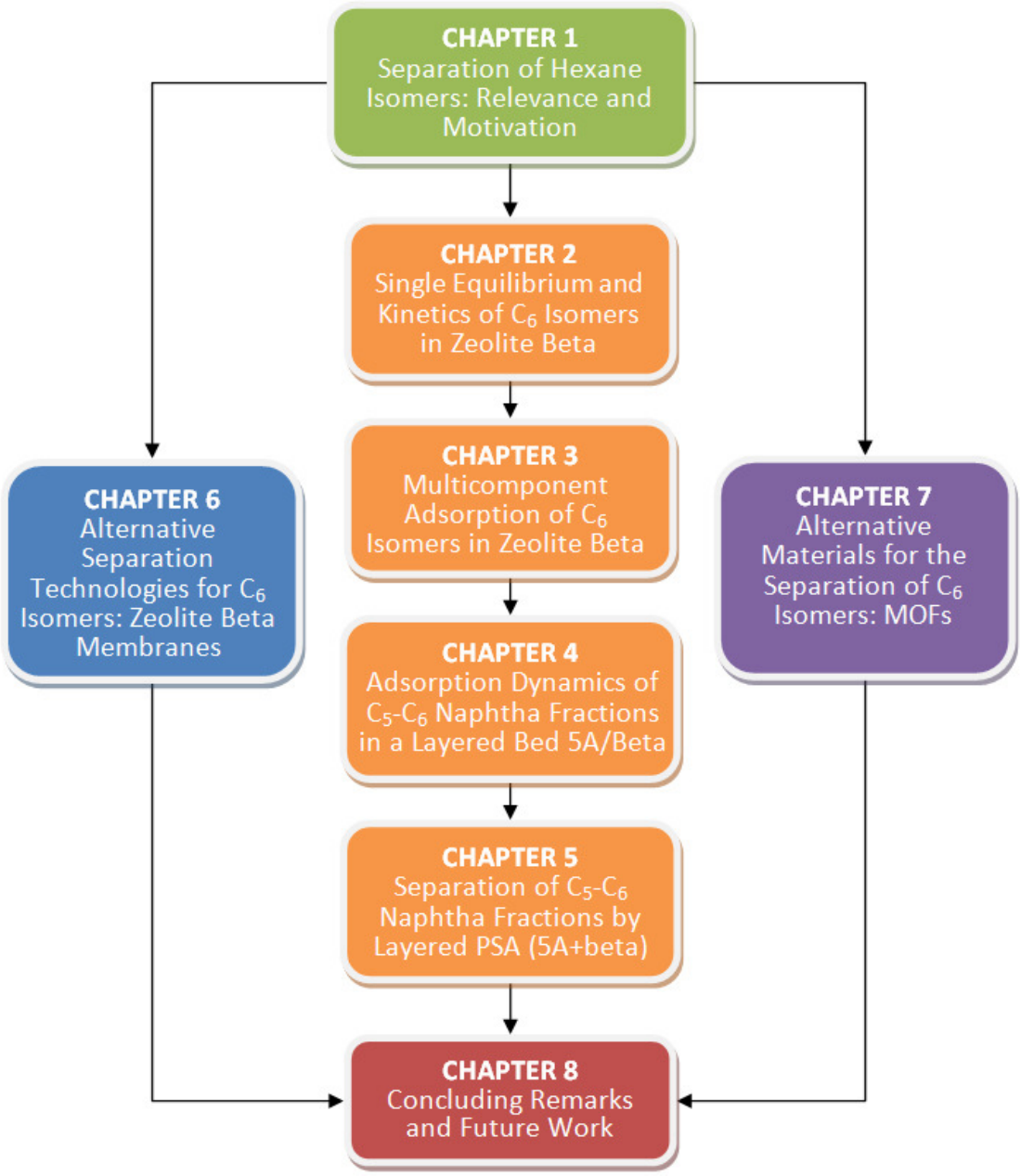


Figure 1.14. Thesis organization.

1.3 References ‡‡

Adsorption Research Inc., http://www.adsorption.com (accessed Nov 2009).

Albemarle Corporation, http://www.albemarle.com (accessed Nov 2009).

Baerlocher, Ch.; McCusker, L. B.; Olson, D. H. Atlas of Zeolite Framework Types, 6th ed.; Elsevier: Amsterdam (2007).

Benazzi, E.; Cameron, C. Future Refinements, *In Fundamentals of the Global Oil & Gas Industry*, Petroleum Economist: London, p. 111-113 (2005).

BASF: The Chemical Company, http://www.basf-futurebusiness.com (accessed Nov 2009).

Burggraaf, A.J.; Vroon, Z.A.E.P.; Keizer, K.; Verweij H. Permeation of Single Gases in Thin Zeolite MFI Membranes. *Journal of Membrane Science* 144, 77–86 (1998).

Britt, D.; Tranchemontagne, D.; Yaghi, O. M. Metal-organic frameworks with high capacity and selectivity for harmful gases. *Proc. Natl. Acad. Sci. U.S.A.* 105, 11623–11627 (2008).

Caro, J.; Noack, M.; Köleck, P.; Schäfer, R. Zeolite Membranes: State of Their Development and Properties. *Micropor. Mesopor. Mater. 38*, 3–24 (2000).

Cavalcante, C.L.; Ruthven, D.M. Adsorption of Branched and Cyclic Paraffins in Silicalite. 1. Equilibrium. *Ind. Eng. Chem. Res.* 34, 177–184 (1995a).

Cavalcante, C.L.; Ruthven, D.M. Adsorption of Branched and Cyclic Paraffins in Silicalite. 2. Kinetics. *Ind. Eng. Chem. Res.* 34, 185–191 (1995b).

Crittenden, B; Thomas, W. J. *Adsorption Technology and Design*, Elsevier: Amsterdam, Chapter 7 (1998).

Cusher, N. A. UCC Total Isomerization Process (TIP). In *Handbook of Petroleum Refining Processes*, Myers, R. A. Ed.; McGraw–Hill: New York, Chapter 5, pp 5–14 (1986a).

Cusher, N. A. UCC (Shell) Hysomer Process. In *Handbook of Petroleum Refining Processes*, Myers, R. A. Ed.; McGraw–Hill: New York, Chapter 5, pp 15–24 (1986b).

Cusher, N. A. UCC IsoSiv Process. In *Handbook of Petroleum Refining Processes*, Myers, R. A. Ed.; McGraw–Hill: New York, Chapter 8, pp 11–18 (1986c).

Cusher, N. A. UOP TIP and Once-Through Zeolitic Isomerization Processes. In *Handbook of Petroleum Refining Processes*; Meyers, R. A., Ed.; 3rd Edition, McGraw Hill: New York, Chapter 9, pp 29–39 (2004a).

Cusher, N. A. UOP IsoSiv Process. In *Handbook of Petroleum Refining Processes*; Meyers, R. A., Ed.; 3rd Edition, McGraw Hill: New York, Chapter 10, pp 63–68 (2004b).

‡‡ Reference list follows the format recommended by *The ACS Style Guide, 3rd edition.*

Denayer, J. F.; Souverijns, W. ; Jacobs, P. A. ; Martens, J. A. ; Baron, G. V. High Temperature Low-Pressure Adsorption of Branched C_5–C_8 Alkanes on Zeolite Beta, ZSM-5, ZSM-22, Zeolite Y, and Mordenite. *J. Phys. Chem. B* 102, 4588–4597 (1998).

Domergue, B; Watripont L. Paraffins Isomerisation Options, *Petrol. Tech. Q.* 10, 21–25 (2005).

Ebner, A.D.; Ritter, J.A. State-of-the-art Adsorption and Membrane Separation Processes for Carbon Dioxide Production from Carbon Dioxide Emitting Industries. *Separ. Sci Technol.* 44, 1273–1421 (2009).

Eddaoudi, M.; Kim, J.; Vodak, D.; Wachter, J.; O'Keeffe, M.; Yaghi, O.M. Systematic Design of Pore Size and Functionality in Isoreticular MOFs and Their Application in Methane Storage. *Science* 295, 469–472 (2002).

Férey, G. Les Nouveaux Solides Poreux ou les Miracles des Trous. *Actual. Chimique* 304, 1–25 (2007).

Flanders, C.L.; Tuan, V.A.; Noble, R.D.; Falconer, J.L. Separation of C_6 Isomers by Vapor Permeation and Pervaporation through ZSM-5 Membranes. *J. Membr. Sci.* 176, 43–53 (2000).

Flanigen, E.M. Molecular Sieve Zeolite Technology — the First Twenty-Five Years. *Pure & Appl. Chem.* 52, 2191–2211 (1980).

Fletcher, A. J.; Thomas, K. M.; Rosseinsky, M. J. Flexibility in Metal-Organic Framework Materials: Impact on Sorption Properties. *J. Solid State Chem*. 178, 2491–2510 (2005).

Fox, J.P.; Rooy, V.; Bates, S.P. Simulating the Adsorption of Linear, Branched and Cyclic Alkanes in Silicalite-1 and AlPO4-5. *Micropor. Mesopor. Mater.* 69, 9–18 (2004).

Funke, H.H.; Argo, A.M.; Falconer, J.L.; Noble, R.D. Separations of Cyclic, Branched, and Linear Hydrocarbon Mixtures through Silicalite Membranes. *Ind. Eng. Chem. Res.* 36, 137–143 (1997).

Gora, L.; Jansen, J.C. Hydroisomerization of C_6 with a Zeolite Membrane Reactor. *J. Catal.* 230, 269–281 (2005).

Graeme, S.; Ross, J. Advanced Solutions for Paraffins Isomerization, In *Proceedings of the National Petrochemical and Refiners Association annual meeting*, San Antonio (TX), 21-23 March. (2004).

Guisnet, M. Introduction to Zeolite Science and Technology, *In Zeolites for Cleaner Technologies*, M. Guisnet and J.-P. Gilson, eds., London: Imperial College Press, p. 1-28 (2002).

Guisnet, M.; Ribeiro, F.R. *Zeólitos: um Nanomundo ao Serviço da Catálise*, Fundação Calouste Gulbenkian: Lisboa (2004).

Haag, W.O.; Tsikoyiannis, J.G. Separation of Mixture Components over Membrane Composed of a Pure Molecular Sieve. US Patent 5,069,794 (1991).

Holcombe, T. C. Total Isomerization Process. US Patent 4,210,771 (1980).

Huddersman, K.; Klimczyk, M. Separation of Hexane Isomers on Zeolites Mordenite and Beta. *J. Chem. Soc., Faraday Trans.* 92, 143–147 (1996a).

Huddersman, K.; Klimczyk, M. Separation of Branched Hexane Isomers Using Zeolite Molecular Sieves. *AIChE J.* 42, 405–408 (1996b).

Hydrocarbon Processing: *Refining Processes 2006 Handbook*, Gulf Publishing Co. (2006).

Jacoby, M. Heading to Market with MOFs. *Chem. Eng. News* 86, 13-16 (2008).

Jensen, R. H. Refining Processes: Setting the Scene, *In Zeolites for Cleaner Technologies*, M. Guisnet and J.-P. Gilson, eds., London: Imperial College Press, p. 75-104 (2002).

Jolimaitre, E. Étude et Modélisation de l'Adsorption et du Transfert de Matière dans les Zéolithes de Structure MFI. Application à la Séparation des Hydrocarbures Saturés mono et di-Branchés. Ph.D. Thesis, LAGEP - Université Claude Bernard, Lyon (1999).

Jolimaitre, E.; Ragil, K.; Fayolle, M.T.; Jallut, C. Separation of Mono- and Dibranched Hydrocarbons on Silicalite. *AIChE J.* 48, 1927–1937 (2002).

Kärger, J.; Ruthven, D.M. *Diffusion in Zeolites and Other Microporous Solids*, Wiley: New York (1994).

Kitagawa, S.; Uemura, K. Dynamic Porous Properties of Coordination Polymers Inspired by Hydrogen Bonds. *Chem. Soc. Rev.* 34, 109–119 (2005).

Krishna, R.; Vlugt, T.J.H.; Smit, B. Influence of Isotherm Inflection on Diffusion in Silicalite. *Chem. Eng. Sci.* 54, 1751–1757 (1999).

Krishna, R.; Baur, R. Separation of Hydrocarbon Mixtures Using Zeolite Membranes: a Modelling Approach Combining Molecular Simulations with the Maxwell–Stefan Theory. *Sep. Purif. Technol.* 21, 111–136 (2000a).

Krishna, R.; Paschek, D. Permeation of Hexane Isomers across ZSM-5 Zeolite Membranes. *Ind. Eng. Chem. Res*. 39, 2618–2622 (2000b).

Kruse, L.W. Fractionation for a C_6 Paraffin Isomerization Process. U.S. Patent 4.831.209 (1989).

Maloncy, M.L. The Potential of Zeolite Membranes in Hydroisomerization Processes. Ph.D. Thesis, Delft University of Technology (2006).

Matsufuji, T.; Watanabe, K.; Nishiyama, N.; Egashira, Y.; Matsukata, M.; Ueyama, K. Permeation of Hexane Isomers through an MFI Membrane. *Ind. Eng. Chem. Res.* 39, 2434-2438 (2000).

McCarthy, J.E.; Tiemann, M. *MTBE in Gasoline: Clean Air and Drinking Water Issues*; CRS Report for Congress: Washington, April (2006).

McLeary, E.E. Perspectives on a Zeolite Membrane Reactor for C_5/C_6 Hydroisomerization. Ph.D. Thesis, Delft University of Technology (2007)

Minkkinen, A.; Mank, L.; Jullian, S. Process for the Isomerization of C_5/C_6 Normal Paraffins with Recycling of Normal of Multicomponent Adsorption Beds, US Patent 5,233,120 (1993).

Morigami, Y.; Kondo, M.; Abe, J.; Kita, H.; Okamoto, K. The First Large-Scale Pervaporation Plant Using Tubular-Type Module with Zeolite NaA Membrane. *Separ. Purif. Technol*. 25, 251–260 (2001).

Mueller, U.; Schubert, M.; Teich, F.; Puetter, H.; Schierle-Arndt, K.; Pastré, J. Metal–Organic Frameworks—Prospective Industrial Applications. *J. Mater. Chem.* 16, 626–636 (2006).

Muraza, O.; Jansen, J.C. An Exploratory Study for Zeolite Membrane Application in Hydrocarbon Separation. *J. Indones. Oil Gas Comm*. 10 (2004).

Ragil, K.; Prevost, I.; Clause, O.; Larue, J.; Millot, B. Process for Separating a C_5-C_8 Feed or an Intermediate Feed into three Effluents, Respectively Rich in Straight Chain, non-Branched and multi-Branched Paraffins. US Patent 6,156,950 (2000).

Ragil, K.; Jullian, S.; Durand, J.; Hotier, G.; Clause, O. High Octane Number Gasolines and their Production using a Process Associating hydro-Isomerization and Separation. U.S. Patent 6.338.791 (2002).

Ribeiro, F.R.; Rodrigues, A.E.; Rollman, D.L.; Nacache, C. *Zeolites: Science and Technology*, Martinus Nijhoff Publishers: The Hague (1984)

Rice, L.H. Processes for the Isomerization of Feedstocks Comprising Paraffins of 5 to 7 Carbon Atoms. US Patent 2009/0069618 A1 (2009).

Ruthven, D. M. *Principles of Adsorption and Adsorption Processes*, Wiley-Interscience: New York, Chapter 11, pp 336–379 (1984).

Schmidt, F.; Köhler, E. C4-C6 Alkanes Isomerization, *In Zeolites for Cleaner Technologies*, M. Guisnet and J.-P. Gilson, eds., London: Imperial College Press, p. 153-166 (2002).

Shavit, D.; Voogd, P.; Kouwenhoven, H.W. Time-Dependent Non-Steady-State Diffusivities of C6 Paraffins in Silicalite by Zero-Length Column Method. *Collect. Czech. Chem. Commun.* 57, 698–709 (1992).

Sie, S.T. Isomerization reactions In *Handbook of Heterogeneous Catalysis,* Knozinger, G.E. and Weitkamp, J. *(eds.),* Wiley-VCH: Weinheim, 1998–2017 (1997).

Silva, J.A.C. Separation of n/iso-Paraffins by Adsorption Process. Ph.D. Thesis, University of Porto (1998).

Skarstrom, C. W. Method and Apparatus for Fractionating Gas Mixture by Adsorption. US Patent 2,944,627 (1960).

Smit, B.; Krishna, R. Molecular Simulations in Zeolitic Process Design. *Chem. Eng. Sci.* 58, 557 (2003).

Sommer, S.; Melin, T.; Falconer, J.L.; Noble, R.D. Transport of C_6 Isomers through ZSM-5 Zeolite Membranes. *J. Membr. Sci.* 224, 51–67 (2003).

Talu, O.; Sun, M.S.; Shah, D.B. Diffusivities of n-Alkanes in Silicalite by Steady-State Single-Crystal Membrane Technique. *AIChE J.* 44, 681–694 (1998).

Tanabe, K.; Höelderich, W. F. Industrial Application of Solid Acid-base Catalysts. *Appl. Catal. A: General* 181, 399–434 (1999).

Treacy, M.M.J.; Newsam, J.M. Two New three-Dimensional Twelve-Ring Zeolite Frameworks of which Zeolite Beta is a Disordered Intergrowth. *Nature* 332, 249–251 (1988).

Trung, T.K.; Trens, P.; Tanchoux, N.; Bourrelly, S.; Llewellyn, P.L.; Loera-Serna, S.; Serre, C.; Loiseau, T.; Fajula, F.; Férey, G. Hydrocarbon Adsorption in the Flexible Metal Organic Frameworks MIL-53(Al, Cr). *J. Am. Chem. Soc.* 130, 16926–16932 (2008).

van de Graaf, J.M.; Zwiep, M.; Kapteijn, F.; Moulijn, J.A. Application of a Silicalite-1 Membrane Reactor in Metathesis Reactions, *Applied Catal. A: Gen.* 178, 225–241 (1999).

van Hoof, V.; Dotremont, C.; Buekenhoudt, A. Performance of Mitsui NaA Type Zeolite Membranes for the Dehydration of Organic Solvents in Comparison with Commercial Polymeric Pervaporation Membranes. *Sep. Purif. Technol.* 48, 304–309 (2006).

Verduijn, J.P.; Bons, A.J.; Anthonis, M.H.C.; Czarnetzki, L.R.; Mortier, W.J. Molecular Sieves and Processes for their Manufacture. US Patent 6,090,289 (2000).

Vermeiren, W.; Gilson, J.-P. Impact of Zeolites on the Petroleum and Petrochemical Industry, *Top. Catal*. 52, 1131–1161 (2009).

Virta, R. Natural and Synthetic Zeolites. *Geotimes*, Jun (2008).

Vlugt, T.J.H. Adsorption and Diffusion in Zeolites: a Computational Study, Ph.D. Thesis, Universiteit van Amsterdam (2000).

Volles, W.K. Adsorptive Separation of Isopentane and di-Methyl Branched Paraffins from mono-Methyl Branched Paraffins. EU Patent 0 473 828 A1 (1992).

Voogd, P.; Bekkum, H.; Shavit, D.; Kouwenhoven, H.W. Effect of Zeolite Structure and Morphology on Intracrystalline n-Hexane Diffusion in Pentasil Zeolites Studied by the Zero-Length Column Method. *J. Chem. Soc. Faraday Trans.* 87, 3575–3580 (1991).

Watripont, L.; Domergue, B. Advanced Solution for Paraffins Isomerization. 4th European Catalyst Technology Conference, Prague. Personal communication (2003).

Weyda, H.; Köhler, E. Modern Refining Concepts — an Update on Naphtha-Isomerization to Modern Gasoline Manufacture, *Catal. Today* 81, 51-55 (2003).

Yaghi, O. M.; Li, H.; Davis, C.; Richardson, D.; Groy, T. L. Synthetic Strategies, Structure Patterns, and Emerging Properties in the Chemistry of Modular Porous Solids. *Acc. Chem. Res.* 31, 474–484 (1998).

Yang, R. T. *Gas Separation by Adsorption Processes*, Imperial College Press: London (1997).

Zhu, W.; Kapteijn, F.; Moulijn, J. A. Diffusion of linear and branched C_6 alkanes in silicalite-1 studied by the tapered element oscillating microbalance. *Micropor. Mesopor. Mater.* 47, 157–171 (2001).

Zhu, W.; Kapteijn, F.; Moulijn J.A. Separation Modeling of Linear and Branched C_6 Alkane Permeation through Silicalite-1 Membranes. *Sep. Purif. Technol.* 32, 223–230 (2003).

2

Single Adsorption Equilibrium and Kinetics of C_6 Isomers in Zeolite Beta

Single adsorption equilibrium and kinetics of hexane isomers were studied in commercial pellets of zeolite beta in the temperature range 423–523 K and partial pressures up to 30 kPa. Different models were used to interpret the equilibrium data. The affinity to the adsorbent measured by the Henry´s constants decreases with the degree of branching, with selectivities that can reach a value of 8.8 between nHEX and 22DMB. The heats of adsorption at zero coverage decrease with the degree of branching, being: 63.4 kJ/mol for nHEX, 59.7 kJ/mol for 3MP, 57.1 kJ/mol for 23DMB and 53.6 kJ/mol for 22DMB. However, the isosteric heat of sorption changes with coverage with a different behavior for the three isomers. Sorption kinetics studied by Zero Length Chromatography (ZLC) technique allowed us to find the nature of controlling diffusion mechanism; for nHEX and 3MP macropore diffusion is controlling with activation energies similar to the heats of sorption at zero coverage. For 23DMB and 22DMB, the controlling mechanism changes, being the system governed apparently by both macropore and micropore diffusion. Data from this work are also compared with those reported in literature for both zeolite beta and MFI.

This chapter is based on the following publications:

P.S. Bárcia, J.A.C. Silva, A.E. Rodrigues, *Micropor. Mesopor. Mater*. 79 (2005) 145-163.
P.S. Bárcia, J.A.C. Silva, A.E. Rodrigues, *Ind. Eng. Chem. Res.* 45 (2006) 4316-4328.

2.1 Introduction

From an engineering point of view it is important to obtain a good analytical description of pure component isotherms for linear and branched hexane isomers since they are the base for estimation of mixture sorption behaviour from multicomponent models. Moreover, detailed knowledge of the transport properties of microporous adsorbents is required for their complete characterization and optimum technological exploitation.

In this chapter pure component adsorption equilibrium isotherms and thermodynamic parameters are measured from breakthrough experiments. Kinetics of sorption is investigated using the zero-length column (ZLC) technique in order to establish the dominant mechanism for diffusion in the pellets (macropore and micropore) and the corresponding time constant for mass transfer. The final goal is to obtain thermodynamic and kinetic parameters to be used later in an accurate model for the adsorption process.

2.2 Adsorption Equilibria

Adsorption is the phenomenon that allows the selective accumulation on a solid surface of particular types of molecules contained in a fluid in contact with the surface itself. In other words, adsorption concerns the distribution of different components at the solid-fluid interphase. A distinction must be done between physical adsorption, involving only relatively weak intermolecular forces, and chemisorption which involves, essentially, the formation of a chemical bond between the sorbate molecule and the adsorbent surface. Most of the adsorptive separation processes depend on physical adsorption rather than chemisorption and this is therefore the focus of the present work.

Adsorption equilibrium data is the most important piece of information in understanding an adsorption process. The experimental measurement of adsorption isotherms provides, at a given temperature, the relationship existing between the partial pressures of the different components in the fluid phase and the concentration existing on the solid surface at equilibrium conditions. Various fundamental equations were developed to interpret the adsorption phenomena, some of which have a theoretical foundation and some being of a more empirical nature.

2.2.1 Langmuir Model

The most basic theory in adsorption is the Langmuir theory (1918). The basis of this theory lays on the assumption that there is a continuous process of bombardment of molecules onto the surface and a corresponding desorption of molecules from the surface to maintain zero rate of accumulation at the surface at equilibrium. The assumptions of the Langmuir model are:

1. Surface is energetically homogeneous;
2. Each site can accommodate only one molecule;
3. Neighbouring adsorbed species do not interact laterally.

The well known form of the Langmuir equation is

$$\theta = \frac{q}{q^m} = \frac{bp}{1+bp} \tag{2.1}$$

where p is the partial pressure, q^m is the total number of sites per unit weight or volume of adsorbent and $\theta = q/q^m$ is the fractional coverage. The adsorption equilibrium constant, b, is a measure of how strong an adsorbate molecule is attracted onto a surface and it shows the usual Arrhenius temperature dependence:

$$b = b^0 e^{\left(\frac{-E}{RT}\right)} \tag{2.2}$$

where b^0 is the frequency factor of the affinity constant, R is the universal gas constant and T is the temperature. The interaction energy between the adsorbate molecule and the sorbent E is equivalent to the enthalpy change for physical adsorption which must be negative because of the exothermic nature of adsorption (Do, 1998). Since the Langmuir model assumes that the surface is energetically homogeneous, the heat of adsorption is a constant, and its value is equivalent to $(-E)$.

At low pressures, the Langmuir isotherm reduces to a linear form, or Henry's law form:

$$q = q^m bp = Hp \tag{2.3}$$

where H is the Henry's constant. Thermodynamically consistent isotherms should reduce to the Henry's law form at extreme dilution.

In practice, the Langmuir isotherm is not always verified, since usually the heat of adsorption changes when the amount adsorbed increases. This means that the surface is not homogenous and that stronger sites are filled in first place. Accordingly, the Langmuir isotherm is valid when the surface of the adsorbent is homogeneous and the adsorbate occupies one active site when it adsorbs which is reasonable when the adsorbate molecule is small.

2.2.2 Nitta Model

In order to account for the effect of the increasing size of the adsorbate molecules Nitta et al. (1984) developed an equilibrium adsorption isotherm assuming localized adsorption in which the adsorbed molecule occupies a certain number of actives sites, n. The isotherm expression is, neglecting the interaction term between adsorbed molecules in the original model:

$$b = \frac{1}{p}\frac{\theta}{(1-\theta)^n} \tag{2.4}$$

According to Nitta et al. (1984) $q^m = A_S / n$, where A_S is the total number of active sites in adsorbent. Silva and Rodrigues (1997, 1999) used with success this isotherm to correlate the adsorption equilibrium data of linear hydrocarbons in the range C_1–C_{10} on zeolite 5A, showing the relation between the parameter n and the size of the adsorbate molecules.

2.2.3 Dual-site Langmuir Model

More recently several authors (Krishna et al., 1999; Krishna and Baur, 2000; Smit and Krishna, 2003) used the Dual-site Langmuir (DSL) model isotherm to make a description of the pure component isotherms of alkanes in zeolite MFI. The DSL model distinguishes two categories of sorption sites in the adsorbent, each one following a Langmuir adsorption behaviour. The adsorption isotherm is,

$$q = q_1^m \frac{b_1 p}{1 + b_1 p} + q_2^m \frac{b_2 p}{1 + b_2 p} \tag{2.5}$$

where q_1^m, q_2^m are the monolayer capacities in each type of sites. Adsorption affinity constant b_1 and b_2 vary with temperature, according to the Arrhenius equation

$$b_1 = b_1^0 e^{(-E_1/RT)} \tag{2.6a}$$

$$b_2 = b_2^0 e^{(-E_2/RT)} \tag{2.6b}$$

where b_1^0 and b_2^0 are the frequency factors of the affinity constants, E_1 and E_2 are the interaction energies of sites 1 and 2. For our system this isotherm seems interesting since there are two different types of channels that can give different active sites for sorption. However, our data does not show any inflection in the adsorption isotherm.

2.2.4 Toth Model

The heterogeneity of the adsorbent surface was included by Toth (1971) isotherm model. The governing equation of Toth isotherm for heterogeneous surfaces is:

$$b = \frac{1}{p}\frac{\theta}{\left(1-\theta^{s}\right)^{1/s}} \tag{2.7}$$

where, s is the dimensionless heterogeneity parameter. The more s is far from one, the more heterogeneous is the system. When s is equal to the unity, the Toth model becomes the Langmuir model.

2.3 Sorption Kinetics

Rates of adsorption and desorption in porous adsorbents are generally controlled by transport within the pore network, rather than by the intrinsic kinetics of sorption at the surface. Commercial adsorbents used for industrial applications consist of small microporous crystals bound into macroporous pellets giving rise to a bidisperse pore structure, as sketched in Figure 2.1. Consequently, such adsorbents offer two distinct diffusional resistances to mass transfer: the micropore resistance of the adsorbent crystal and the macropore diffusional resistance of the pellet.

Conventionally, the transport properties of nanoporous materials are assessed by measuring the rate of molecular uptake or release on adsorbent particles. Such measurements are referred to as macroscopic methods (Kärger, 2002; Kärger and Freude, 2002).

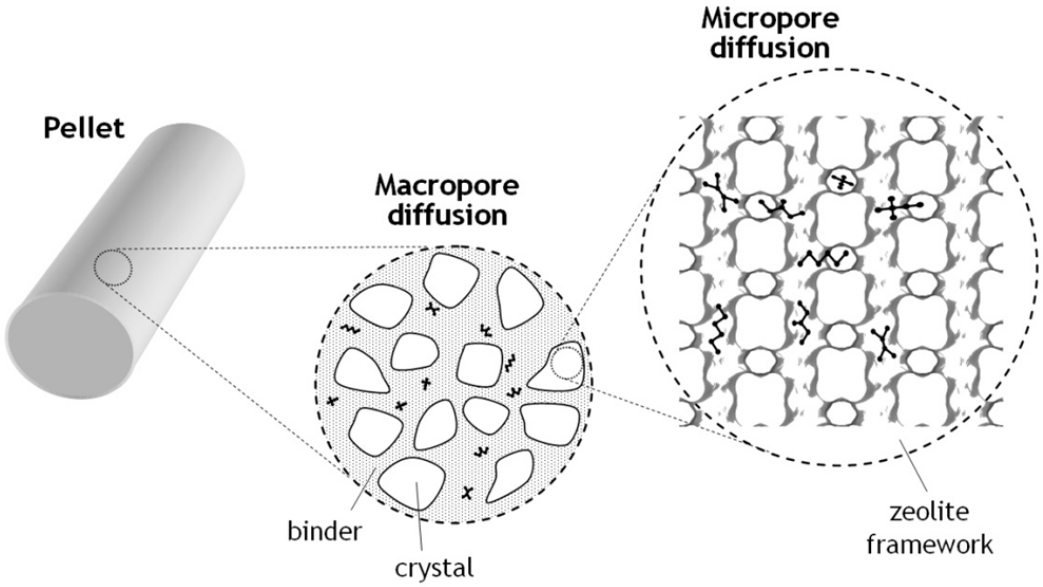


Figure 2.1. Porosity levels within an adsorbent particle and associated diffusion mechanisms. (Adapted from Bárcia, 2006)

The zero-length column or ZLC technique (Eic and Ruthven, 1988) is a macroscopic method widely used for the measurement of diffusion parameters in adsorbents and catalysts. In the ZLC technique a differential bed of porous particles is first saturated with the fluid mixture containing the absorbable species preferably in the Henry's law region of the isotherm; at time zero the carrier gas flows through the ZLC at sufficiently high flow rate, and the desorption curve is analyzed in terms of concentration versus time. Because of the small adsorbent sample, it has been assumed that heat effects due to adsorption are negligible, and consequently isothermal conditions are valid for the modelling of the adsorption cell.

2.3.1 Modelling ZLC Experiments

Data from the ZLC experiments can be modelled by the original model proposed by Eic and Ruthven (1988) in order to obtain the diffusional time constants. This model use the information of desorption curves at long times. The model of the ZLC based on Fick´s law at long times reduces to the following linear equation in a semi-log plot,

$$\ln\left(\frac{c_{out}}{c_0}\right) = \ln\left(\frac{2L}{L^2+\beta_1^2}\right) - \tau_{dif}\beta_1^2 t \tag{2.8}$$

where,

$$\beta_1 J_1(\beta_1) - L J_0(\beta_1) = 0 \tag{2.9}$$

In the previous equations c_{out} is the outlet concentration of the ZLC, c_0 is the saturation concentration of the ZLC cell, t is the time, $J_1(\beta_1)$ and $J_0(\beta_1)$ are Bessel functions of first and zero kind. L is a model parameter calculated as follows:

$$L = \frac{1}{2}\frac{purge\ flowrate}{pellet\ volume}\frac{R_p^2}{\varepsilon_p D_p} \tag{2.10}$$

The parameter τ_{dif} is the reciprocal time constant of diffusion equal to D_c/r_c^2 if the system is controlled by micropore diffusion, or equal to $D_p/R_P^2(1+K)$ if the system is controlled by macropore diffusion. D_c is the crystal diffusivity, r_c the crystal radius, D_p is the macropore diffusivity, R_p is the pellet radius and K a dimensionless parameter related to the Henry's constant. The concept of macropore or micropore diffusion is useful in kinetic studies in bidisperse structures such as the pellets studied in this work.

Using the intercept and slope information from the experimental curves represented in a semi-log plot in conjunction with transcendental equation (2.9), the relevant equations to obtain model parameters by ZLC experiments are,

$$\frac{2L}{L^2+\beta_1^2} = Intercept \tag{2.11}$$

$$-\tau_{dif}\beta_1^2 = Slope \tag{2.12}$$

$$\beta_1 J_1(\beta_1) - L J_0(\beta_1) = 0 \tag{2.13}$$

where *Intercept* and *Slope* are the experimental information needed. This procedure was already used by Silva and Rodrigues (1997) to obtain diffusional time constants.

2.4 Hexane Isomers Configuration

Figure 2.2 shows an approximate three dimensional structure of the hexane isomers studied in this work. It can be seen clearly the structure where *n*-hexane (*n*HEX) is linear, 3-methylpentane (3MP) has one methyl branch, 2,3-dimethylbutane (23DMB) and 2,2-dimethylbutane (22DMB) two methyl branches. In 22DMB, the substitution of the hydrogen by the methyl groups is in the same carbon atom. Also indicated is the molecular kinetic diameter of the molecules which can be important for diffusion along the pores of the zeolite beta. 22DMB is the molecule with the higher molecular kinetic diameter. The hydrocarbons used in this work were purchased from Fluka. The specified purities are over 99%, except for 23DMB (>97%).

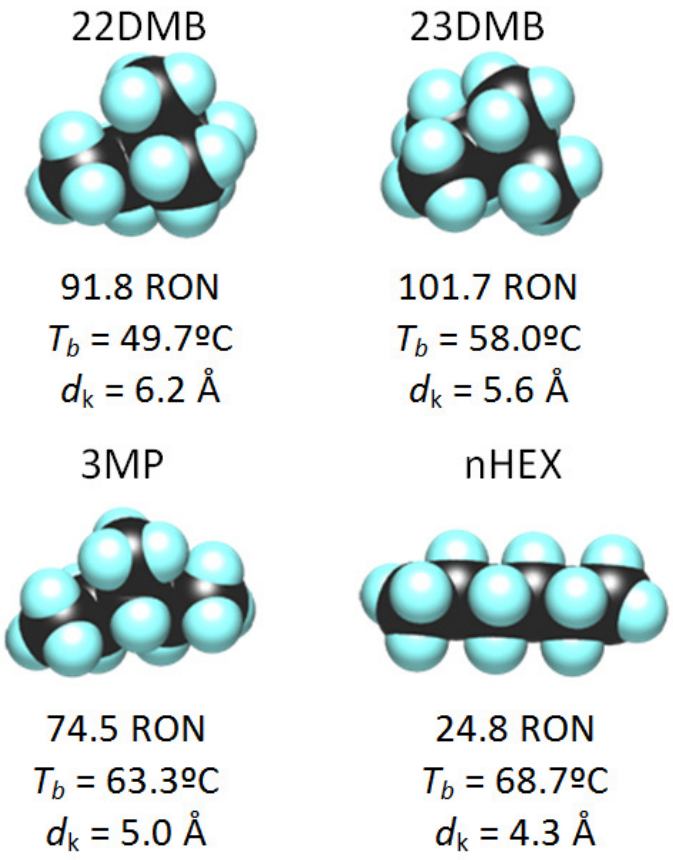


Figure 2.2. Tree-dimensional view, research octane number (RON), boiling point (T_b) and kinetic diameter (d_k) of hexane isomers. Blue spheres are hydrogen atoms and black spheres are carbon atoms. The optimized stuctures were generated with Chemsketch ACD software, and the kinetic diameters were reported by Maloncy et al. (2003).

2.5 Zeolite Beta Structure

Figure 2.3 shows stereographic drawings and perspective views of the zeolite beta structure. Its structure consists in straight 12-membered rings channels of free aperture 6.6 × 6.7 Å viewed along axis [100] and zigzag 12 membered rings channels of 5.6 x 5.6 Å viewed along axis [001]. A perspective of the free aperture of the channels is also shown. The pore architecture consists in the presence of two different types of channels. It should be also noted that the zigzag channels on zeolite beta have a free aperture approximately equal to the ones found in MFI.

2.6 Experimental Section

2.6.1 Adsorbent Characterization

The commercial samples of zeolite beta in the H^+ form used in this study were supplied by Süd-Chemie AG in both powder and pellet form under the reference H-BEA 150. The SiO_2/Al_2O_3 ratio is 150. The 1/16" cylindrical extrudate has an average length of 4 mm (Figure 2.4a).

The surfaces and cross sections of the pellets were examined by scanning electron microscopy (SEM) performed at CEMUP (University of Porto) to determine the morphology, size and homogeneity of the crystals. Panels *b-d* of Figure 2.4 show that the crystals size in the extrudate is between 0.2 to 0.4 μm. Moreover, panel *c* of Figure 2.4 also shows that crystals are smashed at the surface of the pellet probably due to the nature of the extrusion process.

According to the supplier, the inert silica used as binding agent represents 30 wt% of the pellets; this value was experimentally confirmed by comparison of the *n*HEX adsorption in both powder and pellet form.

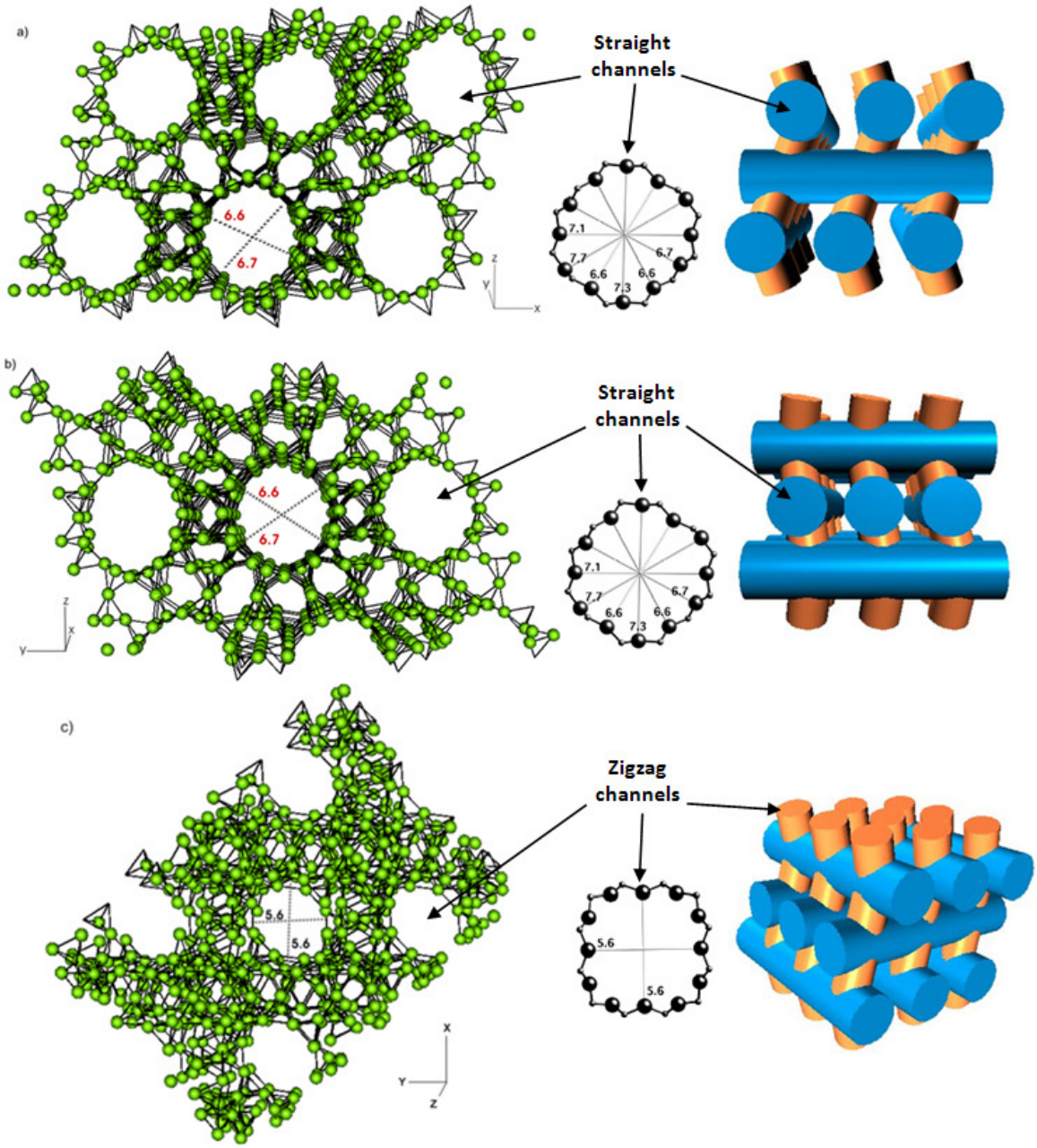


Figure 2.3. Stereographic drawings and perspectives views of zeolite beta viewed along axis (a) [010], (b) [100] and (c) [001]. The 12-MR pores of straight and zigzag channels were also shown for a good visualization of its structure. In the stereographic drawings the spheres represent the oxygen atoms and the tetrahedron which surround the tetrahedrally coordinated Si or Al T-atoms. The stereographic drawings were obtained from http://www.iza-structure.org/databases/. In the right side, the perspective views show the pore network of zeolite beta containing straight (blue) and zigzag (orange) channels. This representation facilitates the visualization of the intersections between the straight and zigzag channels.

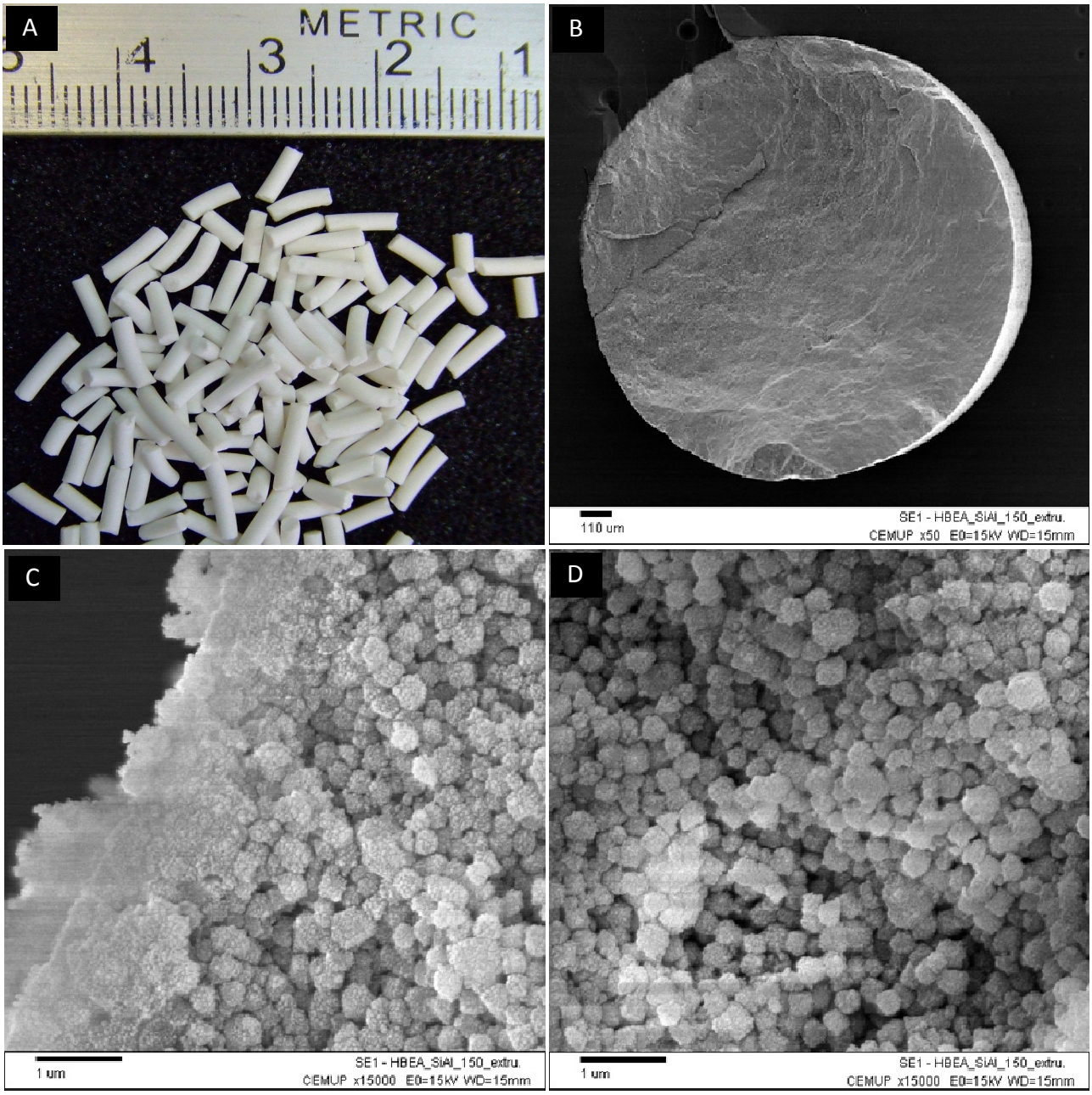


Figure 2.4. (A) Zeolite beta pellets provided by Süd-Chemie AG (Si/Al=75). Scaning electron micrographs (SEM): (B) top view of the pellet (50×); (C) and (D) different view of transversal cut (15.000×).

The commercial powder of zeolite beta used to prepare the pellets was analysed by X-ray diffraction (XRD) performed at the Department of Materials Science and Engineering of the Delft University of Technology (The Netherland) using a Bruker-AXS D5005 with Cu Kα radiation. Figure 2.5 shows the corresponding XRD pattern where it can be seen that the diffraction peaks observed at $2\theta = 7.7^{o}$ and $2\theta = 22.5^{o}$ for all

samples are in agreement with the more intense peaks of the reference simulated pattern for the BEA structure obtained from the Database of Zeolite Structures (http://www.iza-structure.org).

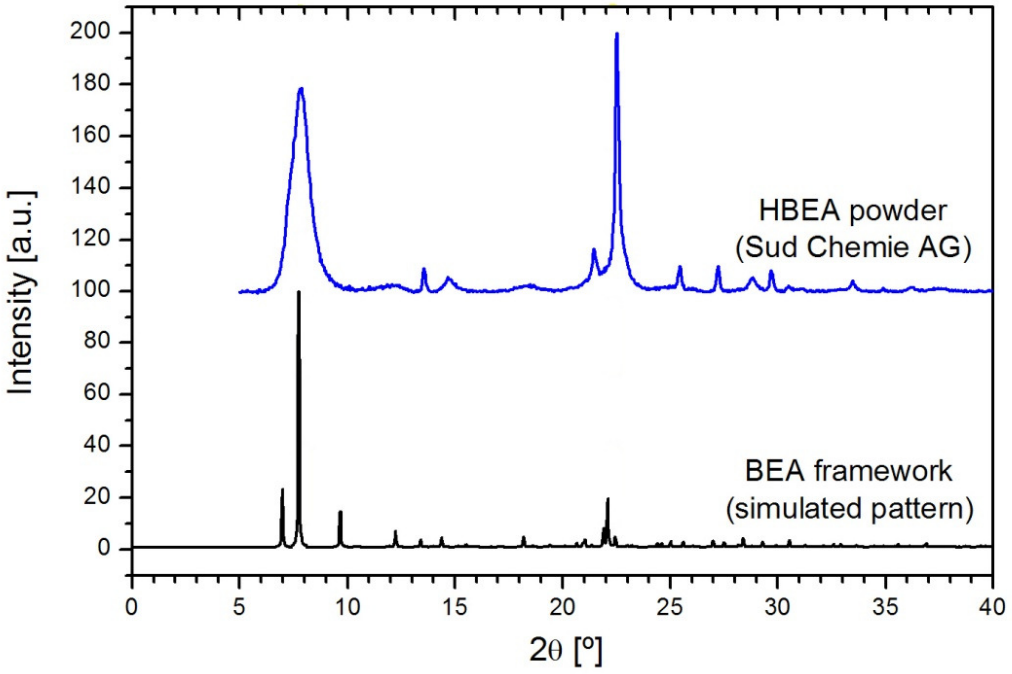


Figure 2.5. XRD pattern of the commercial zeolite beta powder compared with the reference simulated pattern.

N_2 adsorption at 77 K was measured on a Micrometrics ASAP 2000 at LABGRAN (Coimbra, Portugal). The pore size distribution in the commercial zeolite beta was obtained using the Barrett-Joiner-Halenda (BJH) method (Figure 2.6). It can be seen from this figure that these material contains large pore volume in the transition region between mesopores and macropore with a mean pore size of about 75 nm. A smaller peak falling in the range of 3–4 nm also indicates the existence of smaller mesopores.

The mercury porosimetry was performed by LABGRAN (Coimbra, Portugal) with a Micrometrics Poresizer 9320, which operate between 0.5 and 30 000 psia. Mercury porosimetry results for the pellets, and data relative to the zeolite crystals are reported in Table 2.1.

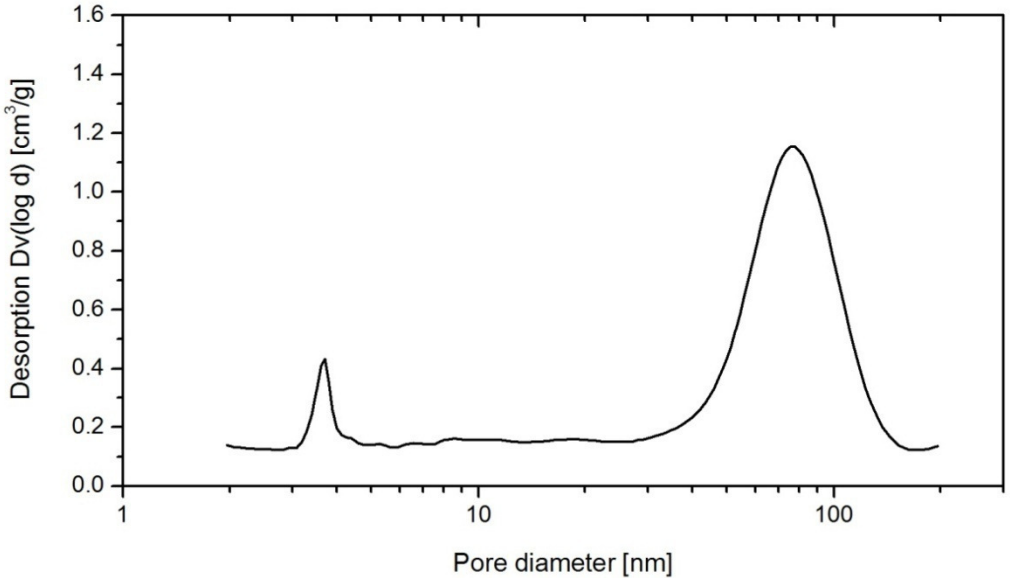


Figure 2.6. Pore size distribution obtained from the N_2 desorption data using the BJH formalism, in the Süd-Chemie AG zeolite beta sample.

Table 2.1. Physical properties of zeolite beta crystals, mercury porosimetry data and N_2 adsorption data of pellets.

Physical properties of crystals	
$^{Si}/_{Al}$ ratio (mol/mol)	75
Particle dimensions (μm)[a]	0.25 – 0.40
Oxygen's in window	12
Channel size (nm)	0.66 × 0.67 ↔ 0.56 × 0.56
Mercury porosimetry data	
Intrusion volume (≈2–30 000 psia) (cm^3/g)	0.14
Pellet density, ρ_p (g/cm^3)	1.18
Porosity (Hg probe), ε_p	0.17
N_2 adsorption data	
S_{BET} (m^2/g)	447.8
Pore volume in the range 20–2000 Å (cm^3/g)	0.32
Porosity (N_2 probe), ε_p	0.40
Average mesopore diameter (Å)	35
Average macropore diameter (Å)	750

[a] Determined by SEM.

2.6.2 Adsorption Equilibrium and ZLC Apparatus

Sorption equilibrium and kinetics studies were performed in the same apparatus shown in Figure 2.7. It consists of three main sections:

- Gas preparation section;
- Adsorption section;
- Analytical section.

The schematic diagram of the apparatus is shown in Figure 2.8. In the gas preparation section the carrier gas (helium > 99.999%, ALPHAGAZ 1, Air Liquide) and the paraffins are introduced in the system. The carrier gas enters the system in two different streams: the first line (1) passes through an electronic pressure controller (EPC) and the second line (2) through a mass flow controller (MFC) GFC17 from AALBORG (New York, USA). The hydrocarbon stream is continuously introduced with a SP100i Syringe Pump (SP) from World Precision Instruments, Inc. (Sarasota, FL, USA) through a heated injection port into the carrier gas that flows through line 2. Both lines (1) and (2) run into a 4-way crossover valve (V_1).



Figure 2.7. Front view of the adsorption equilibrium and ZLC apparatus.

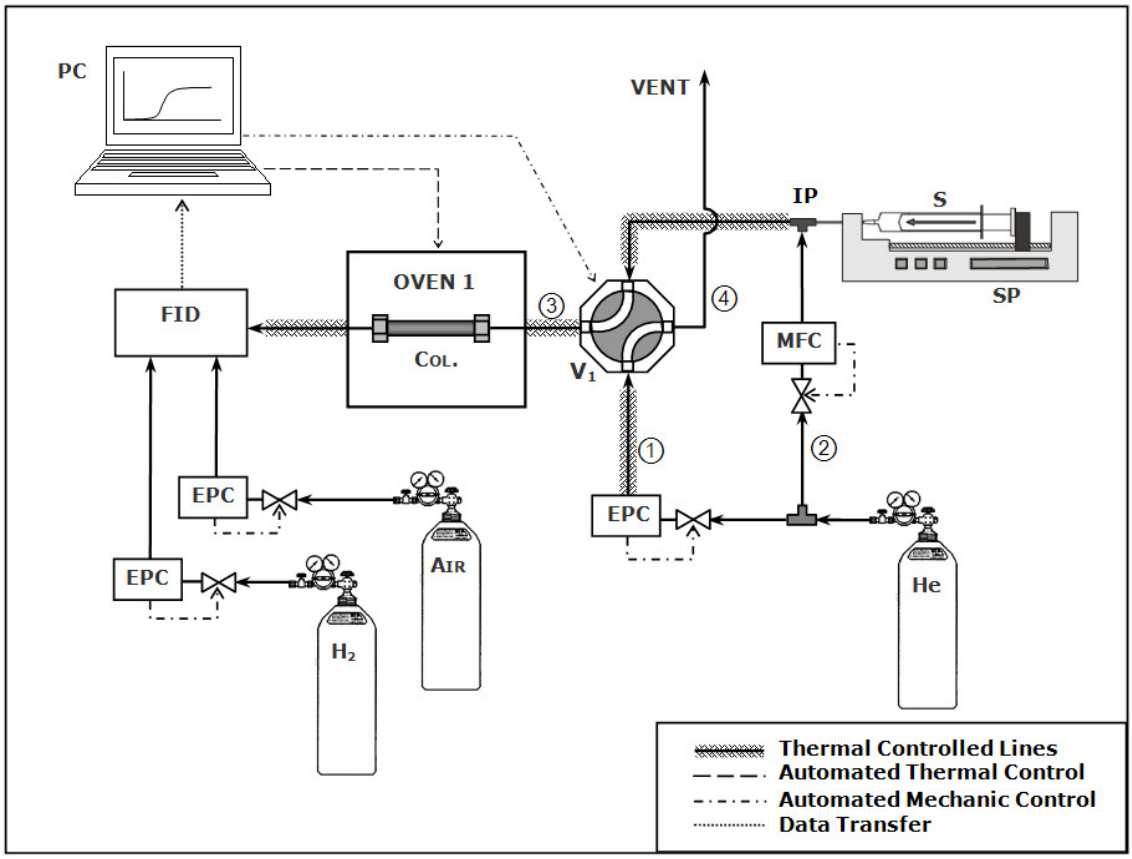


Figure 2.8. Schematic diagram of the ZLC experiment apparatus used to measure adsorption equilibibrium and ZLC data: (Col.) packed column; (EPC) electronic pressure controller; (FID) detector of chromatograph; (IP) injection port; (MFC) mass flow controller; (PC) computer; (S) microliter syringe; (SP) syringe pump; (V_1) 4-way crossover valve; (①②③④) streams.

For adsorption equilibrium experiments the flow from line 2 goes directly into the packed column via line 3, whereas, the pure carrier gas stream flowing through line 1 is directed to vent. At the same time, the output of the column is directed to a flame ionization detector (FID) and the signal continuously recorded in a personal computer.

The first part of a ZLC experiment is similar to an adsorption equilibrium experiment. The second part is a desorption step which starts when the 4-way crossover valve changes its position. Consequently, the hydrocarbon flow coming through line 2 is directed to vent and the pure carrier stream (line 1) goes through the adsorption column. This arrangement ensures that no residual sorbate can be carried to the packed column.

From the injection port to the FID, the transfer lines are thermally controlled to provide good temperature stability and to avoid condensation. Valve position, oven temperature and transfer lines temperature are completely automated.

The adsorption column consists in a 4.6mm i.d. stainless steel column with 100 mm in length. The gas chromatograph SRI 8610c (SRI Instruments, Torrance, CA, USA) is equipped with a forced convection oven in order to keep the column in near-isothermal conditions.

During the adsorption equilibrium studies the column is entirely filled with zeolite pellets. However, in ZLC experiments just the bottom of the column contains some adsorbent particles, being the remaining space filled with small glass spheres.

2.6.3 Experimental Procedure

Pure component isotherms were obtained from breakthrough curves. The experimental procedure is as follows: a bed of adsorbent is saturated by introducing at the inlet the feed containing the adsorbable species diluted in helium at a fixed partial pressure. The experiment consists in measuring continuously the molar rate as a function of time at the outlet of the bed which is kept at fixed temperature. For each experimental breakthrough curve, the amount adsorbed in the solid, which corresponds to *Area A* in Figure 2.9, is obtained by integrating the molar rate history of the complete breakthrough as follows,

$$q = \frac{1}{m_{ads}}\left(F_0\, t_\infty - \int_0^{t_\infty} F\, dt \right) \qquad (2.14)$$

where m_{ads} is the mass of adsorbent in the column, F_0 the feed molar rate, F the molar rate at the column outlet and t_∞ is a time high enough to consider that the bed is already at equilibrium with the feed concentration. It should be noted, that in the

case of gas phase adsorption the amount of sorbate gas in the column void space can be neglected relatively to the amount adsorbed in the solid phase.

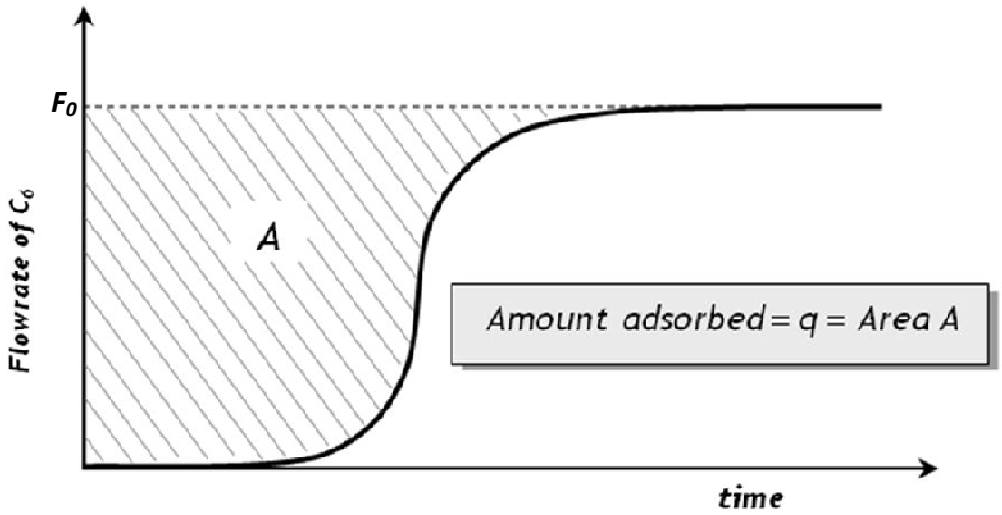


Figure 2.9. Schematic diagram showing the method used to calculate the amount adsorbed from single breakthrough curve experiments.

In ZLC experiments, the adsorption column is filled with a small amount of zeolite beta (approximately 50 mg of adsorbent) in order to set-up a differential bed. The differential bed is first saturated with the fluid mixture containing the adsorbable species preferably in the Henry's law region of the isotherm; at time zero the carrier gas flows through the ZLC, and the desorption curve is analyzed in terms of concentration *versus* time. Prior to each experiment the column is activated for at least three hours at 573 K under helium flow.

2.7 Results and Discussion

2.7.1 Pure component Breakthrough Curves

Figure 2.10 gives an overall perspective of the single breakthrough curves of hexane isomers in the zeolite beta pellets. We plot the breakthrough curves in terms of normalized concentrations of sorbate c/c_0, as a function of time. The stoichiometric time, t_{st}, is also shown in the figures and it is calculated by:

$$t_{st} = \left(\frac{L_B \varepsilon_b}{v_g}\right)\left(1 + \frac{\rho_b q_0}{\varepsilon_b c_0}\right) \qquad (2.15)$$

where v_g is the gas superficial velocity, L_B is the bed length, ρ_b the bulk density, q_0 is the adsorbed concentration in equilibrium with the gas phase concentration c_0 at the inlet of the bed. Figure 2.10 also shows the influence of temperature on breakthrough time at partial pressures near to 12 kPa. Several important conclusions can be obtained from this figure: first, for the same flowrate the stoichiometric time t_{st} decreases significantly as the temperature increases, being 55.4 min for *n*HEX at 423 K compared to 15.2 min at 523 K. For 22DMB, the component with the lower affinity to the adsorbent, it decreases from 45.6 min at 423 K to only 4.8 min at 523 K. The relative stoichiometric times (adsorption capacities) of the hexane isomers fits the following trend, *n*HEX > 3MP > 23DMB > 22DMB. This trend was observed at the three temperatures studied, indicating that the adsorption strengths of the hexane isomers to the adsorbent decreases at the degree of branching increases. This sorption hierarchy is similar to the one reported by Smit and Krishna (2003) for pure component and mixture sorption of hexane isomers in MFI zeolite, in studies performed by Monte Carlo simulations. A more detailed analysis of the pure component breakthrough curves can be found in the literature (Bárcia, 2006).

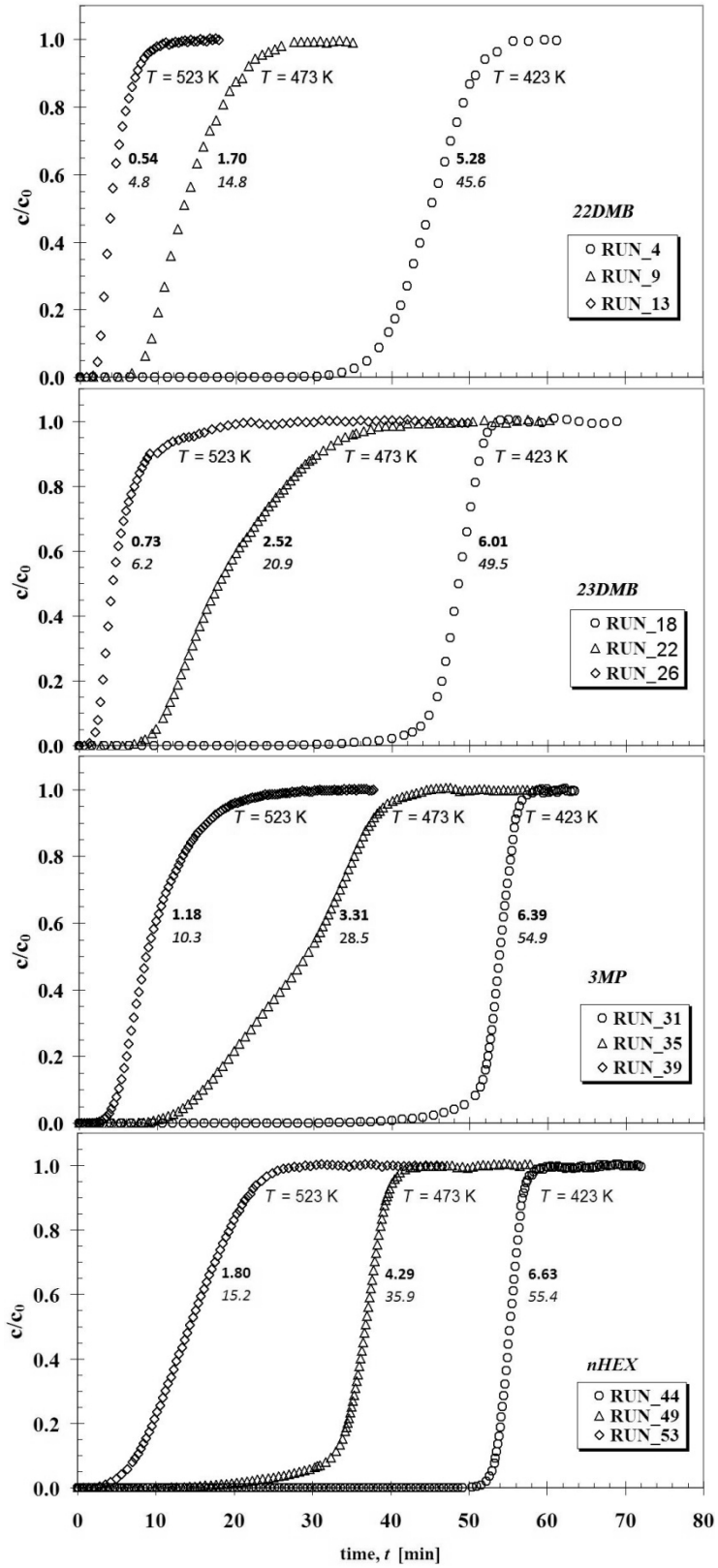


Figure 2.10. Single component breakthrough curves at partial pressure near to 12 kPa, for 22DMB, 23DMB, 3MP and *n*HEX at 423 K, 473 K and 523 K. Experimental conditions are specified in Table 2.2. The amount adsorbed (g/100g_{ads}) in bold and the stoichiometric time (min) in italic are also indicated.

2.7.2 Pure component Equilibrium Data

The adsorption equilibrium data of hexane isomers have been obtained in the adsorption equilibrium setup by estimating the adsorbed concentration as a function of the feed concentration from a mass balance in the fixed-bed. Table 2.2 shows the experimental conditions for the single breakthrough runs, including the hydrocarbon studied, partial pressure, temperature, flowrate, mass of adsorbent in the column and amount adsorbed for each run.

Table 2.2. Experimental conditions for breakthrough curves and amount adsorbed.

Run	Hydrocarbon partial press. (kPa)	Helium flowrate (mL/min)	Hydrocarbon molar rate (μmol/min)	Mass of adsorbent (mg)	Amount adsorbed ($g/100g_{ads}$)	Temp. (K)
			22DMB			
1	0.3	40.0	5.0	924.8	0.48	423
2	1.8	9.8	7.5	924.8	2.01	
3	6.4	3.5	10.0	924.8	4.36	
4	10.7	2.5	12.6	924.8	5.28	
5	19.3	2.0	20.1	924.8	6.33	
6	26.3	1.5	22.6	924.8	6.89	
7	0.3	40.0	5.0	924.8	0.08	473
8	6.4	3.5	10.0	924.8	1.09	
9	10.7	2.5	12.6	924.8	1.70	
10	26.3	1.5	22.6	924.8	3.32	
11	0.3	40.0	5.0	924.8	0.04	523
12	6.4	3.5	10.0	924.8	0.34	
13	10.7	2.5	12.6	924.8	0.54	
14	26.3	1.5	22.6	924.8	1.17	
			23DMB			
15	0.3	39.7	5.1	887.9	0.67	423
16	2.0	9.2	7.7	915.0	2.94	
17	5.9	3.9	10.2	887.9	5.19	
18	11.6	2.3	12.8	887.9	6.01	
19	29.1	1.3	23.0	887.9	6.96	
20	0.3	39.7	5.1	887.9	0.13	473
21	6.0	3.8	10.2	887.9	1.52	
22	11.6	2.3	12.8	887.9	2.52	
23	29.1	1.3	23.0	887.9	4.06	
24	0.3	39.5	5.1	887.9	0.04	523
25	6.0	3.8	10.2	887.9	0.36	
26	11.6	2.3	12.8	887.9	0.73	
27	29.1	1.3	23.0	887.9	1.78	

(cont.)

Table 2.2. Experimental conditions for breakthrough curves and amount adsorbed (*cont*.).

Run	Hydrocarbon partial press. (kPa)	Helium flowrate (mL/min)	Hydrocarbon molar rate (µmol/min)	Mass of adsorbent (mg)	Amount adsorbed ($g/100g_{ads}$)	Temp. (K)
			3MP			
28	0.3	39.7	5.1	923.0	1.89	423
29	1.9	9.3	7.7	923.0	4.17	
30	6.1	3.8	10.3	923.0	5.68	
31	12.5	2.1	12.8	923.0	6.39	
32	26.9	1.5	23.1	923.0	7.23	
33	0.3	39.5	5.1	923.0	0.27	473
34	6.1	3.8	10.3	923.0	2.43	
35	12.5	2.1	12.8	923.0	3.31	
36	26.9	1.5	23.1	923.0	4.50	
37	0.3	39.5	5.1	923.0	0.06	523
38	6.1	3.8	10.3	923.0	0.72	
39	12.5	2.1	12.8	923.0	1.18	
40	26.9	1.5	23.1	923.0	2.04	
			*n*HEX			
41	0.3	40.8	5.1	911.9	2.90	423
42	1.9	9.1	7.6	911.9	4.80	
43	5.9	3.9	10.2	911.9	5.92	
44	12.2	2.2	12.7	911.9	6.63	
45	27.6	1.4	22.9	911.9	7.40	
46	0.3	40.8	5.1	911.9	0.62	473
47	1.9	9.1	7.6	911.9	2.01	
48	5.9	3.9	10.2	911.9	3.36	
49	12.2	2.2	12.7	911.9	4.29	
50	27.6	1.4	22.9	911.9	5.31	
51	0.3	40.8	5.1	911.9	0.14	523
52	5.9	3.9	10.2	911.9	1.18	
53	12.2	2.2	12.7	911.9	1.80	
54	27.6	1.4	22.9	911.9	2.94	

Different feed concentrations were obtained by mixing the hydrocarbon with helium in different proportions. The experiments were performed at temperatures of 423 K, 473 K and 523 K and partial pressures between 0.3 and 30 kPa. The data shown in Table 2.2 were plotted in terms of the amount adsorbed (loading) as a function of the partial pressure giving rise to the adsorption isotherms shown in Figure 2.11. The loading is expressed in terms of the mass of hydrocarbon adsorbed per mass of pellets. It should be noted that the binder – which corresponds to 30 wt% of the pellet – is also included in the calculation of the loadings.

It can be seen that all isotherms are type I in IUPAC classification. The equilibrium data clearly shows that a significant amount of mass of the isomers can be adsorbed in the pellets, with values at 423 K and at a partial pressure of 30 kPa reaching 7g/100g_{ads}; however, with increasing temperature the amount adsorbed decreases to approximately 1.5g/100g_{ads} at 523K. At low partial pressure the *n*HEX is the more strongly adsorbed component followed by 3MP, 23DMB and 22DMB respectively. With increasing partial pressure the difference between the amounts adsorbed for the isomers tends to decrease.

In order to understand better the sorption behaviour, the equilibrium data was plotted in terms of virial plots, *i.e*., semi-log plots of p/q *versus* q, where p is the partial pressure and q is the amount adsorbed, in order to obtain Henry's constant H which can give insight into sorption events. Figure 2.12 shows such representation. Data extrapolation to zero coverage gives us the Henry's constant which are listed in Table 2.3. In the case of experiments at 423 K for 3MP and *n*HEX the best fitted isotherm (Toth) was used to generate the points at low loading and then the extrapolation was a linear one as for the other temperatures. Table 2.3 clearly shows that the affinity to the adsorbent measured by the values of the Henry's constants, decreases in the order *n*HEX > 3MP > 23DMB > 22DMB for all the temperatures. This result is on agreement with the one reported by Denayer et al. (1998b) in pulse chromatography experiments on zeolite beta at 573 K. Indeed, the Henry's constant of C_6 alkanes reported in their work decreases in the following order: *n*HEX > 2MP > 3MP > 23DMB > 22DMB.

Note

It must be noted that similar amounts of monobranched 2MP and 3MP are present in both the LSR naphtha and the hydroisomerization effluent; however, 2MP was not considered for the purpose of this work. This choice was based on the inference arising from the work of Denayer et al. (1998b), i.e., since the affinity of zeolite beta towards 2MP falls between the one for 3MP and nHEX, then 2MP may be discarded to simplify the experimental procedures carried out along this work.

From our data, it can be concluded that *n*HEX is the component with higher affinity to the adsorbent and 22DMB the component with the lower affinity. This can be explained based on the adsorbent structure (Figure 2.3) and the configuration of the hexane isomers (Figure 2.2); since *n*HEX is a linear molecule it can access both the straight and zigzag channels of the adsorbent. As the degree of branching increases, the accessibility of the molecules to the active sites of the channels decreases giving rise to lower values of the Henry's constants. This behaviour is more pronounced for 22DMB, the molecule with the higher molecular kinetic diameter.

We believe that molecules of 22DMB are probably trapped in the intersections of zigzag channels, blocking the access of other molecules to the active sites of the zigzag channels and this effect is accounted for in the Henry's constant. Due to this behaviour, the selectivity between the isomers measured by the values of the Henry's constant with 22DMB as the reference component, increases as the molecule becomes more linear and with a lower molecular kinetic diameter. The values of selectivities are listed in Table 2.4 for the three temperatures studied and range from 8.8 between *n*HEX and 22DMB at 423 K to 1.2 between 23DMB and 22DMB at 473K. From Table 2.4 it seems that as the temperature increases the selectivity decreases. The values of the selectivity are similar to those reported by Denayer et al. (1998b) in crystals of zeolite beta with a Si/Al ratio of 12 synthesized in laboratory, and higher than those reported by Jolimaitre (1999) in studies performed with silicalite pellets. However, it should be now noted that the selectivities can change, when mixtures of the isomers are in contact with structures with different pore channels (Krishna et al., 1999). This point will be addressed in Chapter 3.

The heats of sorption at zero coverage ΔH_0 obtained from the temperature dependence of Henry´s constants according to the van´t Hoff equation are given in Table 2.3. They range from 53.6 kJ/mol for 22DMB to 63.4 kJ/mol for *n*HEX. These results in pellets are similar to some published in literature for crystals of zeolite beta and crystals and pellets of silicalite (Talu et al., 1998; Jolimaitre, 1999; Denayer et al. 1998a, 1998b).

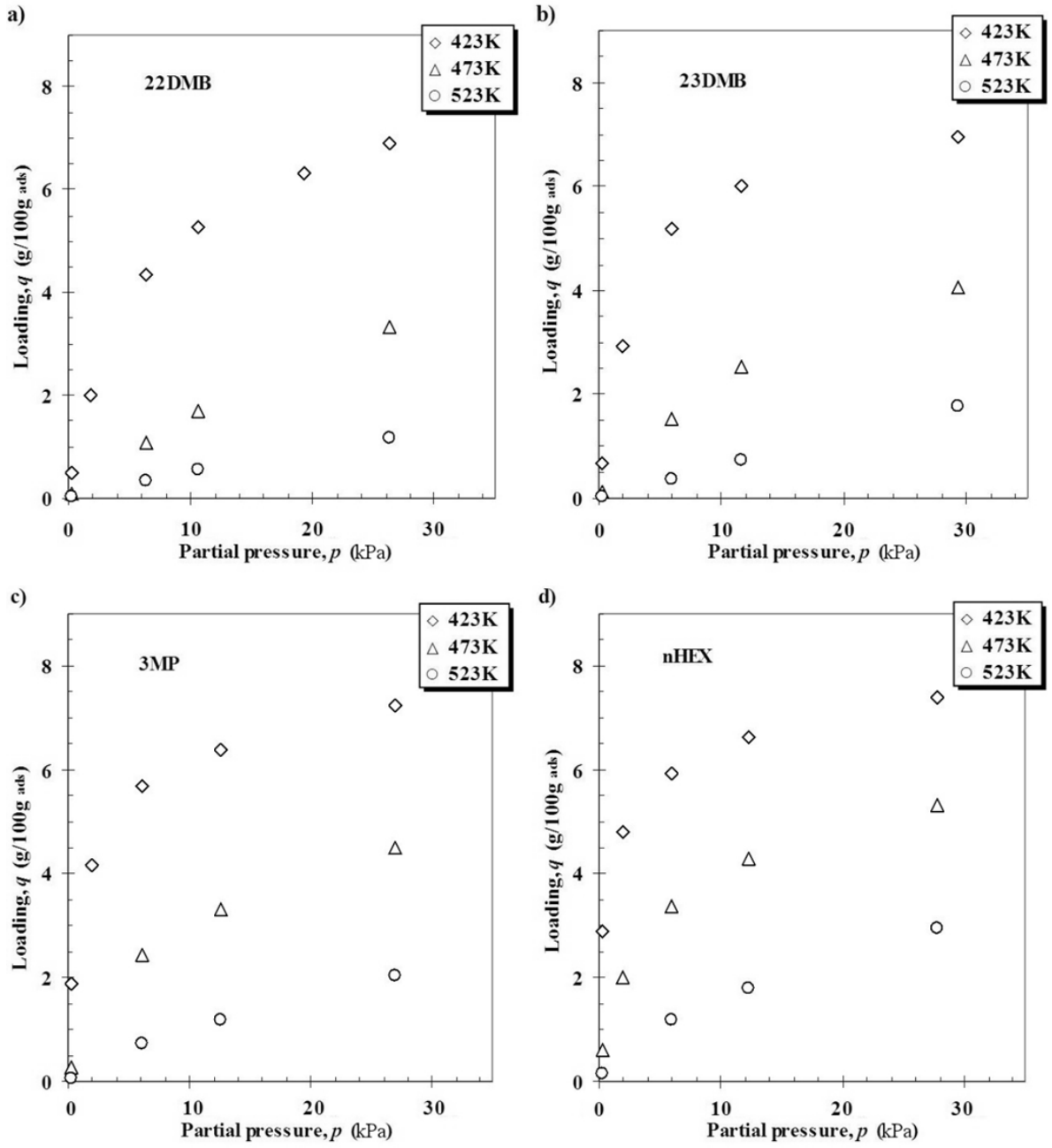


Figure 2.11. Adsorption equilibrium isotherms of hexane isomers on zeolite beta. (a) 22DMB, (b) 23DMB, (c) 3MP and (d) *n*HEX on pellets of zeolite beta at 423K, 473K and 523K.

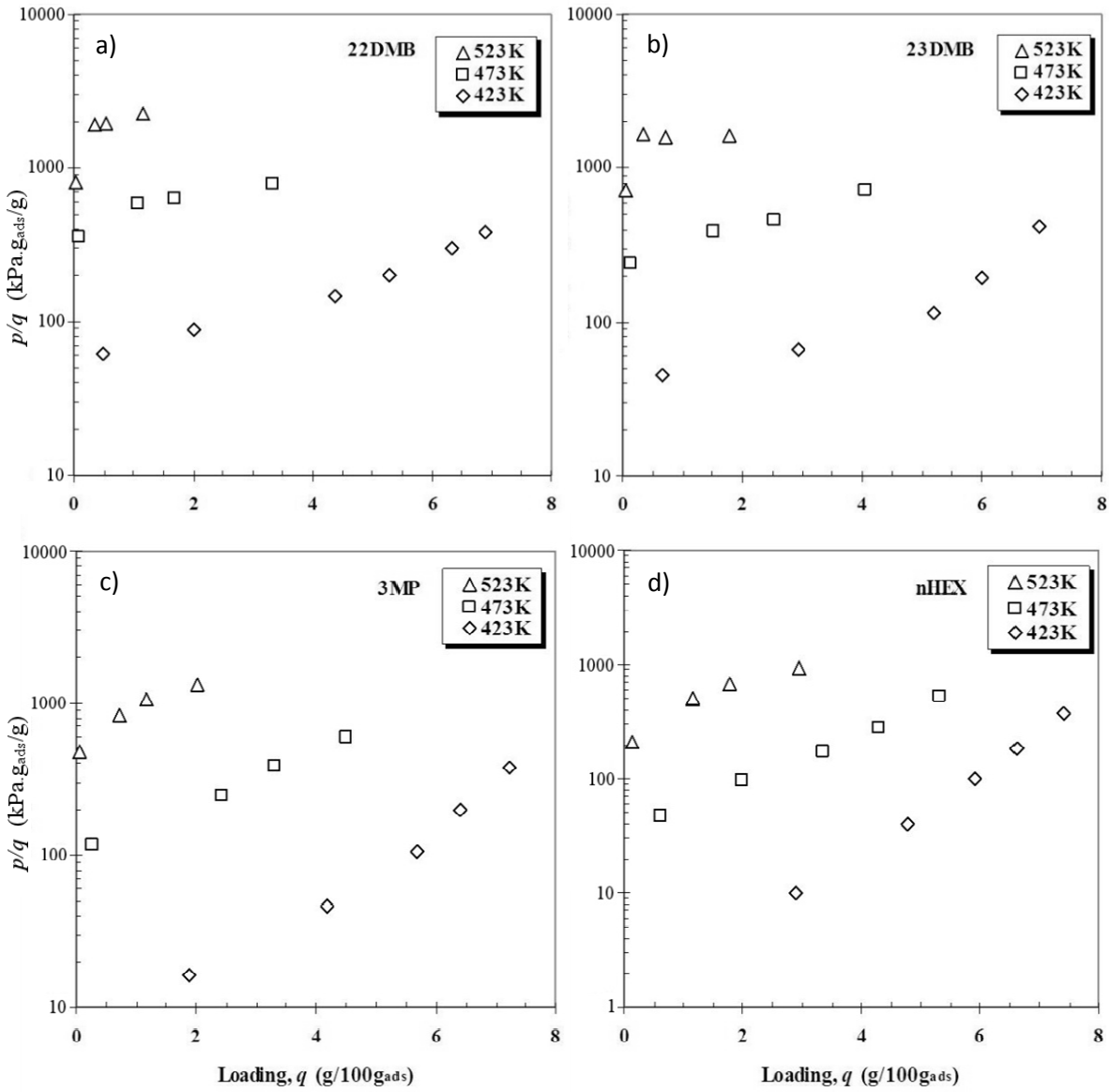


Figure 2.12. Semilog plot of p/q vs. q for analysis of virial isotherm of (a) 22DMB, (b) 23DMB, (c) 3MP, (d) *n*HEX.

Table 2.3. Adsorption enthalpy's at zero coverage ($-\Delta H_0$) and Henry constants (H) on beta zeolite at 423 K, 473 K and 523 K for hexane isomers.

T(K)	$H \times 10^3$ (g/g$_{ads}$·kPa)			
	22DMB	23DMB	3MP	*n*HEX
423	14.0	19.0	59.0	125.0
473	3.8	4.5	10.0	25.0
523	1.4	2.0	2.7	5.9
$-\Delta H_0$ (kJ/mol)	*53.6*	*57.1*	*59.7*	*63.4*

Table 2.4. Selectivities based on Henry's constant between hexane isomers on zeolite beta at 423 K, 473 K and 523 K

T(K)	H_i / H_{22DMB}			
	22DMB	23DMB	3MP	*n*HEX
423	1	1.3	4.1	8.8
473	1	1.2	2.7	6.6
523	1	1.4	1.9	4.1

In adsorption equilibrium studies it is also important to evaluate the influence of coverage on the isosteric heat of sorption q_{st} evaluated from the thermodynamic relation,

$$q_{st_i} = RT^2 \left(\frac{\partial \ln p}{\partial T} \right)_q \tag{2.16}$$

where R is the is the ideal gas law constant and T is the temperature. Figure 2.13 shows the dependence of the isosteric heat of sorption with coverage for the four isomers. Due to the lack of experimental data at very low partial pressure we present only the variation of the isosteric heat of sorption with loading for q > 0.5 g/100g adsorbent. In this calculation the values of partial pressure p, at constant loading q, for different temperatures were taken from the experimental isotherm data. In a general

way, the isosteric heat of sorption slightly decreases with the loading. This result suggests that more active sites are occupied first.

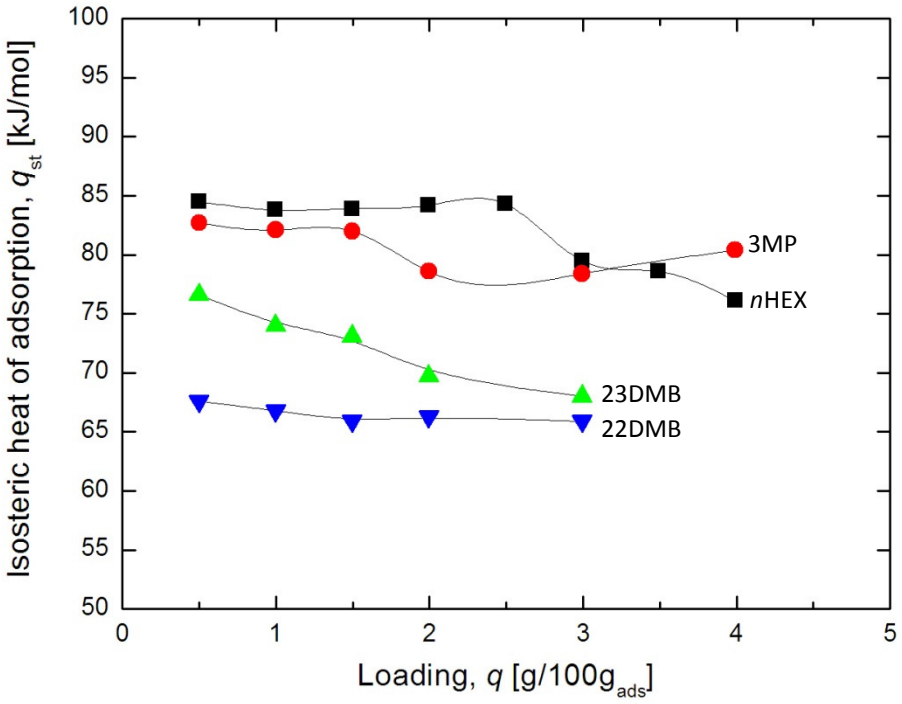


Figure 2.13. Coverage dependence of isosteric heat of adsorption.

2.7.3 Modelling of Pure Component Isotherms

Four different models were used to describe pure component adsorption equilibrium isotherms that can be classified as type I: *i*) Langmuir, *ii*) multi-site Langmuir (or Nitta), *iii*) dual-site Langmuir (DSL) and *iv*) Toth. The experimental sorption isotherms and the description given by the four models are shown in Figure 2.14 for all the isomers studied. The corresponding parameters were determined by using a numerical procedure which minimize the mean absolute deviations, $\overline{\Delta q}$, between the predicted, q, and the experimental, $q_{\exp}$ given by the following expression (Valenzuela and Myers, 1989):

$$\overline{\Delta q} = \frac{1}{M}\sqrt{\sum_{i=1}^{M}\left(q_{\exp,i} - q_i\right)^2} \qquad (2.17)$$

being M the total number of measurements. The fitted parameters for each model are listed in Table 2.5. In order to keep some consistency between the models, the saturation loading capacity is fixed for the four models at $q^m = q_1^m + q_2^m = 9\ \mathrm{g/100g_{ads}}$, a value near the one suggested by Huddersman and Klimcyzk (1996) for the adsorption of hexane isomers in zeolite beta. This value gives approximately a saturating loading capacity of 4 molecules per unit cell, which agrees also with values reported by Jolimaitre (1999) for silicalite. With q^m fixed the fitting procedure consists on the determination of the other parameters of the sorption isotherms by an appropriate numerical routine that minimizes $\overline{\Delta q}$, defined as the average of the absolute difference between experimental and calculated results (Valenzuela and Myers, 1989). The values of $\overline{\Delta q}$ for the fittings are shown in Table 2.5.

Figure 2.14 and the values $\overline{\Delta q}$ in Table 2.5 show that the Langmuir model isotherm does not predict the adsorption for none of the hydrocarbons studied, especially at low temperatures. However, the adsorption equilibrium was satisfactorily described by the DSL, Toth and Nitta models. Apparently, these results show that it is not possible in the range of partial pressures and temperatures studied to discriminate between sorption isotherm models with more than two adjustable parameters.

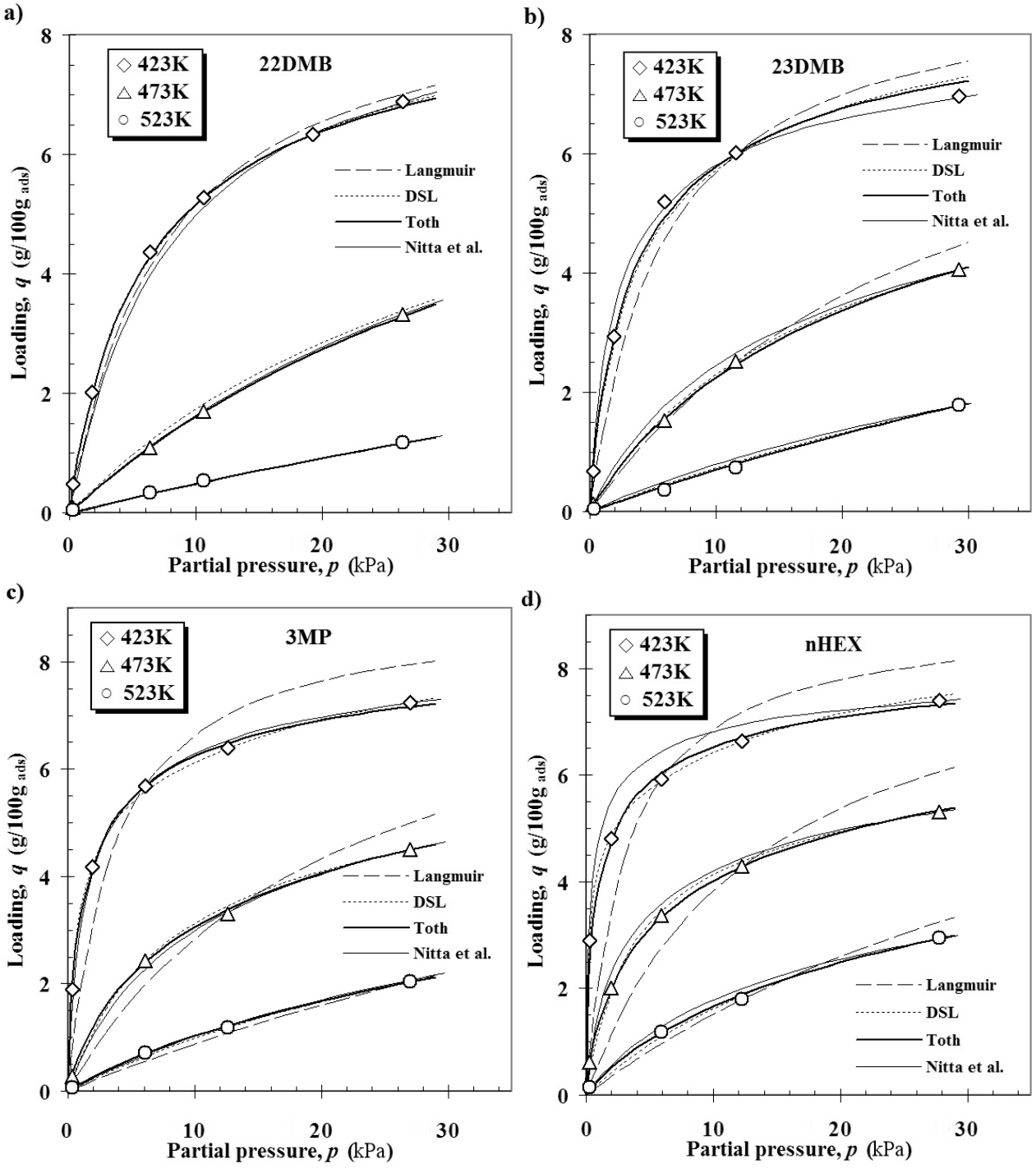


Figure 2.14. Adsorption equilibrium isotherm models fitted to experimental data of (a) 22DMB, (b) 23DMB, (c) 3MP and (d) *n*HEX on pellets of zeolite beta. The represented models are Langmuir, dual-site Langmuir (DSL), Toth and Nitta *et al*.

Table 2.5. Isotherm models parameters for hexane isomers on pellets of zeolite beta and average deviation between predicted values and experimental data.

Isotherm Models		22DMB				23DMB				3MP				*n*HEX			
		Lang.	DSL	Toth	Nitta	Lang.	DSL	Toth	Nitta	Lang.	DSL	Toth	Nitta	Lang.	DSL	Toth	Nitta
q^m	(g/100g_{ads})	9		9	9	9		9	9	9		9	9	9		9	9
$-E$	(kJ/mol)	58.2		64.7	56.8	55.6		72.0	71.7	59.9		89.0	73.3	50.9		90.1	90.7
$q^m{}_1$	(g/100g_{ads})		5				5				5				5		
$-E_1$	(kJ/mol)		65.8				66.5				81.2				84.1		
$q^m{}_2$	(g/100g_{ads})		4				4				4				4		
$-E_2$	(kJ/mol)		52.6				56.2				69.7				72.1		
Temperature 423K																	
$H \times 10^3$	(g/g_{ads}.kPa)	12.0	16.2	16.9	11.2	15.6	28.4	37.7	46.1	25.3	96.0	200.0	69.4	29.2	224.0	495.0	475.0
$b \times 10^3$	(kPa^{-1})	134		188	124	174		418	512	281		2221	772	325		5500	5275
$b_1 \times 10^3$	(kPa^{-1})		276				518				1879				4421		
$b_2 \times 10^3$	(kPa^{-1})		60				62				53				62		
s	(–)			0.83				0.70				0.51				0.46	
n	(–)				1				2				2				3
$\overline{\Delta q}$	(g/100g_{ads})	*0.150*	*0.033*	*0.034*	*0.183*	*0.332*	*0.158*	*0.151*	*0.202*	*0.708*	*0.048*	*0.036*	*0.140*	*0.933*	*0.049*	*0.196*	*0.404*
Temperature 473K																	
$H \times 10^3$	(g/g_{ads}. kPa)	2.0	2.2	2.0	2.0	3.0	3.7	4.0	4.6	4.2	7.2	12.3	6.7	6.7	16.0	37.5	27.9
$b \times 10^3$	(kPa^{-1})	21.9		21.9	22.2	33.6		44.1	51.2	46.3		136.0	74.2	74.3		417.0	310.0
$b_1 \times 10^3$	(kPa^{-1})		34.0				67.0				139.0				313.0		
$b_2 \times 10^3$	(kPa^{-1})		13.0				7.9				6.0				9.4		
s	(–)			1.00				0.76				0.56				0.50	
n	(–)				1				2				2				3
$\overline{\Delta q}$	(g/100g_{ads})	*0.019*	*0.019*	*0.019*	*0.022*	*0.116*	*0.025*	*0.027*	*0.094*	*0.272*	*0.049*	*0.031*	*0.062*	*0.530*	*0.083*	*0.015*	*0.136*
Temperature 523K																	
$H \times 10^3$	(g/g_{ads}. kPa)	0.5	0.5	0.5	0.5	0.8	0.8	0.8	0.9	1.0	1.2	1.6	1.3	1.8	2.4	3.7	3.5
$b \times 10^3$	(kPa^{-1})	5.7		5.7	5.7	8.4		8.4	10.5	10.8		17.7	14.4	20.3		40.7	38.4
$b_1 \times 10^3$	(kPa^{-1})		10.9				14.0				23.0				46.1		
$b_2 \times 10^3$	(kPa^{-1})		0.5				3.0				1.2				1.2		
s	(–)			1.00				1.00				0.65				0.59	
n	(–)				1				2				2				3
$\overline{\Delta q}$	(g/100g_{ads})	*0.019*	*0.005*	*0.019*	*0.017*	*0.039*	*0.039*	*0.039*	*0.080*	*0.075*	*0.075*	*0.019*	*0.037*	*0.151*	*0.052*	*0.033*	*0.089*
$\overline{\Delta q}_{GLOBAL}$ [§]	(g/100g_{ads})	*0.063*	*0.019*	*0.024*	*0.074*	*0.162*	*0.074*	*0.072*	*0.125*	*0.352*	*0.058*	*0.028*	*0.080*	*0.538*	*0.061*	*0.081*	*0.210*
$\overline{\Delta q}_{GLOBAL}$	(mmol/g_{ads})	*0.007*	*0.002*	*0.003*	*0.009*	*0.019*	*0.009*	*0.008*	*0.015*	*0.041*	*0.007*	*0.003*	*0.009*	*0.063*	*0.007*	*0.009*	*0.024*

[§] $\overline{\Delta q}_{GLOBAL}$ is the mean absolute deviation in the temperature range studied (423–523 K).

2.7.4 Kinetics of Sorption

The kinetics of sorption was measured by the ZLC technique in the apparatus shown in Figure 2.8. Data from the ZLC experiments were modelled by the original model proposed by Eic and Ruthven (1988) in order to obtain the diffusional time constants.

In bidisperse porous adsorbents such as zeolite pellets there are in principle two diffusion mechanisms: the macropore diffusion representing the diffusion in the pores between zeolite beta crystals, with reciprocal time constant $\tau_{dif} = D_p / R_p^{\,2}(1+K)$ and the micropore diffusion inside crystals with reciprocal time constant D_c / r_c^2. Assuming that the diffusion mechanisms are in series, Ruchenstein et al. (1971) developed a bidisperse porous model applied to the measurement of transient diffusion. Based in such model Ruthven and Loughlin (1972) developed a criterion to the relative importance of the diffusion mechanisms which is given by γ:

$$\gamma = \frac{D_c / r_c^{\,2}(1+K)}{D_p / R_p^{\,2}} \qquad (2.18)$$

where $K\left(=(1-\varepsilon_p)H_{ad}/\varepsilon_p\right)$ is the capacity factor and $H_{ad}\left(=\rho_p RTH / M_W\right)$ is the dimensionless Henry's constant or local slope of isotherm. ρ_p and ε_p are the density and the porosity of the pellets, respectively. Macropore diffusivity is the controlling mechanism for $\gamma > 10$; crystal diffusivity is the controlling mechanism for $\gamma < 0.1$; if $0.1 < \gamma < 10$ both macropore and micropore diffusivity should be taken into account. For the present system we can first evaluate the possibility of measuring micropore diffusion, since our pellets are formed by small crystals with sizes ranging from 0.2–0.4 μm as confirmed the SEM analysis (Figure 2.4), and we are using a macroscopic technique which is valid for time constants higher than 10 seconds if we want to measure reliable data and eliminate extraneous effects. There are few data in open literature for diffusion of hydrocarbons in zeolite beta; most of the studies are performed in silicalite. However, since our zeolite is a large pore one and silicalite is a

medium pore one, the data obtained from silicalite can serve as a guide to evaluate the possibility of measuring micropore diffusion, i.e., diffusion in zeolite beta is probably higher than in silicalite. Table 2.6 summarizes data obtained from open literature for diffusion of hexane isomers in silicalite and zeolite beta. Table 2.6 shows that data are scattered for all the isomers. This can be explained by the different measurement techniques used. From the data reported on Table 2.6 it is clear that *n*HEX is the component with higher mobility in the zeolites and 22DMB is the component with lower mobility.

As a reference to evaluate time constants, we can use the data measured by Zhu et al. (2001). For *n*HEX the value reported at 408 K is 2.21×10^{-12} m^2/s, which gives a value of r_c^2 / D_c equal to 0.018 s for a crystal with a size of 0.2 μm. This result shows clearly that it is impossible to measure micropore diffusion of *n*HEX using the ZLC technique with the small crystals. Let us now evaluate for the component with the lower mobility, *i.e.* 22DMB. Zhu et al. (2001) does not measure diffusion on this component, but we can use the data measured by Cavalcante and Ruthven (1995b) by a gravimetric technique. For 22DMB the value reported at 423 K is 8.1×10^{-16} m^2/s, which gives a value of r_c^2 / D_c equal to 49 s for a crystal with a size of 0.2 μm. This value indicates that it may be possible to measure micropore diffusion for 22DMB with the ZLC technique.

In our study, several experimental ZLC runs were performed for all the isomers in the pellets of zeolite beta, at the temperatures of 423 K, 472 K and 523 K and at a partial pressure of sorbate of approximately 0.3 kPa. The objective was to study the effect of temperature and flowrate of carrier gas in ZLC desorption curves. Table 2.7 summarizes all the experiments performed including, experimental conditions (carrier gas flowrate and temperature), intercept and slope measured from desorption curves and model parameters obtained from the procedure previously discussed. Figure 2.15 shows typical experimental desorption curves for all the isomers in semi-log plots which show the effect of temperature in desorption curves at a fixed flowrate of carrier gas. From Figure 2.15 the long times straight lines are clearly seen.

Table 2.6 Diffusivity and thermodynamic data reported in the literature for C_6 isomers in silicalite and zeolite beta.

Adsorbent	T(K)	Method	D_c (m^2/s)	E_a (kJ/mol)	$-\Delta H$(kJ/mol)	$H\times10^3$ (g/g.kPa)	References
*n*HEX							
Silicalite	408	TEOM	2.2×10^{-12}	38.1			W. Zhu et al. (2001)
	423	FR	2.9×10^{-13}	17			Van den Begin et al. (1989)
		BD/TST	6.0×10^{-10}	4.7			Maginn et al. (1996)
		SCM	4.8×10^{-12}	12.9	76.2		Talu et al. (1998)
	473	FR	3.9×10^{-13}	17			Van den Begin et al. (1989)
		BD/TST	7.6×10^{-10}	4.7			Maginn et al. (1996)
		SCM	6.4×10^{-12}	12.9	76.2		Talu et al. (1998)
	523	FR	4.8×10^{-13}	17			Van den Begin et al. (1989)
		BD/TST	8.8×10^{-10}	4.7			Maginn et al. (1996)
		SCM	7.7×10^{-12}	12.9	76.2		Talu et al. (1998)
Beta	423	CHROM			62.7		Denayer et al. (1998b)
		ZLC			63.4	125.0	This work
	473	CHROM			62.7		Denayer et al. (1998b)
		ZLC			63.4	25.0	This work
	523	CHROM			62.7		Denayer et al. (1998b)
		ZLC			63.4	5.9	This work
	573	CHROM			62.7	6.9	Denayer et al. (1998b)
3MP							
Silicalite	408	TEOM	4.5×10^{-13}	52.4			W. Zhu et al. (2001)
	423	CHROM	1.2×10^{-15}	56	66.4		Jolimaitre (1999)
		GRAV	1.3×10^{-12}	58	62.7		Cavalcante and Ruthven (1995b)
	473	CHROM	4.9×10^{-15}	56	66.4		Jolimaitre (1999)
		GRAV	7.5×10^{-12}	58	62.7		Cavalcante and Ruthven (1995b)
	523	CHROM	1.5×10^{-14}	56	66.4		Jolimaitre (1999)
		GRAV	3.1×10^{-11}	58	62.7		Cavalcante and Ruthven (1995b)
Beta	423	CHROM			60.0		Denayer et al. (1998b)
		ZLC			59.7	59.0	This work
	473	CHROM			60.0		Denayer et al. (1998b)
		ZLC			59.7	10.0	This work
	523	CHROM			60.0		Denayer et al. (1998b)
		ZLC			59.7	2.7	This work
	573	CHROM			60.0	3.2	Denayer et al. (1998b)
	598	CHROM	2.7×10^{-10}				Huddersman and Klimcyzk (1996)
23DMB							
Beta	423	TEOM	2.1×10^{-14}	63.9			W. Zhu et al. (2001)
		CHROM			59.5		Denayer et al. (1998b)
		ZLC			57.1	19.0	This work
	473	CHROM			59.5		Denayer et al. (1998b)
		ZLC			57.1	4.5	This work
	523	CHROM			59.5		Denayer et al. (1998b)
		ZLC			57.1	2.0	This work
	573	CHROM			59.5	2.1	Denayer et al. (1998b)
	598	CHROM	3.0×10^{-10}				Huddersman and Klimcyzk (1996)
22DMB							
Silicalite	423	CHROM	3.4×10^{-17}	68	55.0		Jolimaitre (1999)
		GRAV	8.1×10^{-16}	77	54.4		Cavalcante and Ruthven (1995b)
	473	CHROM	2.6×10^{-16}	68	55.0		Jolimaitre (1999)
		GRAV	8.2×10^{-15}	77	54.4		Cavalcante and Ruthven (1995b)
	523	CHROM	1.4×10^{-15}	68	55.0		Jolimaitre (1999)
		GRAV	5.3×10^{-14}	77	54.4		Cavalcante and Ruthven (1995b)
Beta	423	CHROM			54.1		Denayer et al. (1998b)
		ZLC			53.6	14.0	This work
	473	CHROM			54.1		Denayer et al. (1998b)
		ZLC			53.6	3.8	This work
	523	CHROM			54.1		Denayer et al. (1998b)
		ZLC			53.6	1.4	This work
	573	CHROM			54.1	1.0	Denayer et al. (1998b)

Figure 2.15 shows that as degree of branching increases the experiments become faster which was apparently not expected since the dibranched paraffins have the lower mobility in the zeolites. The only explanation is that the equilibrium of adsorption plays an important role in the kinetics of sorption. When the process is governed by macropore diffusion the slopes of long time desorption curves shown in Figure 2.15 are directly proportional to $\tau_{dif} = D_p / R_p^2 (1 + K)$ (Equation 2.12), where the parameter K is related to the equilibrium data through Henry's constants. Since K decreases as the degree of branching increases the desorption curves become faster.

Table 2.8 summarizes the values of time constants measured from ZLC data, and the values of the activation energy obtained from an Arrhenius plot, which is represented in Figure 2.16. It is well known that if the time constants of diffusion represented in an Arrhenius plot are strongly temperature dependent with activation energy of the order of the heat of adsorption, this is a clearly indication that macropore diffusion is controlling. According to the values reported in Table 2.8 the activation energies for diffusion of nHEX and 3MP are comparable to the heat of adsorption at zero coverage reported in Table 2.3. This indicates that macropore diffusion is dominant in our studies for *n*HEX and 3MP. For 23DMB and 22DMB the activation energies are different from the values of the heat of adsorption indicating that probably macropore diffusion is not the dominant one. However, we can conclude that micropore diffusion is not dominant since the activation energies of time constants are very high when compared with the values obtained for the diffusion in micropores which are usually not higher than 20 kJ/mol.

Table 2.7. Experimental conditions and model parameters for ZLC experiments.

T(K)	Flowrate (ml/min)	- *slope* (s^{-1})	*intercept*	β_1		τ_{dif} (s^{-1})	L
*n*HEX							
423	20	0.0020	0.87	1.32		0.001	0.66
	40	0.0024	0.74	1.80		0.001	1.42
	60	0.0027	0.61	2.14		0.001	2.35
					avg.	*0.001*	
473	20	0.0093	0.87	1.31		0.005	0.65
	40	0.0107	0.75	1.77		0.003	1.35
					avg.	*0.004*	
523	10	0.0186	0.95	0.89		0.024	0.28
	20	0.0285	0.86	1.35		0.016	0.70
					avg.	*0.020*	
3MP							
423	40	0.0047	0.77	1.72		0.002	1.26
	60	0.0049	0.66	2.01		0.001	1.94
					avg.	*0.001*	
473	20	0.0160	0.91	1.11		0.013	0.45
	40	0.0188	0.74	1.80		0.006	1.42
	60	0.0196	0.64	2.06		0.005	2.09
					avg.	*0.008*	
523	10	0.0303	0.92	1.06		*0.027*	0.40
23DMB							
423	60	0.0068	0.59	2.17		*0.001*	2.47
473	20	0.0217	0.71	1.90		*0.006*	1.64
523	10	0.0519	0.68	1.97		0.013	1.83
	20	0.0611	0.51	2.34		0.011	3.28
					avg.	*0.012*	
22DMB							
423	60	0.0102	0.61	2.13		*0.002*	2.32
473	20	0.0313	0.65	2.03		*0.008*	2.01
523	20	0.0804	0.64	2.08		*0.019*	2.15

If we consider that all the time constants of diffusion shown in Table 2.8 are representative of a mechanism of macropore diffusion, this is $\tau_{dif} = D_p / R_P^2(1+K)$, then we can evaluate the parameter γ defined by Equation 2.18.

Table 2.9 summarizes the data handling. Representative values of diffusion in micropores were obtained from the data of Zhu et al. (2001) and Cavalcante and Ruthven (1995b). Table 2.9 clearly indicates that as expected for *n*HEX and 3MP the

parameter γ is very high indicating that the system is dominated by macropore diffusion. However, for 23DMB and 22DMB the values of γ decrease significantly, allowing us to conclude that probably both micropore and macropore diffusion become of importance. To clarify this point it is interesting to perform experiments with crystals of zeolite beta in powder form. The manufacturer of the pellets sends us zeolite beta crystals with the same size used to produce commercial pellets. Experiments were performed but the data were not reliable due to the fast diffusion of the species leading to ZLC experiments with duration below 5 seconds.

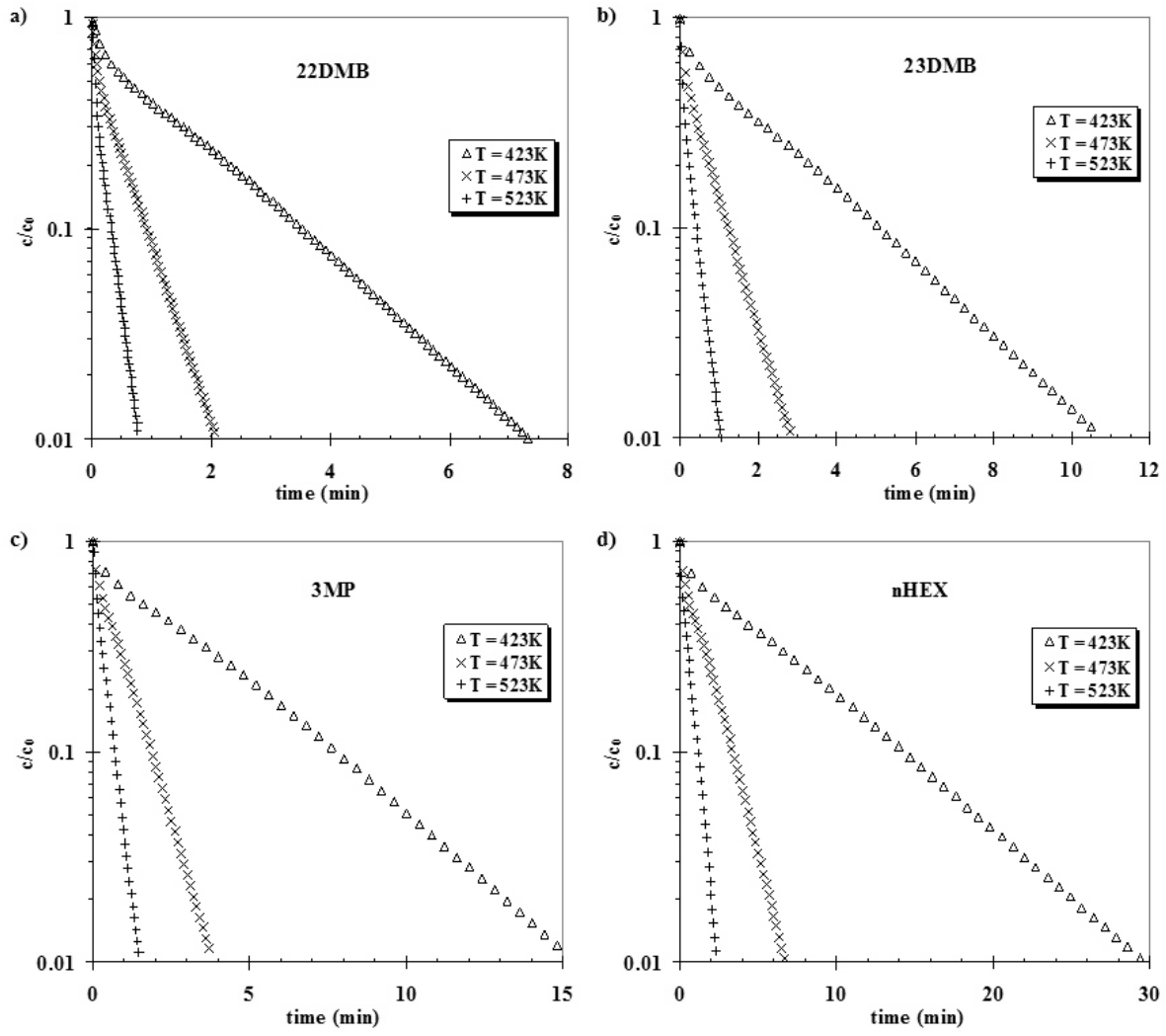


Figure 2.15. Effect of temperature on ZLC desorption curves: (a) 22DMB, (b) 23DMB, (c) 3MP and (d) *n*HEX. Semilog plot of c/c_0 *vs* time.

Table 2.8. Diffusional time constants and activation energies obtained from ZLC experimental data.

T (K)	$\tau_{dif} \times 10^3$ (s^{-1})*			
	22DMB	23DMB	3MP	*n*HEX
423	2.2	1.4	1.4	0.8
473	7.6	6.0	7.8	4.5
523	19.0	12.0	27.0	20.0
E_a (kJ/mol)	39.0	39.6	54.7	58.1

* $\tau_{dif} = D_c / r_c^2$ or $\tau_{dif} = D_p / R_p^2(1+K)$.

Considering that diffusion in macropores is Knudsen diffusivity in series with molecular diffusion, and so the pore diffusivity is

$$D_p = \frac{1}{\Gamma_p\left(\frac{1}{D_m} + \frac{1}{D_K}\right)} \tag{2.19}$$

where Γ_p is the tortuosity. The Knudsen diffusion coefficient D_K is:

$$D_K = 97\, r_{pore}\left(T / M_w\right)^{0.5} \tag{2.20}$$

where r_{pore} is the mean macropore radius (m) and M_w is the molecular weight. An average pore radius of 375 Å was used to estimate the Knudsen diffusivity. The molecular diffusion coefficient D_m is estimated from the Chapman-Enskog equation (Bird et al., 2002). Table 2.10 summarizes the experimental and predicted macropore diffusivities by adjusting the parameter that represents the tortuosity. Table 2.10 shows that tortuosity is approximately constant for a certain isomer; its value increases in the following order: 23DMB > 22DMB > 3MP > *n*HEX.

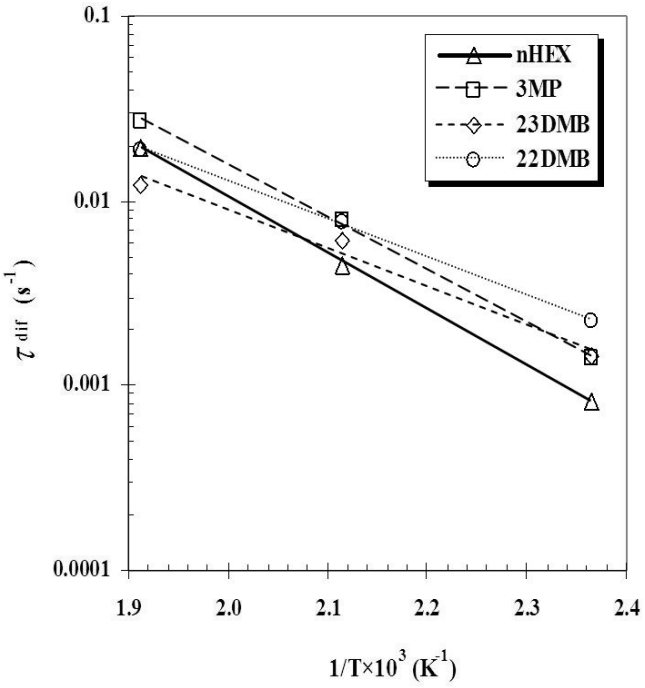


Figure 2.16. Arrhenius plot of τ_{dif} for the hexane isomers.

Table 2.9. Importance of the diffusion mechanisms, measured by, $\gamma = \dfrac{D_c / r_c^2 (1+K)}{D_p / R_p^2}$.

T (K)	τ_{dif} ×10^3 (s^{-1})	$D_{p,exp}$ (m^2/s)	$D_{c,exp}$ (m^2/s)	H×10^3 (g/g.kPa)	K (-)	γ (-)
*n*HEX*						
423	0.8	4.5×10^{-6}	3.5×10^{-12}	125.0	9029	185940
473	4.5	5.4×10^{-6}	1.1×10^{-11}	25.0	2019	111309
523	20.0	6.2×10^{-6}	2.9×10^{-11}	5.9	527	65311
3MP*						
423	1.4	3.6×10^{-6}	8.6×10^{-13}	59.0	4247	27332
473	7.8	3.8×10^{-6}	4.1×10^{-12}	10.0	808	23703
523	27.0	3.9×10^{-6}	1.5×10^{-11}	2.7	241	24324
23DMB*						
423	1.4	1.1×10^{-6}	2.3×10^{-14}	19.0	1387	704
473	6.0	1.2×10^{-6}	1.6×10^{-13}	4.5	363	1153
523	12.0	1.2×10^{-6}	7.4×10^{-13}	2.0	179	2678
22DMB§						
423	2.2	1.4×10^{-6}	8.1×10^{-16}	14.0	1033	16
473	7.6	1.4×10^{-6}	8.2×10^{-15}	3.8	307	48
523	19.0	1.4×10^{-6}	5.3×10^{-14}	1.4	125	126

* Experimental data for micropore diffusivity (D_c) of Zhu et al. (2001) for silicalite by TOEM technique.

§ Experimental data for micropore diffusivity (D_c) of Cavalcante and Ruthven (1995b), for silicalite by the gravimetric technique

Table 2.10. Experimental and predicted pore diffusivities of hexane isomers in zeolite beta.

T (K)	$\tau_{dif}\times10^3$ (s^{-1})	$D_{p,exp}$ (m^2/s)	$H\times10^3$ (g/g.kPa)	K (-)	D_m (m^2/s)	D_k (m^2/s)	Γ_p
*n*HEX							
423	0.8	4.5×10^{-6}	125.0	9029	5.80×10^{-5}	8.06×10^{-6}	1.6
473	4.5	5.4×10^{-6}	25.0	2019	7.01×10^{-5}	8.52×10^{-6}	1.4
523	20.0	6.2×10^{-6}	5.9	527	8.30×10^{-5}	8.96×10^{-6}	1.3
3MP							
423	1.4	3.6×10^{-6}	59.0	4247	5.80×10^{-5}	8.06×10^{-6}	2.0
473	7.8	3.8×10^{-6}	10.0	808	7.01×10^{-5}	8.52×10^{-6}	2.0
523	27.0	3.9×10^{-6}	2.7	241	8.30×10^{-5}	8.96×10^{-6}	2.1
23DMB							
423	1.4	1.1×10^{-6}	19.0	1387	5.80×10^{-5}	8.06×10^{-6}	6.5
473	6.0	1.2×10^{-6}	4.5	363	7.01×10^{-5}	8.52×10^{-6}	6.3
523	12.0	1.2×10^{-6}	2.0	179	8.30×10^{-5}	8.96×10^{-6}	6.7
22DMB							
423	2.2	1.4×10^{-6}	14.0	1033	5.80×10^{-5}	8.06×10^{-6}	5.2
473	7.6	1.4×10^{-6}	3.8	307	7.01×10^{-5}	8.52×10^{-6}	5.5
523	19.0	1.4×10^{-6}	1.4	125	8.30×10^{-5}	8.96×10^{-6}	5.8

The values of tortuosity higher than 5 for 22DMB and 23DMB can be explained by different perspectives such as: *i*) the mobility of these components in the macropore structure is not correctly accounted for by the molecular and Knudsen diffusion; *ii*) the fact that micropore diffusion can also influence the ZLC desorption curves for 22DMB and 23DMB affect the final values of tortuosity increasing the values estimated through Equation 2.19; *iii*) the binder used to form the pellets can influence the mobility of the components in the macropore structure. It is difficult to evaluate which of the previous items is the most important; however, it seems that there is no doubt that macropore diffusion plays an important role in the kinetics of sorption of hexane isomers in the pellets of zeolite beta studied in this work, especially due to the small size of the crystals used to form the pellets. The results from this kinetic study contrast with the ones reported by Jolimaitre (1999) and Jolimaitre et al. (2002) for sorption of hexane isomers in pellets of silicalite, who found that the diffusional resistance of 22DMB and 3MP in the macropores is negligible when compared to diffusional resistance in the micropores.

2.8 Conclusions

A detailed study of equilibrium and kinetics of sorption of hexane isomers in commercial extrudates of zeolite beta was performed. The data obtained show that the pellets have important characteristics that can be useful in future strategies for separation and reaction of the hexane isomers by adsorption techniques. The equilibrium data clearly shows that a significant amount of hexane isomers can be adsorbed in the zeolites, with values at 423 K and at a partial pressure of 30 kPa reaching values of 7g/100g_{ads}; however with increasing temperature the values decrease reaching approximately 1.5 g/100g_{ads} at 523K for the same pressure. At low partial pressures, Henry's constants show that the affinity to the adsorbent of the isomers is: *n*HEX > 3MP > 23DMB > 22DMB or the more carbon skeleton is branched the lower is the Henry's constant. Accordingly, the selectivity measured by the Henry's constants using 22DMB as the reference component varies from approximately 8.8 between *n*HEX and 22DMB at 423 K to 1.2 between 23DMB and 22DMB at 473 K. The heats of sorption at zero coverage are all above 50 kJ/mol and less than 70 kJ/mol, decreasing with the degree of branching. It is also shown that heats of sorption change with the coverage of the adsorbent.

Four different models were used to fit the experimental data named: Langmuir, Dual-site-Langmuir; Multi-site-Langmuir and Toth. It is shown that the Dual-site-Langmuir, Multi-Site-Langmuir and Toth predict satisfactorily the equilibrium data.

The kinetic data measured by the macroscopic ZLC technique indicates that macropore diffusion is the controlling mechanism for *n*HEX and 3MP, but for 23DMB and 22DMB the intrusion of the micropore diffusion in the overall diffusion mechanism is of importance. From the values of tortuosity it is found that *n*HEX is the faster component (lower tortuosity in macropores) and 23DMB is the slower one (higher tortuosity in macropores). Measured by the ratio of tortuosities, *n*HEX has a mobility of approximately four times the mobility of 23DMB and 22DMB in the macropores of the pellet.

2.9 References

Bárcia, P.S.; Silva, J.A.C.; Rodrigues, A.E. Separation by Fixed-Bed Adsorption of Hexane Isomers in Zeolite BETA Pellets. *Ind. Eng. Chem. Res.* 45, 4316–4328 (2006).

Bird, R. B.; Stewart, W. E.; Ligthfoot, E. N. *Transport Phenomena*; Wiley, 1960. 2nd Edition, John Wiley: New York (2002).

Cavalcante, C.L.; Ruthven, D.M. Adsorption of Branched and Cyclic Paraffins in Silicalite. 1. Equilibrium. *Ind. Eng. Chem. Res.* 34, 177–184 (1995a).

Cavalcante, C.L.; Ruthven, D.M. Adsorption of Branched and Cyclic Paraffins in Silicalite. 2. Kinetics. *Ind. Eng. Chem. Res.* 34, 185–191 (1995b).

Database of Zeolite Structures: http://www.iza-structure.org (assessed, Nov 2009)

Denayer, J.F.; Souverijns, W.P.; Jacobs, A.; Martens, J.A.; Baron, G.V. Chromatographic Study of Adsorption of n-Alkanes on Zeolites at High Temperatures. *J. Phys. Chem. B* 102, 3077–3081 (1998a).

Denayer, J.F.; Souverijns, W.; Jacobs, P.A.; Martens, J.A.; Baron, G.V. High Temperature Low-Pressure Adsorption of Branched C_5–C_8 Alkanes on Zeolite Beta, ZSM-5, ZSM-22, Zeolite Y, and Mordenite. *J. Phys. Chem. B* 102, 4588–4597 (1998b).

Do, D.D. *Adsorption Analysis: Equilibria and Kinetics*, Imperial College Press: London (1998).

Eic, M.; Ruthven, D.M. A New Experimental Technique for Measuring Intracrystalline Diffusivity. *Zeolites* 8, 40–45 (1988).

Fox, J.P.; Rooy, V.; Bates, S.P. Simulating the Adsorption of Linear, Branched and Cyclic Alkanes in Silicalite-1 and $AlPO_4$-5. *Micropor. Mesopor. Mater*. 69, 9–18 (2004).

Funke, H.H.; Argo, A.M.; Falconer, J.L.; Noble, R.D. Separations of Cyclic, Branched, and Linear Hydrocarbon Mixtures through Silicalite Membranes. *Ind. Eng. Chem. Res.* 36, 137–143 (1997).

Huddersman, K.; Klimczyk, M. Separation of Branched Hexane Isomers Using Zeolite Molecular Sieves. *AIChE J.* 42, 405–408 (1996b).

Jolimaitre, E. Étude et Modélisation de l'Adsorption et du Transfer de Matière dans les Zéolithes de Structure MFI. Application à la Séparation des Hydrocarbures Saturés mono et di-Branchés, Ph.D. Thesis, LAGEP - Université Claude Bernard, Lyon (1999).

Jolimaitre, E.; Ragil, K.; Fayolle, M.T.; Jallut, C. Separation of Mono- and Dibranched Hydrocarbons on Silicalite. *AIChE J.* 48, 1927–1937 (2002).

Kärger, J. The Random Walk of Understanding Diffusion. *Ind. Eng. Chem. Res*. 41, 3335–3340 (2002).

Kärger, J.; Freude, D. Mass Transfer in Micro- and Mesoporous Materials. *Chem. Eng. Technol.* 25, 769–778 (2002).

Kärger, J.; Ruthven, D. M. *Diffusion in Zeolites and Other Microporous Solids*, Wiley: New York (1994).

Krishna, R.; Baur, R. Separation of Hydrocarbon Mixtures Using Zeolite Membranes: a Modelling Approach Combining Molecular Simulations with the Maxwell–Stefan Theory. *Sep. Purif. Technol.* 21, 111–136 (2000a).

Krishna, R.; Vlugt, T.J.H.; Smit, B. Influence of Isotherm Inflection on Diffusion in Silicalite. *Chem. Eng. Sci.* 54, 1751–1757 (1999).

Langmuir, I. The Adsorption of Gases on Plane Surfaces of Glass, Mica and Platinum. *J. Am. Chem. Soc*. 40, 1361–1403 (1918).

Maginn, E.J.; Bell, A.T.; Theodorou, D.N. Dynamics of Long n-Alkanes in Silicalite: A Hierarchical Simulation Approach. *J. Phys. Chem.* 100, 7155–7173 (1996).

Maloncy, M.L.; Gora, L.; Jansen, J.C.; Maschmeyer, Th. Conceptual processes for zeolite membrane based hydroisomerization of light alkanes. *Ars Separatoria Acta* 2, 18–28 (2003).

Nitta, T.; Shigetomi, T.; Kuro-Oka, M.; Katayama, M. An Adsorption Isotherm of Multi-Site Occupancy Model for Homogeneous Surface. *J. Chem. Eng. Jpn.* 17, 39–45 (1984).

Norberg, V.; Su, B.L. Toward a Better Understanding on the Benzene Location in Sodium-Exchanged Beta Zeolite: An In Situ Infrared Study of Molecular Recognition, Proceedings of the 12th International Zeolite Conference, Baltimore, USA, July 5–10, 1998; Treacy, M.M.J.; Marcus, B.K.; Bisher, M.E.; Higgins, J.B., Eds.; Materials Research Society: Warrendale, PA (1998).

Ruchenstein, E.; Vaidynathan, A.S.; Youngquist, G.R. Sorption by solids with bidisperse pore structures. *Chem. Eng. Sci.* 26, 1305–1318 (1971).

Ruthven, D.M.; Loughlin, K.F. The Diffusional Resistance of Molecular Sieve Pellets. *Can. J. Chem Eng.* 50, 550–552 (1972).

Shavit, D.; Voogd, P.; Kouwenhoven, H.W. Time-Dependent Non-Steady-State Diffusivities of C6 Paraffins in Silicalite by Zero-Length Column Method. *Collect. Czech. Chem. Commun*. 57, 698–709 (1992).

Silva, J.A.C.; Rodrigues, A.E. Sorption and Diffusion of n-Pentane in Pellets of 5A Zeolite. *Ind. Eng. Chem. Res*. 36, 493–500 (1997).

Silva, J.A.C.; Rodrigues, A.E. Multisite Langmuir Model Applied to the Interpretation of Sorption of n-Paraffins in 5A Zeolite. *Ind. Eng. Chem. Res.* 38, 2434–2438 (1999).

Smit, B.; Krishna, R. Molecular Simulations in Zeolitic Process Design. *Chem. Eng. Sci.* 58, 557–568 (2003).

Sommer, S.; Melin, T.; Falconer, J.L.; Noble, R.D. Transport of C_6 Isomers through ZSM-5 Zeolite Membranes. *J. Membr. Sci.* 224, 51–67 (2003).

Talu, O.; Sun, M.S.; Shah, D.B. Diffusivities of n-Alkanes in Silicalite by Steady-State Single-Crystal Membrane Technique. *AIChE J.* 44, 681–694 (1998).

Toth, J. State Equations of the Solid-Gas Interface Layers. *Acta Chim. Acad. Sci. Hung.* 69, 311–328 (1971).

Treacy, M.M. J.; Newsam, J.M. Two New Three-Dimensional Twelve-Ring Zeolite Frameworks of which Zeolite Beta is a Disordered Intergrowth. *Nature* 332, 249–250 (1988).

Valenzuela, D.P.; Myers, A.L. *Adsorption Equilibrium Data Handbook.* Prentice Hall: Englewood Cliffs, NJ (1989).

Van den Begin, Rees, L.V.C., Caro, J.; Bullöw, M. Fast Adsorption-Desorption Kinetics of Hydrocarbons in Silicalite-1 by the Single-Step Frequency Response Method. *Zeolites* 9, 287–292 (1989).

Vlugt, T.J.H. Adsorption and Diffusion in Zeolites: A Computational Study, Ph.D. Thesis, Universiteit van Amsterdam (2000).

Voogd, P.; Bekkum, H.; Shavit, D.; Kouwenhoven, H.W. Effect of Zeolite Structure and Morphology on Intracrystalline n-Hexane Diffusion in Pentasil Zeolites Studied by the Zero-Length Column Method. *J. Chem. Soc. Faraday Trans*. 87, 3575–3580 (1991).

Zhu, W.; Kapteijn, F.; Moulijn, J. A. Diffusion of Linear and Branched C_6 Alkanes in Silicalite-1 Studied by the Tapered Element Oscillating Microbalance. *Micropor. Mesopor. Mater.* 47, 157–171 (2001).

3

Multicomponent Adsorption of C_6 Isomers in Zeolite Beta

An experimental study of the binary, ternary and quaternary fixed bed adsorption of C_6 isomers in zeolite beta was performed covering the temperature range between 423 K and 523 K and partial pressures up to 20 kPa. Adsorption equilibrium isotherms were collected from mixture breakthrough experiments. Based on an analysis of sorption events at the molecular level, a Tri-Site Langmuir model (TSL) was developed to interpret the equilibrium data with good accuracy. At the partial pressures studied, it was found that the degree of branching was related to the affinity; the sorption hierarchy was most favourable towards the linear isomer and least favourable towards the di-branched ones. A mathematical model based on a linear driving force (LDF) was developed and used to test the experimental data. It was found that the model predicted the behaviour of the fixed bed experiments with good accuracy. Zeolite beta demonstrated significant selectivity to separate mono and dibranched C_6 isomers, especially at low coverage.

This chapter is based on the following publication:

P.S. Bárcia, J.A.C. Silva, A.E. Rodrigues, *AIChE J*. 53 (2007) 1970-1981.

3.1 Introduction

Industrial adsorption systems usually involve more than one component, and therefore adsorption equilibria involving competition between different molecules is needed for a good understanding of the system as well as for the design of the separation process. In this chapter, mixture adsorption equilibrium isotherms and thermodynamic parameters are measured from multicomponent breakthrough experiments. A new isotherm model is introduced to properly describe the complex adsorption phenomena. Thereafter, the set of equilibrium and kinetic parameters is used for the development and validation of a simple dynamic adsorption model for the prediction of the fixed bed adsorption dynamics.

3.2 Theoretical Analysis

3.2.1 Equilibrium Data from Multicomponent Breakthrough Curves

Multicomponent isotherms can be obtained from the breakthrough curves as shown in Figure 3.1. In graphical terms, the number of moles of compound 1 retained in the bed is equal to the *Area A* minus the roll-up area *OS*. For the compound 2, the number of moles retained in the bed is equal to *Area A* plus *Area B*. The amount adsorbed of each compound is then calculated by the following relations:

$$q_1 = Area\ A - Area\ OS \tag{3.1a}$$

$$q_2 = Area\ A + Area\ B \tag{3.1b}$$

In the case of an equimolar mixture the selectivity, *S*, is given by the quotient between the amounts adsorbed of the two species as follows:

$$S = \frac{q_2}{q_1} = \frac{A+B}{A-OS} = \frac{1}{1-\dfrac{OS+B}{A+B}} \tag{3.2}$$

It should be noted, that in the case of adsorption from the gas phase, the amount of sorbate gas in the void volumes of the pellet and crystals can be neglected relatively to the amount adsorbed in the solid phase.

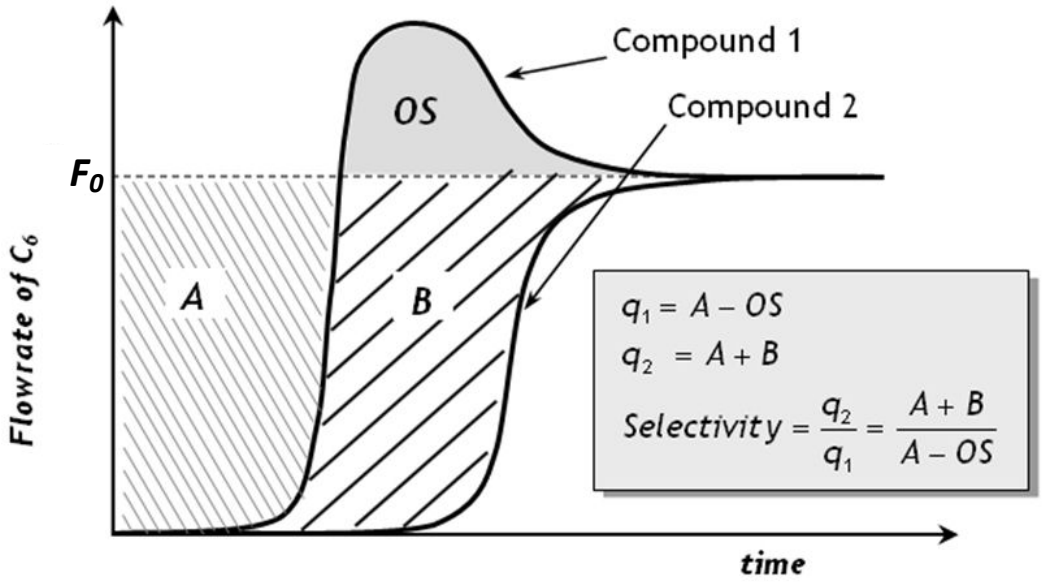


Figure 3.1. Schematic diagram showing the method used to calculate the amount adsorbed from experimental binary breakthrough curves.

3.2.2 Tri-site Langmuir Model

The DSL model – described in chapter 2 – distinguishes two categories of sorption sites in the zeolite framework (e.g., channels and intersections) each one following a Langmuir adsorption behaviour. For instance, Krishna et al. (1999) and Smit and Krishna (2003) have used the Dual-Site Langmuir (DSL) model isotherm to describe the pure component isotherms of several alkanes in zeolite MFI. At first sight, DSL model seems equally interesting for zeolite beta, since there are two different types of channels that can give different kinds of active sites for sorption. Moreover, it was shown in the chapter 2 that the DSL satisfactorily predicts the pure component equilibrium data. Nevertheless, it was found that the extended DSL model does not fit

properly the ternary and quaternary multicomponent data, as shown in Figure 3.2 for the ternary case.

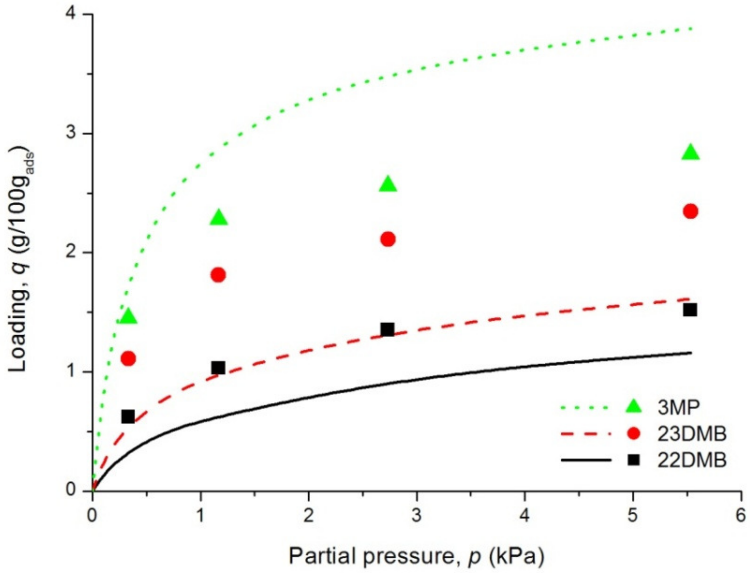


Figure 3.2. Ternary sorption data (22DMB/23DMB/3MP at T = 423K) cannot be predicted using the DSL model parameters from the fitting of the pure component isotherms (Table 2.5).

Additionally, the Ideal Adsorbed Solution theory (IAS) developed by Myers and Prausnitz (1965) was also used to predict the equilibrium of C_6 binary mixtures with the DSL model (Bárcia, 2006), but it fails in predicting the ternary and quaternary equilibrium data. Readers interested in this approach are referred to the article by Bárcia et al. (2006) for more detail.

Consequently, in order to correlate all the experimental sorption equilibrium data of C_6 isomers in zeolite beta, it was developed a hypothetical theory which assumes that the open space at the channels intersection could also represent a different category of active sites. Accordingly, the Langmuir model is expanded to describe the sorption behaviour in three different categories of active sites resulting in a Tri-Site Langmuir (TSL) model isotherm, *i.e.*, a linear superposition of three Langmuir isotherms reflecting the heterogeneity of the adsorbent. The resulting isotherm is

$$q(p,T) = q_S^m \frac{b_S(T)p}{1+b_s(T)p} + q_Z^m \frac{b_Z(T)p}{1+b_Z(T)p} + q_I^m \frac{b_I(T)p}{1+b_I(T)p} \qquad (3.3)$$

Here the superscripts S, Z and I indicate whether the adsorption sites are in a straight channel, zigzag channel, or intersection, respectively. It is shown in Figure 3.3 a simplified schematic representation of the hypothetical localization of different types of sites.

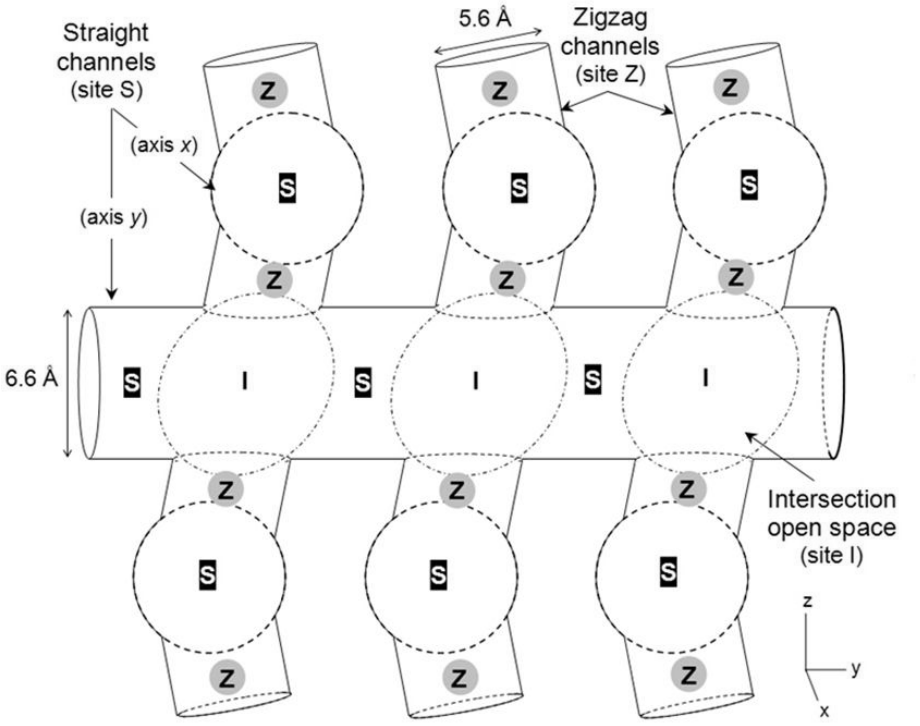


Figure 3.3. Schematic representation of the hypothetical distribution of the sorption sites in the zeolite beta framework.

Taking into account the conformation of the molecules shows in Figure 2.2, it was assumed that *n*HEX and 3MP adsorb into all type of sites, while the bulkier dibranched molecules cannot access to the zigzag channels. According to this assumption, the isotherm equation describing the adsorption equilibrium of 22DMB and 23DMB should not include the term related to the zigzag channels sites (Z). The parameters of the TSL isotherm for the pure C_6 isomers on zeolite beta are determined numerically by using the procedure described in section 2.7.3. There are 30 parameters to be determined

for the four components. However, in order to give thermodynamic consistency to the TSL model, it is assumed that the total saturation loading (i.e., a sum of the maximum loadings on the three sites) is constant for all isomers, eliminating in this manner some degrees of freedom from the optimization procedure.

3.2.3 Support to TSL model Theory from Molecular Simulation

A cooperation with the Materials Computational Group of the University Pablo de Olavide (Seville, Spain) leaded by Prof. Sofia Calero was carried out to provide insights into the sorption behaviours of the hexane isomers in the zeolite beta structure. Preliminary studies of molecular simulation using the Configurational-Bias Monte Carlo (CBMC) method have been performed. The principle of the CBMC technique is to grow an alkane chain, atom by atom, within the zeolite framework (Frenkel and Smit, 2002). Computational details of the implementation of the CBMC algorithm can be found in Vlugt et al. (1999). The computed equipotential energy surfaces of the BEA framework are shown in Figure 3.4. Also shown in this figure is schematic representation of the three different adsorption sites assumed in the TSL model previously described.

The snapshots in Figure 3.5 and Figure 3.6 show at the equilibrium the average position of the C_6 isomers at 423 K and partial pressure high enough to ensure that maximum capacity is attained (100 MPa). It can be seen from Figure 3.5 that dibranched isomers are preferentially located in the straight channels and intersections (see also Figure 3.3). Interestingly, a different feature is observed in Figure 3.6, where it can seen that besides straight channels and intersections, the linear and monobranched isomers are also located in the zigzag channels. Apparently, the presence of two methyl groups in the alkane chain hinders the access to site Z.

In summary, preliminary CBMC results confirm that dibranched C_6 isomers are only located in the straight channels and intersections. This observation is on agreement with our hypothetical theory for the analytical description of the sorption equilibrium with the TSL model.

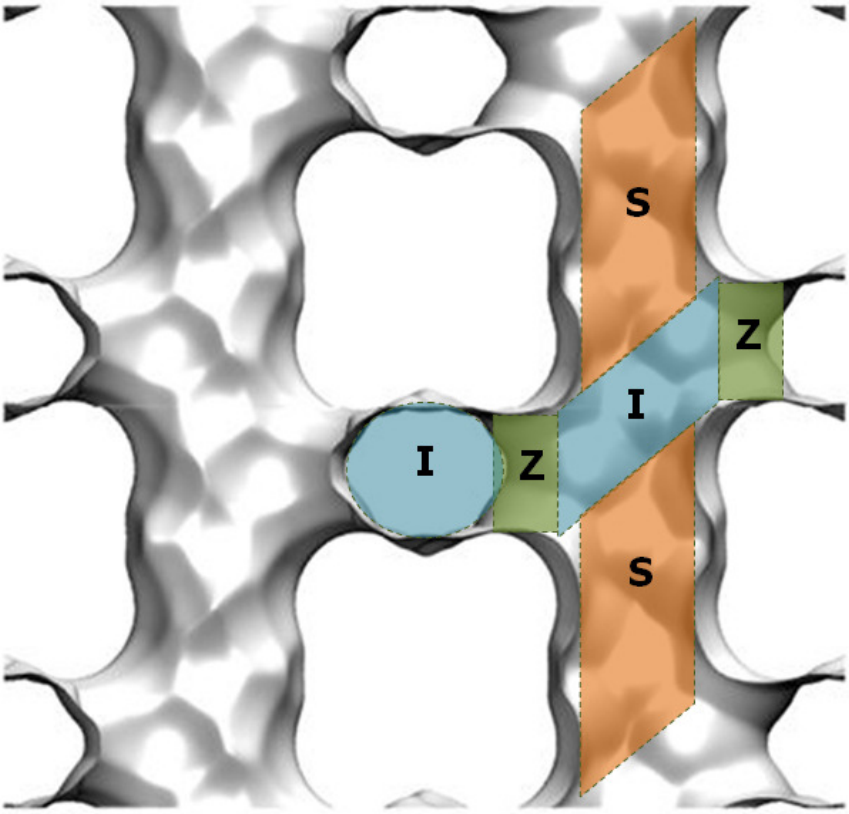


Figure 3.4. Energy profiles for the BEA framework and schematic representation of the adsorption sites: S, straight channels; I, intersection and Z, zigzag channels.

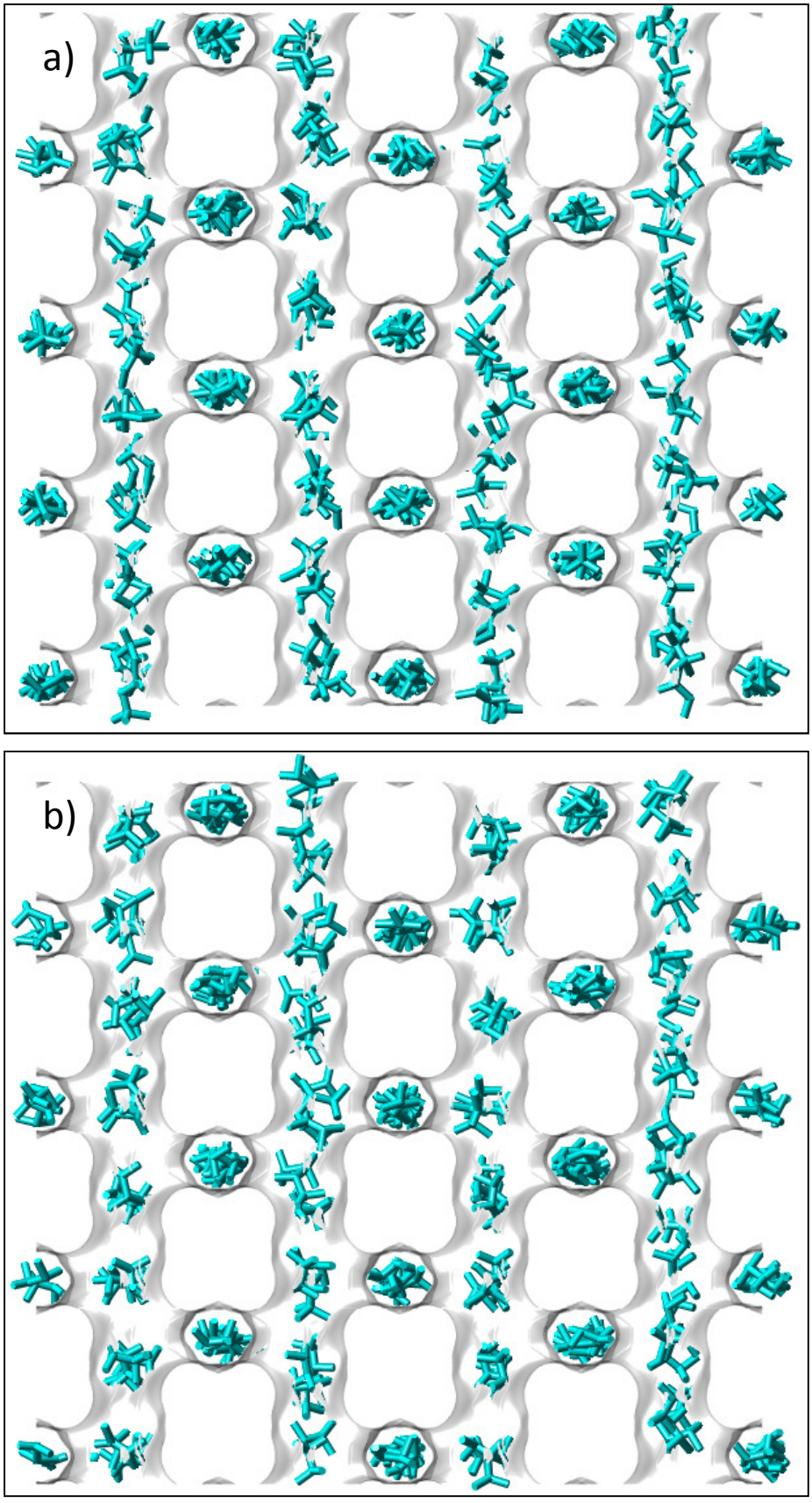


Figure 3.5. Snapshots obtained at 100 MPa and at 423 K for a) 22DMB and b) 23DMB.

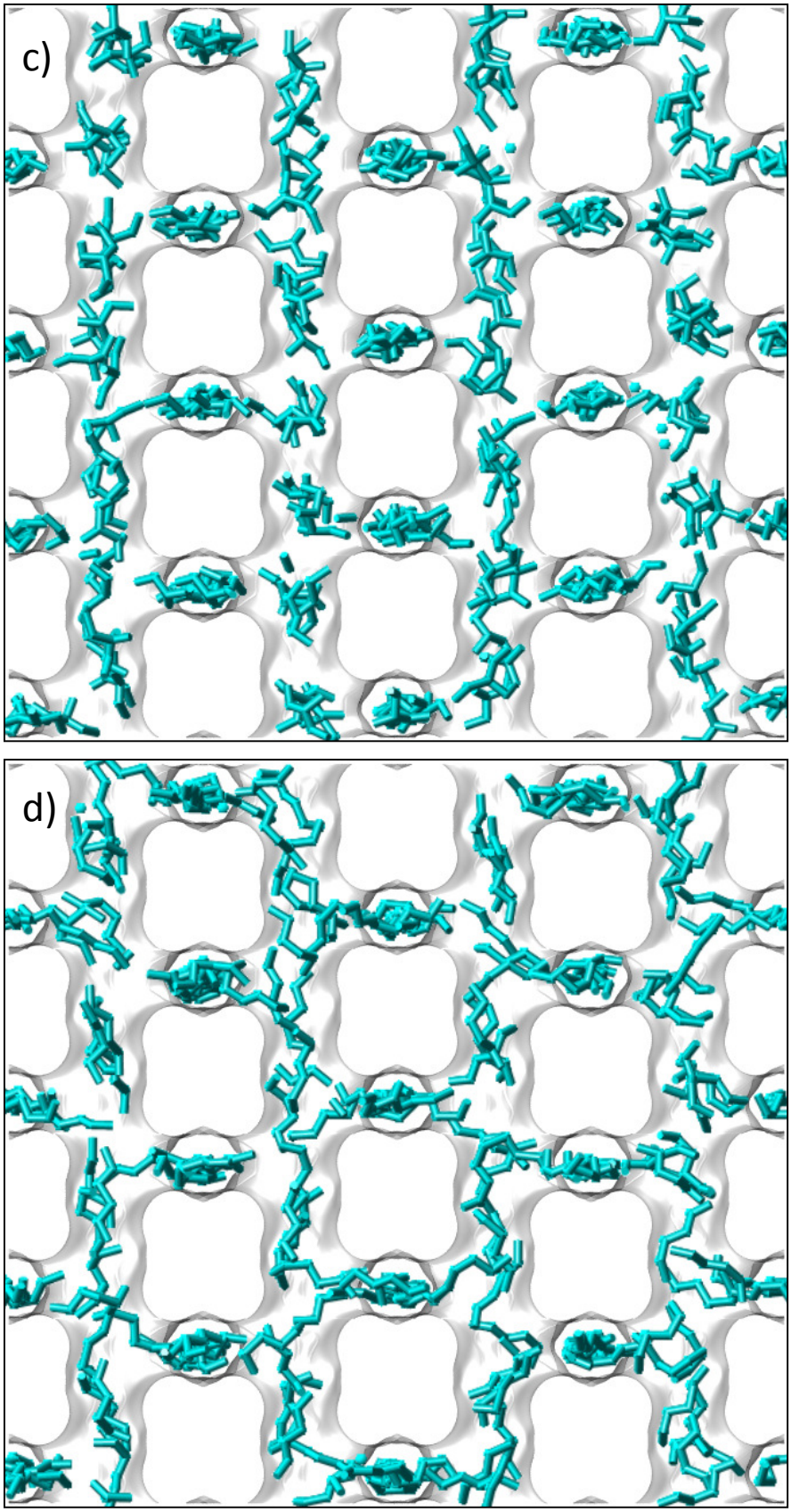


Figure 3.6. Snapshot obtained at 100 MPa and at 423 K for c) 3MP and d) *n*HEX.

3.3 Modeling of Breakthrough Experiments

A fixed-bed of commercial pellets contains three distinct levels of porosity: bed, particles and crystals, each one corresponding to bulk porosity, macropores and micropores, respectively (Figure 3.7). Each level presents different resistances to mass transfer; some of these resistances are placed in series and can be grouped into a single parameter (e.g., film, macropore, and micropore resistances) in order to simplify the numerical procedure. Additionally, the energy balance can be neglected, as a first approach, when the heat exchange with environment is promoted by forced convection (e.g., a thin adsorption column placed in a ventilated oven).

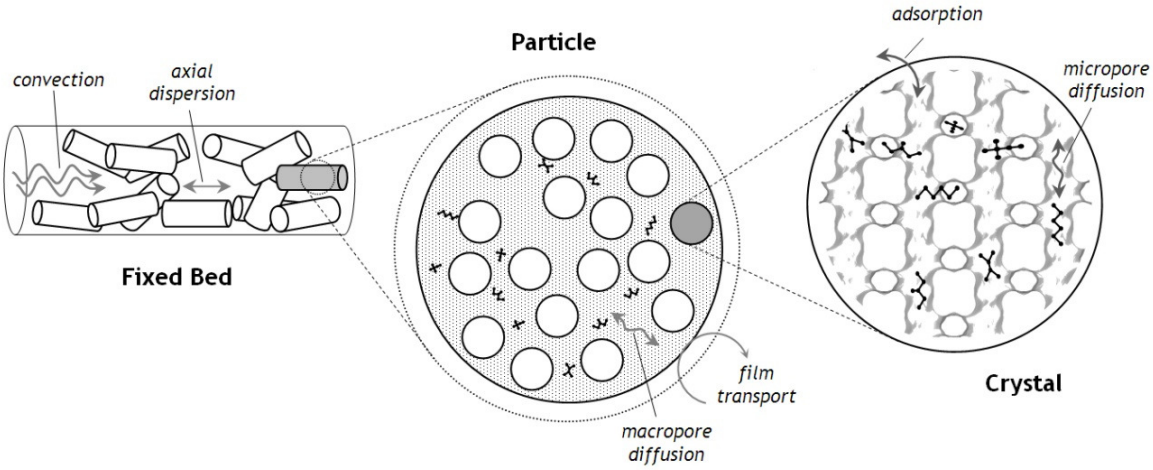


Figure 3.7. Porosity levels in the fixed-bed and corresponding resistance to mass transfer.

Therefore, considering the adsorption system described in section 3.4 as an isothermal column packed with pellets through which an inert gas flows at steady-state. At time zero, a mixture of known composition and an inert gas is introduced at the bottom of column.

The following additional assumptions are made:

1. Ideal gas law applies;

2. The pressure drop through the bed is negligible;
3. The flow pattern is described by the axial dispersed plug flow model;
4. The main resistances to mass transfer for adsorbable species are external fluid film resistance and macropore diffusion as pointed out in chapter 2 from the ZLC studies. External resistance and macropore diffusion can be combined in a global resistance according to a lumped model for the adsorbent particle as suggested by Morbidelli et al. (1982);
5. The column is isothermal.

According to these assumptions model equations are:

Ideal Gas Law

$$Py_i = RT_g c_i \tag{3.4}$$

where, P is the total pressure, y_i is the mol fraction of component i in the gas phase, R is the universal gas constant, T_g is the temperature in bulk gas phase and c_i is the concentration of solute i in fluid.

Mass Balance to Sorbate Species

The mass balance in the gas phase takes into account the effect of the axial dispersion, convection term, gas-phase accumulation, and rate of flux to the adsorbent

$$\varepsilon_b D_{ax} \frac{\partial^2 c_i}{\partial z^2} = \frac{\partial (v_g c_i)}{\partial z} + \varepsilon_t \frac{\partial c_i}{\partial t} + \rho_b \frac{\partial \overline{q}_i}{\partial t} \tag{3.5}$$

where ε_b and ε_t are the interparticle voidage and the total bed voidage, respectively, v_g is the superficial velocity, $\overline{q}_i$ is the average amount of solute i adsorbed in the pellet, ρ_b is the adsorbent bulk density, z and t are the axial coordinate and time, respectively, D_{ax} is the axial dispersion coefficient.

Boundary conditions

At the entrance of the bed ($z = 0$) the flows are equated and the axial dispersion only occurs in the inner side

$$D_{ax}\left.\frac{\partial c_i}{\partial z}\right|_{z=0} = -v_g\Big|_{z=0}\left(c_i\Big|_{z=0^-} - c_i\Big|_{z=0}\right) \tag{3.6a}$$

At the outlet ($z = L_B$) it is assumed that the concentration gradient is null

$$\left.\frac{\partial c_i}{\partial z}\right|_{z=L_B} = 0 \tag{3.6b}$$

where L_B is the length of the fixed-bed.

Overall Mass Balance

The overall mass balance for a multicomponent gas phase accounts for the convection of material, total gas-phase accumulation, and mass transfer from gas to the solid phase. The governing partial differential equation is,

$$\rho_g\frac{\partial v_g}{\partial z} + \varepsilon_t\frac{\partial \rho_g}{\partial t} + \rho_b\sum_{i=1}^{N}\frac{\partial \overline{q}_i}{\partial t} = 0 \tag{3.7}$$

where ρ_g is the total gas-phase concentration.

Mass Transfer Rate

Since the accumulation of mass in gas phase can be neglected relatively to solid phase, the following equation is valid in a lumped particle system controlled by macropore diffusion (Morbidelli et al., 1982):

$$\frac{\partial \overline{q}_i}{\partial t} = k_{MTC_i}\left(q_i - \overline{q}_i\right) \tag{3.8}$$

where $\overline{q}_i$ is the average concentration of sorbate species i in the adsorbent particle, and k_{MTC} is the overall mass transfer coefficient which is used here as a fitting parameter.

Equilibrium Model

The amount adsorbed of component i in a mixture of N components is given by an extended TSL isotherm model

$$q_i = \sum_j \frac{q_{i,j}^m b_{i,j} p_i}{1 + \sum_{i=1}^{N} b_{i,j} p_i}, \qquad \text{with } j = S, Z, I \tag{3.9}$$

Adsorption affinity constant in site j, b_j, is assumed to vary with temperature, according to the Arrhenius equation:

$$b_j = b_j^0 e^{(-E_j / RT)} \tag{3.10}$$

where b_j^0 is the frequency factor of the affinity constant, E_j is the interaction energy of site j, R is the universal gas constant and T is the temperature. The parameters of the TSL isotherm were determined by a numerical procedure assuming that the total saturation loading (i.e., a sum of the maximum loadings on the three sites) is constant for the four isomers.

Axial Dispersion

The axial mass dispersion coefficient, D_{ax}, was estimated from the correlation of Langer et al. (1978),

$$D_{ax} = \Gamma_{ax} D_m + \frac{d_p v_g}{Pe'_\infty \left(1 + \beta \frac{\Gamma_{ax} D_m}{v_g d_p}\right)} \tag{3.11}$$

where Pe'_{∞} is the limiting value of the Peclet number, β is the radial dispersion factor ($\beta = 10$), d_p is the particle diameter, and D_m is the molecular diffusion coefficient calculated by the Chapman-Enskog theory. The axial tortuosity factor, Γ_{ax} is given by

$$\Gamma_{ax} = 0.45 + 0.55\varepsilon_b \tag{3.12}$$

The value of Pe'_{∞} depends on the particle size and for d_p < 3000 μm is given as

$$Pe'_{\infty} = 670 d_p \tag{3.13}$$

where d_p is expressed in meters.

Numerical Solution of Model Equations

The system of partial differential equations previously described (Equations 3.5-3.8), need to be solved numerically. Therefore, the set of coupled partial differential equations was reduced first to a set of ordinary differential/algebraic equations (DAE's) applying orthogonal collocation technique to the spatial coordinate (Villadsen and Michelsen, 1978). The collocation points were given by the zeros of Jacobi polynomials $P_N^{(\alpha,\beta)}(x)$, with $\alpha = \beta = 0$. The resulting system was solved using a fifth order Runge-Kutta code (ODE's) in conjunction with Gauss elimination (algebraic equations). Sixteen collocation points were used for all calculations performed.

The orthogonal collocation method has proven to be a powerful tool to solve fixed-bed multicomponent adsorption problems. For instance, this method was applied by Morbidelli et al. (1985) to the gas-phase separation of xylene isomers on zeolite Y. At LSRE, orthogonal collocation method was used by Silva (1998) to simulate with success multicomponent breakthrough experiments of *n*/iso-paraffins in zeolite 5A. Simulations were run on the Microsoft FORTRAN PowerStation 4.0 environment. Details about the numerical solution of the fixed-bed adsorption model by orthogonal collocation can be found in the literature (Silva, 1998).

3.4 Experimental Section

3.4.1 Experimental Set-up

The multicomponent breakthrough experiments in the vapour phase were performed on the apparatus shown in Figure 3.8 and 3.9. It consists of *i*) gas preparation, *ii*) adsorption, *iii*) sampling, and *iv*) analytical sections. The gas preparation and the adsorption sections are similar to the ones for pure component experiments (see chapter 2).

During the saturation stage, the output of the packed column passes through a 6-way crossover valve (V_1) and then is directed to a heated sample collector with 10 loops of 100 µl each (SL). The stream on line (3) come back to valve V_1 and flows through line (4), being directed to a 4-way crossover valve (V_2), and then to the FID. This setup allows us to monitor the packed column output signal, in order to collect samples during the most important stage of the breakthrough curve. When the saturation state is reached, the crossover valves (V_1 and V_2) are actuated and the composition of each loop is evaluated by chromatography using a 60 m long, 0.28 mm ID, MTX-1 capillary column (Restek Corporation, Bellefonte, PA). Meanwhile, the carrier gas flows through line (2) cleaning the packed column.

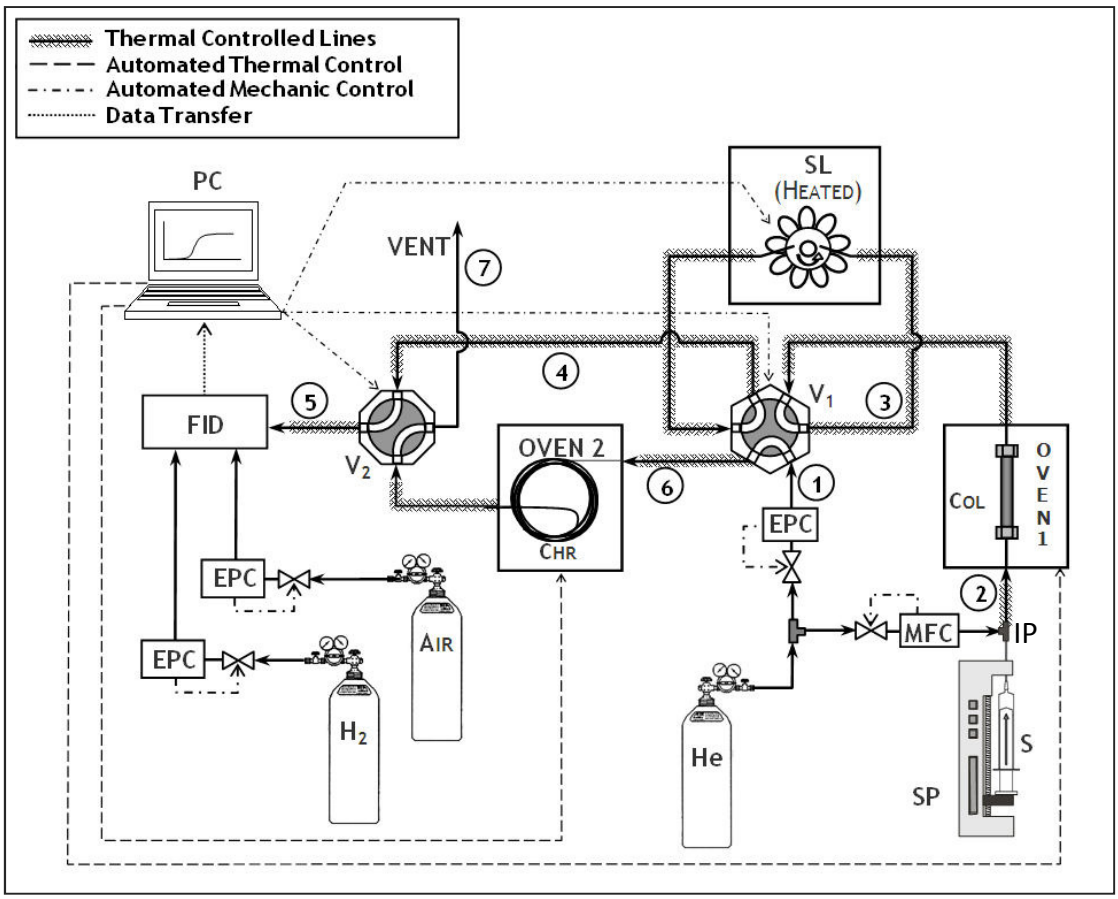


Figure 3.8. Schematic diagram of the multicomponent breakthrough experimental apparatus. (Chr) chromatography column; (Col) packed column; (EPC) electronic pressure controller; (FID) detector of chromatograph; (IP) injection port; (MFC) mass flow controller; (PC) computer; (S) microliter syringe; (SL) 10-loops sample collector; (SP) syringe pump; (V1) 6-way crossover valve; (V2) 4-way crossover valve; (1,2,3,4,5,6,7) streams.

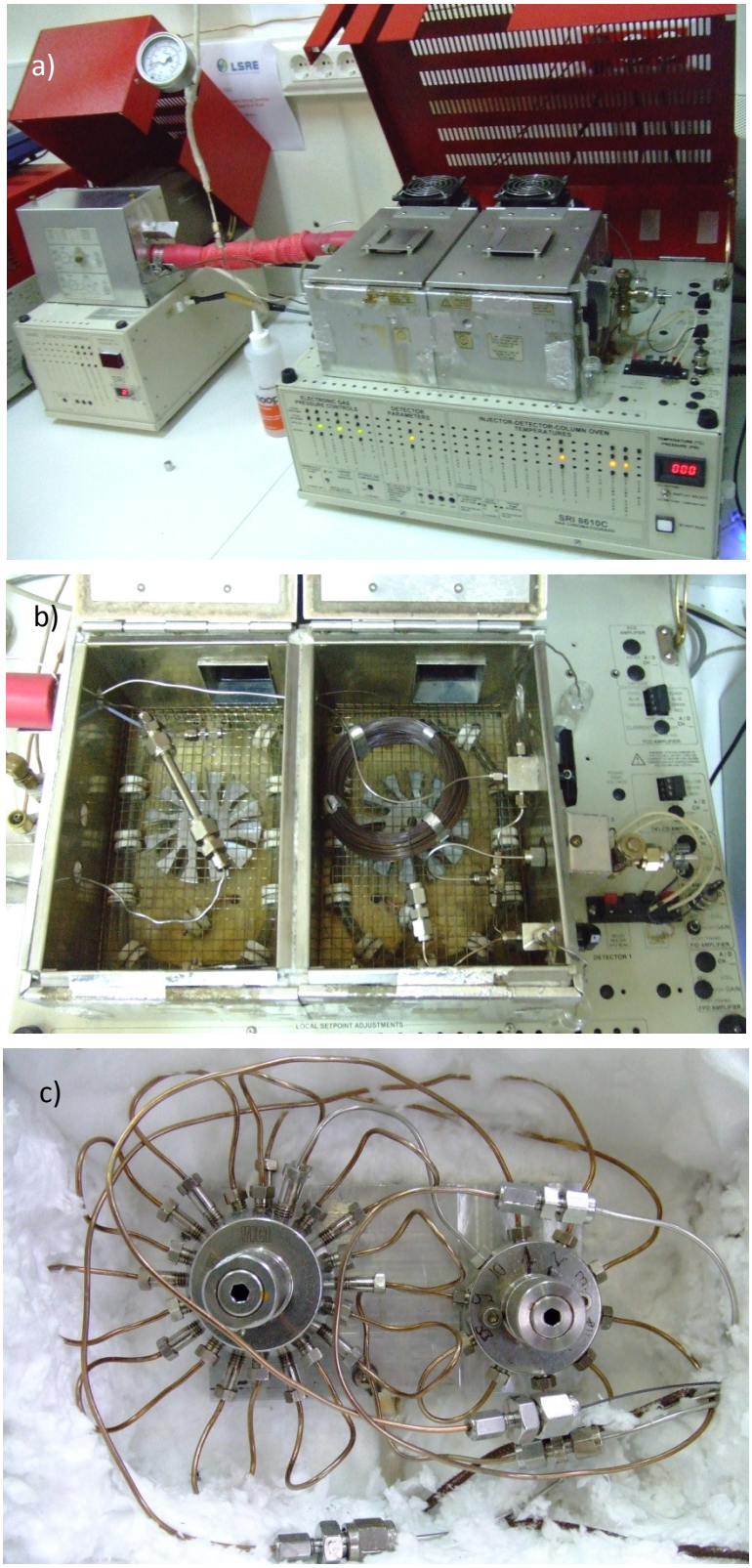


Figure 3.9. View of the multicomponent breakthrough apparatus (a), detailed view of the independent ventilated ovens with adsorbent column (*left*) and chromatographic column (*right*) (b), and 10-loops sample collector (c).

3.4.2 Experimental Procedure

Figure 3.10 shows a schematic representation of the procedure used to measure multicomponent breakthrough curves. The adsorption column packed with pellets of zeolite beta is operated by continuously introducing a C_6 isomers mixture with known composition and molar rate in a helium stream at a fixed total pressure.

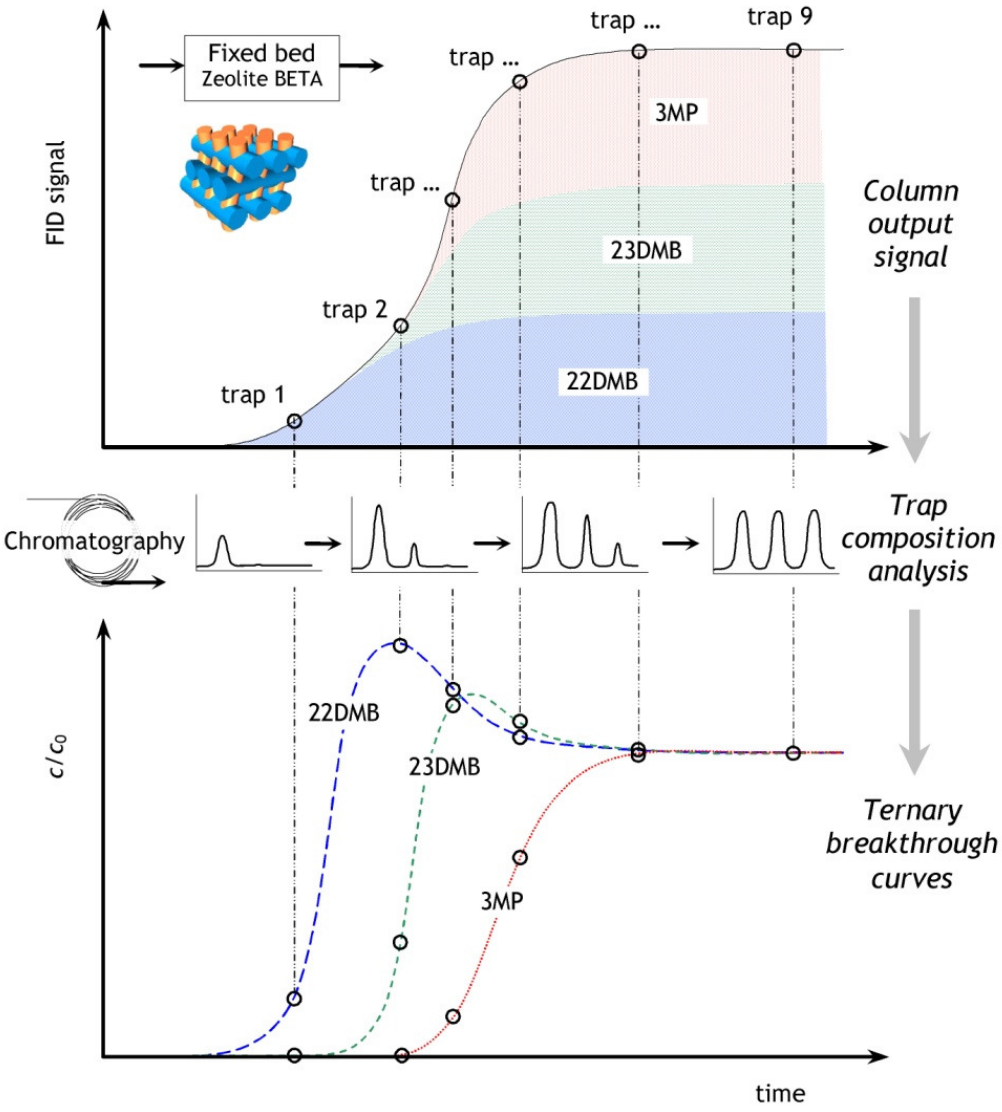


Figure 3.10. Schematic representation of the experimental procedure used for the determination of the multicomponent breakthrough curves (e.g., ternary mixture experiment).

The molar rate at the outlet of the packed bed is continuously measured with a FID chromatograph in order to collect samples during the most relevant part of the breakthrough curve. Each time the 10-loops collector is actuated a sample is trapped. When the saturation is reached, the composition of each loop is evaluated by chromatography.

Figure 3.11 shows a FID chromatogram correspondent to a typical mixture of C_6 isomers and the peak areas calculated by the data acquisition software PeakSimple 3.78 (SRI Instruments). Since the amount of mass of each hydrocarbon introduced in the gas stream is known, the composition of each loop can be calculated relative to the last sample which is trapped once the equilibrium is reached. Thus, collecting time and loop composition are used to rebuild the multicomponent breakthrough curves, as illustrated in Figure 3.10.

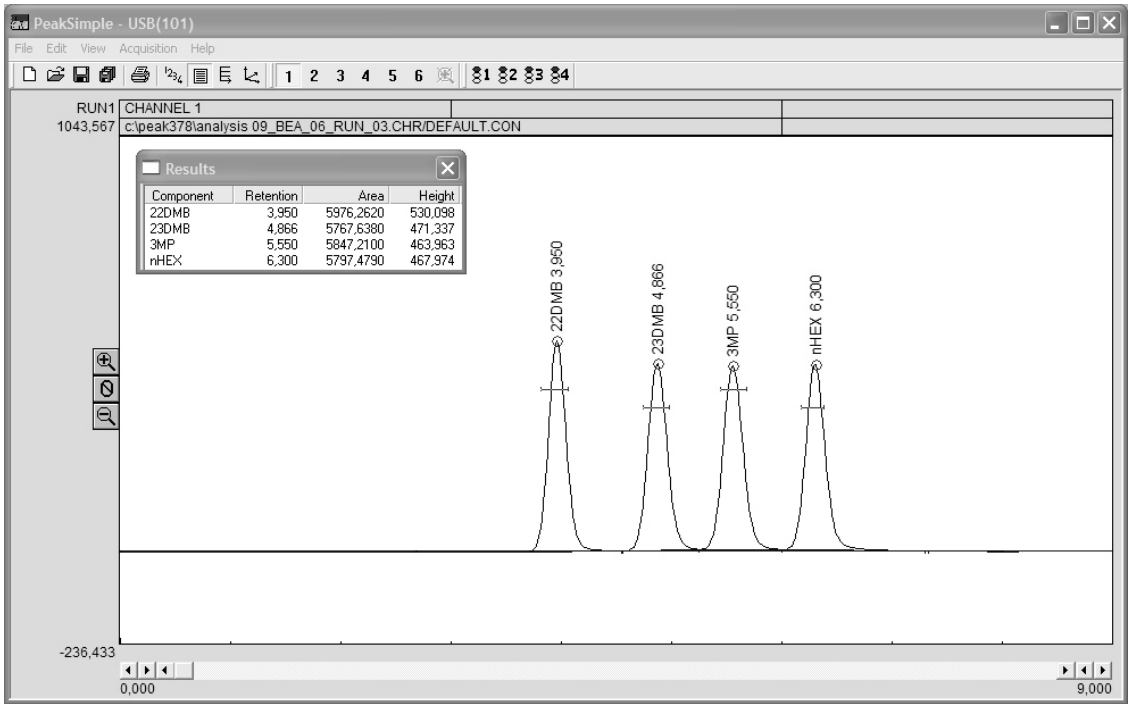


Figure 3.11. FID chromatogram of a C_6 isomers equimolar mixture analyzed in a 60m MTX-1 capillary column at 313 K and 20 psi helium pressure (FID temp = 523 K).

3.5 Results and Discussion

3.5.1 TSL Model Applied to the Adsorption of C_6 Isomers in Zeolite Beta

Figure 3.12 shows the adsorption equilibrium isotherms plotted in terms of the loading in g/100g_{ads} (wt %) as a function of the partial pressure. The equilibrium data shows that *n*HEX is the component more strongly adsorbed followed by 3MP, 23DMB and 22DMB respectively. The amount adsorbed is considerably higher at low partial pressures for *n*HEX and 3MP, but as the partial pressure increases the difference relatively to dibranched molecules decreases.

Single equilibrium data were already discussed in the chapter 2; however the schematic representation in Figure 3.3 together with the snapshots in Figure 3.5 and Figure 3.6 allows us to discuss more deeply these results in terms of the zeolite beta structure. There are two types of channels with different free aperture: 0.66 × 0.67 nm straight channels; and 0.56 × 0.56 nm zigzag channels. At low partial pressure, the lower loading of 22DMB and 23DMB in zeolite beta can be explained by the fact that they cannot access the zigzag channels, since these channels are too narrow for then. On the other hand, the length of 23DMB and 22DMB is lower than for *n*HEX and 3MP (see Figure 1) and this fact implies that when the partial pressure increases, the number of dibranched molecules that can be accommodated into the straight channels increases relatively to 3MP and *n*HEX. Consequently, at high partial pressures, the loading of 22DMB and 23DMB tends to approach the loading of *n*HEX and 3MP. This change of behaviour is known as the length entropy effect (Krishna et al., 1999; Krishna and Baur, 2003; Schenk et al., 2001; Smit and Krishna, 2003).

The pure component isotherms fitted with the TSL model are the lines in Figure 3.12. TSL model parameters obtained from an optimization procedure, as well as the mean absolute deviations between experimental data and predicted values are shown in Table 3.1.

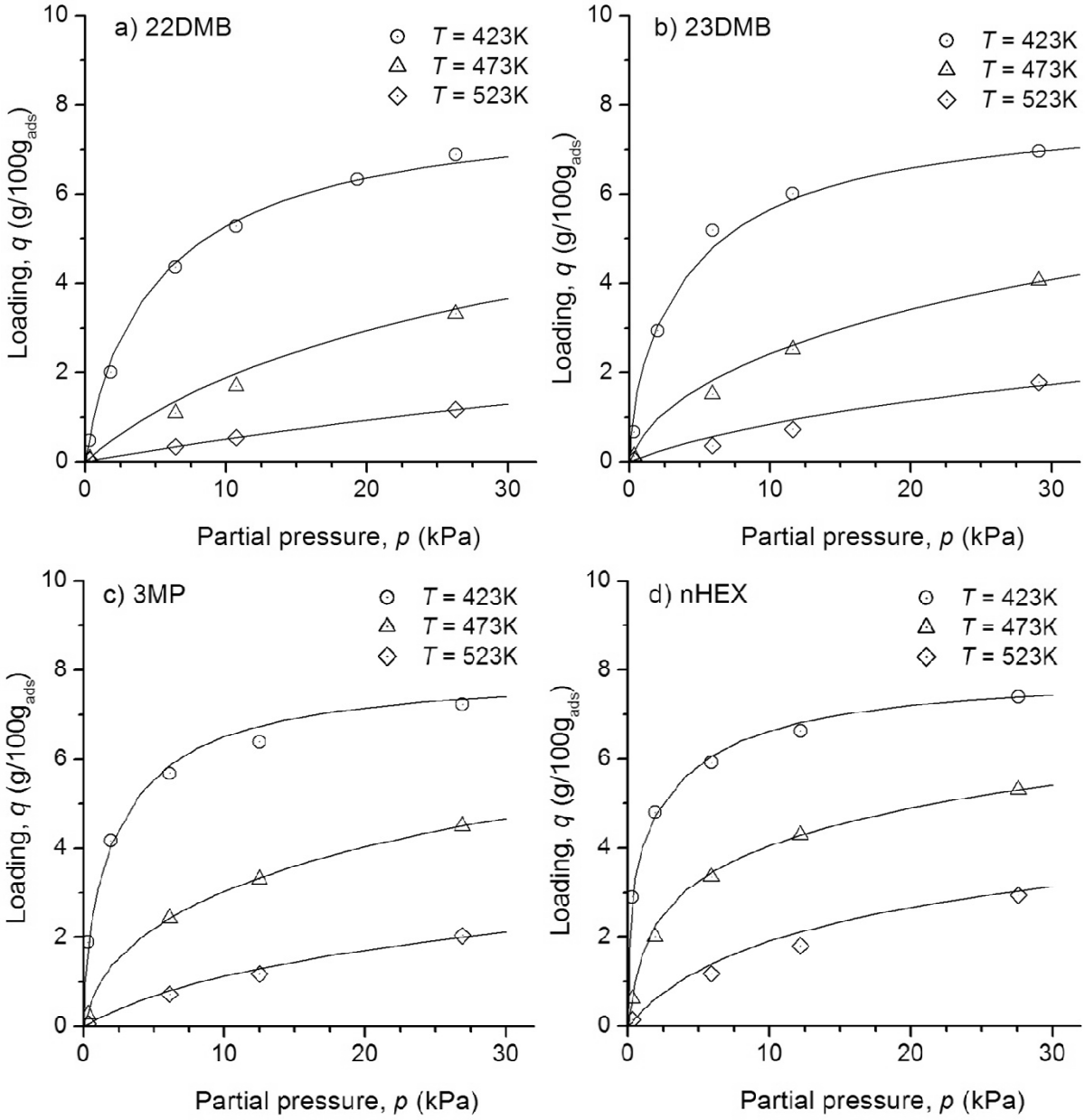


Figure 3.12. Pure component adsorption equilibrium isotherm fitted with the TSL model. Experimental conditions are specified in Table 2.2 (chapter 2).

The total saturation loading was assumed to be constant and equal to 8 g/100g_{ads} for all isomers. Taking into account the values for the maximum loading in each type of site and the representation of the adsorption sites in Figure 3.4, a distinction can be made between site S and site I by considering that the first one corresponds, in a general way, to the site with higher loading capacity.

It is clear from Figure 3.12 that the TSL model is reasonable in predicting isotherm sorption behaviour of pure C_6 isomers, for the temperatures and partial pressures studied. A further comparison with the mean absolute deviation in Table 2.5 allow to notice that the fitting quality of the TSL model for the pure component equilibrium data is comparable to the one shown in chapter 2 for the isotherm models: DLS, Toth and Nitta.

Table 3.1. TSL model parameters and deviations between model and experiments.

Parameter	Unit	*22DMB*	*23DMB*	*3MP*	*nHEX*
q_I^m	(g/100g$_{ads}$)	1.15	1.33	3.49	0.96
b_I^0	(kPa^{-1})	3.21×10^{-9}	6.83×10^{-10}	4.98×10^{-12}	4.63×10^{-12}
b_I (423K)	(kPa^{-1})	*0.8330*	*5.4494*	*0.2873*	*9.8761*
b_I (473K)	(kPa^{-1})	*0.1075*	*0.4894*	*0.0209*	*0.4913*
b_I (523K)	(kPa^{-1})	*0.0205*	*0.0697*	*0.0025*	*0.0434*
$-E_I$	(kJ/mol)	68.18	79.32	87.75	100.33
q_S^m	(g/100g$_{ads}$)	6.85	6.67	2.83	4.55
b_I^0	(kPa^{-1})	1.23×10^{-9}	8.61×10^{-10}	1.97×10^{-9}	4.98×10^{-10}
b_S (423K)	(kPa^{-1})	*0.1696*	*0.1888*	*0.3913*	*0.2412*
b_S (473K)	(kPa^{-1})	*0.0234*	*0.0248*	*0.0519*	*0.0291*
b_S (523K)	(kPa^{-1})	*0.0047*	*0.0048*	*0.0101*	*0.0053*
$-E_S$	(kJ/mol)	65.52	66.66	66.82	69.39
q_Z^m	(g/100g$_{ads}$)	-	-	1.68	2.48
b_Z^0	(kPa^{-1})	-	-	2.95×10^{-10}	1.72×10^{-9}
b_Z (423K)	(kPa^{-1})	-	-	*8.7198*	*9.2124*
b_Z (473K)	(kPa^{-1})	-	-	*0.6819*	*0.8628*
b_Z (523K)	(kPa^{-1})	-	-	*0.0868*	*0.1271*
$-E_Z$	(kJ/mol)	-	-	84.07	77.90
$\overline{\Delta q}$	(g/100g$_{ads}$)	*0.06*	*0.16*	*0.09*	*0.11*

I - Intersection; *S* - Straight channel; *Z* - Zigzag channel.

3.5.2 Binary Adsorption Isotherms

Panels *a1-a3* of Figure 3.13 show the binary adsorption isotherms for an equimolar mixture of 22DMB/3MP and panels *b1–b3* of Figure 3.13 for an equimolar mixture of 23DMB/3MP. The experiments were performed at 423 K, 473 K and 523 K and hydrocarbon pressure up to 15 kPa. The experimental conditions of the multicomponent experiments, as well as the amount adsorbed, are given in Table 3.2.

For the mixture 22DMB/3MP, panels *a1–a3* of Figure 3.13 show that there are significant differences between the amounts adsorbed of the two components being 3MP the more adsorbed one. Relatively to the equimolar mixture of 23DMB/3MP, panels *b1–b3* of Figure 3.13 demonstrate that the difference between the amounts adsorbed is smaller than for the previous case. We note that the extended TSL model prediction represented by the lines in Figure 3.13 gives a proper description of the binary adsorption data. The isotherm model parameters are specified in Table 3.1.

3.5.3 Ternary Adsorption Isotherms

Panels *a–c* of Figure 3.14 show ternary sorption isotherms of equimolar mixtures of 22DMB/23DMB/3MP at 423 K, 473 K and 523 K, and hydrocarbon pressures up to 17 kPa. This C_6 isomer mixture consists in two high RON dibranched molecules, 22DMB and 23DMB, and the 3MP low RON monobranched one. In all the ternary experiments performed, Figure 3.14 shows that 3MP is the more adsorbed molecule followed by 23DMB and 22DMB, respectively. Apparently, the simultaneous presence of monobranched and dibranched isomers in the zeolite beta framework does not seem to significantly affect the sorption behaviour.

The ternary adsorption equilibrium was also fitted with the TSL model from the single-component isotherms. The TSL fitting is represented by the lines in Figure 3.14 and in all cases it gives a good description of the ternary adsorption data for the equimolar mixture 22DMB/23DMB/3MP.

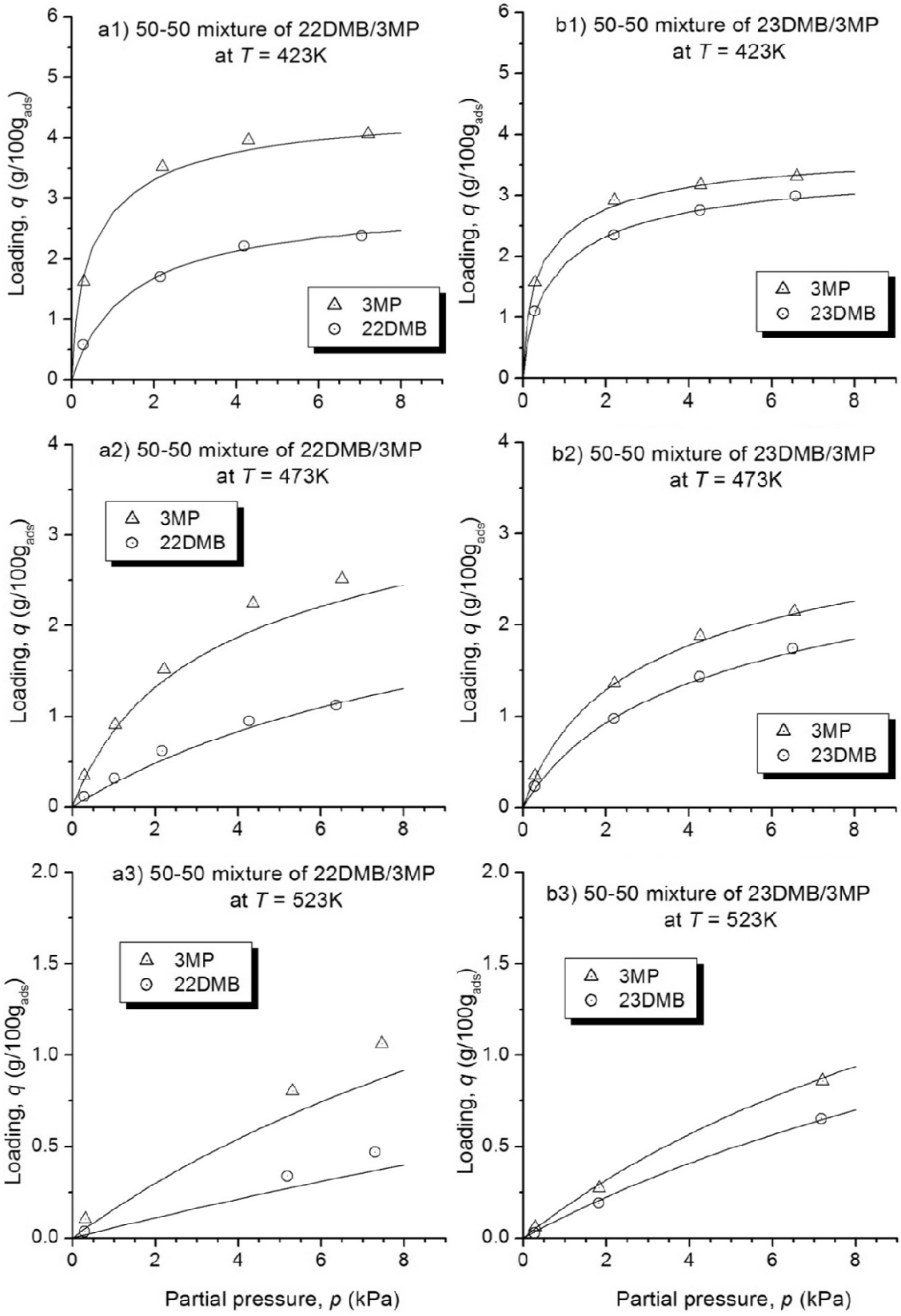


Figure 3.13. Binary adsorption equilibrium isotherms for an equimolar mixture of (a) 22DMB/3MP and (b) 23DMB/3MP.

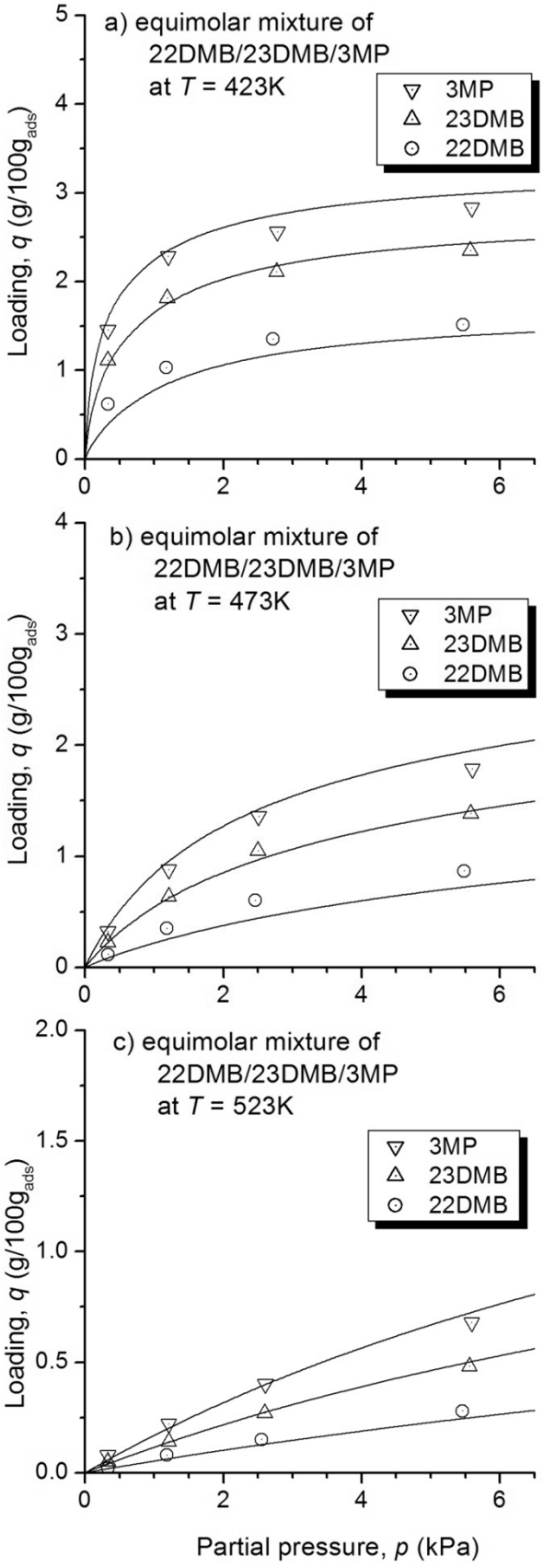


Figure 3.14. Ternary adsorption equilibrium isotherms for an equimolar mixture of 22DMB/23DMB/3MP on pellets of zeolite beta.

3.5.4 Quaternary Adsorption Isotherms

Quaternary breakthrough experiments with equimolar mixtures of 22DMB/23DMB/3MP/*n*HEX were also performed in the temperature range 423–523 K and hydrocarbon pressures up to 17 kPa in order to determine mixture sorption isotherms. The results are shown in Figure 3.15*a-c*. In Table 3.2 we report the experimental conditions. In this case we introduce in the feed to the column the linear isomer *n*HEX which is also the lower RON molecule. We see from Figure 3.15 that the amount adsorbed of *n*HEX is practically twice the one for branched isomers. In terms of loadings the sorption hierarchy is: *n*HEX>>>3MP>23DMB>>22DMB. This can be explained by the fact that the adsorption sites for dibranched molecules are limited to the straight channels and the intersections, while 3MP and *n*HEX can adsorb in all type of sites of the zeolite beta, which include zigzag channels.

The sorption selectivities calculated by Equation 3.2 are shown in Figure 3.16*a1-a3* as a function of the total hydrocarbon pressure and in Figure 3.16*b1-b3* as a function of total hydrocarbon loading for quaternary mixtures. From Figure 3.16*a1-b3* we can conclude that the selectivity between low RON and high RON molecules decreases as the total isomers pressure and mixture loading increases. However, the values of selectivity are much higher between *n*HEX/22DMB and *n*HEX/23DMB relatively to the ones between 3MP/22DMB and 3MP/23DMB.

An important conclusion that can be retained from these results is that to work with an acceptable selectivity for the separation of these isomers we should operate preferably at high temperature (523 K) if the total pressure of the paraffins in the feed range from 5 to 15 kPa. The explanation is that at these conditions the loading of the zeolite structure is not too high (lower than 1.5g/100g_{ads}) as can be seen in Figure 3.16*b3*. When the mixture loading increases to values higher than 4 g/100g_{ads} the selectivity decreases significantly (Figure 3.16*b1-b2*). We also note that the extended TSL model prediction represented by the lines in Figure 3.16 gives a proper description of the sorption selectivity data.

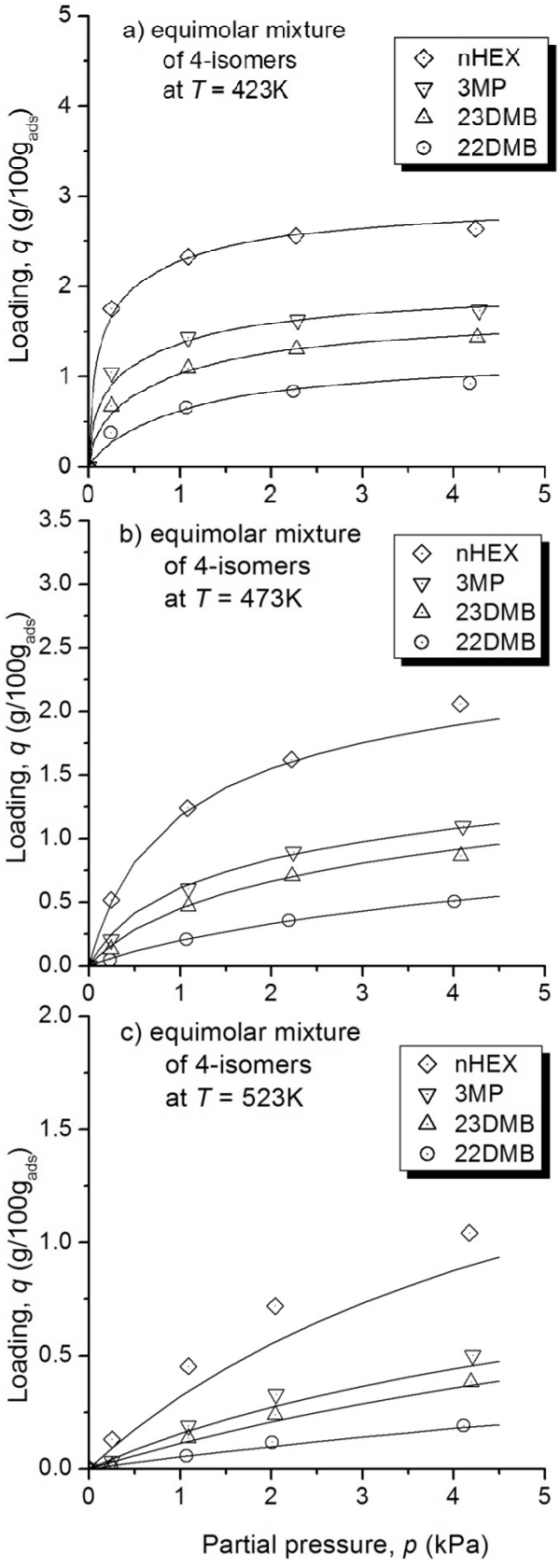


Figure 3.15. Quaternary adsorption equilibrium isotherms for an equimolar mixture of 22DMB/23DMB/3MP/nHEX on pellets of zeolite beta.

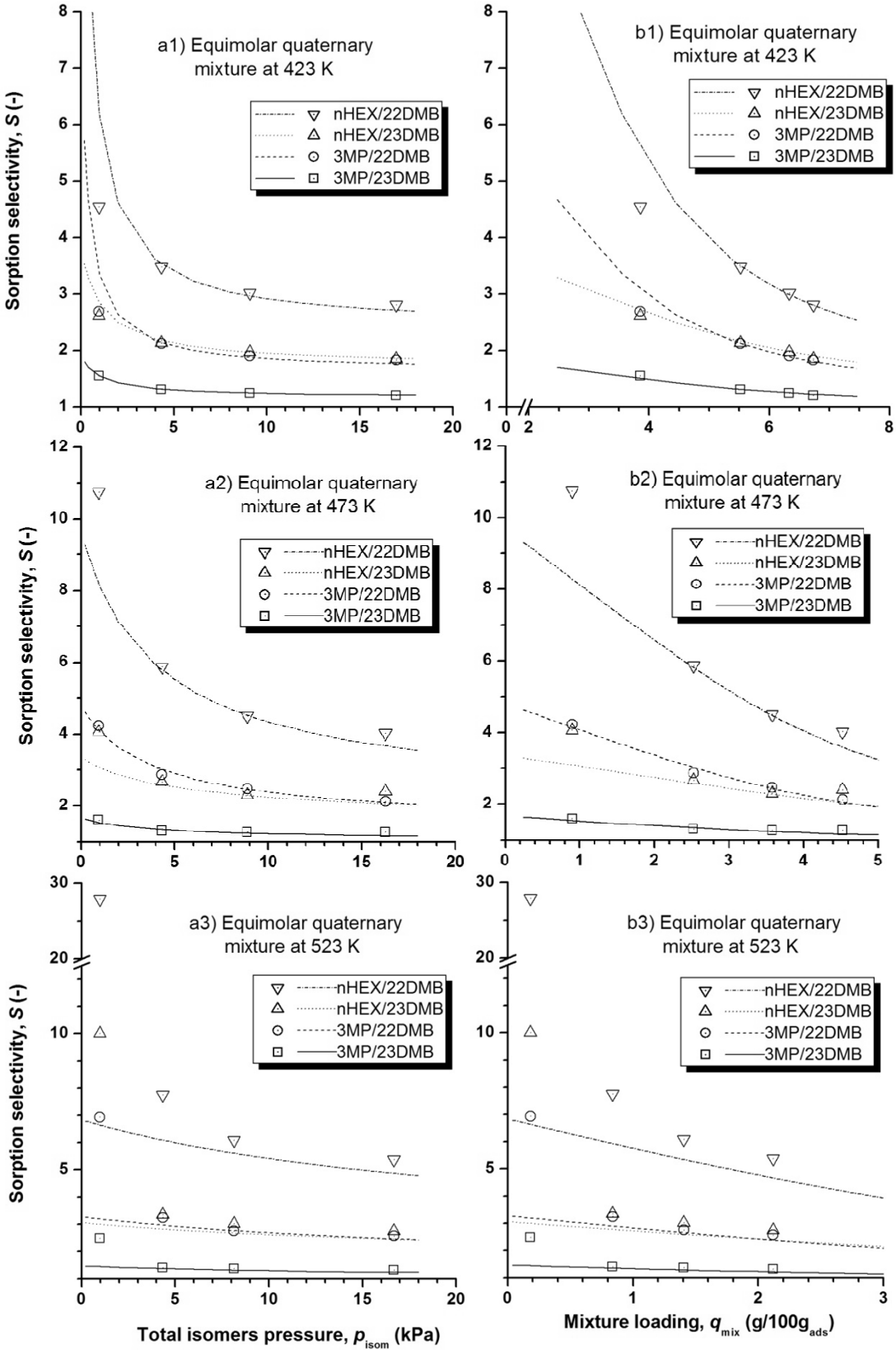


Figure 3.16. Effect of temperature in the sorption selectivity for an equimolar quaternary mixture 22DMB/23DMB/3MP/*n*HEX as a function of a) total hydrocarbon pressure and b) total hydrocarbon loading. The continuous lines are the TSL model predictions.

Table 3.2. Experimental conditions for multicomponent breakthrough curves, and mean absolute deviation between the TSL predictions and the experimental equilibrium data.

Run*	Temp. (K)	Helium flowrate (mL/min)	C_6 flowrate (µmol/min)				Mass of adsorbent (mg)	Hydrocarbon press., p_{isom} (kPa)	Amount adsorbed, q (g/100g_{ads})			
			22DMB	23DMB	3MP	nHEX			22DMB	23DMB	3MP	nHEX
b1_1	423	21.1	2.5	-	2.6	-	900	0.6	0.583	-	1.620	-
b1_2		5.7	5.4	-	5.5	-	900	4.4	1.702	-	3.518	-
b1_3		4.9	9.4	-	9.6	-	900	8.4	2.209	-	3.962	-
b1_4		1.7	5.8	-	5.9	-	900	14.0	2.384	-	4.057	-
b1_5	473	32.2	4.4	-	4.5	-	900	0.6	0.114	-	0.346	-
b1_6		10.2	5.4	-	5.5	-	900	2.0	0.317	-	0.904	-
b1_7		5.7	9.4	-	9.6	-	900	4.4	0.617	-	1.517	-
b1_8		4.9	6.9	-	7.1	-	900	8.4	0.946	-	2.243	-
b1_9		2.2	4.4	-	4.5	-	900	13.1	1.122	-	2.514	-
b1_10	523	10.2	1.3	-	1.3	-	900	0.6	0.033	-	0.103	-
b1_11		2.2	5.4	-	5.5	-	900	10.5	0.339	-	0.803	-
b1_12		1.3	4.6	-	4.8	-	900	14.6	0.469	-	1.062	-
b2_1	423	32.2	-	3.8	3.9	-	900	0.6	-	1.107	1.571	-
b2_2		5.7	-	5.5	5.5	-	900	4.4	-	2.352	2.916	-
b2_3		4.9	-	9.6	9.6	-	900	8.5	-	2.756	3.172	-
b2_4		2.2	-	7.0	7.1	-	900	13.2	-	2.988	3.313	-
b2_5	473	32.2	-	3.8	3.9	-	900	0.6	-	0.233	0.351	-
b2_6		5.7	-	5.5	5.5	-	900	4.4	-	0.975	1.358	-
b2_7		4.9	-	9.6	9.6	-	900	8.5	-	1.430	1.877	-
b2_8		2.2	-	7.0	7.1	-	900	13.2	-	1.743	2.148	-
b2_9	523	22.1	-	2.6	2.6	-	900	0.5	-	0.027	0.058	-
b2_10		9.7	-	7.7	7.7	-	900	3.6	-	0.191	0.273	-
b2_11		4.5	-	16.0	16.1	-	900	14.4	-	0.653	0.859	-
t_1	423	14.0	1.9	1.9	1.9	-	800	1.0	0.620	1.110	1.450	-
t_2		10.0	5.0	5.1	5.1	-	800	3.5	1.030	1.810	2.280	-
t_3		5.1	6.3	6.4	6.4	-	800	8.2	1.350	2.110	2.560	-
t_4		4.5	12.6	12.8	12.8	-	900	16.6	1.517	2.346	2.829	-
t_5	473	14.0	1.9	1.9	1.9	-	800	1.0	0.117	0.223	0.325	-
t_6		10.0	5.0	5.1	5.1	-	800	3.5	0.351	0.635	0.880	-
t_7		5.2	5.6	5.8	5.8	-	800	7.3	0.603	1.048	1.360	-
t_8		4.5	12.6	12.8	12.8	-	900	16.7	0.867	1.381	1.787	-
t_9	523	14.0	1.9	1.9	1.9	-	800	1.0	0.020	0.050	0.080	-
t_10		10.0	5.0	5.1	5.1	-	800	3.5	0.080	0.140	0.220	-
t_11		5.0	5.6	5.8	5.8	-	800	7.5	0.150	0.270	0.400	-
t_12		4.5	12.6	12.8	12.8	-	900	16.6	0.279	0.481	0.679	-
q_1	423	14.0	1.4	1.4	1.4	1.4	900	1.0	0.380	0.673	1.046	1.754
q_2		3.3	1.6	1.6	1.6	1.6	900	4.3	0.660	1.095	1.434	2.332
q_3		3.3	3.5	3.5	3.5	3.5	900	9.1	0.837	1.304	1.627	2.563
q_4		2.2	4.7	4.8	4.8	4.8	900	17.1	0.926	1.433	1.733	2.643
q_5	473	22.2	2.2	2.2	2.3	2.2	900	0.9	0.047	0.128	0.205	0.517
q_6		3.3	1.6	1.6	1.6	1.6	900	4.4	0.208	0.467	0.609	1.240
q_7		3.3	3.5	3.5	3.5	3.5	900	8.9	0.355	0.708	0.895	1.622
q_8		5.4	11.0	11.2	11.2	11.2	900	16.3	0.505	0.863	1.097	2.059
q_9	523	14.0	1.4	1.4	1.4	1.4	900	1.0	0.005	0.013	0.033	0.130
q_10		3.3	1.6	1.6	1.6	1.6	900	4.4	0.058	0.135	0.191	0.453
q_11		10.2	9.4	9.6	9.6	9.6	900	8.1	0.117	0.240	0.329	0.720
q_12		4.5	9.4	9.6	9.6	9.6	900	16.7	0.191	0.382	0.502	1.043
			Binary mixtures				*Ternary mixture*		*Quaternary mixture*			
			22DMB+3MP		23DMB+3MP		22DMB+23DMB+3MP		22DMB+23DMB+3MP+nHEX			
$\overline{\Delta q}$ (g/100g_{ads})			*0.09*		*0.03*		*0.08*		*0.04*			

* *b* – Binary experiments; *t* – Ternary experiments; *q* – Quaternary experiments.

3.6 Multicomponent Breakthrough Curves

3.6.1 Influence of Temperature on Binary Breakthrough Curves of C_6 Isomers

In practice we wish to separate the hexane isomers in a fixed bed by a proper technique. To give an overview of the typical multicomponent breakthrough curves obtained, and also to calibrate a mathematical model to be used in cyclic separation, we show the influence of temperature in a few multicomponent breakthrough curves at fixed partial pressure. In Figure 3.17, the influence of temperature on breakthrough curves of binary equimolar mixtures: panels *a1-a3* for 22DMB/3MP and panels *b1-b3* for 23DMB/3MP are shown for the case where the total hydrocarbon pressure in the mixture is in the range 13–15 kPa. We plot the breakthrough curves in terms of normalized hydrocarbon molar rate F/F_0, as a function of time. The experimental conditions are listed in Table 3.2.

We can see in Figure 3.17 that for both type of mixtures, the breakthrough time decreases considerably as the temperature increases. Interesting to note is the fact that at 423 K and for the mixture 22DMB/3MP, the component 3MP appears at the outlet of the column at a time of approximately 55 min compared to a time value of 40 min for 22DMB. This time difference is reasonable for a separation in a fixed bed. At 523 K the beginning of breakthrough of 3MP decreases to 15 min which compares to a time of 3 min for 22DMB. Accordingly, the breakthrough time difference between 423 K and 523 K and for partial pressures around 14 kPa is practically the same. These results allow us to conclude that the selectivity observed between these isomers could lead to the development of a separation process by adsorption. We note again that for this system, as the partial pressure increases the mixture loading increases and the selectivity decreases. However, the range of partial pressures to achieve a relevant separation degree is higher at high temperatures. For the mixture 23DMB/3MP the separation degree is much smaller as can be seen in Figure 3.17b1-b3.

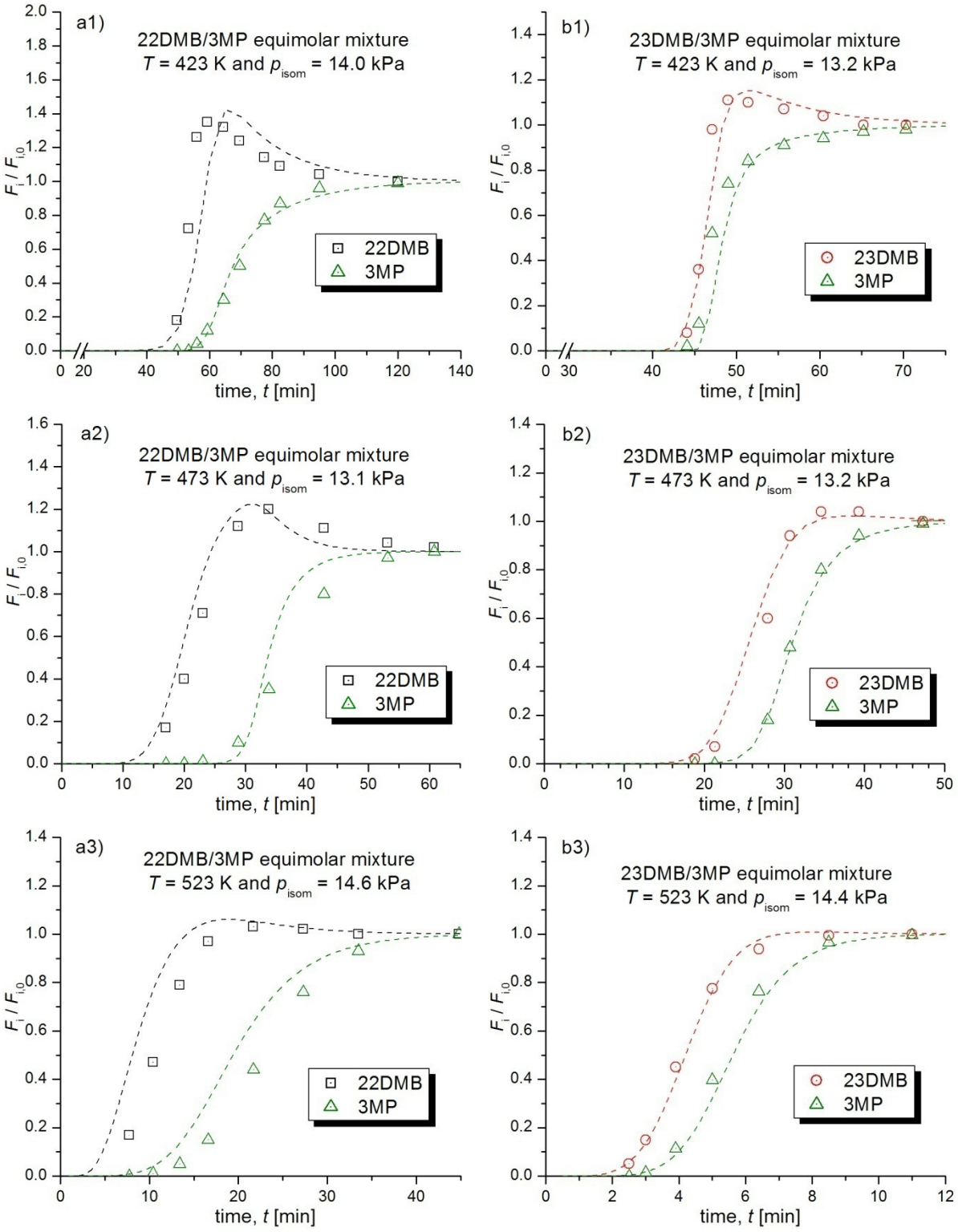


Figure 3.17. Effect of temperature on binary breakthrough curves of equimolar mixtures a) 22DMB/3MP and b) 23DMB/3MP at 1) 423 K, 2) 473 K and 3) 523 K and hydrocarbon pressure near to 14 kPa.

The prediction of breakthrough curves with the LDF-based mathematical model, coupled with the extended TSL isotherm model, can be seen by the lines in Figure 3.17. The model parameters are shown in Table 3.3, where the values of k_{MTC} can be considered as lumped parameters. It can be concluded from Figure 3.17, that this simple model does a good job, and we believe that this is due to the proper description of TSL model to account for the effects of heterogeneity of sites in the adsorbent, and consequently be able to predict with good accuracy the single and multicomponent isotherms.

Table 3.3. Dynamic model parameters for the simulation of multicomponent breakthrough curves.

Run	Temp. (K)	Mass transfer coefficient, k_{MTC} (s^{-1})				D_{ax} (m^2/s)
		22DMB	23DMB	3MP	nHEX	
b1_2	423	0.026	-	0.007	-	4.3×10^{-5}
b1_7	473	0.150	-	0.038	-	5.3×10^{-5}
b1_11	523	0.300	-	0.100	-	6.2×10^{-5}
b2_2	423	-	0.030	0.030	-	4.3×10^{-5}
b2_6	473	-	0.040	0.040	-	5.3×10^{-5}
b2_11	523	-	0.100	0.100	-	6.2×10^{-5}
t_4	423	0.022	0.013	0.006	-	4.4×10^{-5}
t_8	473	0.100	0.060	0.015	-	5.3×10^{-5}
t_12	523	0.200	0.140	0.120	-	6.2×10^{-5}
q_3	423	0.014	0.006	0.003	0.021	4.4×10^{-5}
q_7	473	0.055	0.014	0.008	0.055	5.3×10^{-5}
q_12	523	0.100	0.060	0.060	0.100	6.3×10^{-5}

b – Binary experiments; *t* – Ternary experiments; *q* – Quaternary experiments.

Figure 3.17 also shows some dispersion in the shape of breakthrough curves and this is due to a combined effect of isotherm type, mass transfer resistance and axial dispersion. Generally, type I isotherms give rise to steep breakthrough curves, however, this effect is not so pronounced here since breakthrough curves are performed at low partial pressure.

3.6.2 Influence of Temperature on Ternary Breakthrough Curves of C_6 Isomers

Figure 3.18 shows the influence of temperature in breakthrough curves for a ternary equimolar mixture of 22DMB/23DMB/3MP at hydrocarbon pressure in the range 16–17 kPa.

In this case the simultaneous presence of the three isomers reduces the difference in breakthrough time especially between 22DMB and 3MP. For instance the breakthrough time for 3MP at 523 K is around 4 min compared to 1 min for 22DMB. However, these values are still acceptable for a separation. A direct comparison of these experiments with the ones shown in Figure 3.17 is not possible since the level of occupancy of the zeolite is not the same. Another interesting feature for this system is the high overshoot seen at 423 K, which practically doubles the initial concentration of 22DMB at the inlet of the column. This overshot is an evidence of the strong interactions occurring in the zeolite due to a considerable amount of mass in the zeolite which is in the order of 7g/100g_{ads} (see Figure 3.14). This high amount adsorbed in zeolite structure does not favour the separation.

From Figure 3.18 we conclude once more that the mathematical model is suitable for the prediction of the breakthrough curves, including the overshoots.

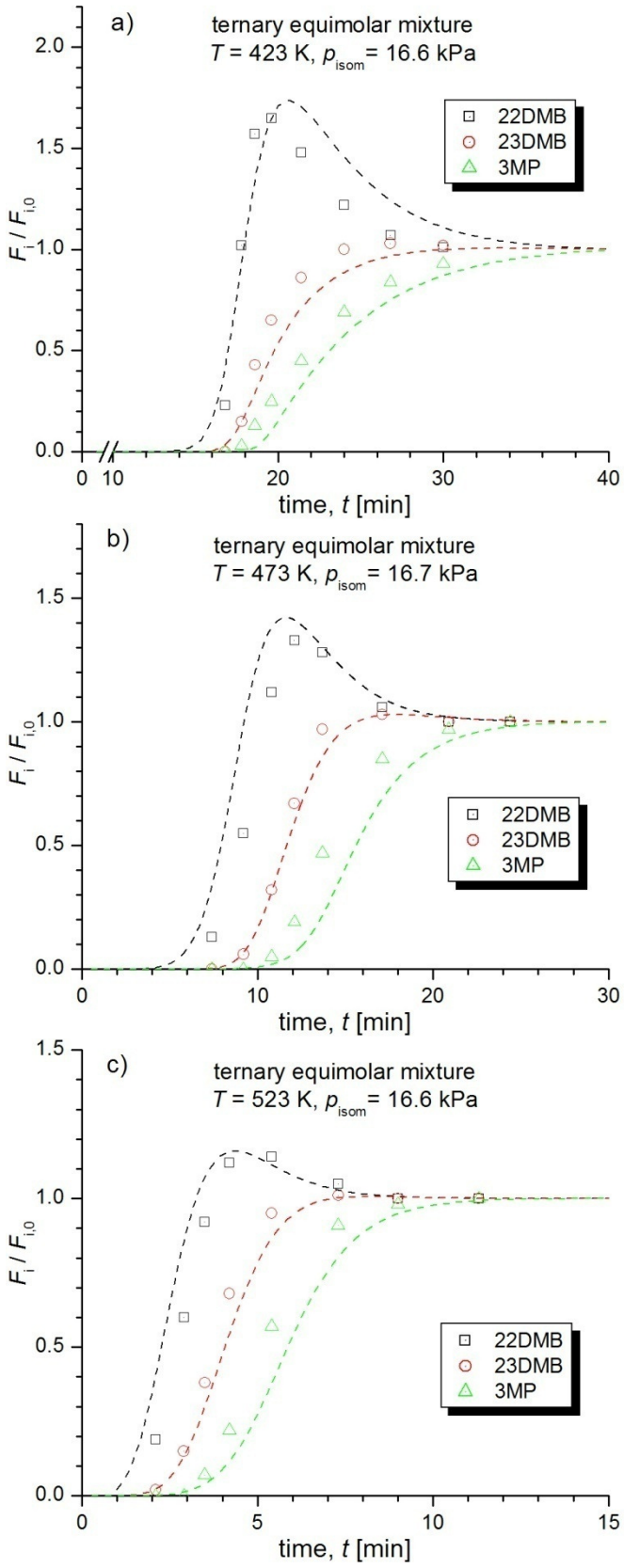


Figure 3.18. Effect of temperature on ternary breakthrough curves of equimolar mixtures 22DMB/23DMB/3MP at a) 423 K, b) 473 K and c) 523 K and hydrocarbon pressure near to 16 kPa.

3.6.3 Influence of Temperature on Quaternary Breakthrough Curves of C_6 Isomers

Figure 3.19a-c shows the effect of temperature in experimental quaternary breakthrough curves for equimolar mixtures of *n*HEX/3MP/23DMB/22DMB in zeolite beta at mixture total isomers pressure in the range 8–9 kPa.

In this set of experiments we can see that *n*HEX is clearly the more strongly adsorbed component, which explains the difference in the amount adsorbed of *n*HEX relatively to the other components, already observed in the quaternary adsorption equilibrium isotherms already shown in Figure 3.15. It should also be noticed that the presence of *n*HEX in the mixture does not affect significantly the sorption selectivity between the mono and dibranched molecules. The total hydrocarbon loading for the quaternary experiments ranges from about 7 g/100g_{ads} at 423 K to 1.5 g/100g_{ads} at 523 K. One interesting note is that at 523 K the component 22DMB practically does not adsorb in the column, and this can be exploited in a separation.

The agreement between experimental data and the mathematical model is reasonable good, and this is remarkable taken into consideration that we are using a simple LDF model in a simulation of a very non-linear multicomponent system of four adsorbable species competing with each other, in a complex zeolite structure.

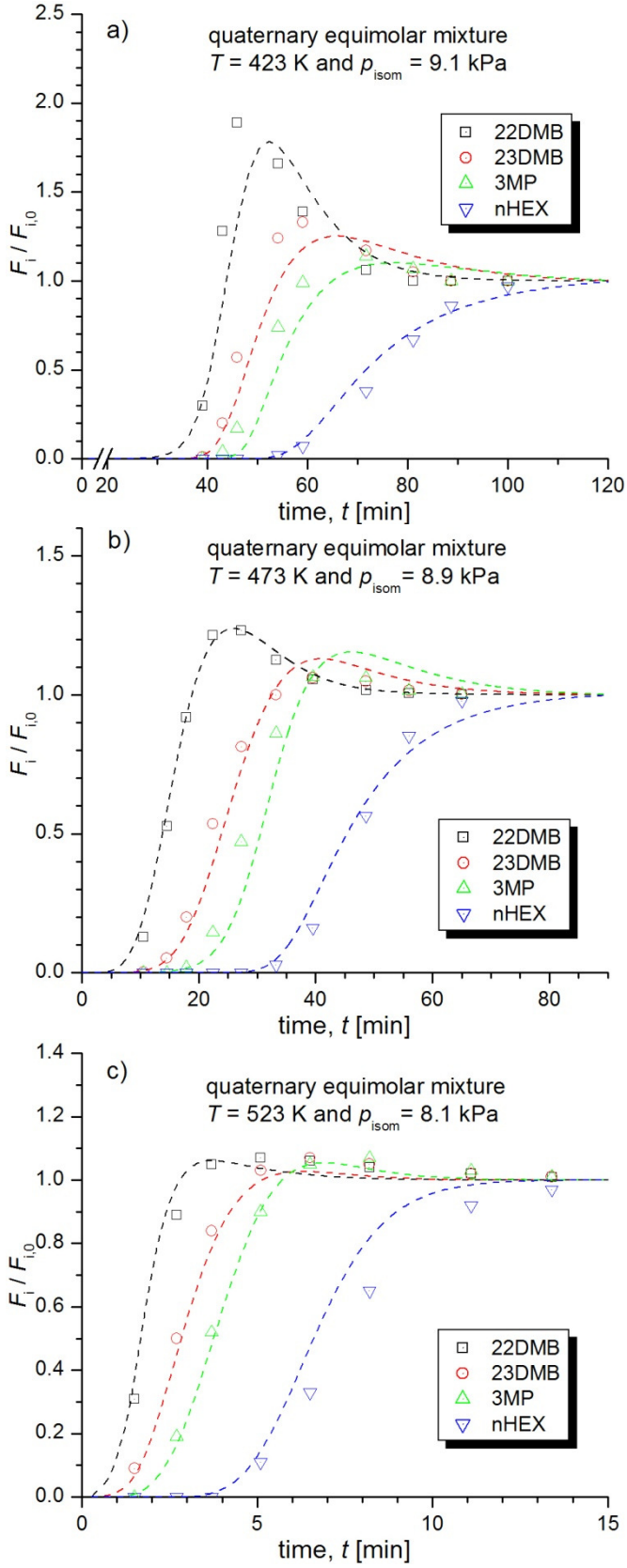


Figure 3.19. Effect of temperature on quaternary breakthrough curves of equimolar mixtures 22DMB/23DMB/3MP/*n*HEX at a) 423 K, b) 473 K and c) 523 K and hydrocarbon pressure near to 9 kPa.

3.7 Conclusions

We have presented a detailed study of sorption of hexane isomers on zeolite beta, which includes breakthrough curves of binary, ternary and quaternary mixtures. These experiments lead to the measurement of single and mixture sorption isotherms, and the determination of selectivities.

In order to model sorption isotherms taking into account the complex zeolite beta structure and consequent heterogeneity of sorption sites probably due to different types of channels, it was developed an expanded Tri-Site Langmuir (TSL) isotherm model taken into account three different types of sites in the structure. The parameters of the model were obtained from the fitting of the single component isotherms of the four hexane isomers studied. Thereafter, the TSL model was extended for the prediction of mixture sorption of hexane isomers and the results compared with the experiments. A good agreement was obtained between the predictions of the TSL model and the experimental results.

Having in mind the separation of the hexane isomers in a fixed bed, a simple LDF mathematical model coupled with the TSL model isotherm was tested in its capability for the simulation of the experimental breakthrough curves. The agreement between the dynamic and experimental data is good, which opens a good perspective regarding future work.

In terms of the experimental data obtained, we conclude that the separation of hexane isomers in zeolite beta is possible, regarding that we work at low hydrocarbon loadings, and this can be achieved at high temperatures (e.g. 523 K). If we work at lower temperatures, for instance 423 K, the total hydrocarbon pressure should not be high.

These data will be used in the next chapter to develop a detailed model to simulate the non-isothermic and non-adiabatic adsorption dynamics of C_5 and C_6 isomers in a fixed-bed packed with different adsorbent layers.

3.8 References

Schenk, M.; Vidal, S.L.; Vlugt, T.J.H.; Smit, B.; Krishna, R. Separation of Alkane Isomers by Exploiting Entropy Effects During Adsorption on Silicalite-1: A Configurational-Bias Monte Carlo Simulation Study. *Langmuir* 17, 1558–1570 (2001).

Bárcia, P.S.; Silva, J.A.C; Rodrigues, A.E. Separation by Fixed-Bed Adsorption of Hexane Isomers in Zeolite BETA Pellets. *Ind. Eng. Chem. Res.* 45, 4316–4328 (2006).

Da Silva, F.A. Cyclic Adsorption Processes: Application to Propane/Propylene Separation. Ph.D. Thesis, University of Porto, Portugal (1999).

Da Silva, F.A.; Silva, J.A.C.; Rodrigues, A.E. A general package for the simulation of cyclic adsorption processes. *Adsorption* 5, 229-244 (1999).

Frenkel, D.; Smit, B. *Understanding Molecular Simulations: from Algorithms to Applications*, 2nd ed., Academic Press, San Diego (2002).

Krishna, R.; Vlugt, T.J.H.; Smit B. Influence of Isotherm Inflection on Diffusion in Silicalite. *Chem. Eng. Sci.* 54, 1751–1757 (1999).

Krishna, R.; Baur, R. Modelling Issues in Zeolite Based Separation Processes. *Sep. Purif. Technol.* 33, 213–254 (2003).

Langer, G.; Roethe, A.; Roethe, K.P.; Gelbin D. Heat and Mass Transfer in Packed Beds - III Axial Mass Dispersion. *Int. J. Heat Mass Transfer* 21, 751–759 (1978).

Morbidelli, M.; Santacesaria, E.; Storti, G.; Carra, S. Separation of Xylenes on Y Zeolites in the Vapor Phase. 2. Breakthrough and Pulse Curves and their Interpretation. *Ind. Eng. Chem. Process Des. Dev.* 24, 83–88 (1985).

Morbidelli, M.; Servida, A.; Storti, G.; Carra, S. Simulation of Multicomponent Adsorption Beds. Model Analysis and Numerical Solution. *Ind. Eng. Chem. Fundam.* 21, 123–131 (1982).

Myers, A.L.; Prausnitz, J.M. Thermodynamics of Mixed-Gas Adsorption. *AIChE J*. 11, 121 (1965).

Silva, J.A.C. Separation of n/iso-Paraffins by Adsorption Process. Ph.D. Thesis, University of Porto, Portugal (1998).

Smit, B.; Krishna, R. Molecular Simulations in Zeolitic Process Design. *Chem. Eng. Sci.* 58, 557–568 (2003).

Villadsen, J.V.; Michelsen, M.L. *Solution of differential equation models by polynomial approximation*; Prentice-Hall Inc.: Englewood Cliffs, New Jersey (1978).

Vlugt, T.J.H.; Krishna, R.; Smit, B. Molecular Simulations of Adsorption Isotherms for Linear and Branched Alkanes and Their Mixtures in Silicalite *J. Phys. Chem. B* 103, 1102 (1999).

4

Adsorption Dynamics of C_5/C_6 Fractions in a Layered Bed of Zeolite Beta and Zeolite 5A

Vapour phase adsorption of C_5/C_6 paraffin fractions in a fixed bed of zeolite beta was addressed. Breakthrough experiments with mixtures containing nPEN, iPEN, nHEX, 3MP, 23DMB and 22DMB demonstrate that the sorption hierarchy is temperature-dependent. At 583 K, an enriched high-octane fraction of 22DMB, iPEN and 23DMB can be selectively separated from the low-octane equimolar C_5/C_6 isomerate feed. For the case of feed mixtures with the typical composition of the hydroisomerization reactor product, the enriched fraction contains low RON nPEN which decreases the octane quality of the product obtained. However, the use of a layered bed with zeolite 5A and zeolite beta can displace the nPEN from the enriched fraction, resulting in a maximum octane number of about 92.5 points. Aspen Adsim was used to simulate the dynamic behaviour of the C_5/C_6 fraction in a non-isothermal and non-adiabatic bed giving a good description of the set of experimental data. An optimal design of a mono/dibranched separation process can be achieved by properly tuning the operating temperature and the zeolite 5A/zeolite beta ratio on a layered fixed bed.

This chapter is based on the following publication:

P.S. Bárcia, J.A.C. Silva, A.E. Rodrigues, *Energy Fuels* 24 (2010) 1931-1940.

4.1 Introduction

The total isomerization process (TIP) consists in converting linear alkanes into their high RON branched isomers by an equilibrium limited catalytic reaction. This stage is followed by the separation of the nonconverted linear molecules in an adsorber packed with zeolite 5A (see Figure 4.1a). However, the final isomerate still contains about one-third of the low RON linear and monobranched alkanes (Holcombe et al., 1990), as shown in Figure 4.1b. The major constituents of a typical isomerate product are represented in Figure 4.2 as a function of their kinetic diameter and octane quality.

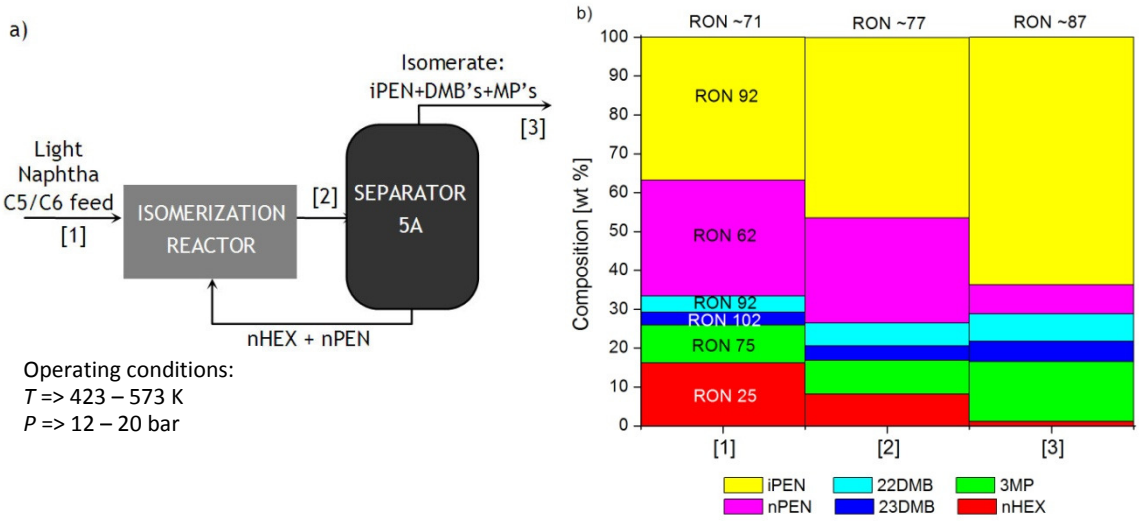


Figure 4.1. a) Simplified scheme of a conventional Total Isomerization Process. b) Typical composition of streams in Figure 4.1a according to Holcombe et al. (1990).

Quite a few papers in the literature deal with the fixed-bed adsorption of hydrocarbons in the C_5-C_6 range; most of them are limited to binary or ternary cases, which hardly represent the complexity of the real operating conditions existing in the refining processes. For instance, an experimental and modelling study by Silva and Rodrigues (1998) shows the fixed-bed dynamics of a ternary mixture *i*PEN, *n*PEN, and *n*HEX in zeolite 5A, demonstrating a good performance for the *n*/iso separation.

It was demonstrated in the previous chapter that zeolite beta can also be an effective adsorbent to separate the low RON *n*HEX and 3MP from the high RON

22DMB and 23DMB in equimolar quaternary mixtures. Thereafter, this chapter will be focused on the development of an adsorptive process combining the selective properties of each zeolite in a layered bed unit.

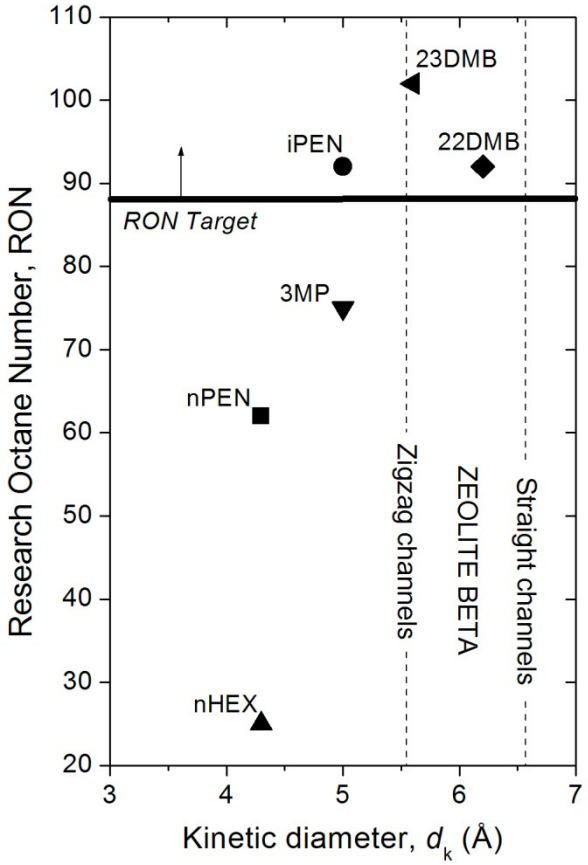


Figure 4.2. RON *versus* kinetic diameter for C_5/C_6 alkanes.

The aim of this chapter is to show the dynamic behaviour of C_5/C_6 isomer fractions in a fixed bed of zeolite beta. For this purpose, a fixed-bed adsorption study of feed fractions containing *n*PEN, *i*PEN, 22DMB, 23DMB, 3MP, and *n*HEX in both equimolar and non-equimolar proportions is addressed. The effect of the operating temperature on the selective adsorption of the C_5/C_6 fractions is analyzed in detail. A commercial process simulator is used for the development of a non-isothermal/non-adiabatic fixed-bed adsorption model incorporating mass, energy, and momentum balances. Simulations for the fixed-bed adsorption of C_5/C_6 fractions in zeolite beta were then compared to the experimental data. Finally, in an attempt to improve the octane

quality of the light product, we present a simulation study showing that a layered bed with zeolite 5A and zeolite beta can significantly improve the performance of the separation process.

4.2 Migration to Aspen Adsim Simulator

In chapter 3, we carried out a first approach to the study of adsorption dynamics of C_6 mixtures in a fixed bed of zeolite beta by using a home-made FORTRAN simulation code developed at LSRE. The results obtained are satisfactory in terms of the prediction of the breakthrough curves; however, keeping in view the development of a cyclic adsorption process it becomes relevant to use a more detailed model accounting for energy and momentum balance along the bed. Furthermore, the use of a home-made code is in a certain manner limitative when it is required to simulate the global performances of an adsorption plant incorporating different operating units such as reactors or flash drums. Therefore, an advanced process design tool, AspenONE Process Engineering (Aspen Technology, Inc.), was for the first time introduced at LSRE during this Ph.D. work. AspenONE Process Engineering is widely used by refining companies (BP, Chevron, ExxonMobil, Petrobras, Total, Sinopec, among others) to develop optimal process designs, analyse design alternatives and identify optimal operating conditions to improve yield, throughput and quality (http://www.aspentech.com).

Included in the AspenONE Engineering package is Aspen Adsim, a flowsheeting environment for the dynamic simulation and optimization of adsorption processes. Aspen Adsim can be used to generate highly detailed and accurate models which allow the development and identification of optimal adsorbents, design better adsorption cycles, and improve general plant operations. Figure 4.3 shows the Aspen Adsim environment running a multicomponent breakthrough curve. It can be seen from Figure 4.3 that the evolution of different variables can be visualized at the same time,

e.g., loading, gas-phase concentration, and temperature profile along the column, and output concentration.

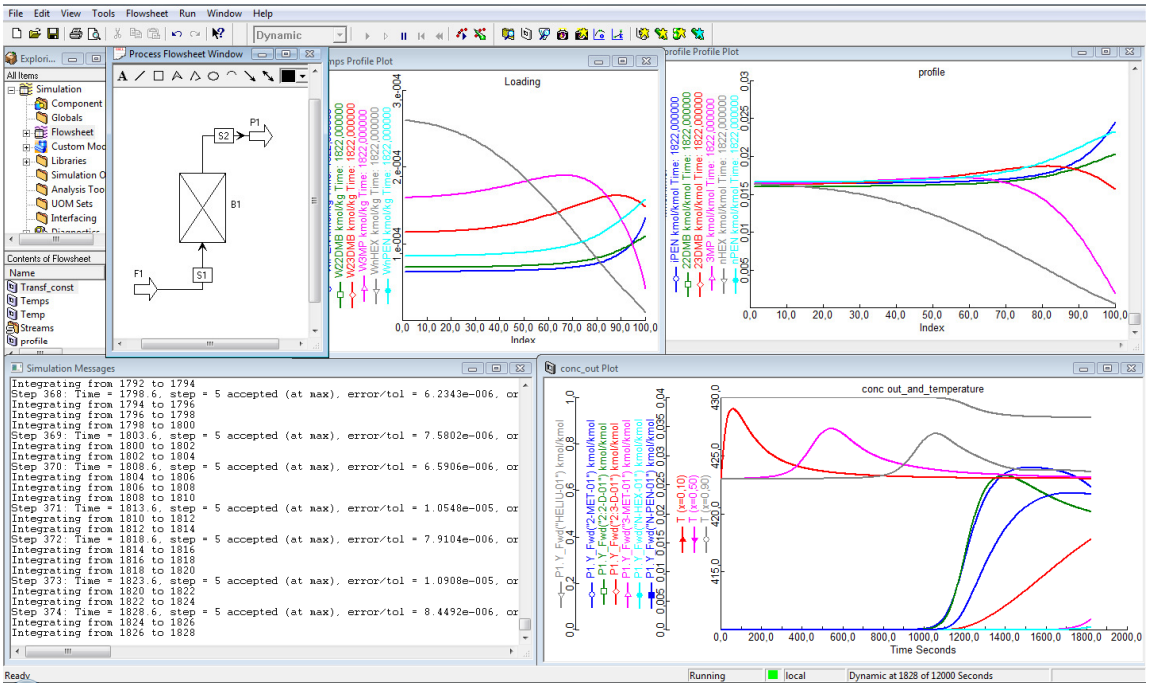


Figure 4.3. Aspen Adsim flowsheeting environment.

In the literature, Aspen Adsim has been used by several authors for the study of cyclic separation/purification processes (Arumugam et al., 1999; Kostroski and Wankat, 2006, 2008; Yang et al., 2009). In chapter 4 and 5, it is explored the potentiality of this platform for simulation/optimization of adsorption processes for the separation of complex alkane mixtures.

To validate the migration from the FORTRAN simulation code used in chapter 3 to Aspen Adsim, we present in Figure 4.4 a comparison of the multicomponent breakthrough curve obtained with both simulators. These simulations refer to run *q_7* in Table 3.2. Equilibrium model parameters, axial dispersion and mass transfer lumped parameters used for the Adsim simulation, were taken from chapter 3 (Table 3.1 and Table 3.3). In a general way, a comparable description of the adsorption dynamics is given by both simulators. It is just observed a slight difference in the dispersion of the breakthrough curve, due to the fact that the simulators use different methods for

solving the partial differential equations; the orthogonal collocation method was applied in the FORTRAN code (collocation points are given by the zeros of Jacobi polynomials), while Aspen Adsim use the numerical method of lines (discretization of spatial derivatives by quadratic interpolation over a fixed, uniform grid of points).

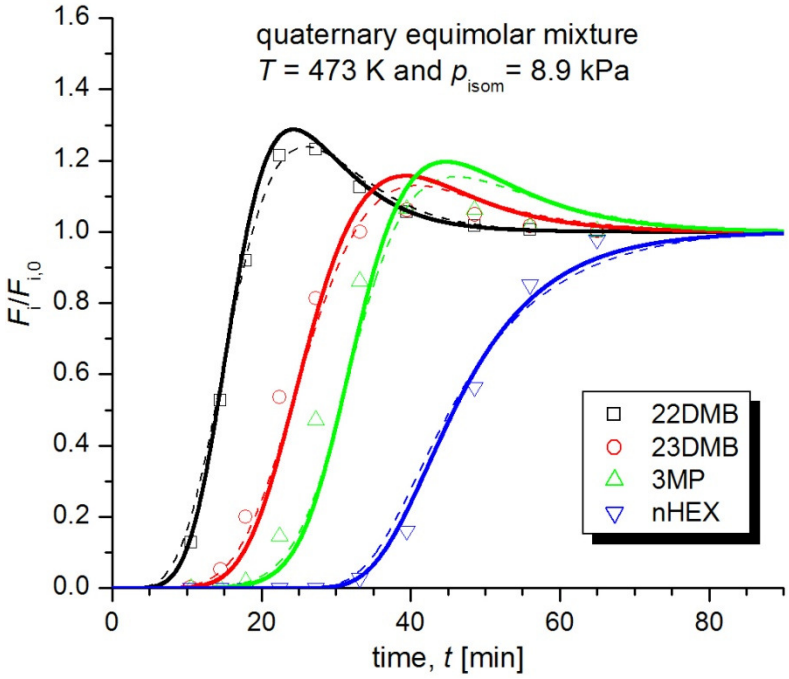


Figure 4.4. Breakthrough curve simulated with the FORTRAN code used in chapter 3 (dashed line) and with Aspen Adsim (solid line), using the model parameters of Table 3.1 and Table 3.3. Points are experimental data; experimental conditions are in Table 3.2 (run *q_7*).

4.3 Model Development

The model used to study the adsorption dynamics of C_5/C_6 mixtures in zeolite beta is implemented within Aspen Adsim 2006.5 (Aspen, 2005) using a simple flowsheet (Figure 4.5) consisting of three blocks: feed (F1), bed (B1), and product (P1). The behaviour of each block is described by a model. The connections S1 and S2 are used between blocks to pass information about material flowrate, composition, temperature, and pressure.

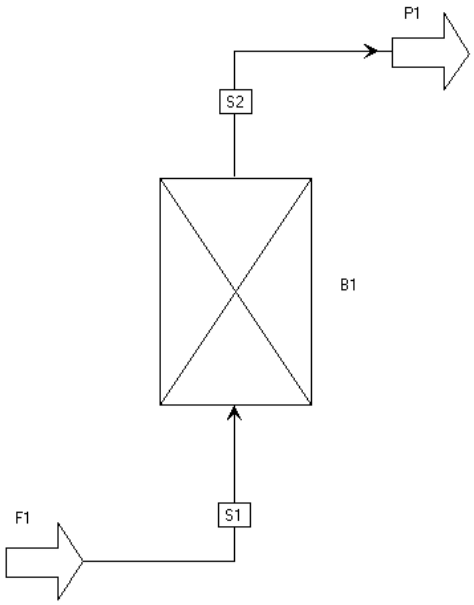


Figure 4.5. Simple flowsheet with three blocks:
feed (F1), bed (B1), and product (P1).

4.3.1 Feed Model

The feed model is used as a flowsheet inlet boundary unit, where the stream composition, flowrate, and temperature are specified, while the pressure is set as a free variable. The model simulates in this way, a forced feed – i.e., fixed molar flowrate – with a constant composition and temperature. The momentum balance in the bed calculates the inlet pressure.

4.3.2 Product Model

The product model is used as a flowsheet outlet boundary unit. Since the fixed bed is operated at atmospheric pressure, the product pressure is set to 100 kPa. The product flowrate is set as free.

4.3.3 Bed Model

The typical output of the hydroisomerization reactor consists predominantly in a stream of inert gas containing 20-50 wt% alkanes in the C_5-C_6 range. Therefore, the velocity variation in the fixed bed should be considered. At the same time, because we are dealing with separation of compounds with a relatively high heat of adsorption (e.g., for *n*HEX, $-\Delta H_0 = 84$ kJ/mol), the non-isothermal behaviour in the fixed bed should be taking into account. Consequently, the model used in this work is based on the following approximations:

- The gas phase is ideal.
- The bed operates in non-isothermal and non-adiabatic conditions with gas and solid heat conduction.
- The bed is initially filled with an inert gas in thermal equilibrium with the feed temperature.
- Radial mass and heat dispersion is neglected, and only axial dispersion occurs.
- The superficial velocity is related to the total pressure gradient according to Ergun's equation.
- The main resistances to mass transfer are combined in a single lumped parameter, where the mass-transfer driving force is a linear function of the solid-phase loading.
- The adsorption equilibrium is described by a TSL model.

Considering the above assumptions, the model equations are as follows.

Ideal Gas Law

$$Py_i = RT_g c_i \tag{4.1}$$

where, P is the total pressure, y_i is the mole fraction of component *i* in the gas phase, R is the universal gas constant, T_g is the temperature in bulk gas phase and c_i is the concentration of solute *i* in fluid.

Mass Balance to Sorbate Species

The mass balance in the gas phase takes into account the effect of the axial dispersion, convection term, gas-phase accumulation, and rate of flux to the adsorbent

$$-\varepsilon_b D_{ax}\frac{\partial^2 c_i}{\partial z^2}+\frac{\partial\left(v_g c_i\right)}{\partial z}+\varepsilon_t\frac{\partial c_i}{\partial t}+\rho_b\frac{\partial \overline{q}_i}{\partial t}=0 \tag{4.2}$$

where, ε_b and ε_t are the interparticle voidage and total bed voidage, respectively, v_g is the gas-phase superficial velocity, *z* and *t* are the axial coordinate and time, respectively, ρ_b is the adsorbent bulk density, and $\overline{q}_i$ is the average amount of solute *i* adsorbed. The dispersion coefficient D_{ax} varies along the length of the bed following the correlation (Ruthven, 1984)

$$D_{ax}=0.73D_m+\frac{v_g R_p}{\varepsilon_b\left(1+9.49\dfrac{\varepsilon_b D_m}{2v_g R_p}\right)} \tag{4.3}$$

Here, R_p is the particle radius. The molecular diffusion coefficient D_m is estimated from the Chapman-Enskog equation (Bird et al., 2002).

Boundary Conditions

The boundary conditions for fluid flow are

$$D_{ax}\left.\frac{\partial c_i}{\partial z}\right|_{z=0}=-v_g\Big|_{z=0}\left(c_i\Big|_{z=0^-}-c_i\Big|_{z=0}\right) \tag{4.4a}$$

$$\left.\frac{\partial c_i}{\partial z}\right|_{z=L_B}=0 \tag{4.4b}$$

Momentum Balance

The superficial velocity is related to the total pressure gradient according to the Ergun's equation (Ergun, 1952)

$$-\frac{\partial P}{\partial z}=\frac{0.15(1-\varepsilon_b)^2}{(2R_p)^2\varepsilon_b^3}\mu v_g+1.75\times10^{-3}M_W\rho_g\frac{(1-\varepsilon_b)}{2R_p\varepsilon_b^3}v_g^2 \qquad (4.5)$$

where *P* is the total pressure expressed in kPa, μ is the dynamic viscosity and M_W is the molecular weight.

Mass Transfer Rate

The mass transfer from the gas to the solid phase is expressed by a linear driving force (LDF) model

$$\frac{\partial\overline{q}_i}{\partial t}=k_{MTC_i}\left(q_i^*-\overline{q}_i\right) \qquad (4.6)$$

with q_i^* being the loading which is in equilibrium with the gas phase composition. The effective mass transfer coefficient k_{MTC} is given as a lumped parameter. This parameter is calculated as a function of the local conditions by an extension of the Glueckauf (1955) approximation for systems in which the resistance to mass transfer in the external fluid film and in the macropores is significant:

$$\frac{1}{k_{MTC_i}}=\frac{R_p\overline{K}_{Ki}}{3k_{fi}}+\frac{R_p^2\overline{K}_{Ki}}{15\varepsilon_p D_{pi}} \qquad (4.7)$$

The adsorption kinetic study in chapter 2 allowed us to conclude that time constant for diffusion in the micropores is not significant comparatively to the other transport mechanisms. Accordingly, the term accounting for mass transfer resistance in the micropores does not appear in Equation 4.7.

The dimensionless Henry's coefficient $\overline{K}_{Ki}$ in Equation 4.7 is obtained from the isotherm model by

$$\overline{K}_{Ki} = RT \frac{\rho_b}{\varepsilon_b} \frac{\partial q_i^*}{\partial p_i} \tag{4.8}$$

where p_i is the partial pressure. The film resistance coefficient k_{f_i} is estimated from the Sherwood number Sh_i using the correlation of Wakao and Funazkri (1978)

$$k_{f_i} = Sh_i \frac{D_{m_i}}{2R_p} \tag{4.9a}$$

$$Sh_i = 2.0 + 1.1 Sc_i^{1/3} Re^{0.6} \tag{4.9b}$$

The macropore diffusion coefficient D_{p_i} is obtained from the Bosanquet equation

$$\frac{1}{D_{p_i}} = \Gamma_p \left(\frac{1}{D_{K_i}} + \frac{1}{D_{m_i}} \right) \tag{4.10}$$

where Γ_p is the tortuosity factor. The Knudsen diffusion coefficient D_{K_i} is

$$D_{K_i} = 97 r_{pore} \left(T / M_{W\,i} \right)^{0.5} \tag{4.11}$$

where r_{pore} is the mean macropore radius (m).

Multicomponent Adsorption Equilibrium Model

The competition of the C_5 and C_6 isomers in a multicomponent system can be predicted from the pure component isotherm model parameters using an extended TSL model, as described in chapter 3. Accordingly, the amount adsorbed of component *i* in a mixture of N components is given by

$$q_i = \sum_j \frac{q_{i,j}^m b_{i,j} p_i}{1 + \sum_{i=1}^{N} b_{i,j} p_i}, \qquad \text{with } j = S, Z, I \tag{4.12}$$

where q is the amount adsorbed, p is the pressure of sorbate and q^m is the saturation loading in each type of sites. The subscripts S, Z and I indicate whether the adsorption sites are in a straight or zigzag channel or in an intersection, respectively. Adsorption affinity constant in site j, b_j, is assumed to vary with temperature, according to the Arrhenius equation

$$b_j = b_j^0 e^{(-E_j / RT)} \tag{4.13}$$

where b_j^0 is the frequency factor of the affinity constant, E_j is the interaction energy of site j. The parameters of the TSL isotherm were determined by a numerical procedure assuming that the total saturation loading only depends upon the number of carbon atoms of the molecule.

Gas Phase Energy Balance

The gas phase energy balance includes axial thermal conduction, convection of energy, accumulation of heat, effect of compression, gas–solid heat transfer, and gas–wall heat transfer. The governing partial differential equation is as follows:

$$-\varepsilon_b k_{gz} \frac{\partial^2 T_g}{\partial z^2} + v_g C_{vg} \rho_g \frac{\partial T_g}{\partial z} + \varepsilon_t C_{vg} \rho_g \frac{\partial T_g}{\partial t} + P \frac{\partial v_g}{\partial z} + h_p a_p (T_g - T_s) + \frac{4 h_w}{d_B} (T_g - T_w) = 0 \tag{4.14}$$

where C_{vg} is the specific gas-phase heat capacity at constant volume, $a_p = 3/R_p(1-\varepsilon_b)$ is the specific particle surface per unit volume of bed, d_B is the internal bed diameter, T_g, T_s and T_w are the gas, solid, and internal wall temperature, respectively. The effective axial gas phase thermal conductivity k_{gz} is calculated on the basis of the axial dispersion coefficient

$$k_{gz} = \rho_g C_{pg} \sum_i D_{ax_i} y_i \tag{4.15}$$

where ρ_g is the gas phase molar density and C_{pg} is the specific gas phase heat capacity at constant pressure.

The boundary conditions for the gas-phase energy balance are

$$k_{gz}\left.\frac{\partial T}{\partial z}\right|_{z=0} = -\rho_g C_{pg} v_g\Big|_{z=0}\left(T\Big|_{z=0^-} - T\Big|_{z=0}\right) \tag{4.16a}$$

$$\left.\frac{\partial T}{\partial z}\right|_{z=L_B} = 0 \tag{4.16b}$$

The gas-solid heat transfer coefficient h_p is estimated using the Colburn *j* factor for heat transfer as follows:

$$h_p = j\,\rho_g C_{pg} v_g\,\mathrm{Pr}^{-2/3} \tag{4.17}$$

where $j = 1.66\,\mathrm{Re}^{-0.51}$ if $\mathrm{Re} < 190$ otherwise $j = 0.983\,\mathrm{Re}^{-0.41}$.

The gas-wall heat transfer coefficient h_w is obtained from the Nusselt number by the following correlation (Kast, 1988)

$$h_w = Nu_w \frac{k_{gz}}{x_{char}} \tag{4.18a}$$

$$Nu_w\left(1 + \frac{12L_B}{d_B(\mathrm{Re}\,\mathrm{Pr})}\right) = -2\times10^{-6}(\mathrm{Re}\,\mathrm{Pr})^2 + 0.0477(\mathrm{Re}\,\mathrm{Pr}) + 22.11 \tag{4.18b}$$

where $x_{char} = 2R_p$ is the characteristic length for a cylinder, and L_B is the height of the bed.

Solid Phase Energy Balance

The solid-phase energy balance includes axial thermal conductivity, enthalpy accumulation, heat of adsorption, and gas-solid heat transfer

$$-k_{sz}\frac{\partial^2 T_s}{\partial z^2}+c_{ps}\rho_b\frac{\partial T_s}{\partial t}+\rho_b\sum_{i=1}^{n}\left(q_{st_i}\frac{\partial \bar{q}_i}{\partial z}\right)-h_p a_p\left(T_g-T_s\right)=0 \qquad (4.19)$$

where k_{sz} is the effective axial solid phase thermal conductivity and C_{ps} is the specific heat capacity of the adsorbent. The isosteric heat of adsorption of component *i*, q_{st_i}, can be calculated from the van't Hoff equation

$$\left.\frac{\partial \ln P}{\partial T}\right|_{q_i}=\frac{q_{st_i}}{RT^2} \qquad (4.20)$$

Taking the total derivative of Equation 4.12 (for $N = 1$) at constant loading and combining with Equation 4.20 we can obtain

$$q_{st_i}=\left[\sum_j q_{i,j}^m b_{i,j}\frac{-E_{i,j}}{\left(1+b_{i,j}p\right)^2}\right]/\left[\sum_j q_{i,j}^m\frac{b_{i,j}}{\left(1+b_{i,j}p\right)^2}\right], \text{ with } j=S,Z,I \qquad (4.21)$$

The above equation allows for the determination of the loading dependence of the isosteric heat as a function of the pressure and can be related to loading via the TSL equation. A detailed description about the derivation of Equation 4.21 is given in the appendix B.

Wall Energy Balance

The effects considered for the wall energy balance include axial thermal conductivity along the wall, heat content of the wall, and both the gas-wall and wall-oven heat exchanges

$$-k_{wz}\frac{\partial^2 T_w}{\partial z^2}+C_{pw}\rho_w\frac{\partial T_w}{\partial t}-h_w\alpha_w\left(T_g-T_w\right)+U_\infty\alpha'_w\left(T_w-T_\infty\right)=0 \qquad (4.22)$$

where k_{wz} is the thermal conductivity of column wall, T_∞ is the oven constant set-point temperature, C_{pw} and ρ_w are the specific heat capacity and the density of the column wall, respectively, α_w is the ratio of the internal surface area to the volume of

the column wall, and α'_w is the ratio of the log mean surface area to the volume of the column wall. The wall-ambient heat transfer coefficient U_∞ was estimated assuming an average of the typical values for forced convection inside an oven, 60 W/m^2/K (Bird et al., 2002).

Numerical Methods

The set of equations was numerically solved using Aspen Adsim 2006.5. Adsim uses the method of lines (Schiesser, 1991) to solve the time-dependent partial differential equations. The spatial derivatives were discretized over a uniform grid of 100 points by the quadratic upwind differencing scheme (QDS) in conjunction with the Gear integration with variable step size of 0.1–5 s. The physical properties of the components in the process are locally estimated through integration with the Aspen Properties database. The input parameters of the model are listed in Table 4.1.

Table 4.1. Operating parameters for fixed bed adsorption and properties of zeolite beta and zeolite 5A. §

Parameters		Values	Unit
Column:			
Internal bed diameter / Bed length / Bulk porosity: $d_B / L_B / \varepsilon_b$	*bed_1*	0.46 / 10 / 0.49	cm / cm / -
	bed_2	0.77 / 10 / 0.42	"
	bed_3	0.46 / 10 / 0.55	"
Wall thickness, δ_w		0.10	mm
Wall density, ρ_w		7.99×10^3	kg/m^3
Wall specific heat capacity, C_{pw}		0.50	kJ/kg/K
Wall thermal conductivity, k_w		17	W/m/K
Wall-oven heat transfer *, U_∞		60	$W/m^2/K$
Adsorbents:	*zeolite beta*	*zeolite 5A*	
Pellet diameter, d_p	1.59×10^{-3}	1.59×10^{-3}	m
Macropore radius, r_{pore}	3.75×10^{-8}	8.50×10^{-8}	m
Adsorbent heat capacity †, C_{ps}	0.865		kJ/kg/K
Adsorbent thermal conductivity ‡, k_{sz}	0.20		W/m/K
Apparent density of pellet, ρ_p	1.18×10^3	1.13×10^3	kg/m^3
Pellet porosity, ε_p	0.40	0.35	–

§ Parameters for zeolite 5A were taken from Silva (1998).
* Bird et al. (2002).
† Boerio-Goates et al. (2002).
‡ Griesinger et al. (1999).

4.4 Experimental Section

4.4.1 Adsorbent and Adsorbates

The properties of the commercial sample of zeolite beta are described in detail in chapter 2. The hydrocarbons used in this work were purchased from Fluka, except for *n*PEN supplied by Riedel-de Haën. The specified purities are over 99%, except for 23DMB (>97%).

4.4.2 Experimental Equipment and Procedure

Multicomponent breakthrough experiments in the vapour phase were performed in a stainless steel column packed with pellets of zeolite beta. Three beds with different properties were used (see Table 4.1). Experimental apparatus and operating procedure were previously described in detail in chapters 2 and 3.

4.5 Results and Discussion

4.5.1 Adsorption Equilibrium of C_5/C_6 Isomers in Zeolite Beta

The analytical description of the adsorption equilibrium of a C_5/C_6 mixture in zeolite beta requires single equilibrium adsorption data for C_5 isomers (*n*PEN and *i*PEN), in order to estimate the fitting parameters of the isotherm model. Therefore, single equilibrium data of C_5 isomers were measured at LSRE with the same apparatus used for the C_6 isomers pure component breakthrough curves (see chapter 2). Experimental conditions and pure component isotherms are presented in detail in appendix A (Table A1 and Figure A1).

The TSL model parameters for the adsorption of C_5/C_6 isomers in pellets of zeolite beta are shown in Table 4.2. The TSL parameters for the C_6 isomers are the same than

those estimated in chapter 3. The TSL model predicts that the maximum amount of C_5 isomers which can fit in the channels of the zeolite beta is slightly higher than for C_6. A similar result was reported by Liu et al. (2008) in a recent molecular simulation study regarding the adsorption equilibrium of linear alkanes in the BEA structure. Since we are dealing with a pelletized sample of beta containing 30 wt% of inert silica binder, it is possible to estimate from the TSL model that the real saturation capacity is 1.35 mmol/g and 1.33 mmol/g for C_5 and C_6 isomers, respectively.

Table 4.2. TSL model parameters for the adsorption equilibrium of C_5/C_6 isomers in pellets of zeolite beta. Overall saturation loading and enthalpy at zero coverage are also represented.

Site	Param.	Unit	*n*HEX	3MP	23DMB	22DMB	*n*PEN	*i*PEN
S	q_S^m	mmol/g_{ads}	0.529	0.329	0.775	0.797	0.608	0.491
	$b_{0,S}$	kPa^{-1}	5.0×10^{-10}	2.0×10^{-9}	8.6×10^{-10}	1.2×10^{-9}	1.0×10^{-8}	1.3×10^{-8}
	$-E_S$	kJ/mol	70.3	67.2	67.5	65.9	59.5	59.1
Z	q_Z^m	mmol/g_{ads}	0.289	0.195	-	-	0.082	0.354
	$b_{0,Z}$	kPa^{-1}	1.7×10^{-9}	3.0×10^{-10}	-	-	9.7×10^{-9}	2.0×10^{-8}
	$-E_Z$	kJ/mol	78.8	84.8	-	-	26.2	52.8
I	q_I^m	mmol/g_{ads}	0.112	0.406	0.155	0.133	0.257	0.100
	$b_{0,I}$	kPa^{-1}	4.6×10^{-12}	5.0×10^{-12}	6.8×10^{-10}	3.2×10^{-9}	8.1×10^{-9}	1.8×10^{-8}
	$-E_I$	kJ/mol	99.8	87.1	80.2	68.1	65.9	60.3
	$q_{overall}^m$	mmol/g_{ads}	0.930	0.930	0.930	0.930	0.946	0.946
	$q_{overall}^m$	*g/100g$_{ads}$*	*8.0*	*8.0*	*8.0*	*8.0*	*6.8*	*6.8*
	$-\Delta H_0$	kJ/mol	84.5	83.8	78.3	66.9	63.8	58.7
	$\overline{\Delta q}$	mmol/g_{ads}	0.013	0.010	0.019	0.007	0.010	0.008
	$\overline{\Delta q}$	g/100g_{ads}	0.11	0.09	0.16	0.06	0.09	0.07

The adsorption enthalpies at zero coverage $-\Delta H_0$ were determined for each alkane calculating the limit of Equation 4.20 at low loading. In principle, these values correspond to the energetic contribution of the strongest sites, which are in theory the preferential locations for adsorption at low coverage (Sircar and Cao, 2002). It can be seen from Table 4.2 that adsorption enthalpies at zero coverage follows the opposite

order of their vapour pressure, *i.e.*, *n*HEX > 3MP > 23DMB > 22DMB > *n*PEN > *i*PEN. The same order was reported by Denayer et al. (1998) in a sodium exchanged zeolite beta. Due to the energetic heterogeneity of the adsorbent surface, the isosteric heat of adsorption will depend on the degree of filling of each type of site. Thus, Equations 4.12 and 4.20 can be combined to describe the loading dependence of the isosteric heat of adsorption according to Equation 4.21.

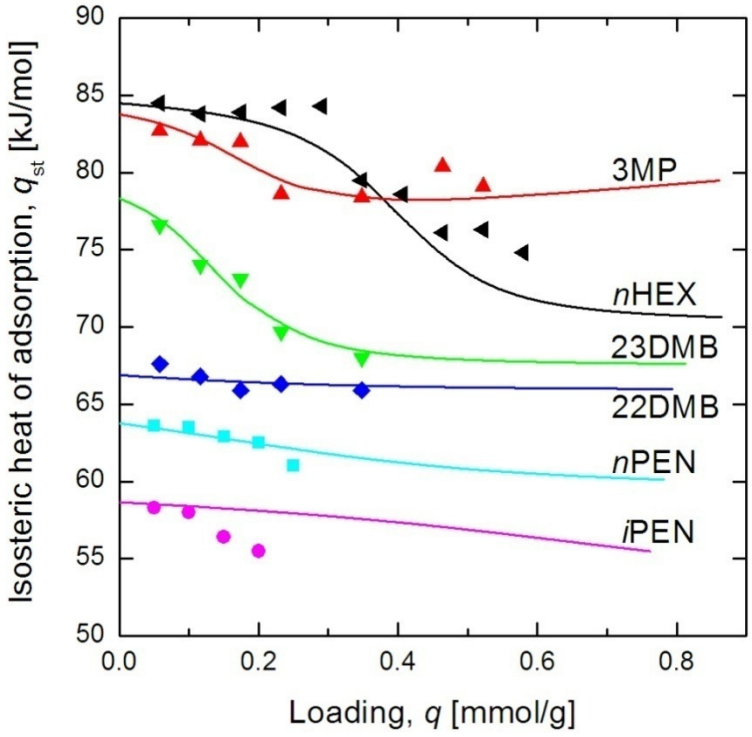


Figure 4.6. Heat of adsorption predicted from TSL isotherm model as a function of the loading. Points are experimental data and lines represent TSL predictions.

The predicted values, which are represented by the lines in Figure 4.6, can be compared with the experimental isosteric heat, represented by points. Figure 4.6 shows a good agreement between experimental data and TSL predictions. Consequently, it can be concluded that for $q_{overall}^{m}$ < 0.4 mmol/g the global adsorption strength follows the opposite order of their vapour pressure, i.e., *n*HEX > 3MP > 23DMB > 22DMB > *n*PEN > *i*PEN. It should be noted that interaction strengths decrease gradually with the pore filling indicating that stronger sites are progressively occupied by the adsorbed molecules. Unexpectedly, 3MP does not exhibit a monotonic

behaviour as observed for the other alkanes; its energetic interaction with beta slightly increases above $q^{m}_{overall}$ = 0.4 mmol/g. This effect could indicate that an extra pressure is required for the adsorption of 3MP in sites with stronger energy, possibly because of steric constraints caused by the methyl branch linked to the central carbon atom of the alkane chain. Interesting is the good description given by the TSL model for the particular feature of the monobranched hexane. Once more, these results indicate that TSL model is appropriate for a correct description of the sorption phenomena of linear and branched C_5/C_6 alkanes in zeolite beta.

Figure 4.7 shows the six-component equilibrium isotherm at temperatures between 423 K and 523 K. This study covers a range of molar ratio alkanes/He up to 0.20, typical of the operating conditions used in hydroisomerization units (Cusher, 2004). The experiments were performed at 100 kPa total pressure; however, this is not a limiting case. It was reported in chapter 3 that in zeolite beta the increase of the partial pressure induce a slight reduction in the selectivity between low RON and high RON C_6 isomers; it was also shown that the temperature has a positive effect on the selectivity. Since the driving force for the separation is the partial pressure, and taking into account that the feed is diluted in inert gas, then the total system pressure could be increased without affecting the hydrocarbons partial pressure, and consequently the degree of separation.

It can be seen in Figure 4.7 that the C_5 isomers have a loading similar to the dibranched C_6 isomers. However, the increase of the temperature originates a progressive change in the loading hierarchy favouring the adsorption of more C_5 alkanes in relation to the dibranched C_6 isomers, as shown in Figure 4.7. Such behaviour could be attributed to thermodynamic effects which results in a lower temperature dependence of the C_5 adsorption equilibria.

The predictions of the TSL isotherm model – represented by the lines in Figure 4.7 – properly correlate the experimental equilibrium data. Well described by the TSL model is also the change in the sorption hierarchical order experimentally observed.

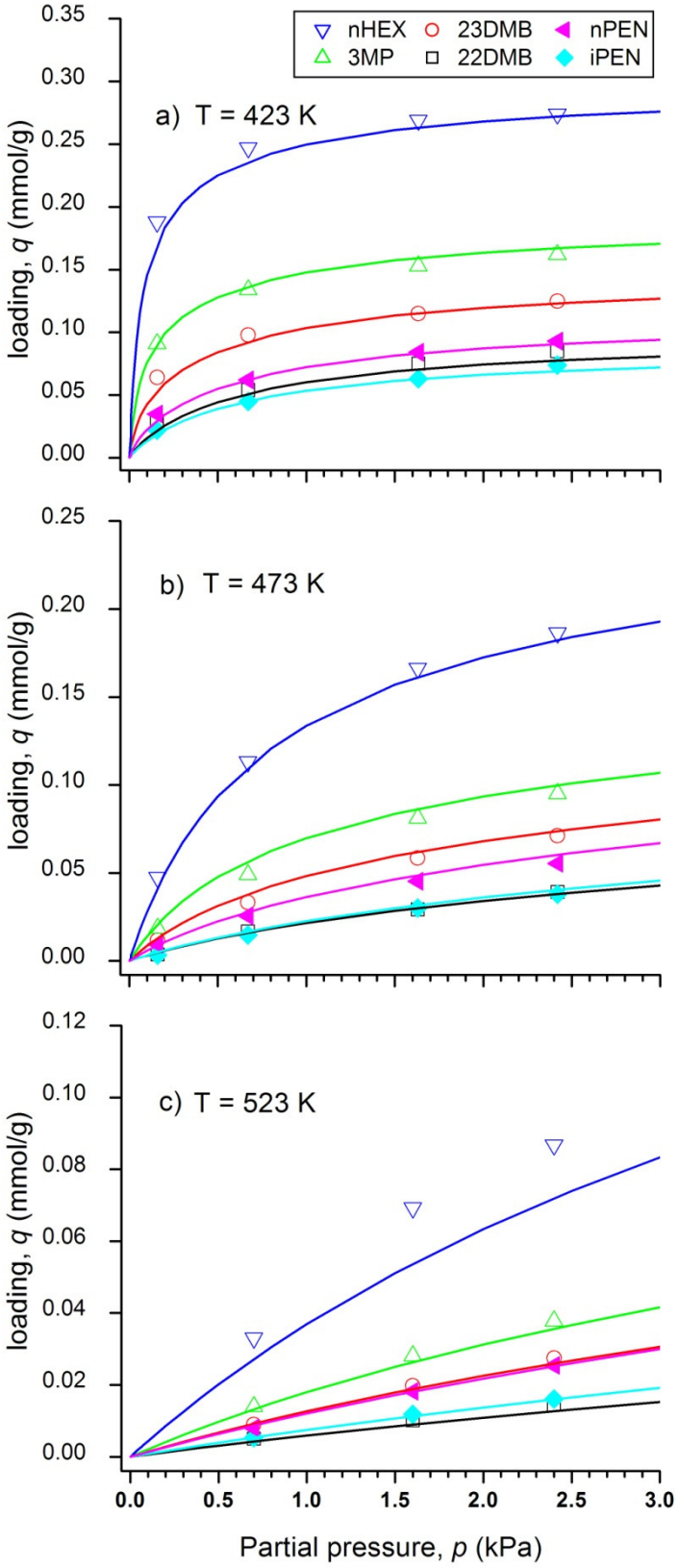


Figure 4.7. Experimental and fitted adsorption equilibrium isotherm for a C_5/C_6 six-component equimolar mixture of 22DMB/23DMB/3MP/*n*HEX/*i*PEN/*n*PEN on pellets of zeolite beta at: a) *T* = 423K; b) *T* = 473K and c) *T* = 523K.

4.5.2 Equimolar C_5/C_6 Six-Component Breakthrough Curves

The effect of the temperature in the breakthrough curves of a C_5/C_6 six-component equimolar mixture is shown in panels *a–c* of Figure 4.8. The experimental conditions are shown in Table 4.3. The breakthrough profiles show that the first components to elute from the column are the dibranched hexanes mixed with the C_5 isomers. Because of its low RON, the presence of *n*PEN decreases the quality of the first eluting faction. Nevertheless, when the temperature increases, a displacement of the breakthrough curves of the C_5 isomers is observed relatively to the dibranched C_6 isomers (see panels *b* and *c* of Figure 4.8). Consequently, it was verified experimentally that the order of the stoichiometric times t_{st} of each component change with the temperature as follows:

$$at\ T = 423K,\ \ t_{st}(iPEN) < t_{st}(nPEN) \cong t_{st}(22DMB) < t_{st}(23DMB) < t_{st}(3MP) < t_{st}(nHEX)$$

$$at\ T = 473K,\ \ t_{st}(iPEN) < t_{st}(22DMB) < t_{st}(nPEN) < t_{st}(23DMB) < t_{st}(3MP) < t_{st}(nHEX)$$

$$at\ T = 523K,\ \ t_{st}(iPEN) \cong t_{st}(22DMB) < t_{st}(23DMB) \cong t_{st}(nPEN) < t_{st}(3MP) < t_{st}(nHEX)$$

Following this tendency, it is expected that an additional increase in temperature could displace the low RON *n*PEN from the high RON components. It was found through preliminaries simulations that the minimum temperature should be close to 583 K. Such result was subsequently confirmed by the experimental breakthrough curve shown in Figure 4.9. From this figure, we can observe a shift in the order of the stoichiometric times. Consequently, at 583 K, we have the following sorption hierarchy:

$$at\ T = 583K,\ \ t_{st}(22DMB) < t_{st}(iPEN) \cong t_{st}(23DMB) < t_{st}(nPEN) \cong t_{st}(3MP) < t_{st}(nHEX)$$

Accordingly, an enriched RON fraction composed of 22DMB, *i*PEN and 23DMB can be separated from the six-component equimolar mixture feed at the optimum temperature of 583 K.

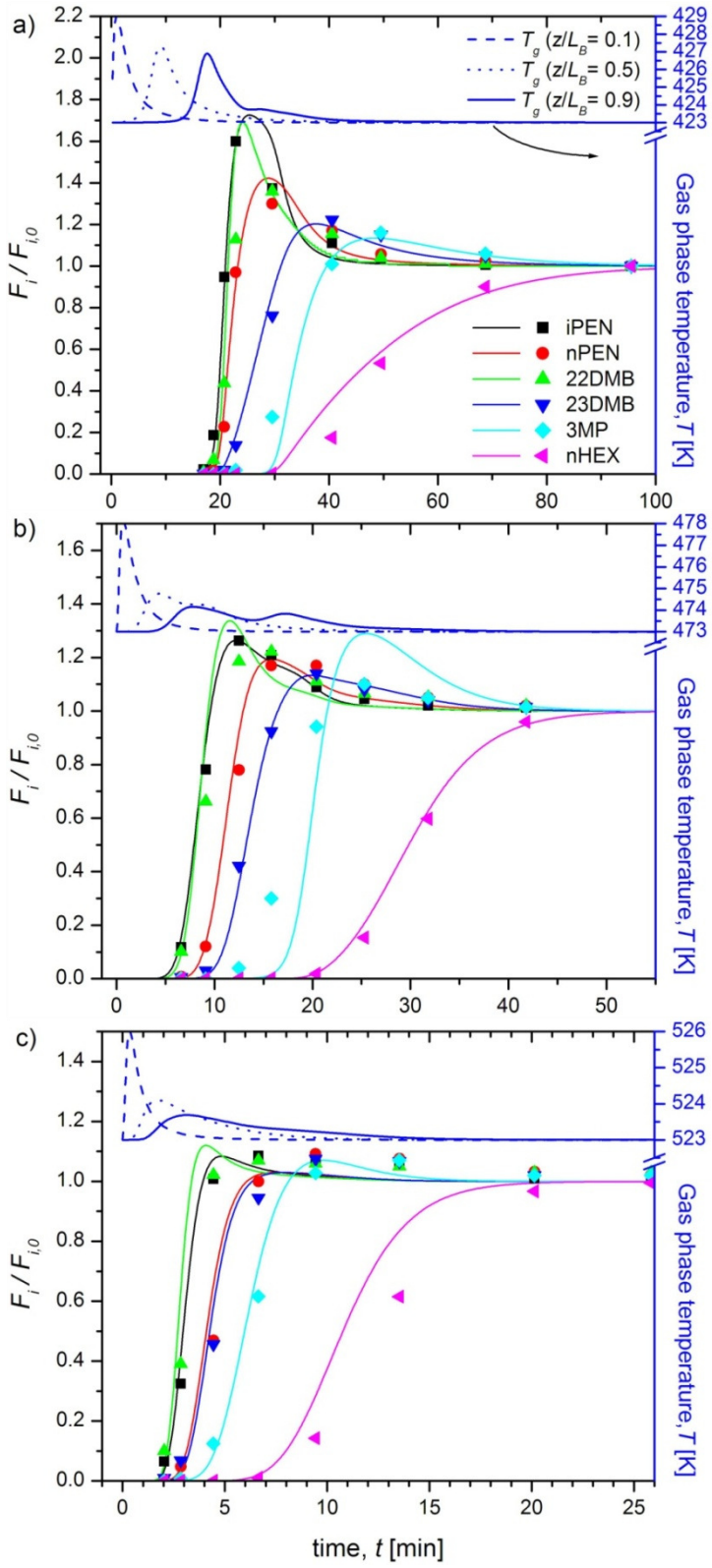


Figure 4.8. Effect of the temperature on the six-component breakthrough curves of the equimolar feed mixtures *i*PEN/*n*PEN/22DMB/23DMB/3MP/*n*HEX at p_{mix} = 9.8 kPa and *a) T* = 423 K (Run *Eq6_3*), *b) T* = 473 K (Run *Eq6_7*) and *c) T* = 523 K (Run *Eq6_10*).

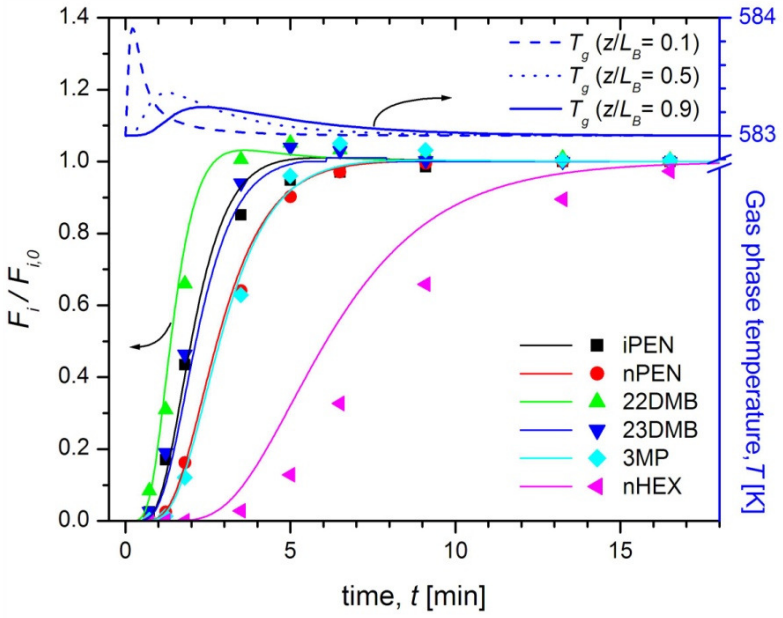


Figure 4.9. Six-component breakthrough curves for an equimolar feed mixture containing *i*PEN/*n*PEN/22DMB/23DMB/ 3MP/*n*HEX at T = 583 K and p_{mix} = 9.7 kPa (Run *Eq6_12*).

Noteworthy is the fact that the sorption hierarchy is in clear agreement with the order of the Henry constants determined by Denayer et al. (1998) for linear and branched alkanes in a sodium exchanged zeolite beta at 573 K using the pulse chromatographic technique: $H_{22\mathrm{DMB}} < H_{i\mathrm{PEN}} < H_{23\mathrm{DMB}} < H_{n\mathrm{PEN}} < H_{3\mathrm{MP}} < H_{n\mathrm{HEX}}$.

In a general way, the simulations, represented by lines in Figure 4.8 and Figure 4.9, describe with a satisfactory accuracy the experimental breakthrough curves at all the temperatures studied, including the overshoot phenomena observed for the less adsorbed components. This is also an indication that the extended TSL model is adequate for the description of the multicomponent adsorption interactions. The slight deviations observed in certain experiments could be justified by the large range of pressure and temperature embraced in this work. Also shown in Figure 4.8 and Figure 4.9 are the predictions of the mathematical model for the temperature history of the gas phase inside the column at three different axial coordinates. The heat balance revealed temperature increases of 6 K and 4 K maximum during the experiments at the column inlet and outlet, respectively. The magnitude of the temperature peaks

decreases as the bed temperature increases, for instance, the maximum peak is 6 K at 423 K and 3 K at 523 K. This effect occurs because the higher the temperature the lower the amount adsorbed, and consequently the lower the energy released.

The model parameters for mass and heat transfer were estimated as a function of the local conditions during the dynamic simulations; the values at the equilibrium are listed in Table 4.4.

4.5.3 Analysis of Heat Effects in Adsorption Column Dynamics

Because of the exothermic nature of adsorption, true isothermality never exists in real adsorbers. Indeed, fixed bed adsorbers behave in the range from near adiabatic to near isothermal. Since the study of the adsorption dynamics presented in chapter 3 was based on the assumption that the fixed bed is isothermal, it is important now to analyze if the isothermal case can be regarded as a reasonable approximation for the present system. Therefore, the importance of heat effects in the adsorption column dynamics was investigated by comparing the simulations for both the isothermal and the non isothermal and non adiabatic cases.

Since the heat effects are more pronounced at low temperature, we show in Figure 4.10 the simulation of run *Eq6_3*. It can be seen from Figure 4.10 that the heat effects have practically no influence on the breakthrough curves. Two conclusions can be drawn from this result: *i)* although the relatively high heat of adsorption of the alkanes in zeolite beta, the forced convection ensures a near-isothermal column; *ii)* the dynamic model assuming isothermality is a valid approximation for the experimental set up used in chapter 3 and 4.

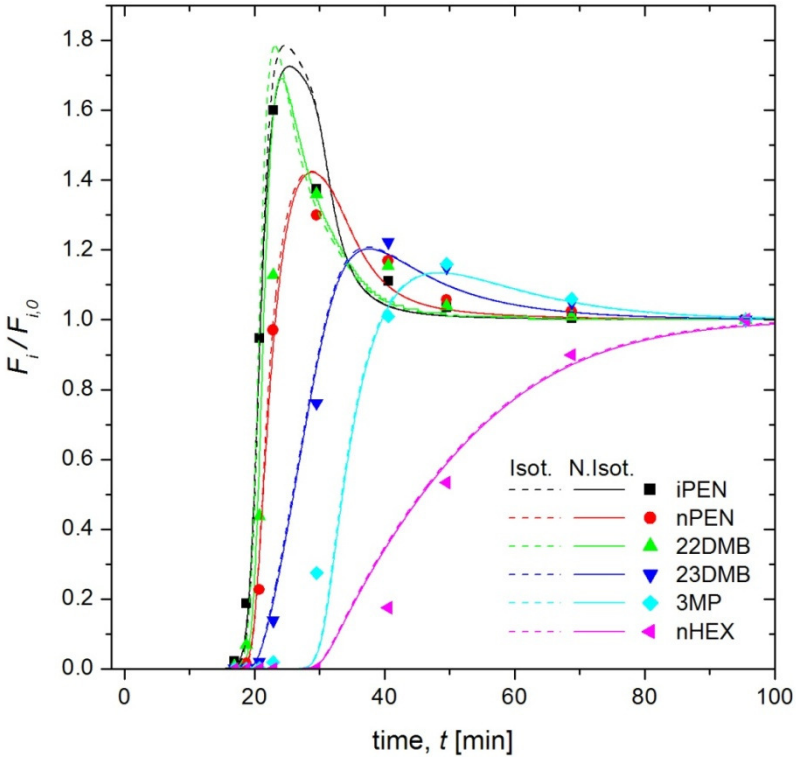


Figure 4.10. Isothermal adsorption (dashed lines) *versus* non-isothermal and non-adiabatic adsorption (solid lines).

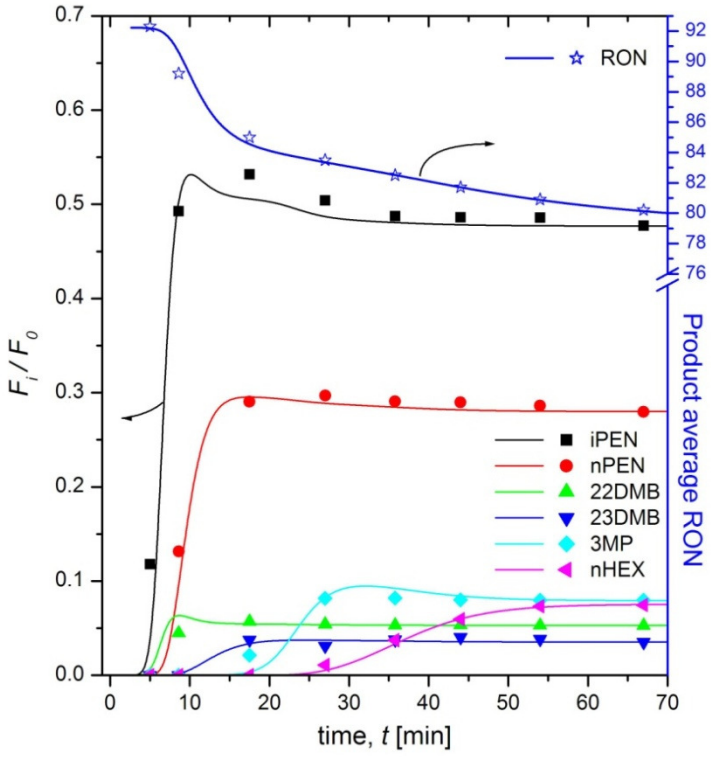


Figure 4.11. Six-component breakthrough curve and RON history of the accumulated product for a feed mixture *i*PEN/*n*PEN/22DMB/23DMB/3MP/*n*HEX at T = 473 K and p_{mix} = 10.2 kPa (Run *Iso6_2*). Feed has molar composition of stream 2 in Figure 4.1.

4.5.4 C_5/C_6 Six-Component Breakthrough Curve of the Typical Hydroisomerization Reactor Product

To check the potentiality of the fixed-bed of zeolite beta in a realistic situation, a breakthrough experiment was performed by injecting a naphtha fraction synthesized in the laboratory with the typical composition of the outlet stream of a hydroisomerization reactor unit, *i.e.*, stream 2 in Figure 4.1 (Holcombe et al., 1990). Figure 4.11 shows a C_5/C_6 six-component breakthrough curve obtained at 473 K and p_{isom} = 10.2 kPa, as well as the corresponding RON history of the accumulated product. The experimental conditions for the breakthrough curves are in Table 4.3. It can be seen that the C_5 isomers elute first from the column. This is due to the larger concentration of *n*PEN in the feed; for favourable isotherms the high-concentration fronts diffuse faster along the adsorption column than the low-concentration fronts. Despite this drawback, if the adsorption step is cut at 12 min, the quality of the hydrocarbon mixture obtained is around 87 RON (see RON history of the accumulated product in Figure 4.11), which is close to octane quality of the product resulting from conventional processes.

The lines in Figure 4.11 clearly demonstrate a good agreement between the experimental breakthrough curves and the dynamic model solution without additional fitting. The model parameters for mass and heat transfer are in Table 4.4.

These results suggest that the performance of the separation between high RON and low RON compounds could be enhanced by operating a layered bed including a *n*/*iso* selective adsorbent (*e.g.*, zeolite 5A) in order to delay the exit of *n*PEN from the bed, and a *mono*/*di*-branched selective adsorbent to separate the 3MP (*e.g.*, zeolite beta).

Table 4.3. Experimental conditions of the six-component breakthrough curves and amount adsorbed of each component in the mixture†

Run	*Column* ‡	T(K)	p_{HC} (kPa)	q (mmol/g)					
				22DMB	23DMB	3MP	*n*HEX	*i*PEN	*n*PEN
Equimolar mixtures									
Eq6_3	*bed_1*	423	9.8	0.0750	0.1150	0.1530	0.2690	0.0630	0.0840
Eq6_7	*bed_1*	473	9.8	0.0290	0.0590	0.0810	0.1660	0.0300	0.0450
Eq6_10	*bed_1*	523	9.8	0.0100	0.0200	0.0280	0.0690	0.0120	0.0180
Eq6_12	*bed_2*	583	9.7	0.0021	0.0031	0.0049	0.0140	0.0035	0.0052
Isomerate mixture *(stream 2 in Figure 4.1)*									
Iso6_2	*bed_3*	473	10.2	0.0164	0.0183	0.0526	0.1112	0.1028	0.0947

† Total system pressure = 100 kPa. Helium flow rate = 7.0 ml/min.

‡ Column properties are in Table 4.1.

Table 4.4. Axial dispersion, macropore diffusion, mass and heat transfer coefficients.

Run	*Column*†	T(K)		$D_{ax}\times10^4$ (m^2/s)		$D_p\times10^6$ (m^2/s)		k_{MTC} (s^{-1})						h_p ($W/m^2/K$)	h_w ($W/m^2/K$)
				C_5	C_6	C_5	C_6	22DMB	23DMB	3MP	*n*HEX	*i*PEN	*n*PEN		
Equimolar mixtures															
Eq6_3	*bed_1*	423	*beta*	0.69	0.66	7.7	7.1	0.0498	0.0123	0.0062	0.0031	0.0670	0.0312	603.8	159.2
Eq6_7	*bed_1*	473	*beta*	0.95	0.90	8.3	7.6	0.3681	0.1268	0.0758	0.0377	0.3857	0.2089	199.0	41.1
Eq6_10	*bed_1*	523	*beta*	1.27	1.20	8.8	8.1	1.8355	0.8165	0.5549	0.2668	1.5698	0.9590	239.2	51.4
Eq6_12	*bed_2*	583	*beta*	1.71	1.62	9.4	8.6	6.4254	3.5989	2.7538	1.2769	4.4922	3.0822	251.6	106.0
Isomerate mixture *(stream 2 in Figure 4.1)*															
Iso6_2	*bed_3*	473	*beta*	0.95	0.90	8.3	7.6	0.4792	0.1653	0.0988	0.0491	0.5030	0.2724	189.6	40.3
Isomerate mixture in layered bed *(stream 2 in Figure 4.1)*															
Lay6_1	‡	473	*5A*	0.95	0.90			–	–	–	0.0577	–	0.4017	189.5	20.5
			beta	0.95	0.90	8.3	7.6	0.5003	0.1725	0.1031	0.0513	0.5251	0.2844	189.5	40.3
Lay6_2	‡	523	*5A*	1.27	1.20			–	–	–	0.2339	–	1.5148	228.2	25.7
			beta	1.27	1.20	8.8	8.1	2.4962	1.1099	0.7545	0.3628	2.1349	1.3043	228.8	50.4

† Column properties are in Table 4.1

‡ The column properties used for the simulation of the layered bed are the following: d_B = 0.46 cm; L_B (5A) = 20 cm; L_B (beta) = 10 cm ε_b = 0.55. The remaining parameters common for all the simulations are listed in Table 4.1

4.5.5 Simulation of C_5/C_6 Six-Component Breakthrough Curves on a Layered Bed

To do this task, we have performed a set of simulations for a layered bed with zeolite 5A and zeolite beta. Silva and Rodrigues (1998) have studied in detail the adsorption of *n*HEX and *n*PEN in a fixed-bed of zeolite 5A. For input parameters of model simulation, the adsorption isotherm data and the adsorbent properties were the same than those published in the previous work (Silva and Rodrigues, 1998). Accordingly, the branched alkanes are considered as non-adsorbing species in zeolite 5A. The physical properties of zeolite 5A are reported in Table 4.1. The fixed-bed considered for these simulations consists of a zeolite 5A layer of 20 cm in height at the feed end and a zeolite beta layer of 10 cm in height above the zeolite 5A layer. The characteristics of this column, as well as the corresponding mass and heat transfer parameters estimated are reported in Table 4.4.

Panels *a* and *b* of Figure 4.12 show the simulated breakthrough curves obtained for a C_5/C_6 six-component feed mixture, composition of stream 2 in Figure 4.1, in a layered fixed-bed at 473 K and 523 K, respectively. Operating conditions for the simulated breakthrough curves, shown in Figure 4.11 and Figure 4.12a, are the same. It can be seen in Figure 4.12a, that the *n*PEN exits the column later comparatively to the branched C_6 isomers; as a result, it is possible to obtain a product composed only by high RON molecules: *i*PEN, 22DMB, and 23DMB. At the higher temperature of 523 K, the *n*PEN is displaced even more but with the inconvenience of reducing the separation between 23DMB and 3MP (see Figure 4.12b). At both temperatures the RON history of the accumulated product exhibits a maximum of about 92.5 points when the 23DMB breakthroughs. This feature is distinct from the one observed in Figure 4.11, where a column containing just zeolite beta exhibits a monotonic decrease in the product average RON, mainly because of the mixing of *n*PEN with the high RON molecules.

These results demonstrate that the combination of zeolite 5A and zeolite beta can be advantageous for the octane boosting of the gasoline feedstock by properly selecting the operating conditions.

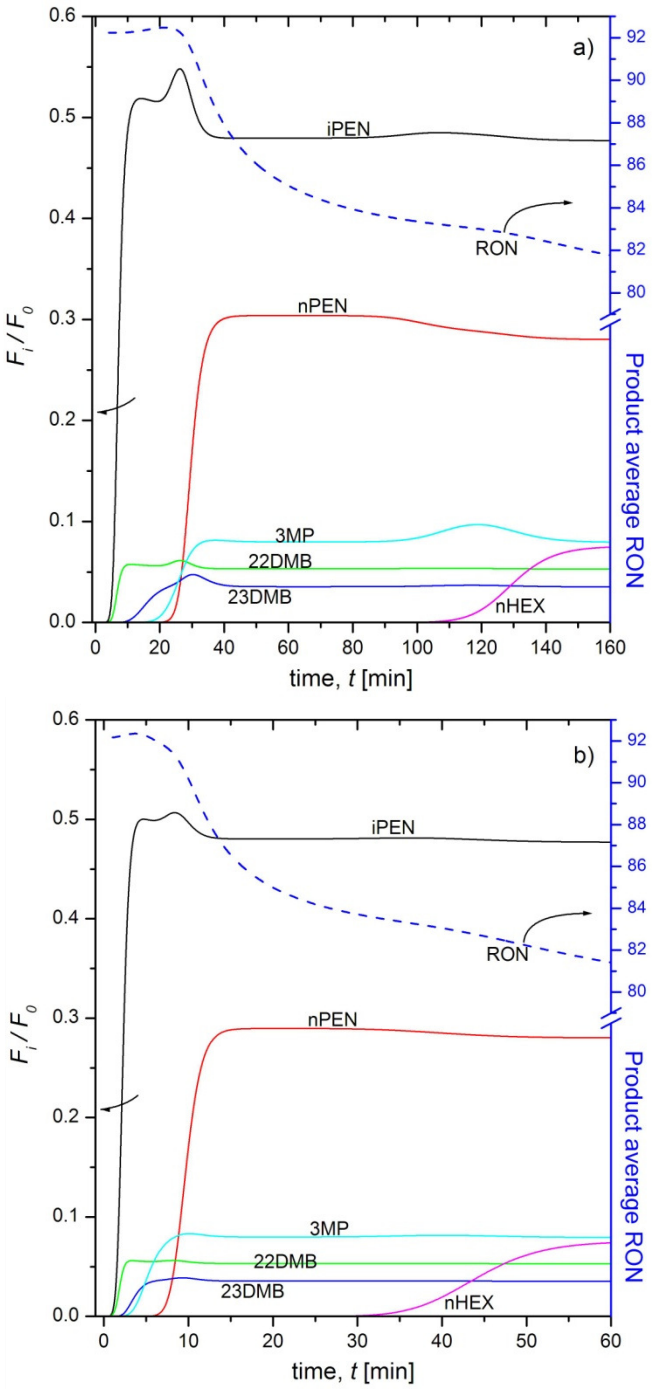


Figure 4.12. Simulation of the six-component breakthrough curve and RON history of the accumulated product for a feed mixture *i*PEN/*n*PEN/22DMB/23DMB/3MP/*n*HEX in a layered bed of zeolite 5A and zeolite beta at p_{mix} = 10.2 kPa: a) at T = 473 K (Run *Lay6_1*); b) at T = 523 K (Run *Lay6_2*). Feed has molar composition of stream 2 in Figure 4.1.

4.6 Conclusions

Multicomponent adsorption experiments of alkanes in the C_5/C_6 range was investigated in commercial pellets of zeolite beta. The TSL isotherm model was used to describe with a good accuracy the complex equilibria of the C_5/C_6 fractions. The six-component breakthrough experiments show that zeolite beta possess interesting properties for the separation of the low RON light naphtha fraction. It was demonstrated that the adsorption equilibrium of the C_6 isomers is more temperature dependent than in the case of the C_5 molecules, allowing the control of the elution order in a C_5/C_6 light naphtha fraction. For instance, at 583 K zeolite beta is able to separate an enriched high RON fraction composed by 22DMB, 23DMB and *i*PEN from an equimolar feed fraction of isomers in the range C_5-C_6. In the case of feed mixtures with the typical composition of the hydroisomerization reactor product, it was demonstrated that the layered bed with zeolite 5A and zeolite beta can significantly enhance the performance of the separation by avoiding the mixing of *n*PEN with the enriched high RON fraction. These results suggest that the ratio of a layered bed of zeolite 5A and zeolite beta and the operating temperature are key parameters to optimize the mono/dibranched separation.

Aspen ADSIM appears to be a very interesting tool for simulating the adsorption dynamics of complex mixtures by making easier the access to the distributed parameters for their graphical monitoring and analysis.

Next chapter will be focused on the simulation of a cyclic process based on the pressure swing adsorption technique using a layered bed of zeolite 5A and zeolite beta in order to improve the quality of the separation.

4.7 References

Aspen Adsim 2004.1 – Adsorption reference guide; Aspen Technology: Cambridge, MA, USA (2005).

Aspen Technology, Inc., http://www.aspentech.com (accessed Dec 2009).

Arumugam, B.K.; Banks, J.F.; Wankat, P.C. Pressure Effects in Adsorption Systems. *Adsorption* 5, 261–278 (1999).

Boerio-Goates, J.; Stevens, R.; Hom, B.K.; Woodfield, B.F.; Piccione, P.M.; Davis, M.E.; Navrotsky, A. Heat Capacities, Third-Law Entropies and Thermodynamic Functions of SiO_2 Molecular Sieves from T = 0 K to 400 K. *J. Chem. Thermodynamics* 34, 205–227 (2002).

Bird, R. B.; Stewart, W. E.; Ligthfoot, E. N. *Transport Phenomena*; Wiley, 1960. 2nd Edition, John Wiley: New York, 2002.

Cusher, N. A. UOP TIP and Once-Through Zeolitic Isomerization Processes. In *Handbook of Petroleum Refining Processes*; Meyers, R. A., Ed.; 3rd Edition, McGraw Hill: New York, Chapter 9, pp 29–39 (2004).

Denayer, J.F.; Souverijns, W.; Jacobs, P.A.; Martens, J.A.; Baron, G.V. High-Temperature Low-Pressure Adsorption of Branched C_5–C_8 Alkanes on Zeolite Beta, ZSM-5, ZSM-22, Zeolite Y, and Mordenite. *J. Phys. Chem. B* 102, 4588–4597 (1998).

Ergun, S. Fluid Flow through Packed Columns. *Chem. Eng. Progr.* 48, 89–94 (1952).

Glueckauf, E. Formulae for Diffusion into Spheres and their Application to Chromatography. *J. Chem. Soc*. 51, 1540–1551 (1955).

Griesinger, A.; Spindler, K.; Hahne, E. Measurements and Theoretical Modelling of the Effective Thermal Conductivity of Zeolites. *Int. J. Heat Mass Transfer* 42, 4363–4374 (1999).

Holcombe, T.C.; Sager, T.C.; Volles, W.K.; Zarchy, A. Isomerisation Process. U.S. Patent 4,929,799 (1990).

Kast, W. *Adsorption aus der Gasphase*; VCH: Weinheim (1988).

Kostroski, K.P.; Wankat, P.C. High Recovery Cycles for Gas Separations by Pressure-Swing Adsorption. *Ind. Eng. Chem. Res.* 45, 8117–8133 (2006).

Kostroski, K.P.; Wankat, P.C. Separation of Dilute Binary Gases by Simulated-Moving Bed with Pressure-Swing Assist: SMB/PSA Processes. *Ind. Eng. Chem. Res.* 47, 3138–3149 (2008).

Liu, H.; Zhang, Z.; Chen, B.H.; Zhao, Y. Comparative Study of Pure Component Adsorption of Linear Alkanes in Zeolites MFI, BEA and MOR. *J. Porous Mater.* 15, 119–125 (2008).

Ruthven, D.M. *Principles of Adsorption and Adsorption Process*; John Wiley & Sons: New York (1984).

Schiesser, W.E. *The Numerical Method of Lines*; Academic Press: San Diego (1991).

Sircar, S.; Cao, D.V. Heat of Adsorption. *Chem. Eng. Technol*. 25, 945–948 (2002).

Silva, J.A.C. Separation of n/iso-Paraffins by Adsorption Process. Ph.D. Thesis, University of Porto, Portugal (1998).

Silva, J.A.C.; Rodrigues, A.E. Separation of n/iso-Paraffins Mixtures by Pressure Swing Adsorption. *Separ. Purif. Tech.* 13, 195–208 (1998).

Wakao, N.; Funazkri, T. Effect of Fluid Dispersion Coefficients on Particle-to-Fluid Mass Transfer Coefficients in Packed Beds: Correlation of Sherwood Numbers. *Chem. Eng. Sci.* 33, 1375–1384 (1978).

Yang, S.I.; Park, J.Y.; Choi, D.K.; Kim, S.H. Effects of the Residence Time in Four-Bed Pressure Swing Adsorption Process. *Separ. Sci. Technol.* 44, 1023–1044 (2009).

5

Separation of C_5/C_6 Light Naphtha by Layered Pressure Swing Adsorption

The performance of a layered pressure swing adsorption (PSA) process for the separation of high research octane number (HRON) paraffins from a C_5/C_6 light naphtha fraction is simulated with a detailed, adiabatic single column PSA model. A zeolite 5A layer is used for selective adsorption of the low RON linear paraffins while a zeolite beta layer is used to separate the intermediate RON 3MP from the HRON fraction. The effects of various independent process variables (zeolite 5A-to-zeolite beta ratio, purge-to-feed ratio, cycle time, operating temperature, and depressurization mode) on the key dependent process variables (product RON, HRON species recovery, HRON purity, and process productivity) are evaluated. It is demonstrated that an optimal zeolite 5A-to-zeolite beta ratio can improve the product average RON up to 1.0 point compared to existing processes using zeolite 5A only. Moreover, process simulations demonstrated that increasing the operating temperature from 523 K to 543 K results in an octane gain of 0.2 RON.

This chapter is based on the following publication:

P.S. Bárcia, J.A.C. Silva, A.E. Rodrigues, (submitted to Energy & Fuels, 2010).

5.1 Introduction

Pressure Swing Adsorption (PSA) processes have been successfully employed for the separation of gases such as air into nitrogen and oxygen, water removal from air, hydrogen purification, and *n*-paraffins separation. The basic concepts and developments of the PSA technique are generally described in several reference books (Ruthven, 1984; Ruthven et al., 1994; Suzuki, 1990; Wankat, 1986; Yang, 1987). The original idea of using pressure swing to separate gases was disclosed in a patent by Skarstrom (1960). Basically, two adsorbent beds are operated in a staggered manner, with each bed repeatedly undergoing a sequence of steps, such as pressurization, adsorption, blowdown, and desorption, in such a way that a nearly continuous flow of product is obtained. The Skarstrom PSA cycle was immediately accepted for commercial application in air drying. Afterwards, many process improvements have been developed, for instance, vacuum desorption blowdown (de Montgareuil and Domine, 1964), co-current depressurization (Kiyonaga, 1965), or pressure equalization (Marsh et al., 1964).

Fewer commercial applications of PSA have been realized for the separation of paraffins. One notable exception is the *IsoSiv* process (Cusher, 2004b) which uses zeolite 5A to remove linear paraffins from the light straight-run (LSR) naphtha. Other variations of the *IsoSiv* process have been developed as part of commercial processes for the octane upgrading of the LSR naphtha, some examples are the Total Isomerisation Process (TIP) from UOP (Cusher, 2004a), and more recently, the *Ipsorb* process (Minkkinen et al., 1993; Deschamps and Jullian, 2000) from Axens. These processes combine a hydroisomerization reactor for the conversion of linear molecules into branched ones, and a separation unit for the recycling of low RON components (see also chapter 1). Most patent applications in the field are assigned to UOP (Holcombe, 1979, 1980; Holcombe et al., 1990; Volles, 1992), and IFP (Minkkinen et al., 1993). Despite the major relevance of this industrial separation process, the experimental and modelling work of Silva (1998) is, as far as our knowledge goes, one

of the few examples in the literature, which deepened the application of the PSA process to the separation of *n*-paraffins from a mixture containing *n*HEX, *n*PEN, and *i*PEN with zeolite 5A. The study of Silva was performed using data from a patent assigned to IFP, where a lab-scale unit operates at 573K with a high-pressure of 15 bar and low-pressure of 2 bar and total cycle time 12 min (panel *a* of Figure 5.1). Desorption is performed by purging the adsorber with an *i*PEN stream produced from

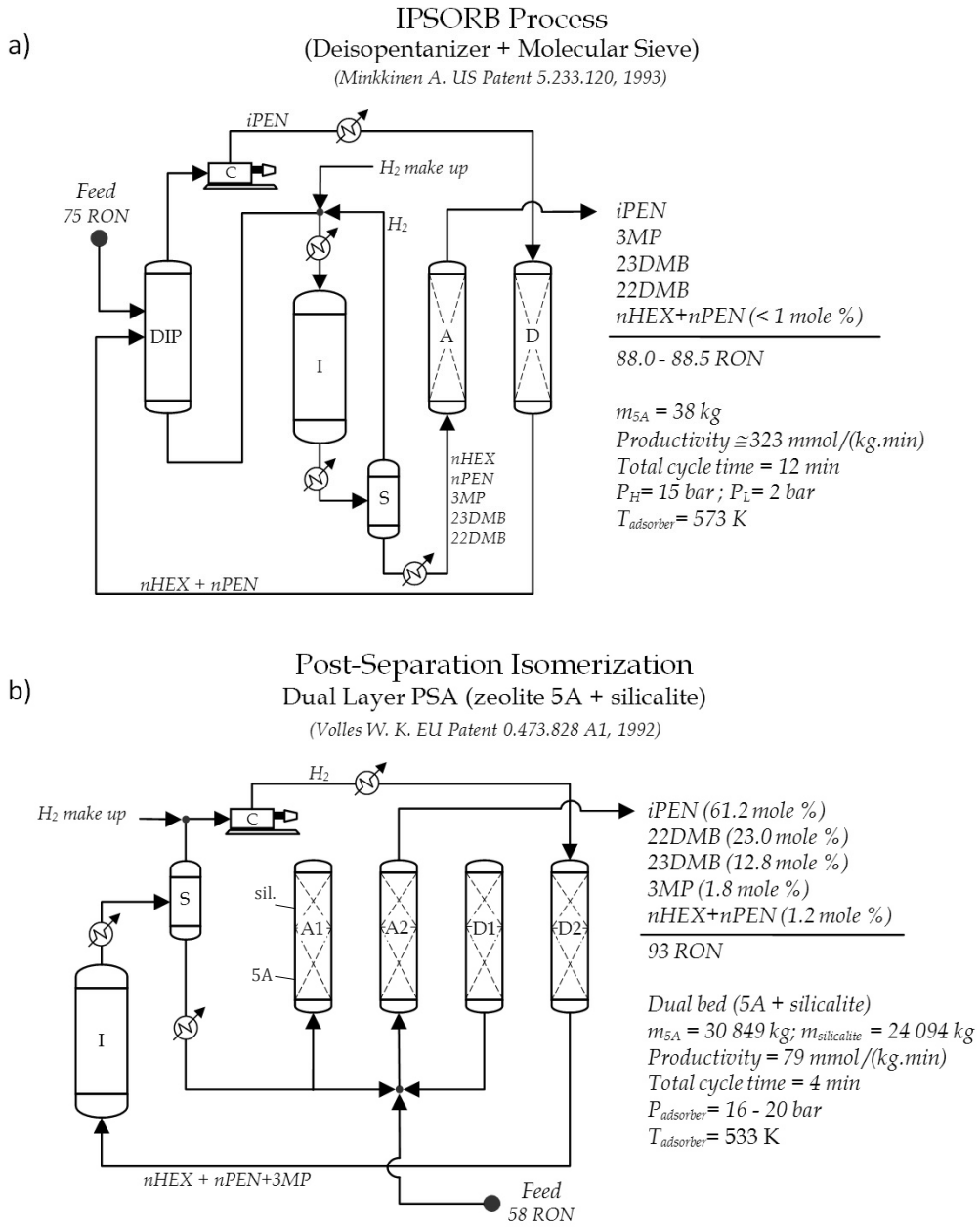


Figure 5.1. Schematic diagram and details of the product obtained through the process disclosed by a) Minkkinen et al (1993), and b) Volles (1992).

a deisopentanizer (DIP) column. The huge adsorbent productivity of the *Ipsorb* process, 323 mmol/(min·kg_{ads}) (productivity along the text is calculated based on the production of 22DMB, 23DMB, 3MP, *n*HEX, *i*PEN, and *n*PEN), is mainly achieved thanks to the energy-intensive DIP column, and also to the detriment of the RON gain in the final product; there is only a difference of 13 RON between the DIP feed and the adsorber product (streams average RON is calculated considering only the contribution of 22DMB, 23DMB, 3MP, *n*HEX, *i*PEN, and *n*PEN). The ability of zeolite 5A in removing the *n*-paraffins from their branched isomers is remarkable; the *n*/iso alkane sorption selectivity is practically infinite (Silva, 1998). However, to meet the octane targets for the modern gasoline, it is also required to separate monobranched hexanes from the isomerate mixture. For this, Volles (1992) proposed an interesting variation of the PSA process by using two adsorbents, zeolite 5A and silicalite, placed as layers in the bed, as shown in Figure 5.1 b). The role of the silicalite layer is to reduce the concentration of LRON monobranched alkanes in the enriched fraction. The high octane gain claimed in the patent comes from the low productivity of the adsorbent, approximately 79 mmol/(min·kg_{ads}). One of the drawbacks of this scheme is the significant amount of HRON *i*PEN recycled to the hydroisomerization reactor, due to its relatively strong adsorption in the silicalite; unlike zeolite beta which discriminates between *i*PEN and *n*PEN (see chapter 4), in the silicalite the adsorption strengths towards these isomers are similar at low and medium coverage (Schenk et al., 2001; Calero et al., 2001).

Despite the fast growth in the industrial applications of PSA, the design and optimization of a practical PSA scheme still remains a complex and expensive task (Sircar, 2002). However, with the recent development of powerful adsorption simulation packages, such as Aspen Adsim (Aspen Technology), gPROMS (Process System Enterprise Limited), or even the home-made simulator developed at LSRE by da Silva (1999), it becomes possible to perform efficient PSA simulations that can replace many expensive and time-consuming laboratory and pilot-scale studies (da Silva et al., 1999; Kostroski and Wankat, 2006; Ribeiro et al, 2008; Warmuziński and Tańczyk, 1997). The rigorous mathematical model presented in chapter 4, can be used now for a

rapid evaluation of innovative designs that can improve the separation of C_5/C_6 naphtha fractions, in order to achieve the octane upgrading of the final product.

5.2 Study of a Single Column Layered PSA Cycle

5.2.1 PSA Process Description

It was demonstrated in the previous chapter, that a layered fixed bed of zeolite 5A and zeolite beta can be used to produce an enriched fraction, mainly consisting of HRON molecules *i*PEN, 22DMB, and 23DMB, from a C_5/C_6 light naphtha fraction. In this chapter, dynamic simulation will be used to study the performance of the layered bed in a single column PSA cycle. The proposed scheme is in part based on the separation section of the TIP described by Cusher (2004a) (see Figure 5.2, and also chapter 1), but incorporates some specifications of the schemes disclosed by Minkkinen et al (1993), and Volles (1992).

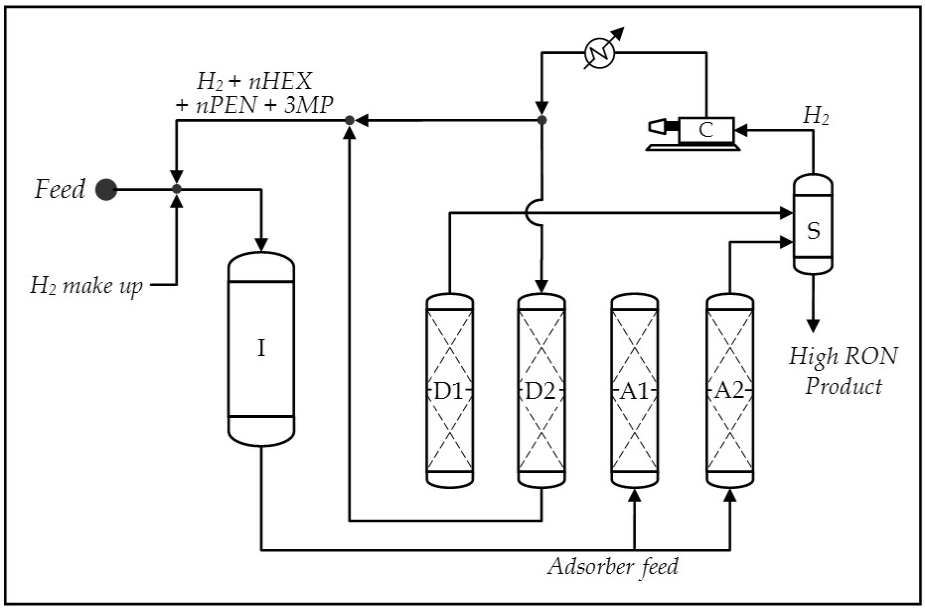


Figure 5.2. Proposed scheme: *TIP* process incorporating a dual-layer PSA unit.

The composition and flowrate of the adsorber feed are based on typical specifications from a 10,000 BPD UOP commercial unit, and is also given by Cusher (2004a). The design of the adsorbent column is based on specifications for commercial units, described in two patents assigned to UOP. The total mass of adsorbent per bed, 54.9 tons, is given by Volles (1992), and the adsorbent column diameter, 3.66 m, is given by Holcombe (1980) for a typical TIP unit. The adsorbent bed consists of a zeolite 5A layer placed at the feed end, and a zeolite beta layer above the zeolite 5A layer. A bulk porosity of approximately 0.35 is typically achieved for 1/16" pellets, using the *Catapac*

Table 5.1. Operating parameters common to all simulations for the layered PSA, and properties of zeolite 5A (Silva, 1998), and zeolite beta (this work).

Column:			
Internal bed diameter, d_B		36.6	cm
Bed length, L_B		67.7	cm
Bulk porosity, ε_b		0.35	-
Adsorber feed flowrate		1.6	kmol/hr
Adsorber feed molar composition:	22DMB	3.70	mol %
	23DMB	1.85	mol %
	3MP	4.60	mol %
	*n*HEX	4.45	mol %
	*i*PEN	22.05	mol %
	*n*PEN	13.35	mol %
	H_2	50.00	mol %
Absorber feed RON		76.9	-
High-pressure, P_H		5	bar
Low pressure, P_L		1	bar
Adsorbents:	*zeolite 5A*	*zeolite beta*	
Pellet diameter, d_p	1.59×10^{-3}	1.59×10^{-3}	m
Macropore radius, r_{pore}	8.50×10^{-8}	3.75×10^{-8}	m
Adsorbent heat capacity, C_{ps}	0.865 §	0.865 §	kJ/kg/K
Adsorbent thermal conductivity, k_s	0.3 †	0.3 †	W/m/K
Apparent density of pellet, ρ_p	1.13×10^{3}	1.18×10^{3}	kg/m^3
Pellet porosity, ε_p	0.35	0.40	–

§ Taken from Boerio-Goates et al. (2002).

† Taken from Griesinger et al. (1999).

technology from Axens, which ensures homogenous dense loading (http://www.axens.net). The adsorbent properties are the same than those used in chapter 4. The data for zeolite 5A were taken from the work of Silva (1998). The corresponding values are reported in Table 5.1.

In order to operate in the range of partial pressure covered in the adsorption equilibrium study of C_5/C_6 isomers mixtures (see chapter 4) it is necessary to scale down the process. Accordingly, both the volume of the column and the adsorber feed flowrate were reduced 1000 times. The operating pressures used in the *Ipsorb* process for the feed step (15 bar) and the purge step (5 bar) were reduced to 5 bar (P_H) and 1 bar (P_L), respectively. The characteristics of the column are reported in Table 5.1.

In this PSA study, it is assumed that the adsorber feed comes directly from the hydroisomerization reactor without previous H_2 separation stage. Accordingly, the temperature of the adsorber feed was fixed to 523 K, which is a typical value for hydroisomerization reactors operating with zeolite-based catalysts. It was also assumed a molar ratio hydrocarbon/hydrogen equal to 1 in the adsorber feed. As it was shown in chapter 3, the mono-/dibranched selectivity in zeolite beta increases as the partial pressure decreases. Consequently, the adsorption properties of zeolite beta might be energetically advantageous for the proposed scheme, compared to the *Ipsorb* process, where the intermediate H_2 separation stage requires the subsequent vaporization of the hydrocarbon adsorber feed.

The steps sequence for the proposed scheme is similar to the one used in the *Ipsorb* process, with the exception of including a co-current depressurization (COD) step. The COD step was implemented for the first time in an *IsoSiv* plant in Texas in 1961 (Yang, 1987). The COD allows flow out of the bed in the adsorption flow direction. The major function of the COD step is to increase the product recovery of the weak adsorptive (HRON components), which in turn enhances the purity of the strong adsorptive (LRON components) in the recycled stream. The 4-steps of the PSA cycle are:

- *Pressurization (column A1 in Figure 5.2):* the adsorbent column, mainly filled with H_2, is pressurized with the feed mixture. The pressure in the column is raised from P_L to P_H (see also Figure 5.3);
- *Feed (column A2 in Figure 5.2):* the feed mixture at pressure P_H is passed through the layered bed, and a HRON enriched fraction at pressure $\approx P_H$ is withdrawn through the product end (see Figure 5.3);
- *Co-current depressurization (column D1 in Figure 5.2):* the column is then co-currently depressurized from P_H to P_L. Part of the weakly adsorbed HRON molecules are desorbed, increasing in this manner the gas phase HRON fraction, which is withdrawn through the product end (see Figure 5.3);
- *Countercurrent H_2 purge (column D2 in Figure 5.2):* the column is countercurrent-tly purged at P_L using a H_2 stream. The effluent mainly consisting of LRON components and H_2 is recycled to the hydroisomerization reactor (see Figure 5.3).

The performance of the proposed scheme will be compared with the *Ipsorb* PSA cycle which uses countercurrent depressurization (CTD). For this, a CTD step will be simulated for the case where the adsorber contains only zeolite 5A. Panel *a* of Figure 5.3 shows the sequence of the 4-step PSA cycle with CTD, while panel *b* represents the 4-step PSA cycle with COD. It should be noted that the production step of the first cycle is limited to the feed step, whereas in the second case the enriched fraction is produced during feed and COD steps.

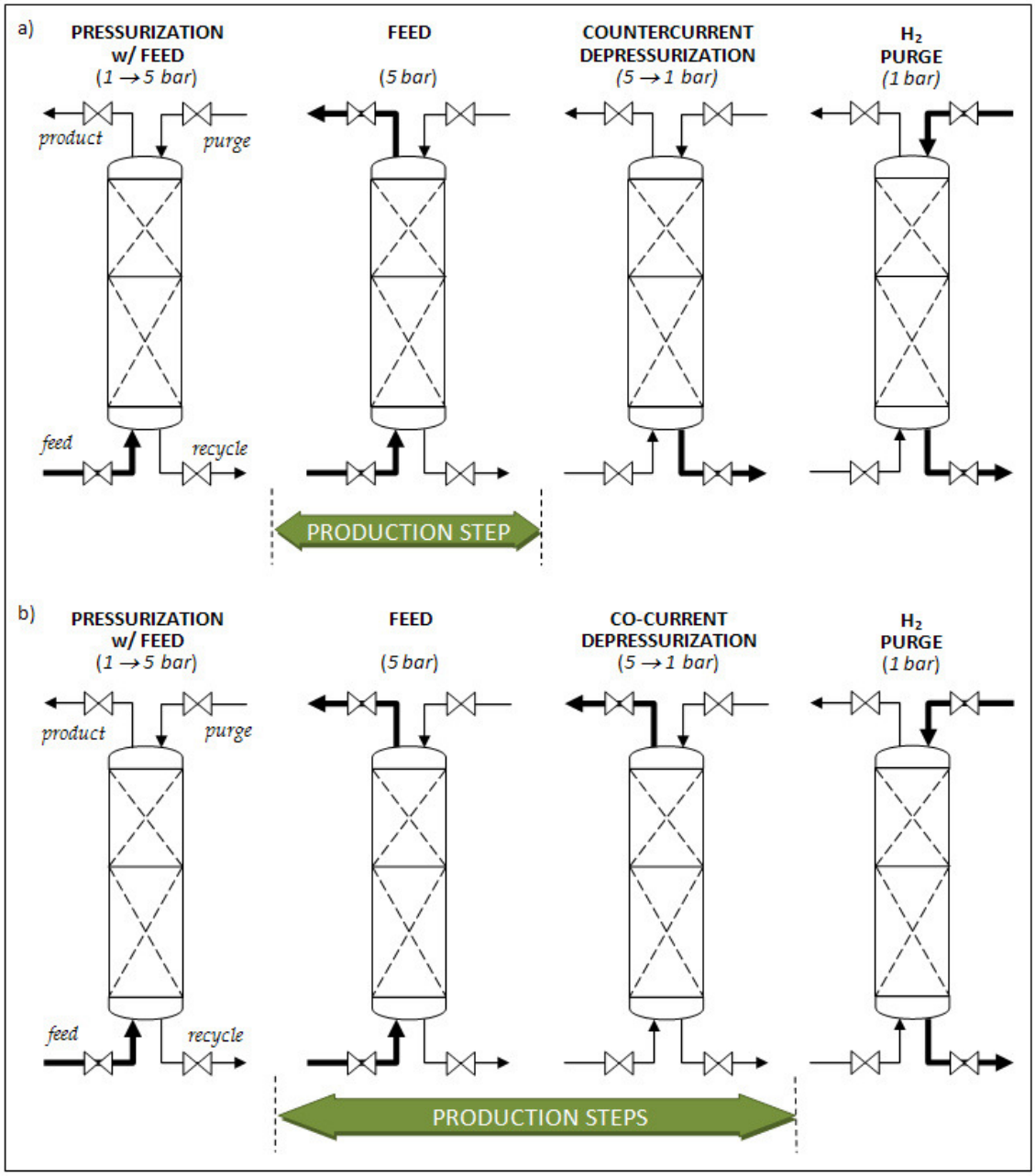


Figure 5.3. Sequence of the 4-steps PSA cycle with (a) countercurrent and (b) co-current depressurization mode.

5.2.2 Definition of the Parametric Study

The performance of the PSA cycle with a layered bed depends on several process variables, such as the fraction of zeolite 5A in the column, which is defined here as,

$$L_{5A}/L_B = \frac{zeolite\ 5A\ layer\ lenght}{total\ bed\ lenght} \quad (5.1)$$

and the purge-to-feed ratio,

$$P/F = \frac{Amount\ of\ H_2\ used\ in\ purge\ step}{Amount\ of\ gas\ fed\ in\ pressurization\ and\ feed\ step} \quad (5.2)$$

Table 5.2. Map of the parametric study for the optimization of the process.

L_{5A}/L_B	P/F	$t_{feed} = t_{purge}$	T	DPR
0.0				
0.2	1.0	80 s	523 K	COD
0.33				
0.5	1.25			
0.67				
0.8	1.5	60 s	543 K	CTD
1.0				

Others variables which can influence the process performances are the time of feed step (t_{feed}), and the operating temperature. To elucidate about the effect of these variables, it was created a parametric study, whose map and corresponding values are listed in Table 5.2. First, the range of *P*/*F* ratios was simulated for the different values of L_{5A}/L_B. Then, the intermediate *P*/*F* ratio was simulated for a shorter time of feed step. Finally, the effect of the temperature was addressed by repeating the simulations at t_{feed} = 60 s, but for *T* = 543 K.

5.2.3 Process Performance Criteria

The main products of the conventional recycling schemes for isomerization processes are the monobranched and dibranched C_5/C_6 paraffins. In the process herein disclosed, the HRON molecules (*i*PEN, 22DMB, and 23DMB) are the desired product. Accordingly, the performance of the PSA cycle with COD step will be assessed by the following parameters:

$$Product\ RON = Accumulated\ product\ average\ RON \tag{5.3}$$

$$HRON\ recovery\ (molar\ basis) = \frac{Amount\ of\ HRON\ withdrawn\ in\ production\ steps}{Amount\ of\ HRON\ fed} \tag{5.4}$$

$$Adsorbent\ productivity = \frac{Amount\ of\ paraffins\ withdrawn\ in\ production\ steps}{Mass\ of\ adsorbent \times Time\ of\ production\ step} \tag{5.5}$$

Alternatively to the *Product RON*, octane quality can also be defined by the product purity as follows,

$$HRON\ purity\ (molar\ basis) = \frac{HRON\ withdrawn\ in\ production\ step}{Paraffins\ withdrawn\ in\ production\ step} \tag{5.6}$$

By analogy, other performance criteria relevant for the process are,

$$Recycle\ RON = Accumulated\ recycle\ average\ RON \tag{5.7}$$

$$LRON\ recovery\ (molar\ basis) = \frac{LRON\ recovered\ in\ purge\ step}{LRON\ fed\ in\ pressurization\ and\ feed\ steps} \tag{5.8}$$

$$LRON\ purity\ (molar\ basis) = \frac{LRON\ recovered\ in\ purge\ step}{Paraffins\ recovered\ in\ purge\ step} \tag{5.9}$$

5.3 Model Development

The model used to study the single column PSA cycle is implemented within Aspen Adsim 2006.5 (Aspen, 2005) using a flowsheet (Figure 5.4) consisting of five different types of blocks: feed (F1 and F2), product (P1 and P2), valves (VF1, VF2, VP1, and VP2), bed (B1), and void tank (1 and 2). The behaviour of each block is described by a model. The connections between blocks are used to pass information about material flowrate, composition, temperature, and pressure.

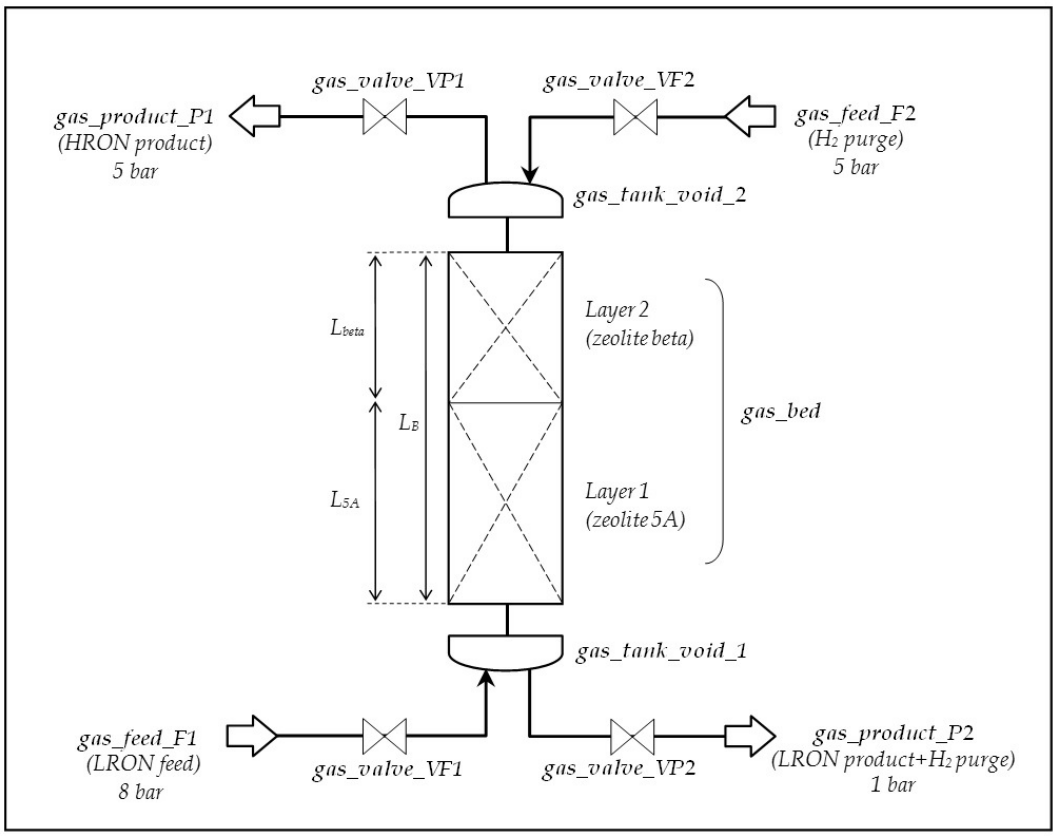


Figure 5.4. Schematic diagram of the single layered bed PSA with input/output streams and *gas_model* blocks used for the Aspen Adsim simulations.

5.3.1 Feed Model

The feed model (F1 and F2) is used as a flowsheet inlet boundary unit, where the stream composition, pressure, and temperature are specified, while the flowrate is set as a free variable. The model simulates in this way, a constant pressure reservoir with a given composition and temperature. Based on the feed pressure and the column inlet pressure, the feed valve unit (VF1 and VF2) determines the inlet flowrate. The feed pressure of units F1 and F2 was set to 8 bar and 5 bar, respectively.

5.3.2 Valve Model

The flowrate through the valve is approximated by the valve model to a linear function of the pressure drop across the valve:

$$F = C_v(P_{IN} - P_{OUT}) \tag{5.10}$$

where F is the molar flowrate through the valve, P_{IN} and P_{OUT} are the pressure upstream and downstream the valve, respectively. The value of the linear valve constant C_v for a pressurization step can be estimated through the following expression,

$$C_v = \frac{V_B}{RT\, t_{press}} \ln\left(\frac{P_{OUT}^i - P_{IN}}{P_{OUT}^f - P_{IN}}\right) \tag{5.11}$$

where V_B is the effective volume of the bed, t_{press} is the time of pressurization step, P_{OUT}^i and P_{OUT}^f are the initial and final pressure in the column, respectively. Accordingly, for a depressurization step we have,

$$C_v = \frac{V_B}{RT\, t_{dpress}} \ln\left(\frac{P_{IN}^i - P_{OUT}}{P_{IN}^f - P_{OUT}}\right) \tag{5.12}$$

where t_{dpress} is the time of depressurization step. It was assumed for all the simulations $t_{press} = t_{dpress} = 20\,s$.

5.3.3 Tank Void Model

The tank void model uses well mixed tank assumption for simulating absorbent bed dead spaces, tanks, pressure receivers or piping nodes. The volume of the void tanks was set to its minimum value (1×10^{-5} m^3) which corresponds approximately to 0.01 % of the volume of the adsorption column.

5.3.4 Product Model

The product model (P1 and P2) is used as a flowsheet outlet boundary unit which receives material from the flowsheet. Similarly to the feed model, the product model simulates a constant pressure reservoir, being the corresponding flowrate determined by the outlet valve unit (VP1 and VP2), based on the column outlet pressure. The pressure for unit P1 was set to 5 bar during feed step, and 1 bar during depressurization step. Unit P2 was set to 1 bar pressure.

5.3.5 Bed Model

The model used in chapter 4 to predict the adsorption dynamics of a C_5/C_6 light naphtha fraction in a layered bed of zeolite 5A and zeolite beta will be used here for the parametric study of the layered PSA. However, it is considered here the adiabatic condition, which is nearly approached in industrial large-size units. Consequently, the wall energy balance is not included in the model equations. Table 5.3 summarizes the mathematical model.

The bed is initially filled with pure H_2, and the thermal equilibrium between the feed stream and the adsorbent column is assumed. The boundary conditions are formulated separately for each single PSA step. For the feed end (z = 0) and the product end ($z = L_B$) the boundary conditions can be written as shown in Table 5.4.

Table 5.3. Mathematical model for the study of the layered bed PSA cycle.

Ideal gas law	$Py_i = RT_g c_i$
Mass balance to sorbate species	$-\varepsilon_b D_{ax}\frac{\partial^2 c_i}{\partial z^2}+\frac{\partial(v_g c_i)}{\partial z}+\varepsilon_t\frac{\partial c_i}{\partial t}+\rho_b\frac{\partial \overline{q}_i}{\partial t}=0$
Axial dispersion	$D_{ax}=0.73D_m+\frac{v_g R_p}{\varepsilon_b\left(1+9.49\varepsilon_b D_m/2v_g R_p\right)}$
Momentum balance (Ergun's equation)	$-\frac{\partial P}{\partial z}=\frac{1.5\times10^{-3}(1-\varepsilon_b)^2}{(2R_p)^2\varepsilon_b^3}\mu v_g+1.75\times10^{-5}M_W\rho_g\frac{(1-\varepsilon_b)}{2R_p\varepsilon_b^3}v_g^2$
Mass transfer rate to the solid	$\frac{\partial \overline{q}_i}{\partial t}=k_{MTC_i}\left(q_i^*-\overline{q}_i\right)$
LDF coefficient	$\frac{1}{k_{MTC_i}}=\frac{R_p\overline{K}_{Ki}}{3k_{fi}}+\frac{R_p^2\overline{K}_{Ki}}{15\varepsilon_p D_{pi}}$; $\quad\overline{K}_{Ki}=RT\frac{\rho_b}{\varepsilon_b}\frac{\partial q_i^*}{\partial p_i}$; $D_{p_i}=\left(\Gamma_p\left(D_{K_i}^{-1}+D_{m_i}^{-1}\right)\right)^{-1}$; $\quad D_{K_i}=97\,r_{pore}\left(T/M_{W\,i}\right)^{0.5}$ †
Multicomponent adsorption equilibrium	zeolite 5A (Nitta model)§: $\theta_i=b_i p_i\left(1-\sum_{i=1}^{N}\theta_i\right)^{n_i}$; $\quad\theta_i=q_i/q_i^m$; $\quad b_i=b_i^0 e^{(-E_i/RT_S)}$ zeolite beta (TSL model): $q_i=\sum_j\frac{q_{i,j}^m b_{i,j}p_i}{1+\sum_{i=1}^{N}b_{i,j}p_i}$; $\quad b_{i,j}=b_{i,j}^0 e^{(-E_{i,j}/RT_S)}$ with $j=S,Z,I$
Gas phase energy balance	$-\varepsilon_b k_{gz}\frac{\partial^2 T_g}{\partial z^2}+v_g C_{vg}\rho_g\frac{\partial T_g}{\partial z}+\varepsilon_t C_{vg}\rho_g\frac{\partial T_g}{\partial t}$ $+P\frac{\partial v_g}{\partial z}+h_p a_p(T_g-T_s)=0$
Solid phase energy balance	$-k_{sz}\frac{\partial^2 T_s}{\partial z^2}+c_{ps}\rho_b\frac{\partial T_s}{\partial t}+\rho_b\sum_{i=1}^{n}\left(q_{st_i}\frac{\partial \overline{q}_i}{\partial z}\right)-h_p a_p\left(T_g-T_s\right)=0$ Zeolite 5A: $q_{st\,i}=-E_i$ Zeolite beta: $q_{st\,i}=\left[\sum_j\frac{-E_{i,j}q_{i,j}^m b_{i,j}}{\left(1+b_{i,j}p_i\right)^2}\right]/\left[\sum_j\frac{q_{i,j}^m b_{i,j}}{\left(1+b_{i,j}p_i\right)^2}\right]$
External mass transfer coefficient	$k_f=Sh_i D_{m_i}/2R_p$; $Sh_i=2.0+1.1Sc_i^{1/3}Re^{0.6}$
Gas-solid heat transfer coefficient	$h_p=j\rho_g C_{pg}v_g\,\mathrm{Pr}^{-2/3}$; $j=1.66\mathrm{Re}^{-0.51}$ *if* $\mathrm{Re}<190$ *or* $j=0.983\mathrm{Re}^{-0.41}$ *if* $\mathrm{Re}>190$

† r_{pore} is expressed in meters.

§ Equilibrium data taken from Silva (1998).

Table 5.4. Boundary conditions associated with the 4-steps of the PSA cycle.

STEP 1	*Pressurization with Feed*	
	Inlet, $z = 0$	$z = L_B$
	$P\big\|_{z=0} = P_{inlet}$	$v_g\big\|_{z=L_B} = 0$
	$D_{ax}\left.\frac{\partial c_i}{\partial z}\right\|_{z=0} = -v_g\big\|_{z=0}\left(c_i\big\|_{z=0^-} - c_i\big\|_{z=0}\right)$	$\left.\frac{\partial c_i}{\partial z}\right\|_{z=L_B} = 0$
	$k_{gz}\left.\frac{\partial T_g}{\partial z}\right\|_{z=0} = -\rho_g C_{pg} v_g\big\|_{z=0}\left(T_g\big\|_{z=0^-} - T_g\big\|_{z=0}\right)$	$\left.\frac{\partial T_g}{\partial z}\right\|_{z=L_B} = 0$
STEP 2	*High Pressure Feed*	
	Inlet, $z = 0$	Outlet, $z = L_B$
	$v_g\big\|_{z=0} = v_g\big\|_{z=0^-}$	$P\big\|_{z=L_B} = P_{exit}$
	$D_{ax}\left.\frac{\partial c_i}{\partial z}\right\|_{z=0} = -v_g\big\|_{z=0}\left(c_i\big\|_{z=0^-} - c_i\big\|_{z=0}\right)$	$\left.\frac{\partial c_i}{\partial z}\right\|_{z=L_B} = 0$
	$k_{gz}\left.\frac{\partial T_g}{\partial z}\right\|_{z=0} = -\rho_g C_{pg} v_g\big\|_{z=0}\left(T_g\big\|_{z=0^-} - T_g\big\|_{z=0}\right)$	$\left.\frac{\partial T_g}{\partial z}\right\|_{z=L_B} = 0$
STEP 3	*Co-current Depressurization (COD)*	
	$z = 0$	Outlet, $z = L_B$
	$v_g\big\|_{z=0} = 0$	$P\big\|_{z=L_B} = P_{exit}$
	$\left.\frac{\partial c_i}{\partial z}\right\|_{z=0} = 0$	$\left.\frac{\partial c_i}{\partial z}\right\|_{z=L_B} = 0$
	$\left.\frac{\partial T_g}{\partial z}\right\|_{z=0} = 0$	$\left.\frac{\partial T_g}{\partial z}\right\|_{z=L_B} = 0$
	or *Countercurrent Depressurization (CTD)*	
	Outlet, $z = 0$	$z = L_B$
	$P\big\|_{z=0} = P_{exit}$	$v_g\big\|_{z=L_B} = 0$
	$\left.\frac{\partial c_i}{\partial z}\right\|_{z=0} = 0$	$\left.\frac{\partial c_i}{\partial z}\right\|_{z=L_B} = 0$
	$\left.\frac{\partial T_g}{\partial z}\right\|_{z=0} = 0$	$\left.\frac{\partial T_g}{\partial z}\right\|_{z=L_B} = 0$
STEP 4	*Low Pressure Purge (countercurrent)*	
	Outlet, $z = 0$	Inlet, $z = L_B$
	$P\big\|_{z=0} = P_{exit}$	$v_g\big\|_{z=L_B} = v_g\big\|_{z=L_B^+}$
	$\left.\frac{\partial c_i}{\partial z}\right\|_{z=0} = 0$	$D_{ax}\left.\frac{\partial c_i}{\partial z}\right\|_{z=L_B} = v_g\big\|_{z=L_B}\left(c_i\big\|_{z=L_B^+} - c_i\big\|_{z=L_B}\right)$
	$\left.\frac{\partial T_g}{\partial z}\right\|_{z=0} = 0$	$k_{gz}\left.\frac{\partial T_g}{\partial z}\right\|_{z=L_B} = \rho_g C_{pg} v_g\big\|_{z=L_B}\left(T_g\big\|_{z=L_B^+} - T_g\big\|_{z=L_B}\right)$

5.3.6 Cycle Organizer

The steps which define the cyclic operation of the PSA process can be created in Adsim by using the *Cycle Organizer* option. This option can be used to generate an unlimited number of cycle descriptions. The user can also define an unlimited number of steps in a cycle, establishing at the same time how the step will be controlled, i.e., time driven, or discrete event driven (Figure 5.5).

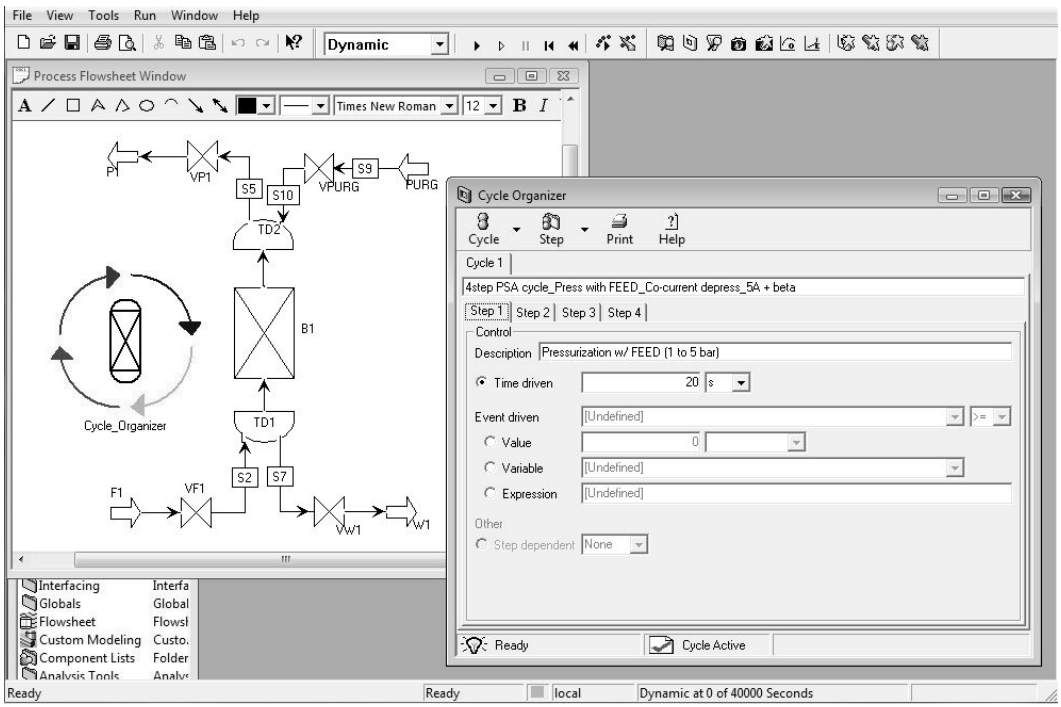
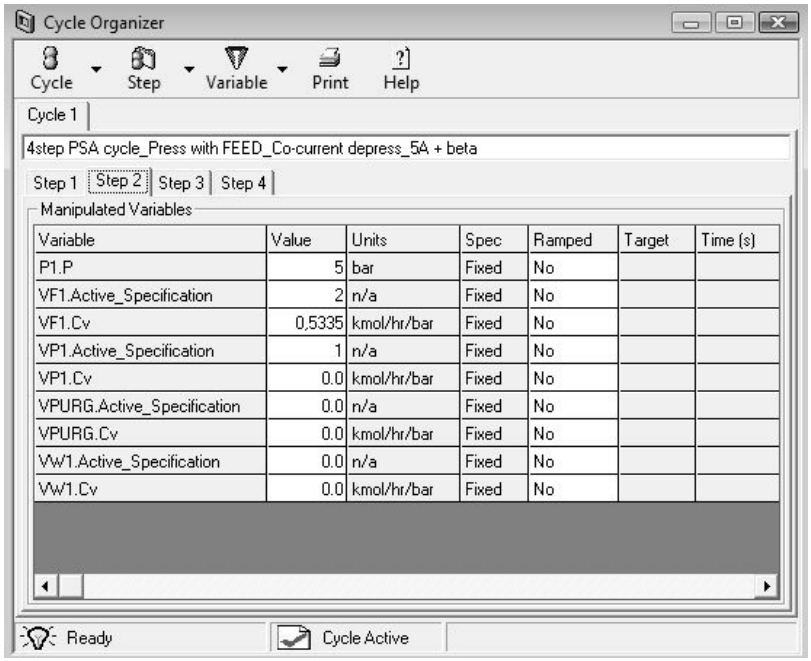


Figure 5.5. Cycle organizer: Steps and cycle description.

The *Cycle Organizer* option allows also the user to define which variables are to be manipulated, for instance, change in boundary conditions such as flowrate, composition, or pressure. The variable can be changed to the defined value in one integration step, or by using a ramp function (linear, or sinusoidal ramp). The example in Figure 5.6 shows the variable manipulated when the feed step starts: valve VP1 is fully open, and the linear valve constant for VF1 is set to 0.5335 kmol/hr/bar.



Variable	Value	Units	Spec	Ramped	Target	Time (s)
P1.P	5	bar	Fixed	No		
VF1.Active_Specification	2	n/a	Fixed	No		
VF1.Cv	0,5335	kmol/hr/bar	Fixed	No		
VP1.Active_Specification	1	n/a	Fixed	No		
VP1.Cv	0.0	kmol/hr/bar	Fixed	No		
VPURG.Active_Specification	0.0	n/a	Fixed	No		
VPURG.Cv	0.0	kmol/hr/bar	Fixed	No		
VW1.Active_Specification	0.0	n/a	Fixed	No		
VW1.Cv	0.0	kmol/hr/bar	Fixed	No		

Figure 5.6. Cycle organizer: Manipulated variables. Example given for step 2 (feed).

The *Cycle Organizer* contains a *Cyclic Steady State Testing* box which allows testing when the simulation has reached a cyclic steady state (CSS). A relative tolerance has to be defined for this option. During the simulation, the total loading and solid temperature at the end of each cycle are compared to the value of the previous cycle; when their relative difference is below the defined tolerance, the simulation pauses. In this work, the relative tolerance of the *Cyclic Steady State Testing* was set to 1×10^{-4}.

5.3.7 Numerical Methods

The set of equations was numerically solved using Aspen Adsim 2006.5. Adsim uses the method of lines (Schiesser, 1991) to solve the time-dependent partial differential equations. The spatial derivatives were discretized over a uniform grid of 42 points by the upwind differencing scheme (UDS) in conjunction with the Gear integration with variable step size of 0.01–5 s.

The physical properties of the components in the process are locally estimated through integration with the Aspen Properties database.

5.4 Results and Discussion

In this section, the results obtained for the simulation of the single column PSA process are presented. First, the general behaviour of the system will be discussed considering the results of one simulation. Afterwards, the effect of several variables on the process performances will be evaluated.

5.4.1 Layered PSA –General Dynamics

The pressure and molar rates history obtained at the column outlet during one cycle in cyclic steady state (CSS) is shown in Figure 5.7. The simulation refers to the run which offers the best result in terms of product RON *(Run_32).* The operating conditions for all the simulations are listed in Table 5.5.

It can be seen from Figure 5.7 that the COD step causes a sharp increase of the molar flow at the bed outlet, which in principle, breathes out a large amount of molecules from the gas phase, as well as, weakly adsorbed molecules from the zeolite beta layer.

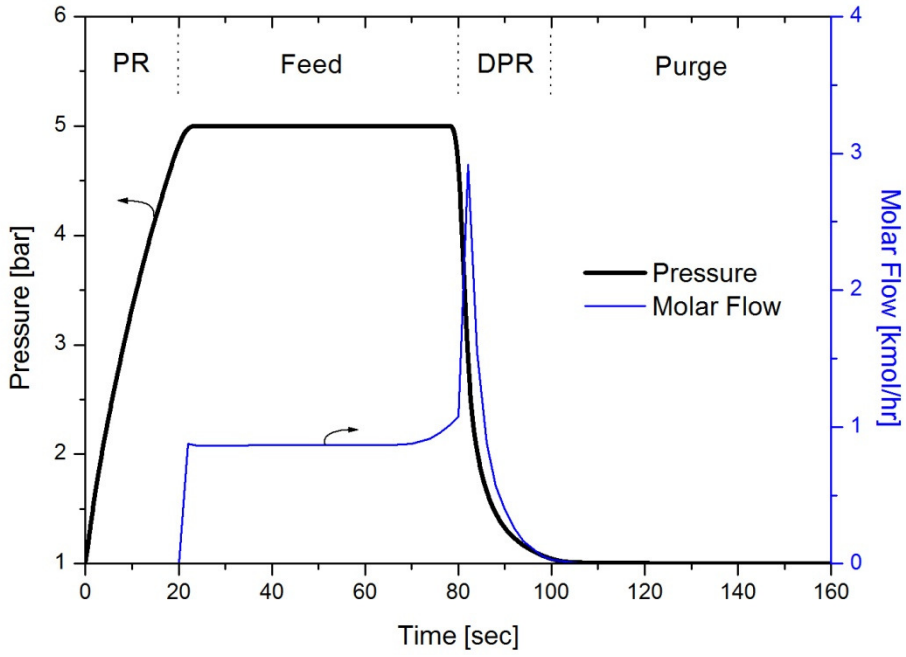


Figure 5.7. Historical of the pressure and molar flow obtained at the column outlet at CSS (*Run_32*).

Table 5.5. Operating conditions and process performance of the PSA cycles simulated. (pressurization with feed, t_{press} = t_{dpress} = 20 s, t_{feed}= t_{purge})

Run	*T* (K)	*DPR*	t_{press} (s)	t_{feed} (s)	P/F	L_{5A}/L_B	HRON purity (%)	HRON recovery (%)	Adsorbent productivity (mmol/min/kg)	Product RON (-)	LRON purity (%)	LRON recovery (%)	Recycle RON (-)
A	523	CTD	20	80	1.0	1.0	99.4	87.5	137.6	90.16	84.1	80.8	59.47
B	523	CTD	20	80	1.25	1.0	99.9	87.3	137.4	90.32	83.9	80.5	59.55
C	523	CTD	20	80	1.5	1.0	100.0	87.1	138.2	90.34	83.8	80.7	59.61
1	523	COD	20	80	1.0	0.0	63.4	26.0	51.0	80.51	47.2	79.5	75.79
2	523	COD	20	80	1.0	0.2	68.4	45.3	82.8	82.99	52.4	72.3	73.30
3	523	COD	20	80	1.0	0.33	74.3	50.9	85.9	85.44	56.5	76.4	71.59
4	523	COD	20	80	1.0	0.5	81.9	55.0	84.5	88.44	60.7	83.2	69.95
5	523	COD	20	80	1.0	0.67	85.2	67.3	99.6	89.77	68.1	83.5	66.81
6	523	COD	20	80	1.0	0.8	84.9	77.8	115.8	89.82	75.3	80.5	63.53
7	523	COD	20	80	1.0	1.0	81.3	98.8	154.7	88.64	97.7	69.9	53.03
8	523	COD	20	80	1.25	0.0	64.4	25.3	48.7	80.98	47.3	80.7	75.72
9	523	COD	20	80	1.25	0.2	72.9	33.9	58.1	84.74	51.0	82.5	74.11
10	523	COD	20	80	1.25	0.33	80.1	39.0	61.1	87.52	54.1	86.3	72.88
11	523	COD	20	80	1.25	0.5	86.6	46.1	66.9	89.99	58.0	89.3	71.30
12	523	COD	20	80	1.25	0.67	87.6	59.2	85.2	90.61	64.1	87.8	68.64
13	523	COD	20	80	1.25	0.8	86.8	73.2	106.5	90.49	72.2	84.4	65.00
14	523	COD	20	80	1.25	1.0	84.6	98.5	147.7	89.96	97.6	75.5	53.39
15	523	COD	20	80	1.5	0.0	67.9	21.9	40.1	82.50	47.6	85.0	75.64
16	523	COD	20	80	1.5	0.2	75.6	29.4	48.7	85.71	50.5	87.9	74.37
17	523	COD	20	80	1.5	0.33	83.6	33.9	50.9	88.63	53.1	90.1	73.41
18	523	COD	20	80	1.5	0.5	89.0	41.1	58.1	90.70	56.5	92.0	72.06
19	523	COD	20	80	1.5	0.67	88.1	56.6	81.1	90.74	63.0	89.0	69.18
20	523	COD	20	80	1.5	0.8	87.3	71.6	103.7	90.60	71.4	85.4	65.46
21	523	COD	20	80	1.5	1.0	85.5	98.6	146.4	90.26	97.7	77.0	53.46
22	523	COD	20	60	1.25	0.0	65.2	23.7	44.1	81.36	47.3	81.7	75.75
23	523	COD	20	60	1.25	0.2	75.0	29.9	48.6	85.50	50.5	85.2	74.36
24	523	COD	20	60	1.25	0.33	84.4	32.6	47.9	88.91	52.8	90.0	73.54
25	523	COD	20	60	1.25	0.5	89.5	38.9	53.5	90.88	55.6	91.6	72.35
26	523	COD	20	60	1.25	0.67	88.5	52.1	71.5	90.80	60.8	89.0	70.20
27	523	COD	20	60	1.25	0.8	87.2	67.8	96.0	90.57	68.9	85.2	66.48
28	523	COD	20	60	1.25	1.0	84.5	98.2	143.7	89.91	97.0	74.1	53.69
29	543	COD	20	60	1.25	0.0	69.7	26.3	45.7	83.40	48.6	83.1	75.17
30	543	COD	20	60	1.25	0.2	79.2	30.3	48.1	86.94	51.6	87.0	73.96
31	543	COD	20	60	1.25	0.33	87.0	34.7	49.7	89.67	53.9	91.2	73.09
32	543	COD	20	60	1.25	0.5	90.4	42.7	58.0	91.04	57.2	91.9	71.79
33	543	COD	20	60	1.25	0.67	89.1	52.6	72.7	90.92	61.3	89.9	69.99
34	543	COD	20	60	1.25	0.8	87.7	69.9	98.2	90.67	70.3	85.4	65.99
35	543	COD	20	60	1.25	1.0	84.7	98.3	143.1	89.98	97.0	74.5	53.69
32b	543	CTD	20	60	1.25	0.5	93.8	6.5	11.4	91.82	46.5	99.6	76.18

PR – pressurization with (F) Feed or (H_2) pure hydrogen; *DPR* – depressurization with pure hydrogen in (CTD) counter-current or (COD) co-current mode.

The process performance of a PSA cycle is only evaluated when the system reaches its CSS. However, it is important to study the behaviour of the PSA cycle in the unsteady state to have a good understanding of the transport phenomena involved in the process. The evolution of the product RON and product stream temperature is shown in Figure 5.8 for *Run_32*. It can be seen from the figure that CSS is only reached after approximately 75 cycles. About 50 cycles were simulated in the work of Silva (1998) for the separation of *n*/iso-paraffins in zeolite 5A. The main reason for this delay in achieving CSS is the stabilization of the temperature profiles within the bed, as it is shown in Figure 5.9, where the gas phase temperature profile at the end of the feed step is plotted for different cycle numbers. The existence of two distinct regions in Figure 5.9 is explained by the difference between the adsorption properties of the adsorbent layers. It should be noted that, unlike the zeolite beta layer where all the components can adsorb, in the zeolite 5A layer the adsorption is restricted to the LRON molecules *n*HEX and *n*PEN. The temperature oscillation in the bed exceeds 30 K during the first cycles, and progressively decreases to approximately 15 K at the CSS.

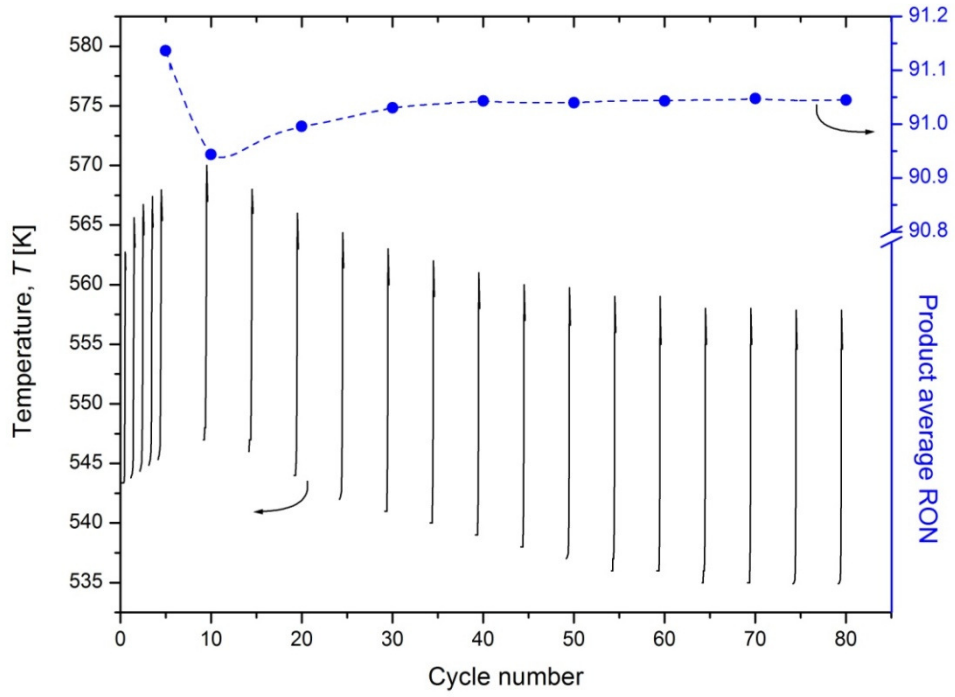


Figure 5.8. Transient variation of the gas phase temperature at the column outlet and average RON of the accumulated product (*Run_32*). *Note that not all the cycles are represented: after cycle #5 the temperature variation was recorded at each 5 cycles.*

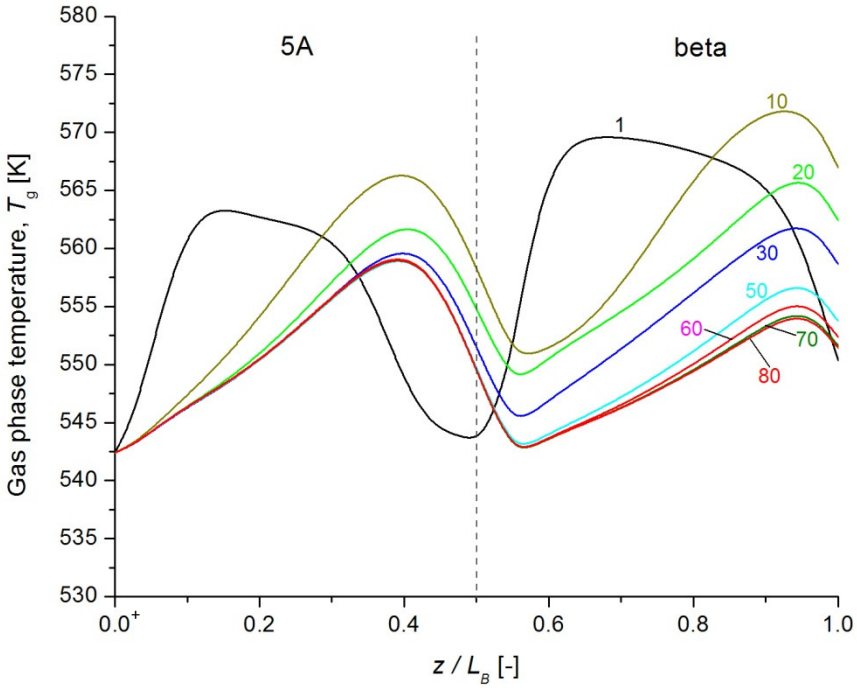


Figure 5.9. Evolution of the gas phase temperature profile at the end of the feed step with the cycle number (*Run_32*).

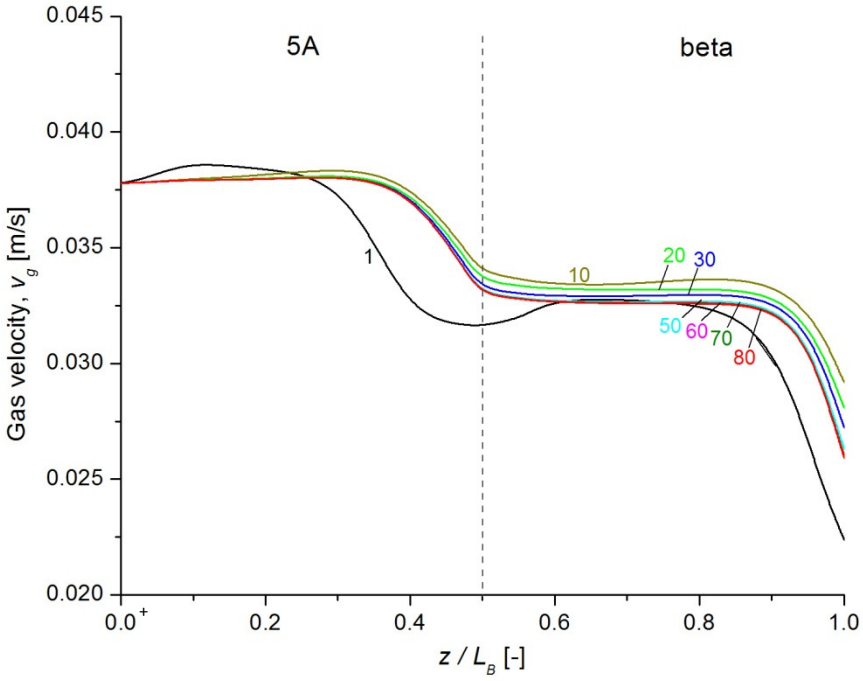


Figure 5.10. Evolution of the gas velocity profile at the end of the feed step with the cycle number (*Run_32*).

Figure 5.10 shows the gas phase velocity profiles at the end of the feed step for different cycle numbers (*Run_32*). As it was expected, material balance converges faster towards CSS than energy balance.

The evolution of the gas velocity profiles during each step is shown in Figure 5.11. The gas velocity decreases during the pressure-changing steps (panels *a* and *c*). As it

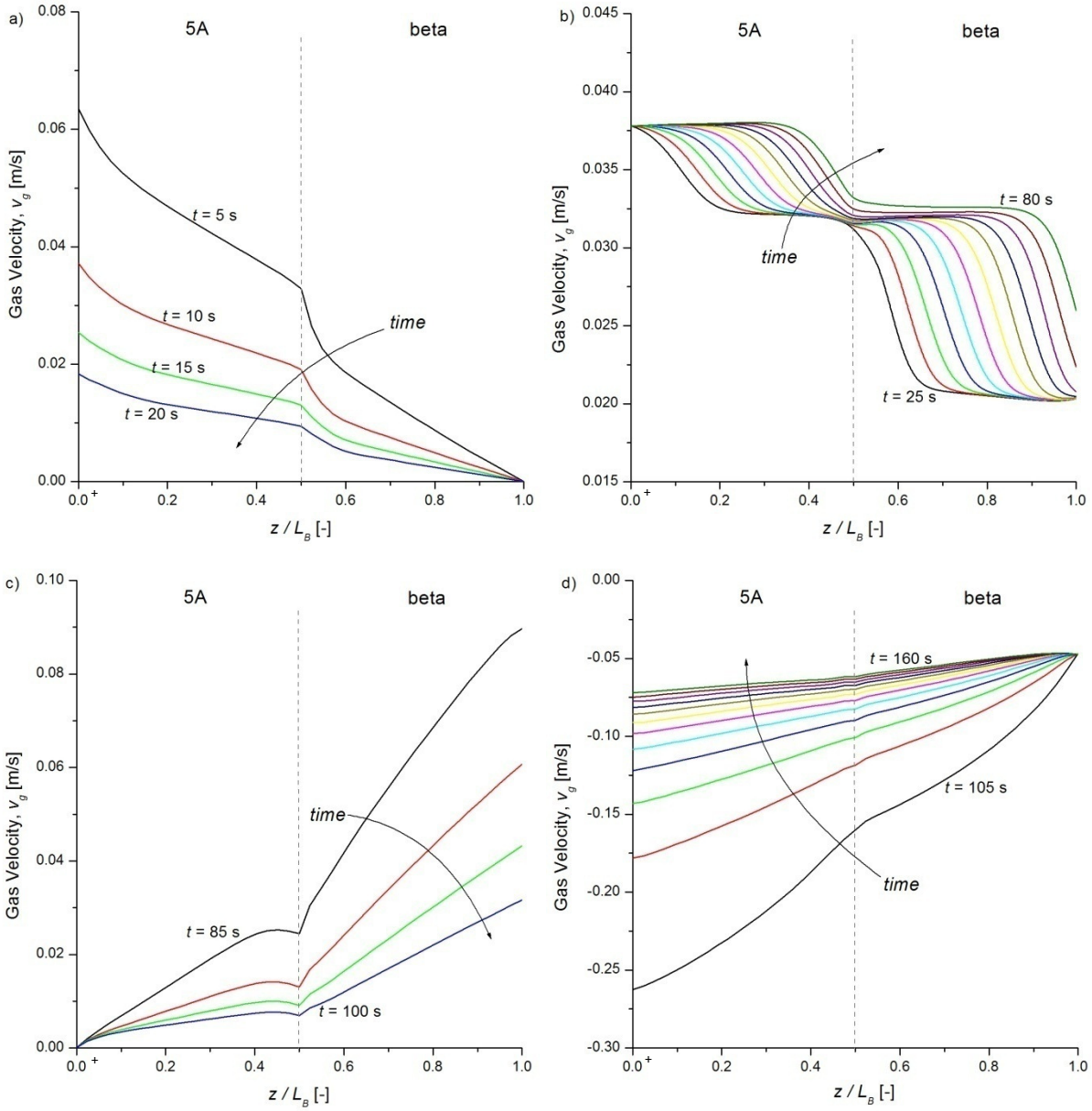


Figure 5.11. Evolution of the gas phase velocity profile obtained along the bed at CSS (*Run_32*): a) pressurization with feed; b) adsorption; c) co-current depressurization and d) counter-current purge with pure H_2.

was stated in the boundary conditions, gas velocity is zero at the closed terminal valve of the adsorption bed (panels *a* and c). In the purge step, the negative velocity is because of reversed direction of entrance stream. As it will be shown later in the text, the central plateau in the gas velocity profile of the feed step (panel *b* of Figure 5.11) is mainly due to accumulation of *i*PEN in the gas phase.

5.4.2 Concentration Profiles in the Layered Bed at Cyclic Steady State

After a certain number of cycles, the PSA system runs a CSS, representing normal production. Gas phase and solid phase concentration profiles at the end of each step at CSS are depicted in Figure 5.12 and Figure 5.13, respectively, for *Run_32*. At the end of the feed step (panel *b* of Figure 5.12 and Figure 5.13), the gas phase in the zeolite beta layer is mainly composed by *i*PEN, followed by 22DMB, 3MP, and 23DMB. There is practically no *n*HEX and *n*PEN in the gas phase of this layer, because these components are strongly adsorbed in the zeolite 5A layer (panel *b* of Figure 5.13). Also, it can be seen from the axial loadings in Figure 5.13, the assumption of the model in which *i*PEN, 22DMB, 23DMB, and 3MP are not adsorbed in zeolite 5A.

Due to its high concentration in the gas phase, *i*PEN is the component more adsorbed in the zeolite beta layer. Interesting is the adsorption capacity of zeolite beta layer towards 3MP. Although the fraction of 3MP in the adsorber feed is 5 times lower than the *i*PEN at the end of the feed step, the loading of 3MP is practically half of the *i*PEN.

Equally remarkable, is the effect of the COD step on the desorption of the weak adsorptive in the zeolite beta layer (panels *b* and *c* of Figure 5.13). It can be seen that the COD step leads to a significant reduction of the loading of *i*PEN, and 22DMB. As a consequence, the composition of the gas which goes out of the bed during depressurization step is enriched with HRON molecules.

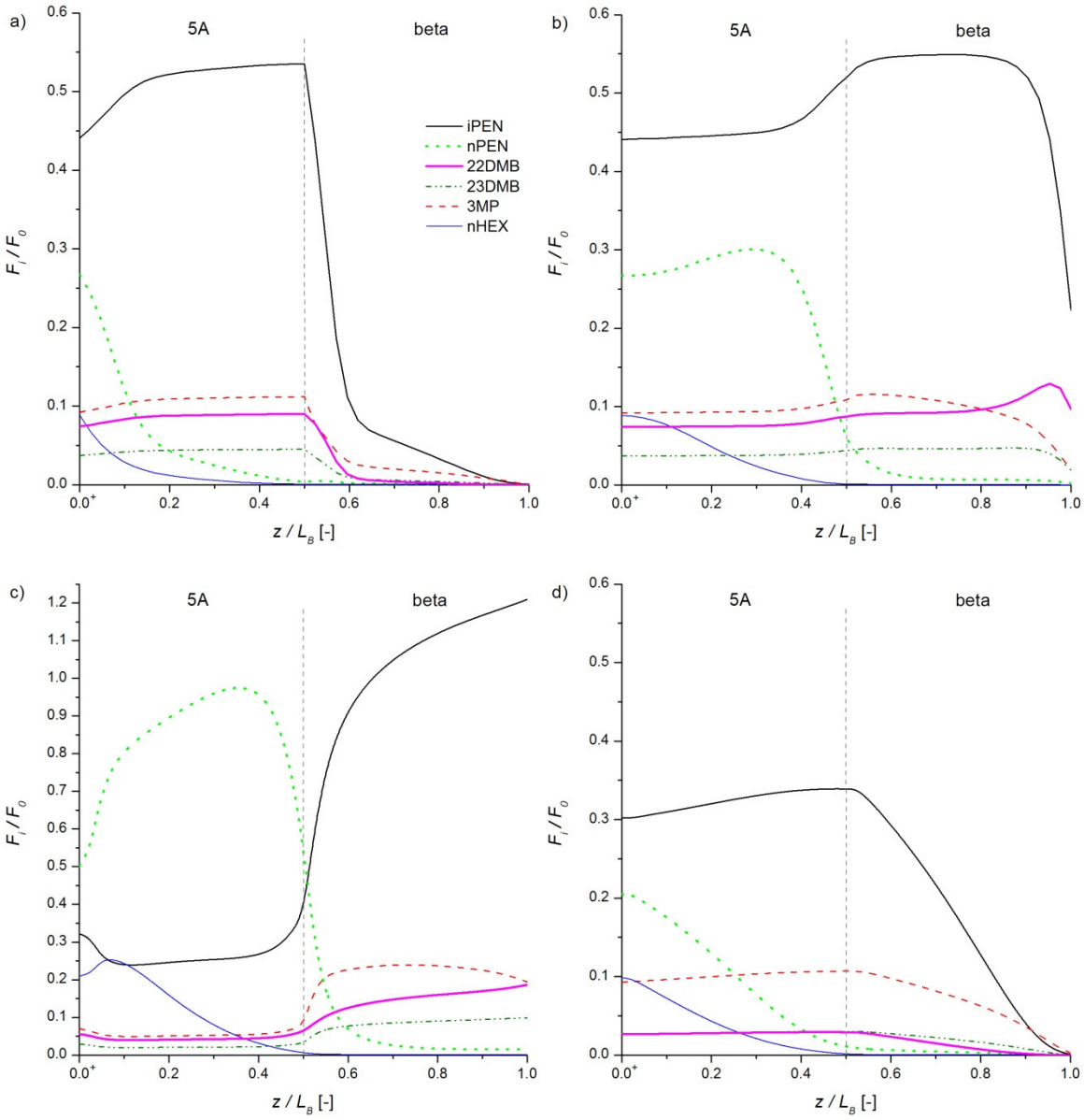


Figure 5.12. Gas phase concentration profile obtained along the bed at the end of each step at CSS (Run_32): a) pressurization with feed; b) adsorption; c) co-current depressurization and d) counter-current purge with pure H2.

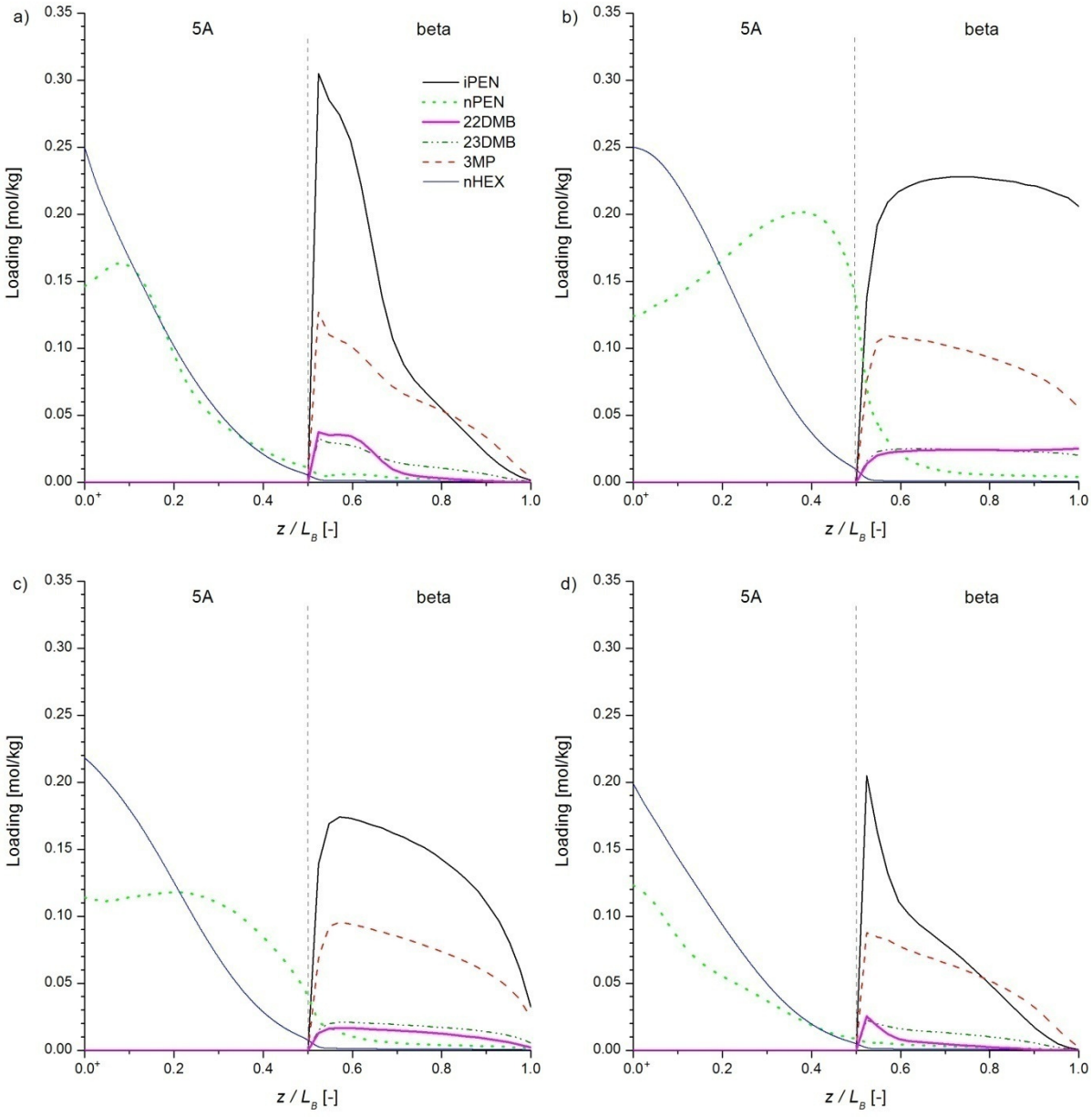


Figure 5.13. Solid phase concentration profile obtained along the bed at the end of each step at CSS (*Run_32*): a) pressurization with feed; b) adsorption; c) co-current depressurization and d) counter-current purge with pure H_2.

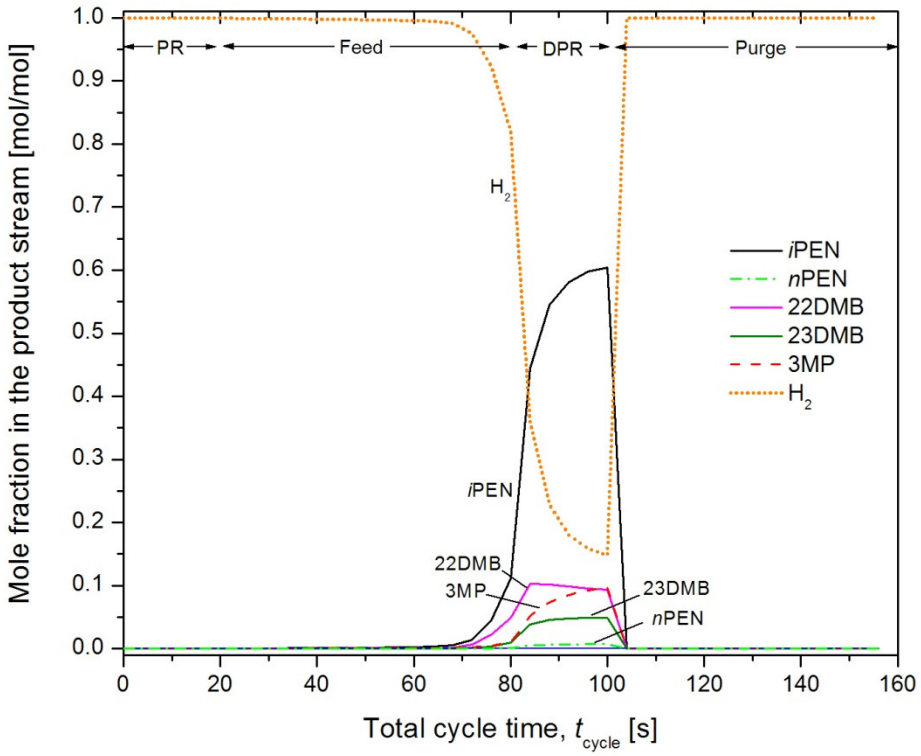


Figure 5.14. Molar composition of the product stream as a function of the total cycle time at CSS.

The breakthrough curves obtained at CSS are represented in Figure 5.14 for *Run_32*. Only a residual amount of *n*PEN, and practically no *n*HEX are recovered during production steps. As it was previously discussed, the depressurization step strongly increases the amounts of *i*PEN and 22DMB in the gas stream. At a first sight, Figure 5.14 suggests that at least four columns are required to produce a continuous stream of product.

The exothermic nature of adsorption combined with the gas flow gives rise to a temperature wave that propagates along with the concentration wave, as shown in Figure 5.15. In a PSA process, the temperature wave goes forward during the feed step (adsorption), and goes behind during the purge step (desorption). This temperature excursion can be useful to control the steps sequence by simply using thermocouples along the adsorption column. In Figure 5.15, the temperature oscillation during the feed step does not exceed 35 K. In general, the temperature excursion is greater under

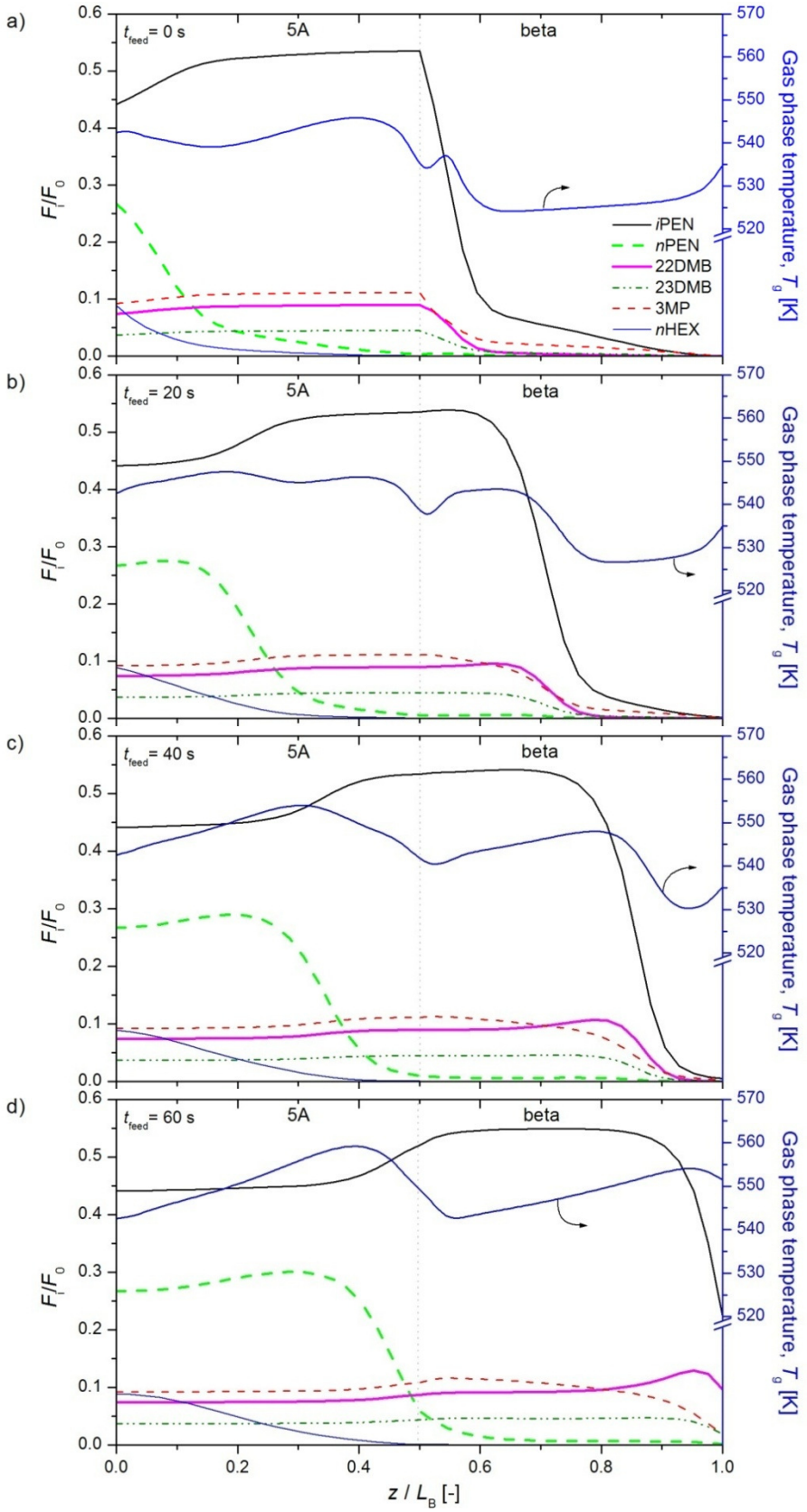


Figure 5.15. Evolution of the gas phase molar fraction and temperature profiles during the adsorption step at CSS (*Run_32*): a) t_{feed} = 0 s, b) t_{feed} = 20 s, c) t_{feed} = 40 s and d) t_{feed} = 60 s.

adiabatic conditions, which worsens the separation. Therefore, it can be stated that the case depicted here, represents the worse scenario.

Concerning the displacement of the mass fronts during the feed step, the first remarks from Figure 5.15 are that *n*HEX does not cross the limit of the zeolite 5A layer, and there is just a residual fraction of *n*PEN which reaches the zeolite beta layer. It is well known from the equilibrium theory that for a favourable isotherm, high-concentration fronts travel faster along the adsorption column than low-concentration fronts. This fact, along with the adsorption hierarchy in zeolite beta (see chapter 4), explains why the mass front of *i*PEN travels faster during the feed step (Figure 5.15). The roll-up that can be observed in the concentration profile of *i*PEN is explained by its lower affinity towards zeolite beta. The *i*PEN molecules are successively displaced from the solid phase by the more strongly adsorbed components resulting in accumulation of *i*PEN in the gas phase.

It is interesting now to examine the propagation of the mass fronts of 3MP, 23DMB, and 22DMB, during the feed step. At the beginning, the mass front of 3MP leads, but it is progressively exceeded by the 22DMB. More, at the end of the feed step, the mass front of 3MP is even overlapped by the mass front of 23DMB, which is two times more diluted than the first one. This is the evidence that the zeolite beta layer can be used as a barrier for the monobranched C_6, in order to reduce its concentration in the product stream.

5.4.3 Effect of the P/F Ratio for Different Values of L_{5A}/L_B

In practice the volume of the purge (measured at P_L) should be equal to or greater than the volume of the feed stream (measured at P_H). The increase in volume on depressurization means that the actual H_2 molar flow (F_{purge}) required to purge the hydrocarbon in the column must be equal to or greater than one fifth (i.e., P_L/P_H) of

the molar flow of feed (F_{feed}). The case where F_{purge} = (1/5) F_{feed} corresponds to a *P*/*F* ratio equal to unity.

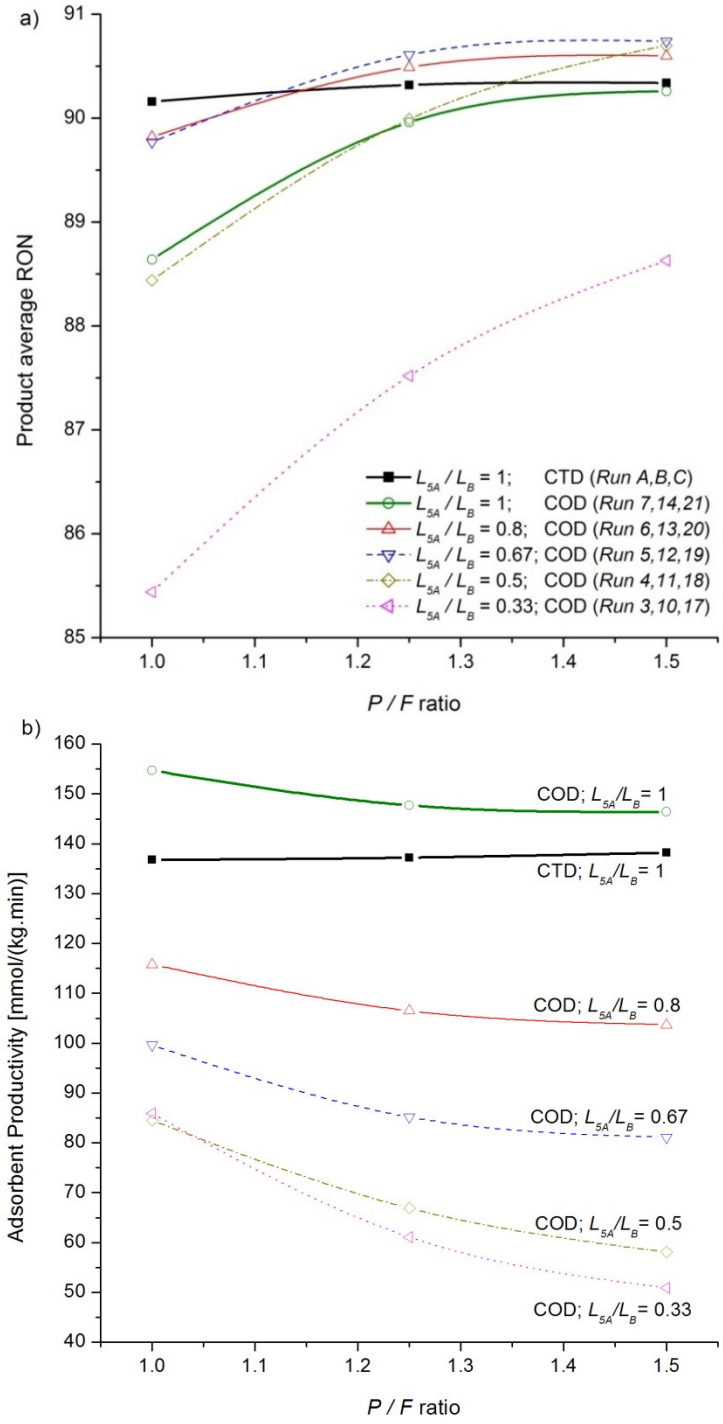


Figure 5.16. Effect of the *P*/*F* ratio on the (a) product average RON and (b) adsorbent productivity, at CSS (*T* = 423K, t_{feed}= t_{purge}= 80 s). Comparison between the all-zeolite 5A PSA column operating in CTD mode and the dual-layer PSA column with different zeolite 5A/zeolite beta ratio operating in COD mode

In order to have a reference basis to study the performance of the proposed layered PSA unit, we first simulate cycles with a single layer of zeolite 5A and CTD step, for different *P*/*F* ratio (*Run_A* to *Run_C*), henceforth mentioned as the reference cycles. The operating conditions and process performance are in Table 5.5. It can be seen from runs *A* to *C* that the product RON is slightly improved as the purge is increased; however, the gain is marginal. Panel *a* of Figure 5.16 shows a comparison between the product average RON obtained with the single layer PSA cycle with CTD step and the dual layer PSA with COD step. If the faction of zeolite 5A in the dual layer (L_{5A}/L_B) is comprised in the range 0.67 – 0.8 and the *P*/*F* ratio is greater than 1.15, then the RON of the product will be higher than the one obtained by the reference cycle. It should be noted that the limiting cases, $L_{5A}/L_B = 0$, and $L_{5A}/L_B = 1$, correspond to single layer of zeolite beta, and single layer of zeolite 5A, respectively. Comparing the reference cycles with the case where $L_{5A}/L_B = 1$ and COD step is used, then it can be seen that the product RON is higher for the reference cycles. This result suggests that, the COD step is not useful when the bed consists only of zeolite 5A, because the HRON molecules are not adsorbed. In terms of productivity, it is clearly seen from panel *b* of Figure 5.16 that zeolite beta inevitably decreases the recovery of HRON components, because HRON species are also retained in the adsorbent layer. Also, it can be seen that for a all-zeolite 5A column, at *P*/*F* ratio 1.5, the COD step can be used to increase the productivity without significantly reducing the octane quality of product obtained.

The combined effect of *P*/*F* and L_{5A}/L_B on the composition of both product and recycle streams is shown in Figure 5.17. Panel *a* shows that when the *P*/*F* ratio is increased, the product RON is boosted. This is mainly due to a significant reduction in the concentration of *n*PEN, and *n*HEX, along with an increase in the concentration of 22DMB and *i*PEN. This effect is more pronounced when the fraction of zeolite beta in the bed increases. Depending on the value of the *P/F* ratio, the maximum product RON is obtained when L_{5A}/L_B ranges from 0.67 to 0.8. For instance, for $L_{5A}/L_B = 0.67$ and *P*/*F* = 1.5 (*Run_19*), we obtain a final product with 90.74 RON, which represent an octane boosting of +0.40 RON comparatively to the reference cycle (*Run_C*). Less marked is

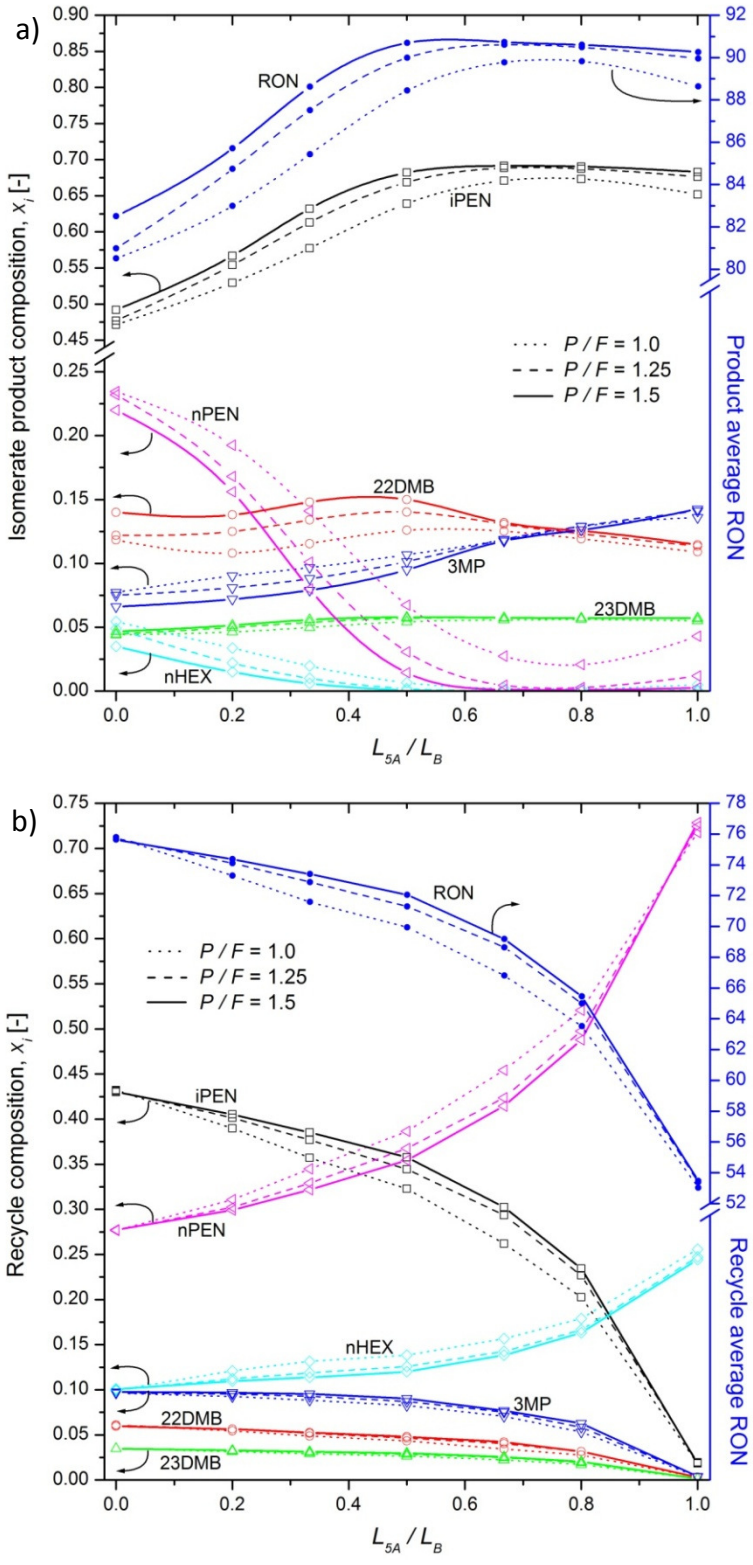


Figure 5.17. Effect of the *P/F* ratio on the composition of a) isomerate product, and b) recycle stream, and corresponding accumulated RON. The dotted lines represent *Runs 1-5,* dashed lines *Runs 8-14* and continuous lines *Runs 15-21*.

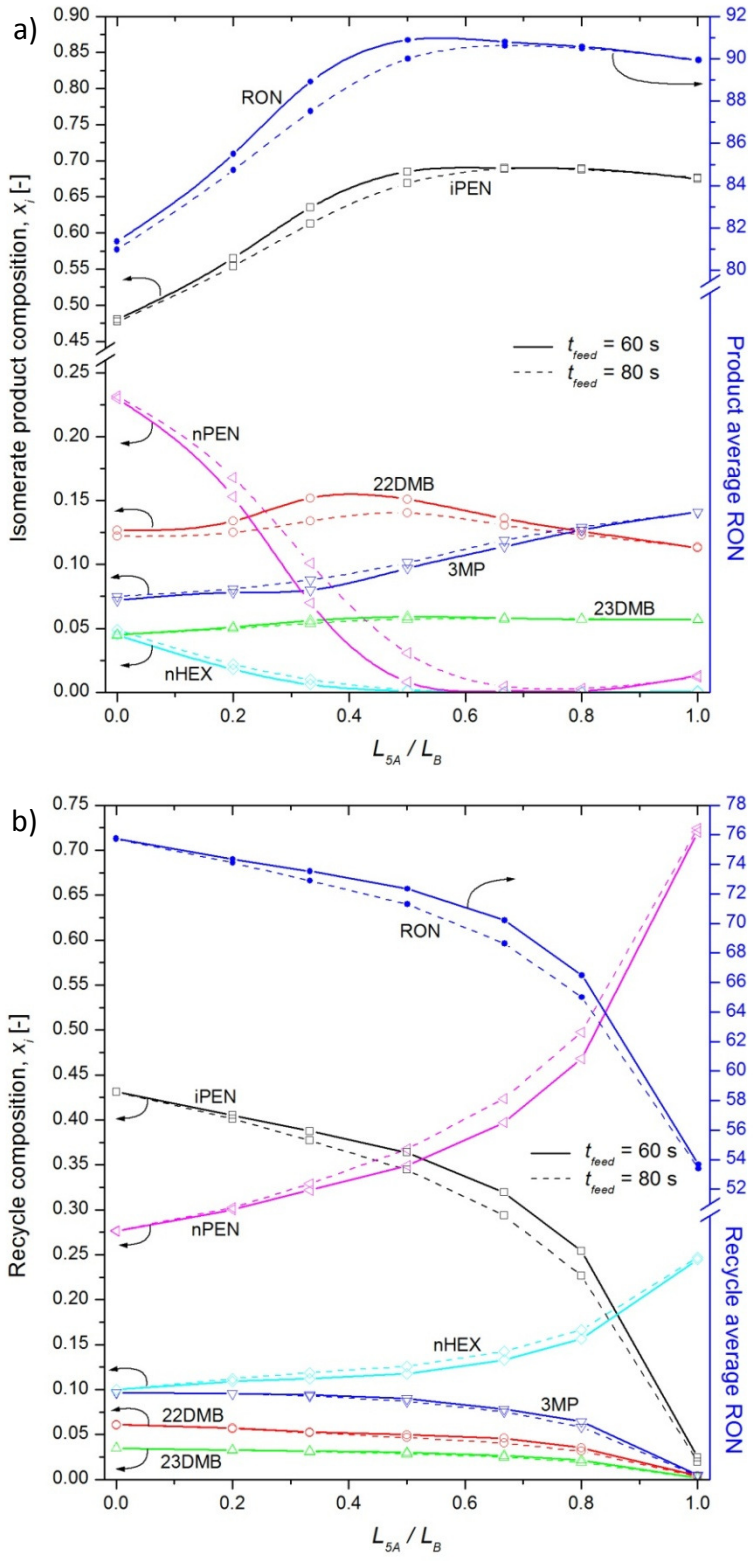


Figure 5.18. Effect of the cycle time on the composition of a) isomerate product, and b) recycle stream, and corresponding accumulated RON. The dashed lines represent *Runs 8-14* and continuous lines *Runs 22-28*.

the effect of the *P*/*F* ratio on the composition of the recycle stream (panel *b*), although a slight increase of the *i*PEN fraction is observed for intermediate values of L_{5A}/L_B.

5.4.4 Effect of the Cycle Time for Different Values of L_{5A}/L_B

The performance of the PSA cycle can be enhanced by the judicious choice of the cycle time. To study the effect of the cycle time, the simulations performed at 523 K and *P*/*F* = 1.25 (from *Run_8* to *Run_14*) were repeated for a feed step (t_{feed}) of 60 s (from *Run_22* to *Run_28*). It should be noted that for all the simulations, feed step and purge step have the same duration. The effect of the reduction of the feed step is shown in Figure 5.18. An enhancement of the product RON is achieved for L_{5A}/L_B in the range 0.2 – 0.5 (panel *a*). For instance, at L_{5A}/L_B = 0.33 the octane gain is + 1.39 RON. This improvement is mainly obtained thanks to an increase in the concentration of 22DMB, and significant reduction of the concentration of *n*PEN. The maximum product RON obtained (90.88) represents an octane boosting of + 0.56 RON comparatively to the reference cycle *Run_B*. The influence of the shortening of feed and purge steps on the recycle stream is shown in panel *b* of Figure 5.18.

5.4.5 Effect of the Temperature for Different Values of L_{5A}/L_B

It was demonstrated in the previous chapter that the raise of the temperature can have a significant impact in the separation of the C_5/C_6 isomers in zeolite beta. To study the effect of the operating temperature on the process performances, the simulations performed at 523 K, *P*/*F* = 1.25, and t_{feed} = 60 s (from *Run_22* to *Run_28*) were done for an operating temperature of 543 K (from *Run_29* to *Run_35*). It was assumed that the adsorber feed and the bed are at the same temperature. Figure 5.19 shows that a raise of 20 K in the operating temperature results in additional increase of the product RON especially for L_{5A}/L_B lower than 0.5, i.e. when the majority of the bed consists of zeolite beta. At 543 K, it is possible to reach a maximum RON of 91.04, for

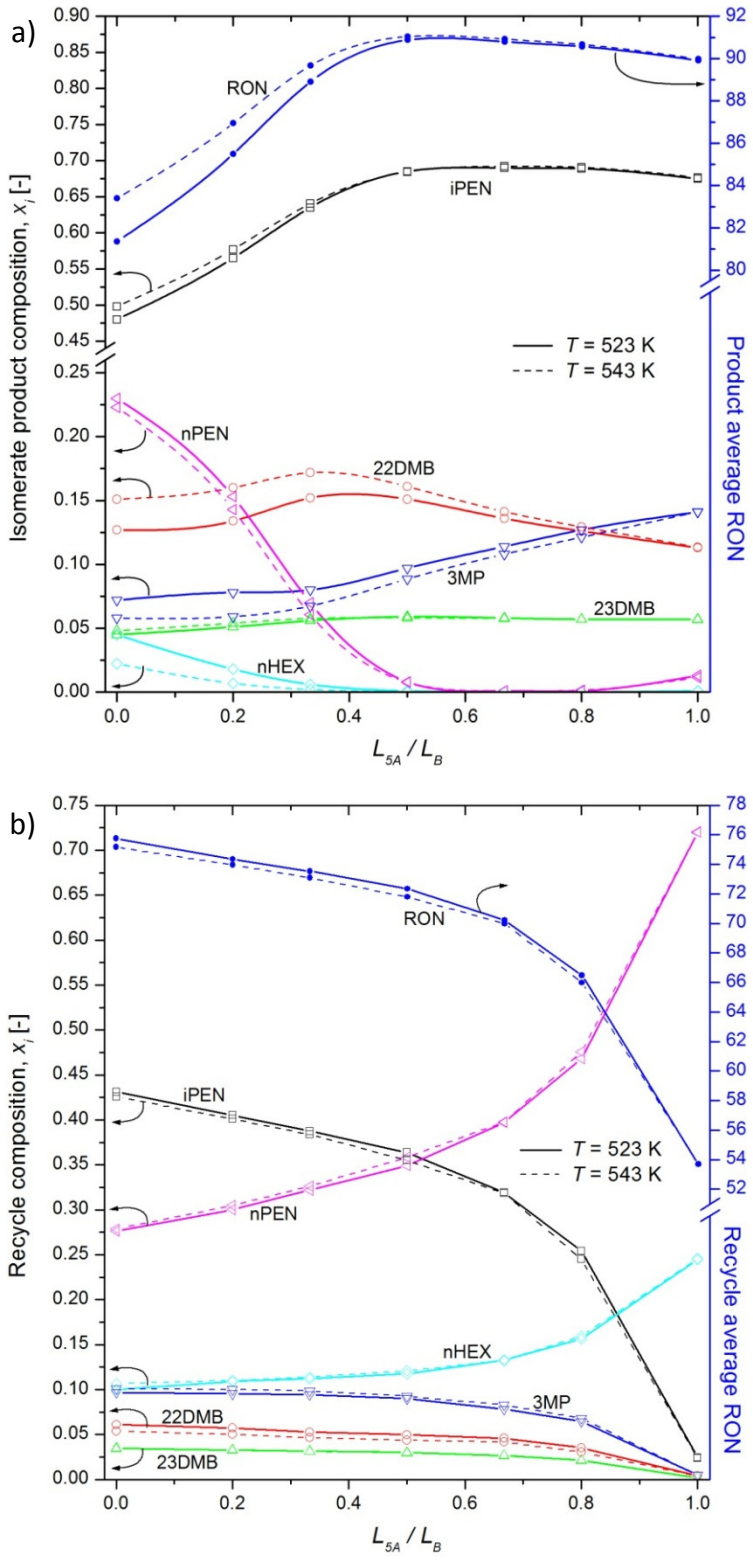


Figure 5.19. Effect of the operating temperature on the composition of a) isomerate product, and b) recycle stream, and corresponding accumulated product RON. The continuous lines represent *Runs 22-28* and dashed lines *Runs 29-35*.

L_{5A}/L_B = 0.5. Concerning the recycle stream, it is clearly seen from panel *b* of Figure 5.19 that the temperature has no significant effect on the composition.

5.4.6 Effect of the Depressurization Mode

The depressurization step can be performed either co-currently or countercurrently to the feed flow direction. The major function of the COD step in the layered PSA is to increase the recovery of the HRON molecules (weak adsorptive). However, the COD step also gives rise to the partial desorption of 3MP from the zeolite beta layer, resulting in a slight reduction of the product purity.

Table 5.6. Process performance: comparison between COD and CTD step.

Run	*DPR*	HRON purity (%)	HRON recovery (%)	HRON productivity (mmol/min/kg)	Product RON (-)	LRON purity (%)	LRON recovery (%)	Recycle RON (-)
32	*COD*	90.4	42.7	58.0	91.04	57.2	91.9	71.79
32b	*CTD*	93.8	6.5	11.4	91.82	46.5	99.6	76.18

Table 5.6 shows the effect of the depressurization mode on the process performances. When the process operates with CTD, there is a clear increase of the purity in both the product and the recycle streams. The octane quality of the product can be boosted up to 91.82 RON, i.e. a gain of + 0.78 points comparatively to the cycle operating with COD step. However, the large drawback of the CTD step is the strong reduction of the HRON recovery, almost six times less HRON recovered than the cycle operating with COD step.

5.4.7 General Performance of the Layered PSA Process

The simulations from *Run_1* to *Run_21* were performed at the same conditions of temperature, cycle time, and depressurization mode. Therefore, it is possible to represent the process performance in a surface graph as a function of L_{5A}/L_B and P/F.

Figure 5.20 is for the product RON, and the line indicates the operating conditions that yield the maximum product RON. This operating line is also shown in Figure 5.21, for the HRON purity of the product stream, in Figure 5.22, for the recovery of HRON component, and also in Figure 5.23, for the adsorbent productivity. These graphical representations allow the reader to readily find out relevant information about the process performance for a given set of operating conditions. For instance, if L_{5A}/L_B = 0.75, and P/F = 1.42, then it can be found from the surface graphs that the octane quality of the product stream will be in the range 90.6-90.7 RON, the product purity, ≈ 87.5 %, HRON molecules recovered in the production steps, 68 %, and adsorbent productivity, 95 mmol/(kg_{ads}·min). Comparing to the performance of the reference cycles *Run_B* and *Run_C*, the proposed scheme supplies an octane gain up to + 0.4 RON with a reduction of approximately 30 % in the adsorbent productivity.

Considering the data from Albemarle Corporation (http://www.albemarle.com) for a 10,000 BPSD hydroisomerization unit, the added value for an octane gain of + 0.4 RON will be close to 400,000 US$ per year. Of course, the use of more adsorption beds will be required to balance the reduction of the adsorbent productivity. Nevertheless, it was seen that both the operating temperature and the cycle time can be also tuned to obtain an extra boosting in product RON.

Further analysis will require the simulation of a multicolumn PSA system with equalization steps in order to have a more realistic representation of the actual PSA operation.

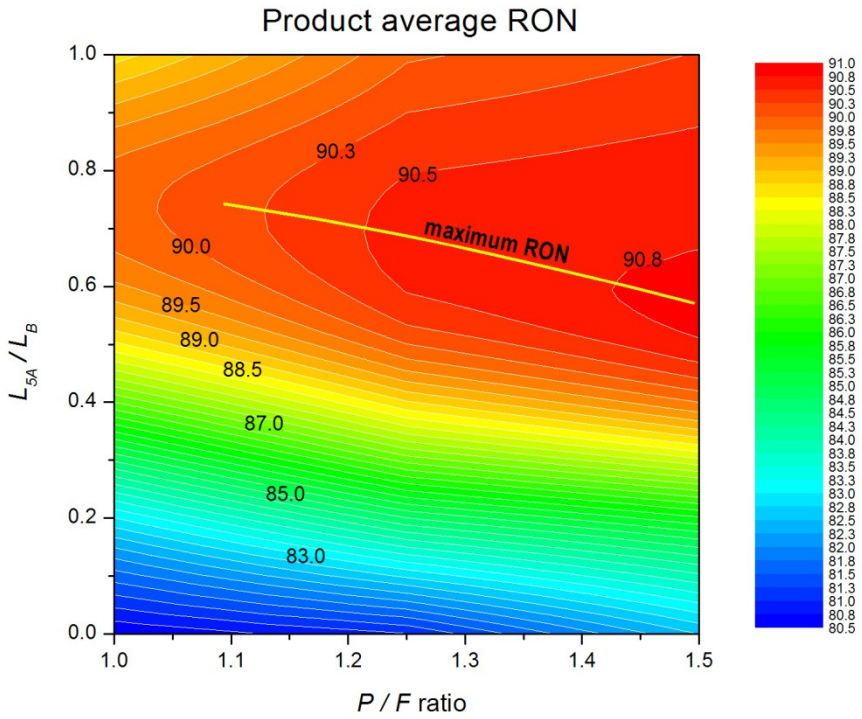


Figure 5.20. Product average RON as a function of the zeolite 5A layer length and purge-to-feed ratio at T = 523 K and t_{press}/t_{feed} = 20/80 s (*Run 1-21*).

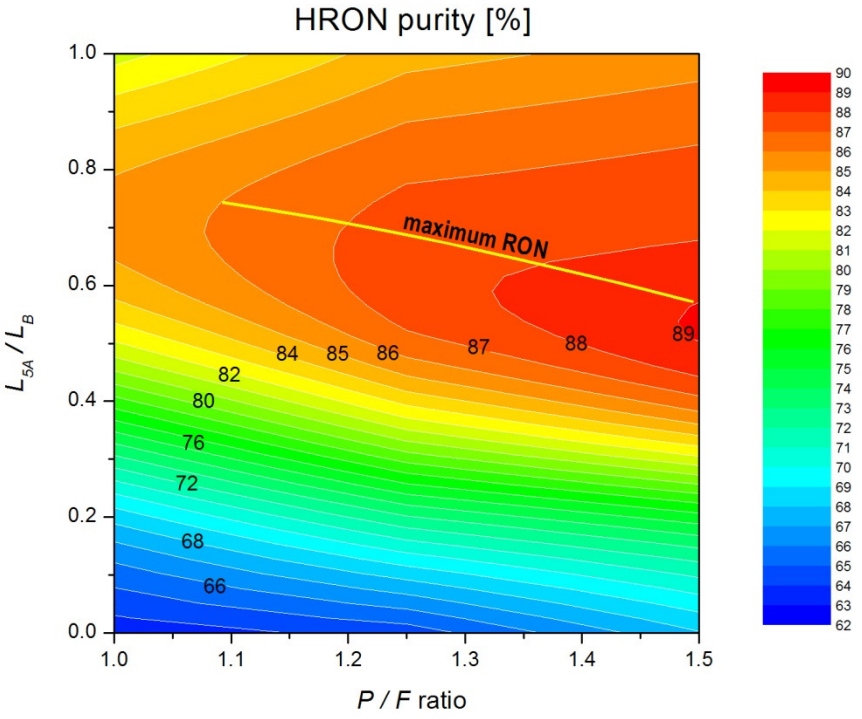


Figure 5.21. HRON purity as a function of the zeolite 5A layer length and purge-to-feed ratio at T = 523 K and t_{press}/t_{feed} = 20/80 s (*Run 1-21*).

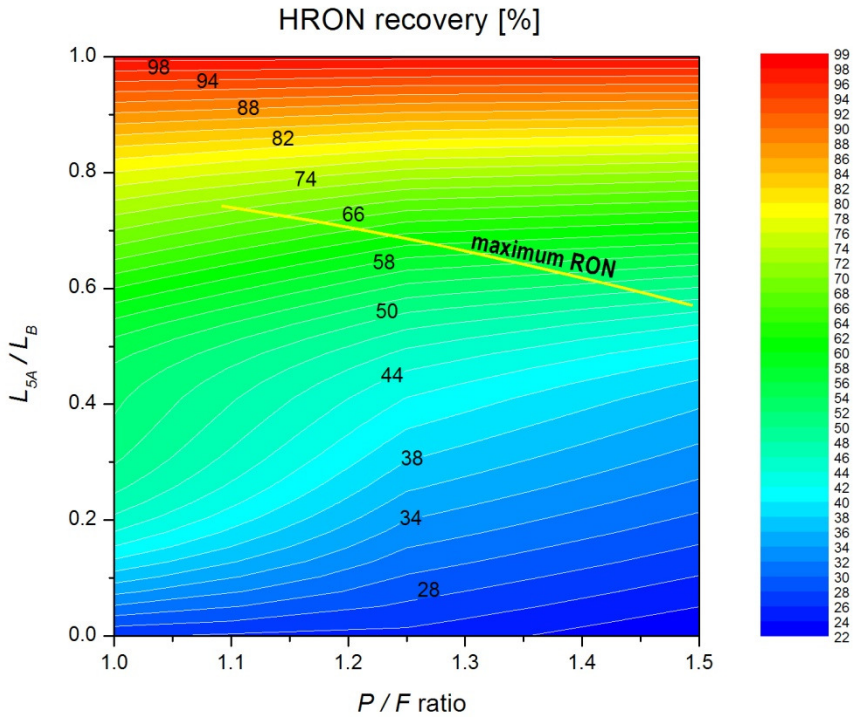


Figure 5.22. Recovery of HRON molecules as a function of the zeolite 5A layer length and purge-to-feed ratio at T = 523 K and t_{press}/t_{feed} = 20/80 s (*Run 1-21*).

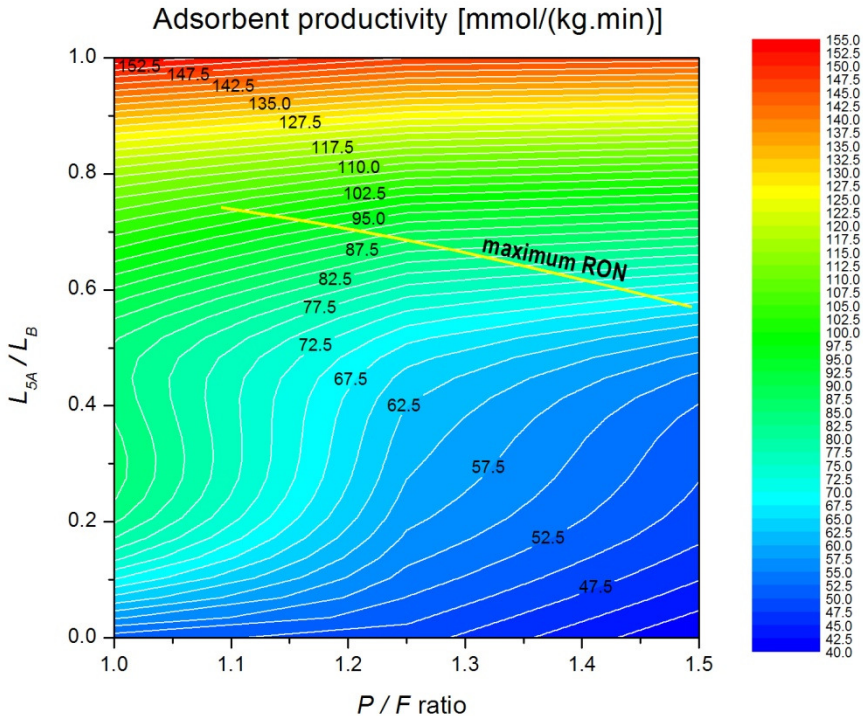


Figure 5.23. Adsorbent productivity as a function of the zeolite 5A layer length and purge-to-feed ratio at T = 523 K and t_{press}/t_{feed} = 20/80 s (*Run 1-21*). *Mass of adsorbent varying between 52.6 and 55.0 kg and production time 80 s (feed step + depressurization step).*

5.5 Conclusions

The model developed in the previous chapter in Aspen Adsim was used for a rapid evaluation of an adiabatic single column 4-steps PSA cycle with a dual layer of adsorbent. The bed consists of a zeolite 5A layer to retain linear paraffins, and a zeolite beta layer to separate monobranched C_6 from the enriched fraction. The proposed scheme is in part based on the separation section of the conventional TIP, but incorporates some variations, such as the pressure step sequence of the *Ipsorb* process, and a co-current depressurization (COD) step. The effect of different process variables, the zeolite 5A-to-zeolite beta ratio, the purge-to-feed ratio, the cycle time, the depressurization mode, and the operating temperature on the process performances were evaluated. The dynamic simulations demonstrate that the judicious choice of theses variables can improve the octane quality of the enriched fraction comparatively to the conventional processes for the separation of *n*-paraffins. The key conclusions reached from this study are:

a) The zeolite beta layer works like a barrier for the monobranched C_6, reducing its concentration in the enriched fraction;

b) The COD step causes the desorption of the weak adsorptive molecules from the zeolite beta layer, enriching in that manner the composition of product stream with HRON molecules.

c) Increasing the *P*/*F* ratio boosts the octane quality of the enriched fraction. At 423 K, the maximum product RON is obtained when L_{5A}/L_B ranges from 0.67 to 0.8;

d) For L_{5A}/L_B in the range 0.67 – 0.8 and *P*/*F* ratio greater than 1.15, the product RON yield by the dual layer operating with COD will be higher than the one obtained using the single layer of zeolite 5A with CTD. For instance, keeping constant the *P*/*F* ratio, it is possible to have an octane gain of + 0.26 RON with a reduction of 25 % in the adsorbent productivity.

e) At 543 K, and L_{5A}/L_B in the range 0.2 – 0.5, the octane quality can be boosted by reducing the feed step in 20 s. This variation reduces the amount of *n*PEN in the product;

f) Product RON can also be increased by raising the operating temperature, when the majority of the bed consists of zeolite beta. This effect results from the higher selectivity of the zeolite beta towards less branched isomers at high temperature;

g) The COD step in the layered PSA increases the recovery of the HRON molecules. A higher product RON can be obtained using CTD step; however, with a strong reduction of the HRON recovery.

5.6 References

Albemarle Corporation, http://www.albemarle.com (accessed Nov 2009).

Aspen Technology, http://www.aspentech.com (accessed Nov 2009).

Aspen Adsim 2004.1 – Adsorption reference guide; Aspen Technology: Cambridge, MA, USA (2005).

Axens IFP Group Technologies, http://www.axens.net (accessed Nov 2009).

Boerio-Goates, J.; Stevens, R.; Hom, B.K.; Woodfield, B.F.; Piccione, P.M.; Davis, M.E.; Navrotsky, A. Heat Capacities, Third-Law Entropies and Thermodynamic Functions of SiO_2 Molecular Sieves from T = 0 K to 400 K. *J. Chem. Thermodyn.* 34, 205–227 (2002).

Calero, S.; Smit, B.; Krishna, R. Separation of Linear, mono-Methyl and di-Methyl Alkanes in the 5-7 Carbon Atom Range by Exploiting Configurational Entropy Effects during Sorption on Silicalite-1. *Phys. Chem. Chem. Phys*. 3, 4390–4398 (2001).

Cusher, N. A. UOP TIP and Once-Through Zeolitic Isomerization Processes. In *Handbook of Petroleum Refining Processes*; Meyers, R. A., Ed.; 3rd Edition, McGraw Hill: New York, Chapter 9, pp 29–39 (2004a).

Cusher, N. A. UOP IsoSiv Process. In *Handbook of Petroleum Refining Processes*; Meyers, R. A., Ed.; 3rd Edition, McGraw Hill: New York, Chapter 10, pp 63–68 (2004b).

da Silva, F.A. Cyclic Adsorption Processes: Application to Propane/Propylene Separation. Ph.D. Thesis, University of Porto (1999).

da Silva, F.A.; Silva, J.A.C.; Rodrigues, A.E. A General Package for the Simulation of Cyclic Adsorption Processes. *Adsorption* 5, 229–244 (1999).

de Montgareuil, P.G.; Domine, D. Process for Separating a Binary Gaseous Mixture by Adsorption. U.S. Patent 3,155,468 (1964).

Deschamps, A.; Jullian, S. Adsorption in the Oil and Gas Industry. In *Petroleum Refining: Separation Processes, Volume 2*; Wauquier, J.P., Ed.; Editions Technip: Paris (2000).

Griesinger, A.; Spindler, K.; Hahne, E. Measurements and Theoretical Modelling of the Effective Thermal Conductivity of Zeolites. *Int. J. Heat Mass Tran.* 42, 4363–4374 (1999).

Holcombe, T.C. n-Paraffins - Isoparaffins Separation Process. U.S. Patent 4,176,053 (1979).

Holcombe, T.C. Total Isomerization Process. U.S. Patent 4,210,771 (1980).

Holcombe, T.C.; Sarger, T.; Volles, W.K.; Zarchy, A.S. Isomerization Process. U.S. Patent 4,929,799 (1990).

Kiyonaga, K. Adsorption Separation Process. U.S. Patent 3,176,444 (1965).

Kostroski, K.P.; Wankat, P.C. High Recovery Cycles for Gas Separations by Pressure-Swing Adsorption. *Ind. Eng. Chem. Res.* 45, 8117–8133 (2006).

Marsh, W.D.; Pramuk, F.S.; Hoke, R.C., Skarstrom, C.W. Pressure Equalization Depressuring in Heatless Adsorption. U.S. Patent 3,142,547 (1964).

Minkkinen, A.; Mank, L.; Jullian, S. Process for the Isomerization of C_5/C_6 Normal Paraffins with Recycling of Normal of Multicomponent Adsorption Beds. U.S. Patent 5,233,120 (1993).

Process System Enterprise Limited, http://www.psenterprise.com (accessed Nov 2009).

Ribeiro, A.M.; Grande, C.A.; Lopes, F.V.S.; Loureiro, J.M.; Rodrigues, A.E. A Parametric Study of Layered Bed PSA for Hydrogen Purification. *Chem. Eng. Sci.* 63, 5258–5273 (2008).

Ruthven, D.M. *Principles of Adsorption and Adsorption Processes*; John Wiley: New York (1984).

Ruthven, D.M.; Farooq, S.; Knaebel, K.S. *Pressure Swing Adsorption*; VCH Publishers: New York (1994).

Schenk, M.; Vidal, S.L.; Vlugt, T.J.H.; Smit, B.; Krishna R. Separation of Alkane Isomers by Exploiting Entropy Effects during Adsorption on Silicalite-1: A Configurational-Bias Monte Carlo Simulation Study. Langmuir 17, 1558–1570 (2001).

Schiesser, W.E. *The Numerical Method of Lines*; Academic Press: San Diego (1991).

Silva, J.A.C. Separation of *n*/iso-Paraffins by Adsorption Process. Ph.D. Thesis, University of Porto (1998).

Sircar, S. Pressure Swing Adsorption. *Ind. Eng. Chem. Res.* 41, 1389 (2002).

Skarstrom, C.W. Method and Apparatus for Fractionating Gaseous Mixtures by Adsorption. U.S. Patent 2,994,627 (1960).

Suzuki, M. *Adsorption Engineering*; Kodansha: Tokyo (1990).

Volles, W.K. Adsorptive Separation of Isopentane and di-Methyl Branched Paraffins from mono-Methyl Branched Paraffins. EU Patent 0 473 828 A1 (1992).

Waldron, W.E.; Sircar, S. Parametric Study of a Pressure Swing Adsorption Process. *Adsorption* 6, 179–188 (2000).

Wankat, P.C. *Large-scale Adsorption and Chromatography Vol.1*; CRC Press: Stoneham, MA (1986).

Warmuziński, K.; Tańczyk, M. Multicomponent Pressure Swing Adsorption Part I. Modelling of Large-Scale PSA Installations. *Chem. Eng. Process.* 36, 59-99 (1997).

Yang, R.T. *Gas Separation by Adsorption Processes*; Butterworth Publishers: Boston (1987).

6

Zeolite Beta Membranes for the Separation of C_6 Isomers

The preparation of α-alumina supported zeolite beta membranes was successfully achieved and sped up by exploring combinations of three seeding techniques and three synthetic methods. The surface of the membranes was completely covered by well intergrown crystals; the thickness of the zeolite layers ranged from 2 μm to 6 μm depending on the synthesis method used. The quality of the membranes was tested by means of pervaporation of ethanol/1,3,5-triisopropylbenzene (TIPB) mixtures together with permporometry experiments. The performance in the vapour separation of quaternary equimolar mixtures of n*HEX, 3MP, 23DMB and 22DMB in the range 343–443 K showed that permeate flux decreases as the branching degree increases following the order: nHEX >> 3MP > 23DMB > 22DMB. In the retentate, the fractions of monobranched and normal hexane decrease while the concentration of dibranched isomers is increased compared to the feed composition. The influence of the temperature in the permeation fluxes indicates the existence of an activated transport mechanism which favours the permeation of more nHEX and 3MP with regard to their dibranched isomers. The octane number (ON) of the quaternary mixture was enhanced up to 5 points with the best synthesized membrane.*

This chapter is based on the following publication:

P.S. Bárcia, A. Ferreira, J. Gascon, S. Aguado, J.A.C. Silva, A.E. Rodrigues, F. Kapteijn, Micropor. Mesopor. Mater. 128 (2010) 194-202.

6.1 Introduction

As it was shown in chapter 5, zeolite beta can be a useful adsorbent for the vapour phase separation of C_6 isomer mixtures at low partial pressure by cyclic adsorption process. Nevertheless, continuous processes are generally preferred for economic reasons. This is why zeolite membranes have attracted the attention of many scientific and industrial groups.

In the literature, most studies concerning the separation of branched C_6 isomers with zeolite membranes focus on the use of MFI (Silicalite-1 or ZSM-5) as separating media. In preceding works, experimental measurements (Flanders et al., 2000), and subsequent modelling of the transport of hexane isomers through ZSM-5 membranes (Sommer et al., 2003), showed selectivities nHEX/3MP and nHEX/22DMB up to 100 and 1000, respectively, based on permeation rates of the hydrocarbons across the membrane. However, Gora and Jansen (2005) found much lower selectivity, only 24 for the vapour permeation of a mixture nHEX/2MP with a molar ratio of 80:20 (22 mol % in Helium) at 393 K with a Silicalite-1/TiO_2/stainless steel tubular membrane. Similar nHEX/2MP and nHEX/3MP selectivities, 22 and 24 respectively, were reported by Funke et al. (1997) for the permeation of equimolar mixtures through ZSM-5 membranes (2-10 μm thickness) on γ-alumina tubular support at 363 K. Interestingly, in the same work separation of 3MP/22DMB mixtures was not possible at the same conditions.

Recently, Maloncy et al. (2005) used two different methods to synthesize zeolite beta membranes by seeding and secondary growth technique on TiO_2 coated stainless steel disk supports. These membranes were afterwards used in pervaporation of equimolar mixtures of 2MP and 22DMB at 303 K showing selectivities of 1.5 in favour of the monobranched isomer. In situ crystallization was used by Tuan et al. (2002), resulting in highly crystalline zeolite beta membranes which were tested for the separation of organic compounds. The same crystallization technique was used by

Torres et al. (2003, 2008) on porous Al_2O_3 supports using a three-step method with different gel precursor dilutions resulting in a homogenous zeolite beta film.

Based on these results, it might be interesting to study the efficiency of zeolite beta membranes in the separation of hexane isomers, in order to compare their performance with the one obtained for the cyclic fixed bed process, analyzed in the previous chapter. This study makes part of a project proposal presented during this Ph.D. work to Fundação para a Ciência e a Tecnologia (FCT), and afterwards approved and accepted for financing in 2007 (reference: PTDC/EQU-EQU/69731/2006). The aim of this project is the development of a novel conceptual process combining in a single unit the separation and hydroisomerization of the linear and monobranched hexanes. The zeolite membrane reactor (ZMR) could give rise to a higher conversion of LRON compounds than the TIP, by controlling the feed composition to the reaction. Figure 6.1 shows the conceptual design of the proposed ZMR process.

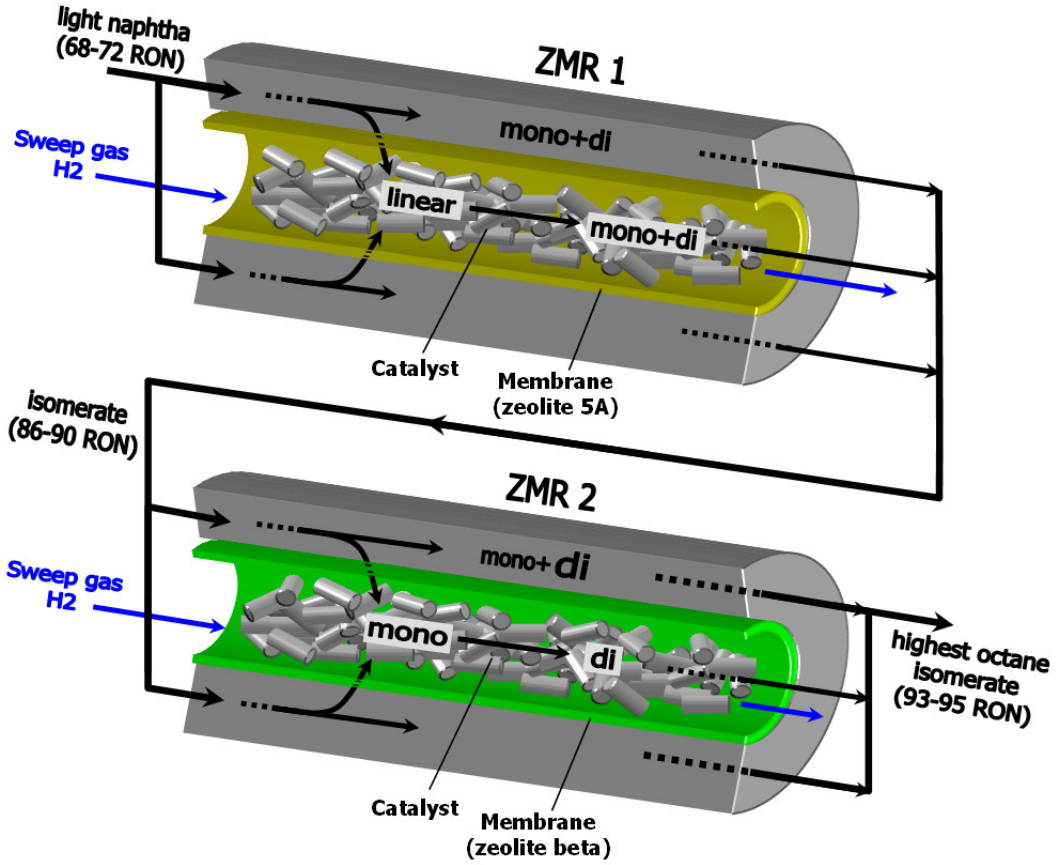


Figure 6.1. Conceptual design of a novel ZMR process.

In Figure 6.1, the first module (ZMR1) contains an *n*/iso selective zeolite membrane, e.g. zeolite 5A, and the second one (ZMR2) contains of a mono-/dibranched selective zeolite membrane, e.g. zeolite beta. Both modules contain a bed of C_6 isomerization catalyst, e.g. Pt/H-MOR, which is packed either in the tube side or the shell side, according to the case where light naphtha is fed either in the shell side or in the tube side, respectively. The basic idea of the concept illustrated in Figure 6.1 is the decoupling of the hydroisomerization reaction into two distinct stages. In ZMR1, only linear molecules are selectively supplied from LSR naphtha, through the membrane, to a packed bed of catalyst. In ZMR2, most part of the monobranched hexane permeates from a mixture mainly composed by mono- and dibranched hexanes, through the membrane, to the catalyst, being converted into dibranched molecules. A sweep gas such as hydrogen should be used in the two units because of the need to maintain the catalyst bed under a hydrogen partial pressure to prevent cocking and also to increase the driving force for the fluxes in the membrane. Comparatively to the TIP, the ZMR can shift the overall conversion above thermodynamic equilibrium by controlling the feed composition to the reaction. Additional advantages of the ZMR include the extended catalyst lifetime, and the operating energy saving realized by the elimination of intermediate processing stages.

To develop the ZMR process, it was necessary first to introduce in our team, technical expertise in the synthesis of zeolite materials and zeolite membranes. For this purpose, it was carried out during this Ph.D., a collaboration work between LSRE and the Catalysis Engineering group (section The Pore) at the Delft University of Technology (Delft, The Netherland) under the supervision of Prof. Freek Kapteijn. The main objective of this training was the synthesis and characterization of zeolite beta membranes and their applications for the separation of hexane isomers.

Afterwards, it was developed at LSRE-IPB, an experimental unit called ZEOPERM, for the dynamic characterization of zeolite membranes, and the study of mixture separation by vapour permeation. This apparatus was also ready to operate with ZMRs

however, this part of the research is still under development, and consequently, it is not included in this Ph.D. thesis.

In this chapter, various synthesis procedures of zeolite beta membranes were evaluated for their applicability in the vapour phase separation of C_6 isomers. Zeolite beta membranes were prepared by secondary growth method combining different seeding techniques, seeding materials and posterior hydrothermal synthesis conditions reported elsewhere (Maloncy et al., 2005; Tuan et al., 2002; Torres, 2008; Camblor, 1997). These membranes were characterized, and their potential for the separation of mixture of branched C_6 isomers by vapour permeation was studied. Finally, their performances are compared with the *state of the art* membrane processes.

6.2 Experimental

6.2.1 Preparation of α-Alumina Supported Zeolite Beta Membranes

Zeolite beta membranes were grown on the inner surface of asymmetric tubular α-Al_2O_3 supports (Inocermic GmbH, Germany) with a $D_{i/o}$ of 7/10 mm, and a length of 80 mm having a top layer on the inner surface containing pores of 200 nm (Figure 6.2). The effective length was about 54 mm because a glazing of 13 mm was applied at both ends. After coating on each support end with the glazing (IN 1001 Clear, Envision Glaze, Duncan) the supports were heated at 1273 K for 15 min at a heating rate of 1-3 K min^{-1}. During the membrane synthesis, the outer side of the tube was covered with Teflon tape to avoid crystallization on this side.

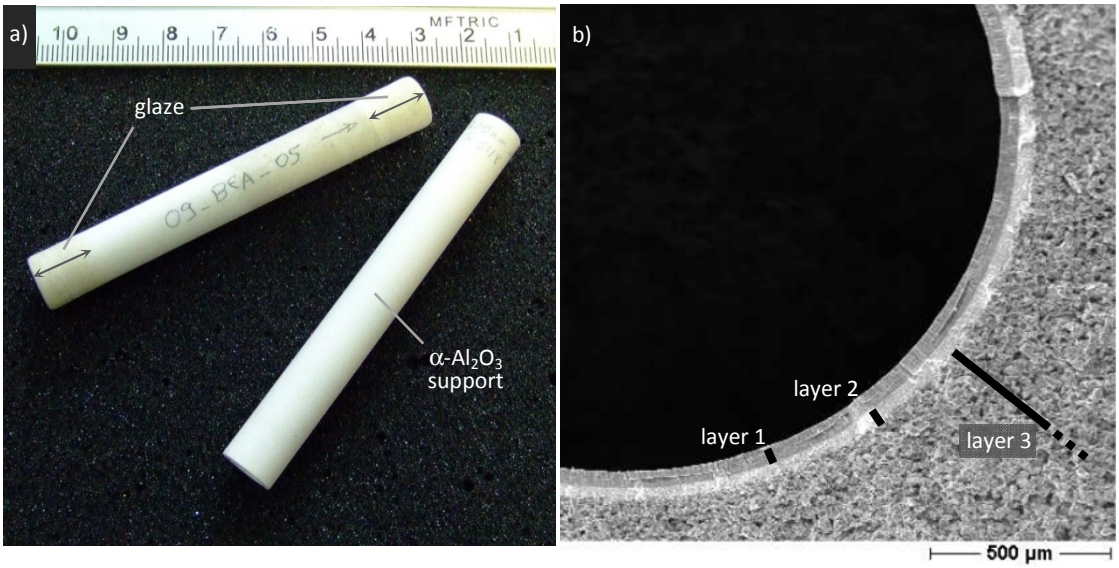


Figure 6.2. Tubular α-Al_2O_3 support from Inocermic GmbH, and application of glaze (a); SEM observation of the support cross-section showing the asymmetric structure (b).

The zeolite beta membranes were prepared by a secondary growth method combining three different types of seeding techniques and materials at three different crystallization conditions (see Table 6.1).

The first seeding method is based on a pressure gradient technique: vacuum was applied inside a flask containing plugged supports previously filled with a suspension (15 ml) of commercial beta crystals (crystal size: 0.1-0.4 µm; Si/Al = 12.5) in the H-form (10 g/l). The commercial beta crystals were supplied by ZEOCHEM AG under the reference ZEOcat PB/H. The water is then filtered through the vertically placed support tube, where the seed crystals are deposited on its inner surface. The process was repeated twice while inverting the orientation of the support to achieve a homogeneous distribution of the seeds.

The same pressure gradient technique was applied in the seeding method 2 using a colloidal suspension of Na-BEA prepared as described elsewhere (Maloncy et al., 2005). Dip-coating was used in method 3 to fix nanocrystalline zeolite beta on the internal surface of the supports (Camblor, 1997).



Figure 6.3. View of the autoclave used for hydrothermal synthesis, with PTFE liner.

The colloidal suspensions used in methods 2 and 3 were prepared by hydrothermal synthesis in 45 ml PTFE lined stainless steel autoclaves (model 4744) from Parr Instruments (Moline, Illinois, USA). A view of the autoclave is shown in Figure 6.3. Both the gel phase composition and the hydrothermal synthesis conditions are summarized in Table 6.1. The seeded supports were then hydrothermally treated twice using three different mixtures containing tetraethylammonium hydroxide (TEAOH) as a structure directing agent (SDA). The crystallization methods used in this work are summarized in Table 6.1. After each crystallization step, the membranes were brushed, thoroughly washed with distilled water, and dried in air at 373 K for 12 h. Finally the template was removed from the membranes by calcination in air at 753 K for 8 h at a heating rate of 0.3 K min^{-1}.

The main steps for the preparation of the zeolite beta membranes are shown in Figure 6.4

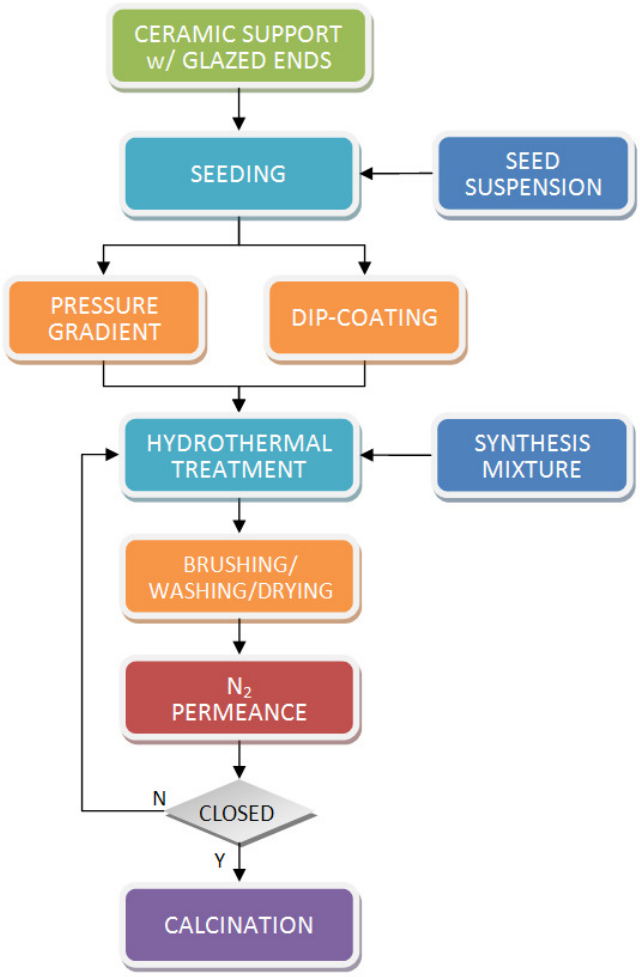


Figure 6.4. Flowchart for the preparation of zeolite membranes.

6.2.2 *Static Characterization of Membranes and Materials*

After hydrothermal synthesis, the powders collected from the bottom of the autoclaves were analysed by XRD, performed at the Department of Materials Science and Engineering of the Delft University of Technology (The Netherland), using a Bruker-AXS D5005 with Cu Kα radiation. The surfaces and cross sections of the supports were examined by scanning electron microscopy (SEM) at DelftChemTech (Delft University of Technology), on a Phillips XL20 (15 kV) microscope to determine the morphology, homogeneity, adhesion and thickness of the zeolite layer as well as the crystal sizes.

Table 6.1. N_2 permeance of the zeolite beta membranes after second synthesis and after calcination. Transmembrane pressure difference of 200 kPa. Room temperature. Si/Al ratio calculated from the composition of the synthesis mixture.

N_2 permeance, Π (mol/(m^2 s Pa))		**Secondary growth**		
		Synthesis A (Torres et al., 2008)[d] Si/Al = 45 Synthesis conditions (2 syntheses): 443 K / 3 days	**Synthesis B** (Maloncy et al., 2005)[e] Si/Al =192 Synthesis conditions (2 syntheses): 423 K / 4 days	**Synthesis C** (Tuan et al., 2002)[f] Si/Al =12 Synthesis conditions (2 syntheses): 393 K / 6 days
Seeding 1 [a] Si/Al = 12.5	After 2nd synth.	MB_1: $\Pi = 1.4\times10^{-9}$ MB_2: Π => Gas tight	MB_7: $\Pi = 1.6\times10^{-9}$ MB_8: $\Pi = 1.0\times10^{-9}$	MB_13: $\Pi = 2.0\times10^{-7}$ MB_14: $\Pi = 3.4\times10^{-7}$
Seeding by vacuum	Calcined	MB_1* MB_2: $\Pi = 7.7\times10^{-7}$	MB_7* MB_8: $\Pi = 1.5\times10^{-6}$	MB_13: $\Pi = 1.8\times10^{-6}$ MB_14*
Seeding 2 (Maloncy et al., 2005)[b] Si/Al = 25 Synthesis conditions: 423 K / 40 hr *Seeding by vacuum*	After 2nd synth.	MB_3: $\Pi = 3.0\times10^{-10}$ MB_4: Π => Gas tight	MB_9: $\Pi = 2.7\times10^{-9}$ MB_10: $\Pi = 8.6\times10^{-8}$	MB_15: $\Pi = 3.6\times10^{-10}$ MB_16: $\Pi = 3.2\times10^{-9}$
	Calcined	MB_3* MB_4: $\Pi = 6.3\times10^{-7}$	MB_9: $\Pi = 8.8\times10^{-7}$ MB_10*	MB_15: $\Pi = 6.0\times10^{-7}$ MB_16*
Seeding 3 (Camblor et al., 1997)[c] Si/Al = 100 Synthesis conditions: 413 K / 4 days / 60 rpm *Seeding by dip-coating*	After 2nd synth.	MB_5: Π => Gas tight MB_6: Π => Gas tight	MB_11: $\Pi = 4.6\times10^{-8}$ MB_12: $\Pi = 1.7\times10^{-7}$	MB_17: Π => Gas tight MB_18: $\Pi = 3.8\times10^{-10}$
	Calcined	MB_5: $\Pi = 4.4\times10^{-7}$ MB_6: $\Pi = 4.9\times10^{-7}$	MB_11: $\Pi = 1.4\times10^{-6}$ MB_12*	MB_17: $\Pi = 7.9\times10^{-7}$ MB_18*

* Non-calcined membranes: broken for SEM analysis after 2nd synthesis;

[a] Commercial beta crystals (H-form) supplied by ZEOCHEM in distilled water (10 g/l);

Gel composition:

[b] $SiO_2 : 0.02Al_2O_3 : 0.25(TEA)_2O : 15H_2O : 0.0394Na_2O : 0.02K_2O : 0.058HCl$;

[c] $200SiO_2 : Al_2O_3 : 53(TEA)_2O : 3000H_2O$;

[d] $90SiO_2 : Al_2O_3 : 22.5(TEA)_2O : 1.62K_2O : 3.20Na_2O : 4320H_2O$;

[e] $SiO_2 : 0.0026Al_2O_3 : 0.269(TEA)_2O : 15.5H_2O$;

[f] $TEOS : 0.0429Na_2Al_2O_4 : 0.313(TEA)_2O : 10.393H_2O$.

6.2.3 Dynamic Characterization of Supported Membranes

The dynamic characterization of the zeolite membranes was evaluated by N_2 permeance, 1,3,5-triisopropylbenzene (TIPB) pervaporation, nano-permporometry, and vapour separation. The experiments were first performed in an experimental apparatus available at laboratory The Pore (Delft University of Technology). Afterward, these set of experiments (except for nano-permporometry) were repeated at LSRE-IPB (Instituto Politécnico de Bragança, Portugal) in a new apparatus developed during this Ph.D. thesis, the ZEOPERM unit. This home-made apparatus was designed to measure N_2 permeance, TIPB pervaporation, and vapour separation. The good agreement between the results obtained in both labs, allowed the validation of our experimental unit. For simplicity, it is only described here the ZEOPERM apparatus from LSRE-IPB, and the nano-permporometry setup from laboratory The Pore.

N_2 Permeance

The quality of the membranes was evaluated after each synthesis as well as after the calcination by measuring the permeance of pure N_2 at room temperature in the ZEOPERM unit. The membranes were accommodated in a module developed at LSRE-IPB for the ZMR operation (Figure 6.5). The module is assembled (Figure 6.5*b*-*c*), and connected to the ZEOPERM unit as shown in Figure 6.5e. Schematic representation of the ZEOPERM setup operating in the N_2 permeance mode is shown in Figure 6.6. A constant flowrate of N_2 is fed to the tube side of the membrane, which is kept at constant pressure by a back pressure controller (BPC1) placed in the retentate stream. The permeate side is at atmospheric pressure, and valve V1 is closed. The flux of N_2 through the membrane is then measured at the steady-state in a bubble soap meter (BSM). The permeance Π was calculated based on the measured flow and on the membrane area, considering a transmembrane pressure difference (ΔP) of 200 kPa. This arrangement allows for checking the sealing quality inside the module, by measuring the permeance for different values of ΔP. If the selling is perfect, then the value of the permeance should not change with ΔP.

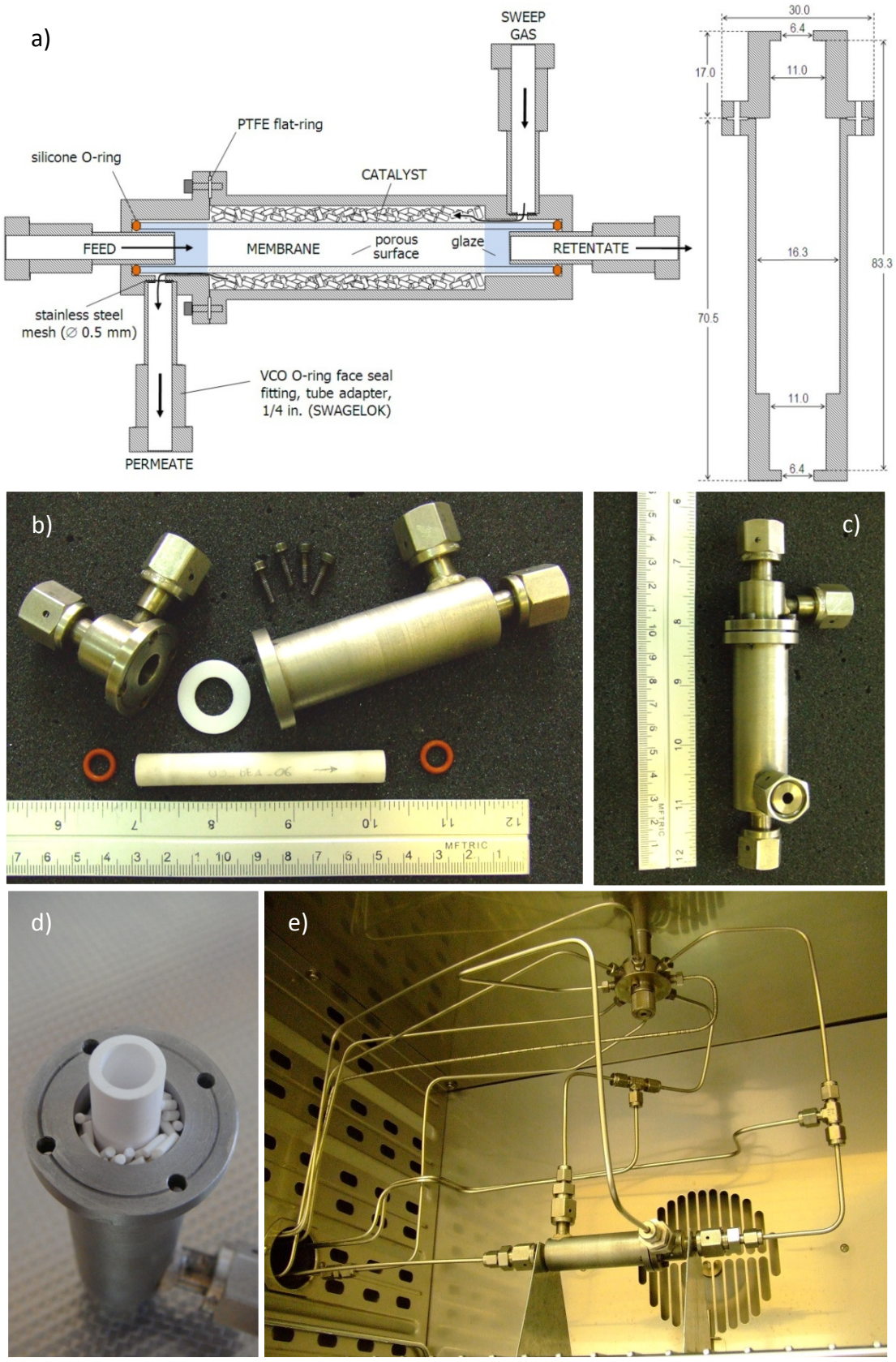


Figure 6.5. Views of the membrane module developed at LSRE: (a) cut view; (b) disassembled module with rings and flange screws; (c) assembled module; (d) ZMR with catalyst packed in the shell side (vol. = 10 cm^3); (e) connection to the 8-way crossover valve of the ZEOPERM unit.

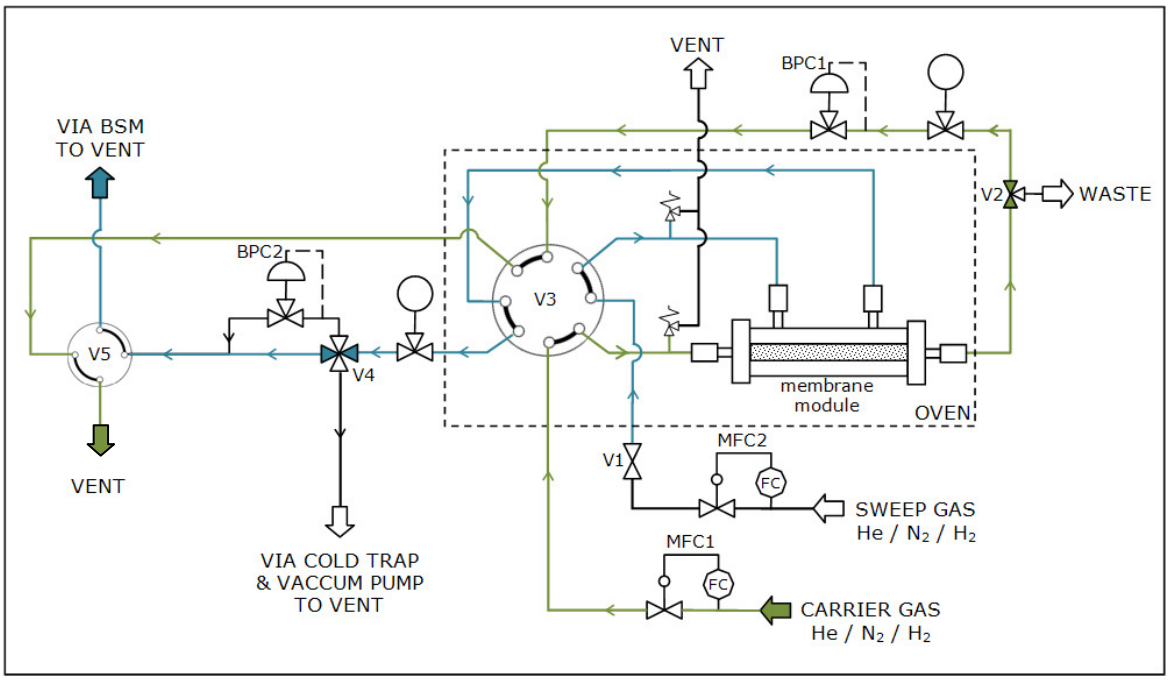


Figure 6.6. Schematic representation of the ZEOPERM setup operating in the N_2 permeance mode: *BPC – back pressure controller; BSM – bubble soap meter; MFC – gas mass flow controller; V1 – on/off valve; V2 – three-way diverter valve; V3 – eight-port crossover valve; V4 – four-way diverter valve; V5 – four-port crossover valve.*

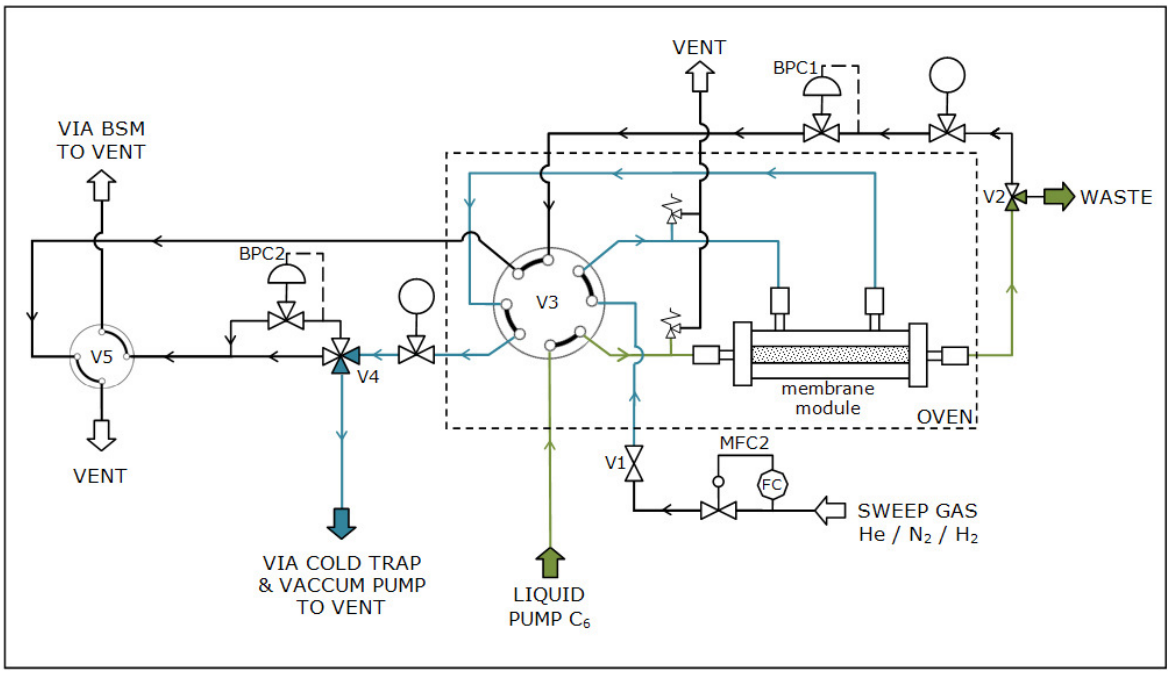
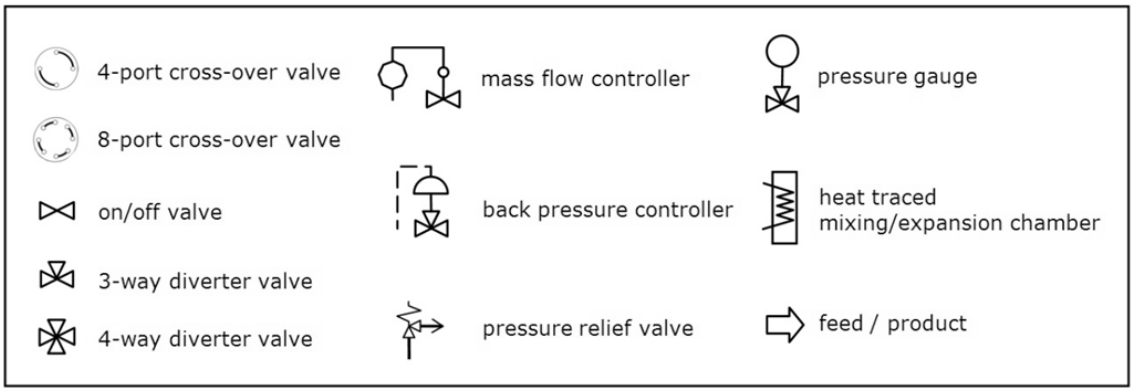


Figure 6.7. Schematic representation of the ZEOPERM setup operating in the pervaporation mode: *V1 – on/off valve; V2 – three-way diverter valve; V3 – eight-port crossover valve; V4 – four-way diverter valve.*

Legend for the ZEOPERM schema:



TIPB Pervaporation

The existence of defects in the zeolite beta membranes was examined by pervaporation of 1,3,5-triisopropylbenzene (TIPB) in ethanol (10 wt % of TIPB) at room temperature (Nishiyama et al., 1996). The ZEOPERM setup can operate in the pervaporation mode (Figure 6.7) directing valve V2 to WASTE, and actuating valve V4 to a cold trap. The TIPB/ethanol mixture was fed by an HPLC pump. The permeate side was kept under vacuum (ΔP_{max} = 985 Pa) using a vacuum pump Büchi Vac-500, from Büchi Labortechnik AG (Flawil, Switzerland). The cold trap cooled with liquid nitrogen was used to continuously collect the permeate vapour which was later analysed by chromatography. The mixture separation factor, *S*, is given by the following expression:

$$S_{12} = \frac{(x_1/x_2)_{Permeate}}{(x_1/x_2)_{Feed}} \qquad (6.1)$$

here, x is the molar fraction, with component 1 being the more permeable molecule.

Nano-Permporometry

Quantification of the amount of defects in the zeolite membranes was determined by nanopermporometry experiments, performed at The Pore (DelftChemTech) in a home-made setup (Figure 6.8) using *n*-heptane as condensable.

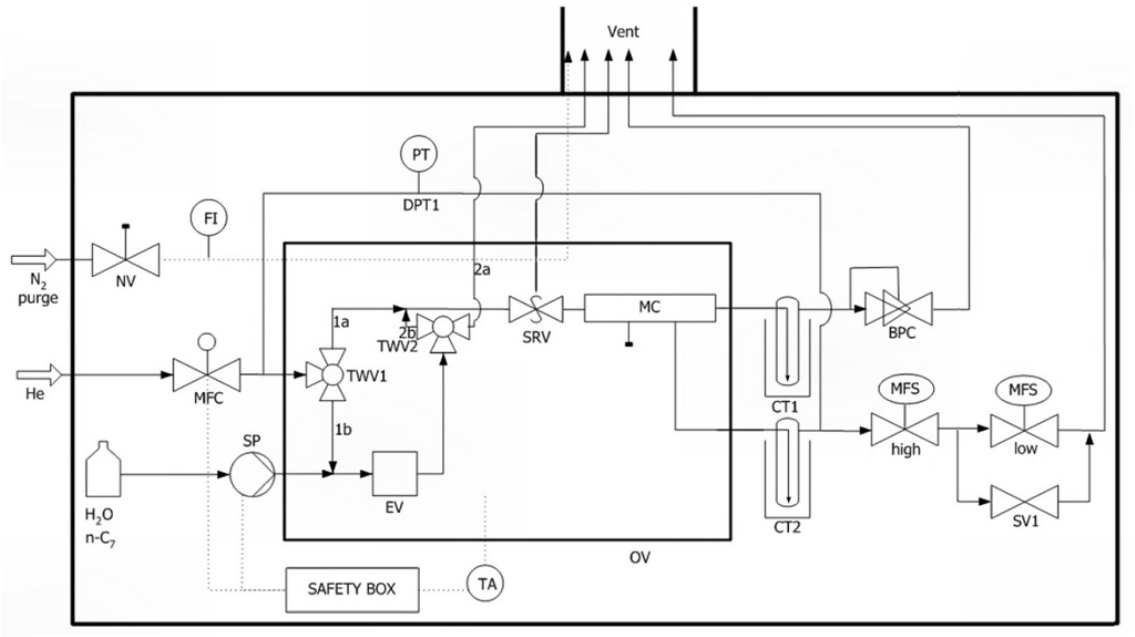


Figure 6.8. Schematic representation of the nano-permporometry setup: BPC – back pressure controller; CT – cold trap; DPT – differential pressure transmitter; EV – evaporation vessel; FI – flow indicator; MC – membrane cell; MFC – mass flow controller; MFS – mass flow system; NV – needle valve; OV – oven; SP – syringe pump; SV – shutoff valve; SRV – safety relief valve; TA – temperature alarm; TWV – three way valve.

First the permeation of dry Helium was measured at the studied temperature (323 K), then the vapour pressure of *n*-heptane was increased gradually in a stepwise manner to a specific partial pressure while measuring the He permeate flow. The pressure difference between permeate and retentate was fixed at 25 kPa. For the measurement of the pore size distribution of defects, the Kelvin equation was used:

$$RT \ln\left(\frac{P}{P_s}\right) = -2V_m \frac{\sigma \cos\theta}{r_{pore}} \qquad (6.2)$$

where V_m, σ, θ and r_{pore} are the molar volume, surface tension, contact angle and pore radius, respectively. R is the universal gas constant and T is the temperature. Capillary condensation occurs in smaller pores at vapour pressure P lower than the saturated vapour pressure P_S. Since the condensed vapour can be assumed to block the permeation of the non-condensable gas, it is possible to estimate the pore size distribution by measuring the permeation rate as a function of the vapour pressure of the condensable gas in the feed stream (Caro and Noack, 2008; Jareman et al., 2005).

Mixture separation by Vapour Permeation

The vapour separation tests were performed in the ZEOPERM setup, operating in the vapour permeation mode, as schematized in Figure 6.9. The liquid hydrocarbon is continuously introduced with a syringe pump (an HPLC pump can be also used when higher flowrates are needed) into an evaporator. The evaporator shown in Figure 6.10*a2* consists of a Swagelok stainless steel sample cylinder, heat traced and insulated with ceramic wool and aluminium tape. The vaporization of the hydrocarbon is promoted by the expansion inside the cylinder at 453 K. The temperature of the evaporator is controlled by a temperature regulator HT-MC1 (Figure 6.9*a3*), from Horst GmbH (Lorsh, Germany). The vapour is then mixed with helium at a fixed partial pressure.

The permeation experiments were carried out at 373 K in an oven equipped with forced convection. The total pressure on both sides of the membrane was set to a value slightly above the atmospheric pressure (e.g., 105 kPa) using the back pressure controllers BPC1 and BPC2. This is essential to ensure that ΔP = 0, because it avoids pressure effects, originated by the difference of the pressure drop associated to both tubing for permeate and retentate.

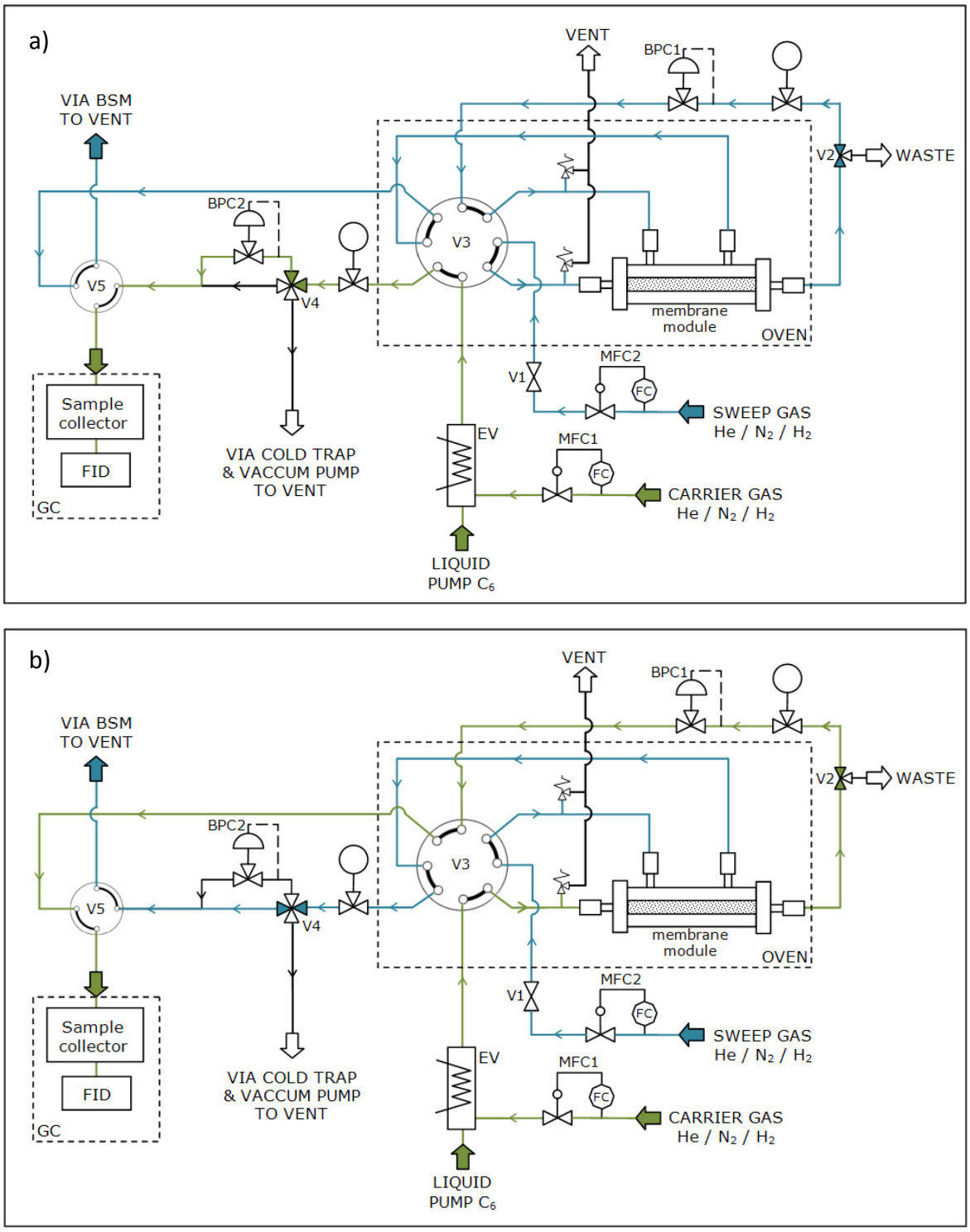


Figure 6.9. Schematic representation of the ZEOPERM setup operating in the vapour separation mode: a) before permeation (feed analysis); b) during permeation (permeate and retentate analysis). *BPC – back pressure controller; BSM – bubble soap meter; EV – evaporator; FID – flame ionization detector; GC – gas chromatograph; Liquid Pump – HPLC pump or syringe pump; MFC – gas mass flow controller; V1 – on/off valve; V2 – three-way diverter valve; V3 – eight-port crossover valve; V4 – four-way diverter valve; V5 – four-port crossover valve.*



Figure 6.10. Details of the ZEOPERM setup: a1) valves and manometers lateral panel; a2) close-up of the evaporator; a3) close-up of the microprocessor controlled temperature regulator for heat tracing.

The feed consisted on an equimolar mixture of 22DMB, 23DMB, 3MP and *n*HEX. Both helium carrier gas flow rate and helium sweep flow rate were set to 50 ml/min. A molar feed ratio of 99/1 He/C_6, was used. The composition of the feed can be measured prior to the permeation experiment, by actuating valves V3 and V5, as shown in Figure 6.9*a*. By actuating again valve V3, the feed is diverted to the membrane module, as schematized in Figure 6.9*b*. The evolution of hydrocarbon flow in both retentate and permeate streams is continuously measured by means of a flame ionization detector (FID). Once the stationary state is reached, the samples are trapped from both the permeate and the retentate streams, being the composition of each

hydrocarbon in the mixture evaluated by chromatography using a 60 m long, 0.28 mm ID, MTX-1 capillary column (Restek Corporation, Bellefonte, PA). The analytical procedure is described in detail in chapter 3. The separation factor, *S*, is given by Equation 6.1.

6.3 Results and Discussion

6.3.1 XRD Patterns

Figure 6.11 shows the XRD patterns of every powder sample collected from the bottom of the autoclave after the hydrothermal synthesis. The diffraction peaks observed at $2\theta = 7.7^{o}$ and $2\theta = 22.5^{o}$ for all samples are in agreement with the more intense peaks of the reference commercial zeolite beta crystals (H-form) provided by Süd-Chemie (Si/Al = 75). It is noted that the reference commercial beta sample and the commercial sample used for the seeding method 1 do not originate from the same manufacturer. The commercial reference zeolite beta sample has been studied in detail in previous chapters for the separation of hexane isomers in fixed bed. The slight shift of all samples relatively to the reference sample is due to the fact the latter was a calcined sample. Despite the different synthesis conditions, the intensity of the characteristic reflections observed for all the samples does not change significantly, suggesting a similar degree of crystallinity. The broad reflection at $2\theta = 7.7^{o}$ indicates all membranes are an intergrowth mixture of polymorph A and B of the zeolite beta. However, the additional features at $2\theta = 9.2^{o}$ for the powder collected from synthesis method A (Seed 1 and 2) could indicate that the presence of polymorph A correspond at least to 80 % of the crystalline structure (Treacy and Higgins, 2007).

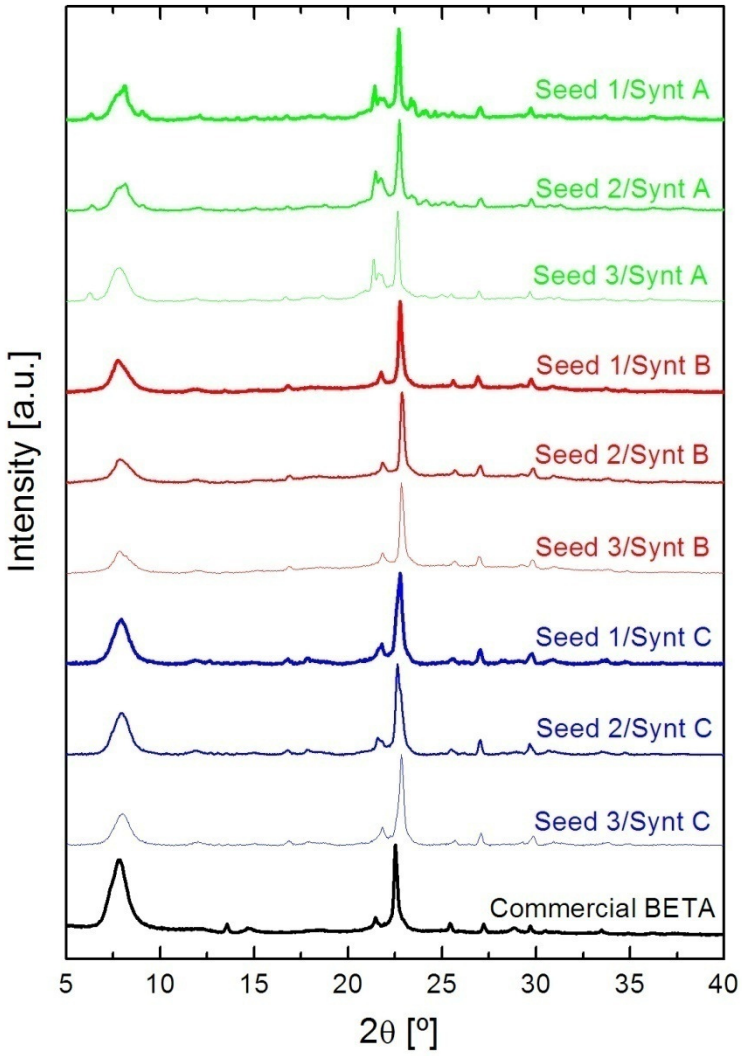


Figure 6.11. XRD patterns of uncalcined powder collected from the beta membranes synthesis compared with the (calcined) reference commercial zeolite beta.

6.3.2 N_2 Permeation

Single gas permeation measurements using N_2 were carried out after each synthesis, at room temperature, on every membrane to verify the quality of the zeolite films. The addition of a second zeolite beta layer onto the supports decreased the N_2 permeance of at least 80%, except for membranes MB_9, MB_10 and MB_12, prepared by synthesis method B. The higher concentration of the solution used in this synthesis has

probably contributed to homogenous nucleation (in solution/liquid phase) causing at the same time the partial dissolution of the zeolite film formed during the first synthesis. Results in Table 6.1 show that leak tight beta membranes can be obtained after two hydrothermal treatments using the synthesis method A. The combination of seeding method 3 with synthesis method A seems to be the most effective procedure to obtain good quality membranes, although the type of seeding hardly affected the quality of the membranes. After calcination, the N_2 permeation indicates values varying from 10^{-7} to 10^{-6} mol/(m^2 s Pa), much lower than those of the α-Al_2O_3 support ($\sim 10^{-5}$ mol/(m^2 s Pa)). The N_2 permeance measured for the membranes MB_5 and MB_6 is similar to that obtained by Flanders et al. (2000) through an alumina supported H-ZSM-5 membrane.

Noteworthy is the influence of the use of seeds in the preparation of beta membranes by method C, since only two syntheses were required to obtain permeances of the same order of magnitude (10^{-7} mol/(m^2 s Pa)) as obtained by Tuan et al. (2002) after five syntheses of 6 days each. Such results clearly show that seeding could account for the compactness of the zeolite beta films.

6.3.3 Morphology

Figures 6.12 to 6.15 show the cross sectional view and top view micrographs of four zeolite beta membranes. The cross sectional views clearly show the zeolite layer on the top of the alumina layer. The zeolite and the alumina layers are well intergrown for all the membranes. SEM images suggest a zeolite layer thickness of about 4-6 μm for the membranes synthesized through method A (Figure 6.12*a* and Figure 6.13*a*), while methods B and C produce thinner layers of about 2.0–2.5 μm (Figure 6.14a and Figure 6.15*a*). Both thickness and morphology of membrane MB_10 were in agreement with the results of Maloncy et al. (2005) using the same synthesis conditions on TiO_2 coated stainless steel disk supports.

The top views in Figures 6.12 to 6.15 (panel *b*) show that the surface of the membranes has a continuous layer of well intergrown crystals with a non-uniform size distribution ranging from 0.2 to 0.7 μm in diameter, except for MB_3, in which the size of the crystals seems to be slightly bigger (around 2 μm). The polycrystalline network of membrane MB_10 appears to be better plugged, nevertheless this type of surface is more susceptible to form cracks during the calcination procedure due to differences in thermal expansion between the zeolite and the support.

6.3.4 TIPB Pervaporation

In order to evaluate the compactness of the most promising zeolite beta membranes, pervaporation experiments of a mixture containing 10 wt % of TIPB diluted in ethanol were carried out at room temperature for 30 min. The results of the pervaporation experiments are given in Table 2. Low concentrations of TIPB were detected in the permeate side for all the membrane tested. Since the kinetic diameter of TIPB (8.5 Å) is greater than the pore size of zeolite beta (7.6 x 6.4 Å), these results indicate that the membranes contain some larger, non-zeolitic pathways. The most selective membranes MB_5, MB_6 and MB_9 exhibited a separation factor ethanol/TIPB $\geq$ 30.

Table 6.2. Pervaporation experiments at room temperature with a 10 wt% TIPB mixture in ethanol.

Membrane	Permeate composition (wt % of TIPB)	ethanol/TIPB separation factor
MB_2	0.7	16
MB_4	0.9	12
MB _5	0.3	32
MB _6	0.4	30
MB _9	0.3	32
MB _15	0.8	14

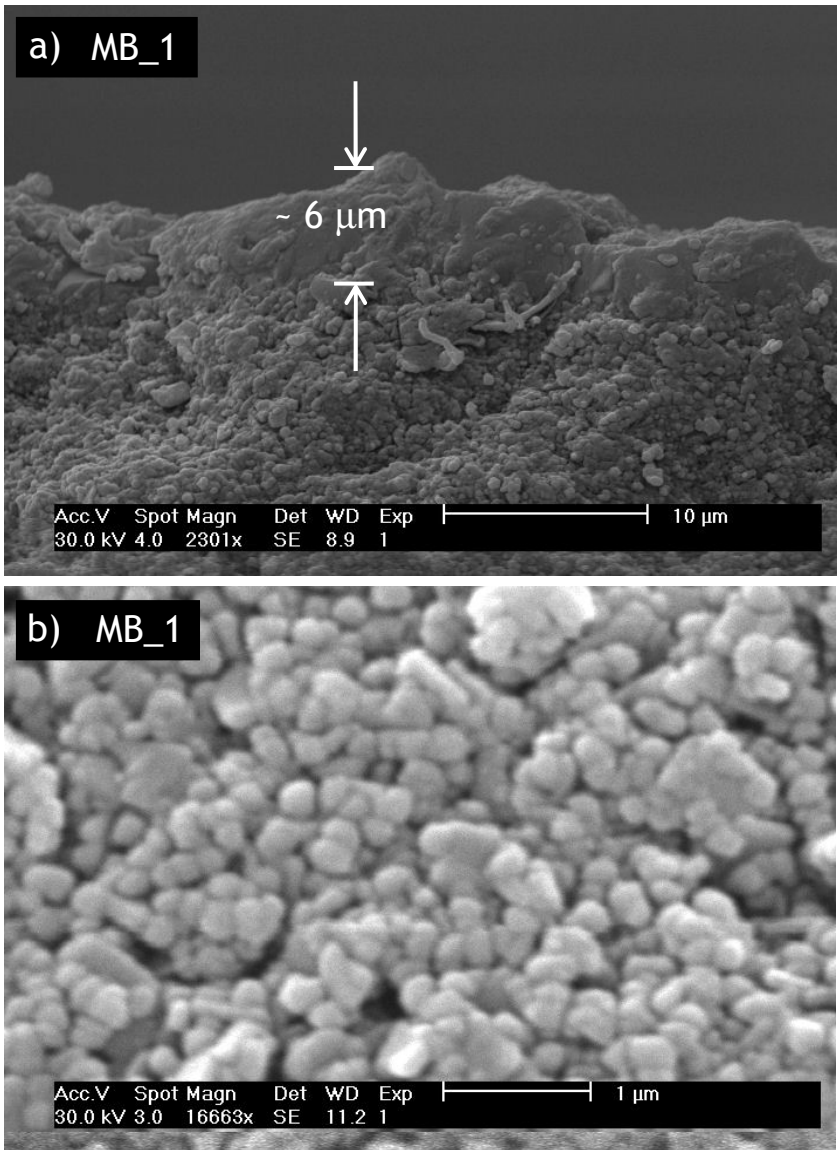


Figure 6.12. SEM micrographs of non-calcined beta membrane MB_1: (a) cross section view; (b) top view.

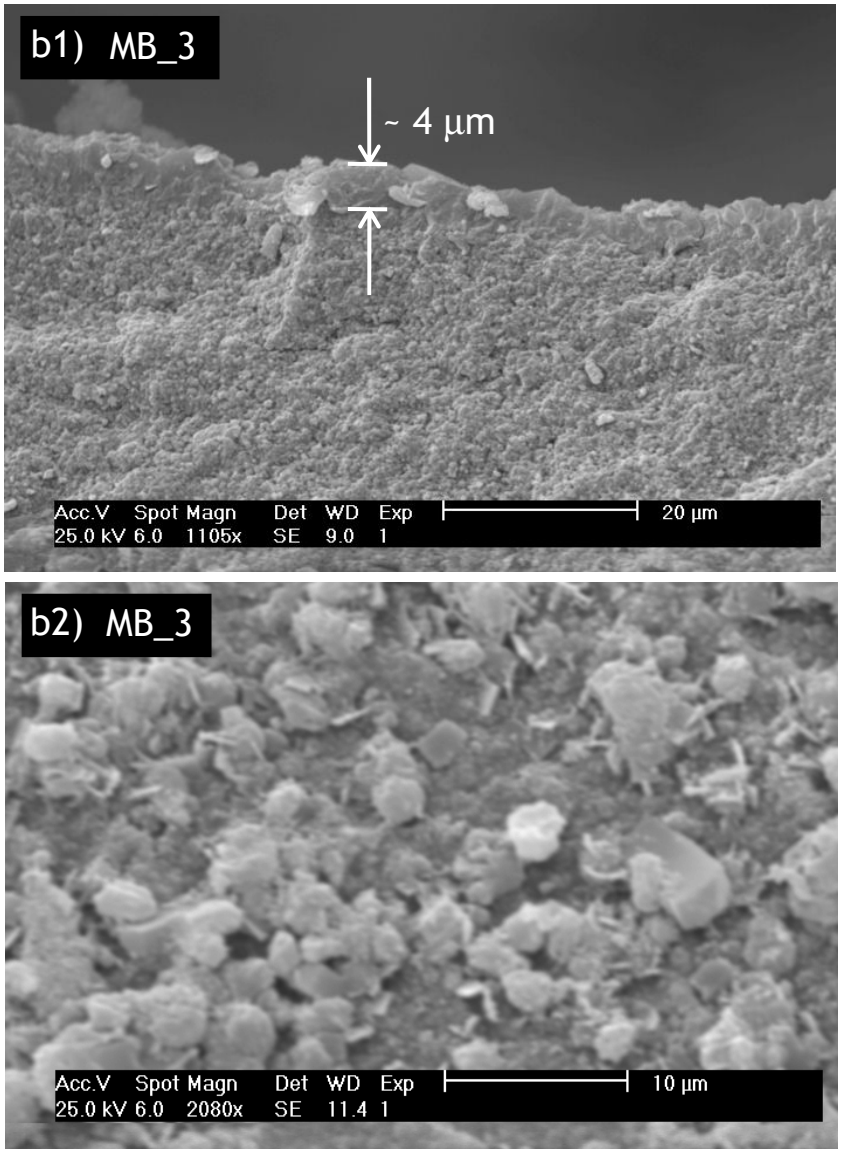


Figure 6.13. SEM micrographs of non-calcined beta membrane MB_3: (a) cross section view; (b) top view.

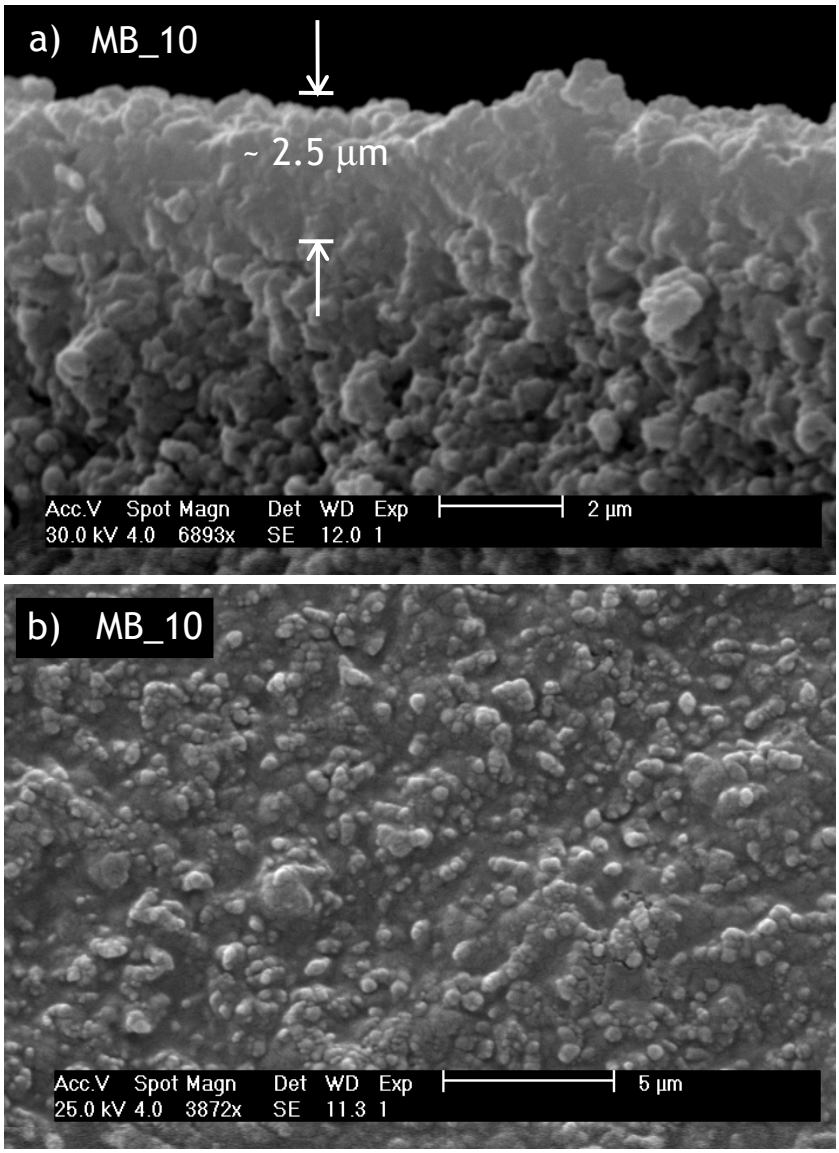


Figure 6.14. SEM micrographs of non-calcined beta membrane MB_10: (a) cross section view; (b) top view.

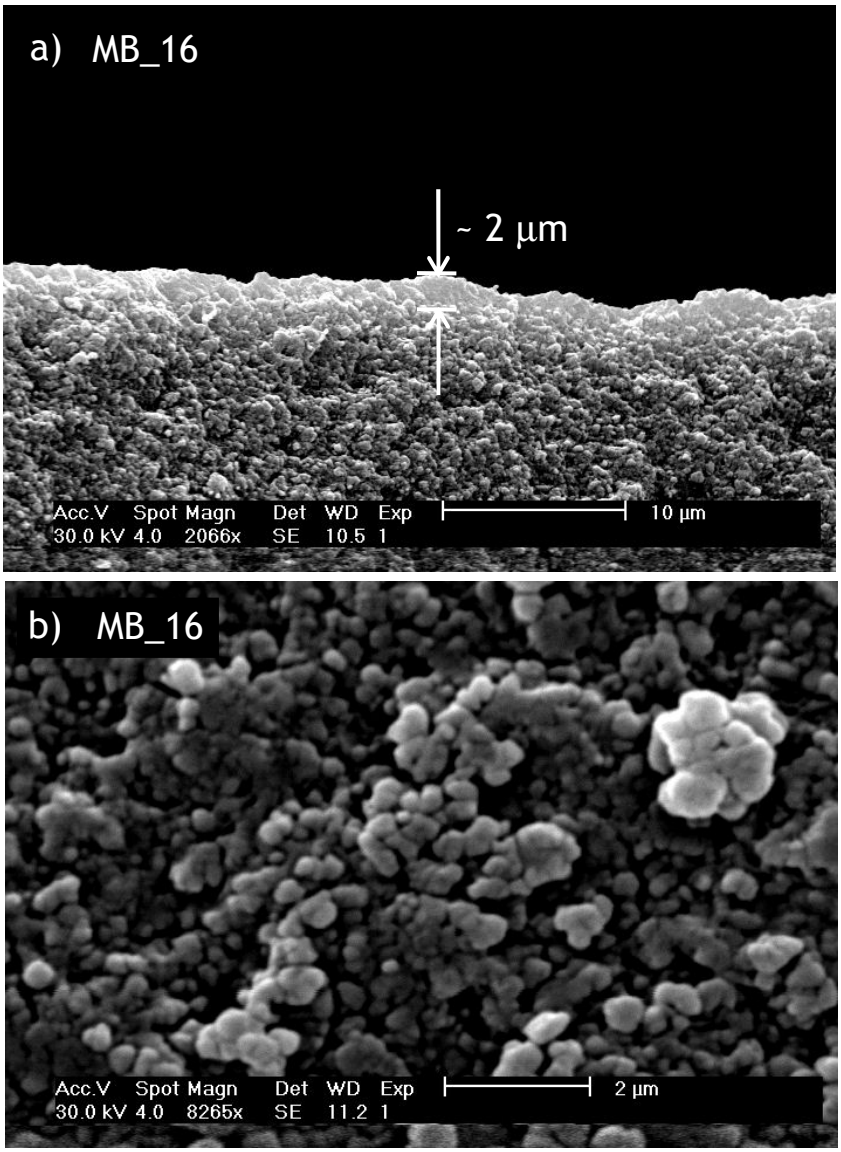


Figure 6.15. SEM micrographs of non-calcined beta membrane MB_16: (a) cross section view; (b) top view.

6.3.5 Permporometry

Quantification of the amount of defects in the zeolite membranes was determined by permporometry. In Figure 6.16, the residual Helium permeance was plotted as a function of the Kelvin diameter, which can be directly calculated from Equation 6.2. The permporometry results are in fair agreement with the pervaporation of TIPB results. MB_15 and MB_4 exhibited in both cases the worst performance, a low ethanol/TIPB separation factor together with a high contribution of defects. Among the other membranes, MB_5 and MB_6 present less than a 5 % of defect contribution to the total flux. Membrane MB_4 showed interestingly a relatively high contribution (8 %) of small defects (< 3 nm) but a negligible contribution of large defects. This is attributed to permeation along grain boundaries. All membranes show this phenomenon to a more or lesser extent.

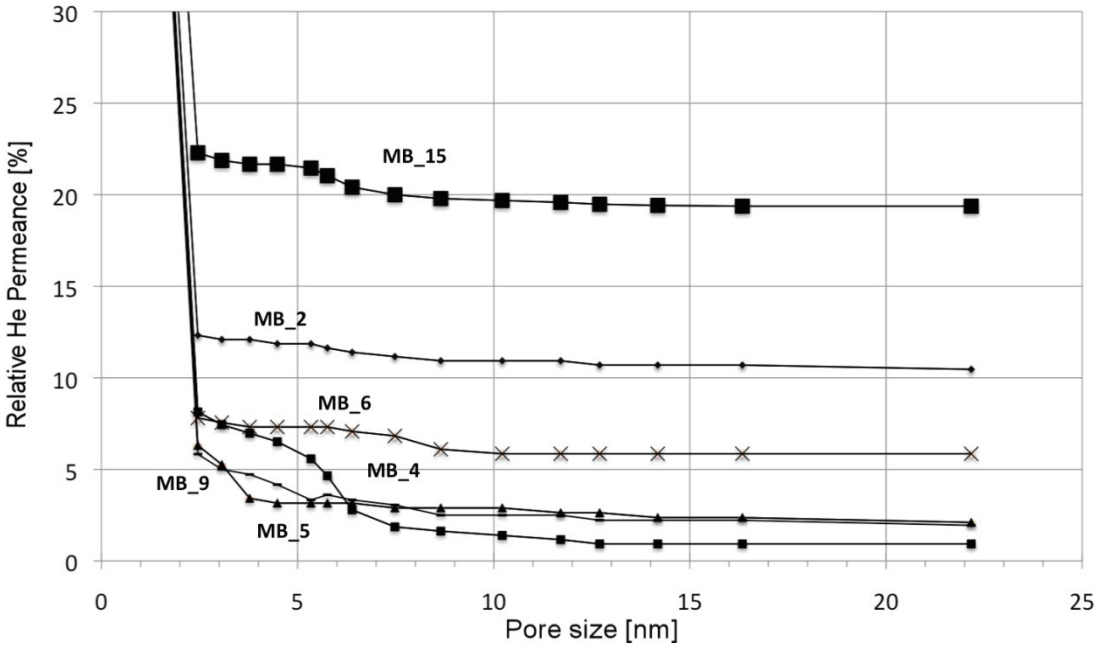


Figure 6.16. Permporometry characterization of the different zeolite beta membranes showing the residual Helium permeance as a measure of the defect concentration. Pore diameters were calculated according to Equation 6.2 considering cos (θ) = 1. T = 323 K, ΔP = 25 kPa.

6.3.6 Mixture Separation Measurements

The separation performance of the characterized membranes was tested in the separation of quaternary equimolar mixtures of nHEX, 3MP, 23DMB and 22DMB through vapour permeation at 373 K. The FID analysis indicated that steady-state was attained in less than 1 h for all the membranes tested, being the steady-state permeate fluxes compared in Figure 6.17. The permeate flux decreases as the degree of branching increases following the order: nHEX >> 3MP > 23DMB > 22DMB. Such result suggests that permeation hierarchy can be dictated by the mobility as well as the sorption affinity of the molecules. Assuming a similar degree of crystallinity for all the membranes synthesized the main factors which may affect their separation performances include: open grain boundaries (which can act as non-zeolitic pores); cracks resulting from detemplation or thermal expansion; Si/Al ratio; film thickness and preferential crystal orientation (Andersson, 2007). All these factors may account for the features shown in Figure 6.17, but the differences of the fluxes are not significant enough to allow distinction between the influence of any of the parameters previously mentioned.

Approximately 40 % of the feed flow crosses the membranes, except for MB_2 and MB_15 where the permeation fraction represents 24 % and 49 % of the feed flow, respectively (see Table 6.3). Such differences in hydrocarbon fluxes are in agreement with the film thickness of their peer membrane MB_1 and MB_16 which are 6 μm and 2 μm thick, respectively (see Figure 6.12 and Figure 6.15).

At 373 K the best membranes in terms of mono-/dibranched isomer separation are MB_4 and MB_5 (Table 6.3), with MB_5 having the highest selectivity with $S_{3MP/22DMB}$ = 1.4. A comparable value was obtained by Maloncy et al. for pervaporation of a binary mixture 2MP/22DMB at 303 K (Maloncy et al., 2005). Also the values for the permeances of the different isomers are of the same order as reported by Maloncy et al. (2005) for BEA membranes of similar thickness. However, comparisons should be made with caution since in the present study a more complex quaternary system is

considered. Funke et al. (1997) obtained no selectivity 3MP/22DMB when using a Silicalite-1 membrane, suggesting a better performance of beta for the branched hexanes separation. Surprisingly, membrane MB_2 exhibits a high separation factor for nHEX (for instance, $S_{nHEX/22DMB}$ = 1.81), while it shows the expected low selectivity for separation of the mono- from dibranched isomers. The selectivity nHEX/dibranched isomers reported in the literature for MFI membranes (Flanders et al., 2000; Gora and Jansen, 2005; Funke et al., 1997) are significantly higher than those measured in this work for zeolite beta membranes. However it should be emphasized that the separation mono-/dibranched C_6 isomers is the key factor for improving the octane quality of the gasoline.

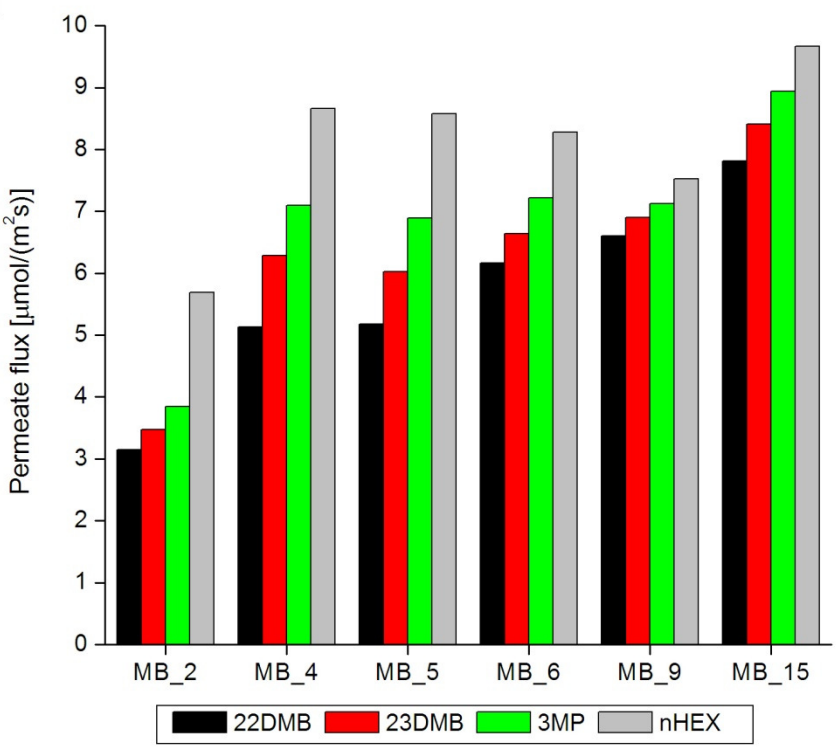


Figure 6.17. Permeate fluxes of 22DMB, 23DMB, 3MP and nHEX equimolar mixture at T = 373 K and p_{mix} = 1 kPa through α-Al_2O_3 supported zeolite beta membranes.

Clearly, the narrower pores of MFI perform better in the separation of the linear from branched isomers, whereas the wider BEA pores discriminate between monobranched and dibranched isomers. In principle, interesting results could be

obtained combining the performances of both structures in such a way that linear/branched and mono-/dibranched separations could be achieved in two subsequent steps.

Table 6.3. Vapour separation experiments of an equimolar mixture nHEX/3MP/23DMB /22DMB in He as carrier gas 50 ml/min; He sweep gas 50 ml/min; p_{mix} = 1 kPa.

Membrane	Temp. (K)	Total isomer permeate flux ($\times 10^{-6}$ mol/(m^2 s))	Permeation fraction	Separation factor, *S*				ΔON†
				3MP/ 22DMB	3MP/ 23DMB	nHEX/ 22DMB	nHEX/ 23DMB	
MB_2	*373*	16.2	0.24	1.22	1.11	1.81	1.64	*+2.2*
MB_4	*373*	27.2	0.40	1.38	1.13	1.69	1.38	*+3.7*
MB_5	*343*	24.0	0.36	1.40	1.15	1.78	1.46	*+3.4*
MB_5	*373*	25.2	0.38	1.40	1.17	1.82	1.52	*+3.9*
MB_5	*403*	26.7	0.40	1.39	1.17	1.83	1.53	*+4.4*
MB_5	*443*	27.5	0.41	1.46	1.18	1.88	1.53	*+4.7*
MB_6	*373*	28.0	0.43	1.22	1.10	1.48	1.33	*+3.3*
MB_9	*373*	27.1	0.39	1.11	1.04	1.19	1.11	*+1.1*
MB_15	*373*	33.7	0.49	1.15	1.06	1.25	1.15	*+2.1*

† $\Delta ON = ON_{Retentate} - ON_{Feed}$

It has been reported by Lee et al. (2008) that adsorption of *n*HEX in MFI may induce crystal swelling. Although XRD and optical microscopy studies show that crystal expansion is less than 0.5 %, such expansion can essentially seal 2 nm membranes (Lee et al., 2008). It has been also suggested that the degree of sealing micro-defects depends on both arrangement/orientation of the crystals and thickness of the membrane (Lee et al., 2008). A combination of these effects could account for the peculiar separation performance of membrane MB_4.

Figure 6.18 shows the molar composition of the retentate stream for vapour permeation of an equimolar quaternary mixture nHEX/3MP/23DMB/22DMB through the zeolite membranes at 373 K. For all the membranes examined, the concentration of the dibranched hexane isomers was increased, while the amount of nHEX was

significantly reduced. The figure also shows the octane number (ON) gain in the retentate, ΔON, which corresponds to the difference, $ON_{Retentate} - ON_{Feed}$. Considering an average value of 74.4 ON in the hydrocarbon feed, then, the ON of the mixture can be boosted up to 4 points with the membrane produced by the combination seeding 3 /synthesis A (MB_5), as shown in Figure 6.18. This figure also shows that the relatively good performance of MB_2 is essentially due to the selective permeation of nHEX. The preferential adsorption of the linear isomer together with the higher thickness of the zeolite film (considering ≈ 6 μm thickness observed by SEM for MB_1) could account for the results obtained with MB_2.

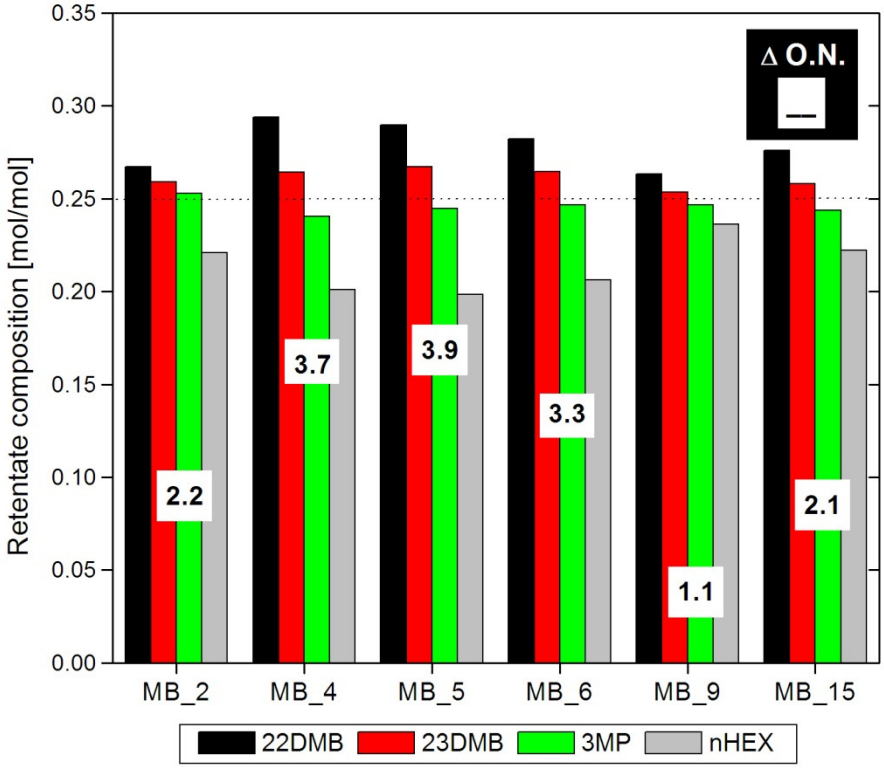


Figure 6.18. Composition of the retentate 22DMB, 23DMB, 3MP and nHEX equimolar mixture at T = 373 K and p_{mix} = 1 kPa through α-Al_2O_3 supported zeolite beta membranes.

Especially noteworthy is the difference in separation performance of MB_5 versus MB_9 when compared with the pervaporation and permporometry results. Despite the similar degree of defects of MB_5 and MB_9, the latter is much less selective. Taking into account that the Si/Al ratio of the synthesis solution used for MB_5 is four

times lower than for MB_9 (see Table 6.1), these results could indicate that the aluminium content plays a role in the separation. In a recent adsorption equilibrium study on MFI samples with different Si/Al ratio, Ferreira et al. (2008) reported that the sorption affinity of hexane isomers increases with aluminium content. Jareman et al. (2003) compared the hydrocarbon isomers separation performance of MFI membranes with almost identical thickness and defects distribution but different Si/Al ratio (Silicalite-1, Si/Al = ∞; ZSM-5, Si/Al = 100). They found that in the range 373-473 K the nHEX/22DMB selectivity of the Silicalite-1 membrane was almost half of the one obtained for the ZSM-5 membrane (Jareman et al., 2003).

From these permeation results combined with the permporometry results, we conclude that small defects (< 3 nm) do not affect strongly the separation performance of the membrane, while thickness and aluminium content may have a larger impact, as apparent from comparing the performance of membranes MB_2 and MB_15 as well as MB_5 and MB_9. The presented results also show permporometry as a more convenient and informative technique to measure defects in microporous membranes than the pervaporation of ethanol/TIPB (Nishiyama et al., 1996).

The influence of the temperature on the separation performance of membrane MB_5 was investigated by studying the vapour permeation of an equimolar hexane isomer mixture in the range 323 – 443 K. Permeation data and selectivity at different temperatures are presented in Table 6.3. The hydrocarbons permeate faster as the temperature increases, indicating the presence of an activated transport mechanism. There is a sigificant increase in the separation factors for membrane MB_5 with temperature up to 443 K; the nHEX/dibranched separation being more temperature dependent than for the case 3MP/dibranched. As a result, an additional improvement of 1.3 ON is obtained by increasing the temperature from 343 K to 443 K. This temperature dependence of the selectivity is in agreement with the results reported in chapter 3, for the fixed bed adsorption of quaternary mixtures of hexane isomers in pellets of zeolite beta.

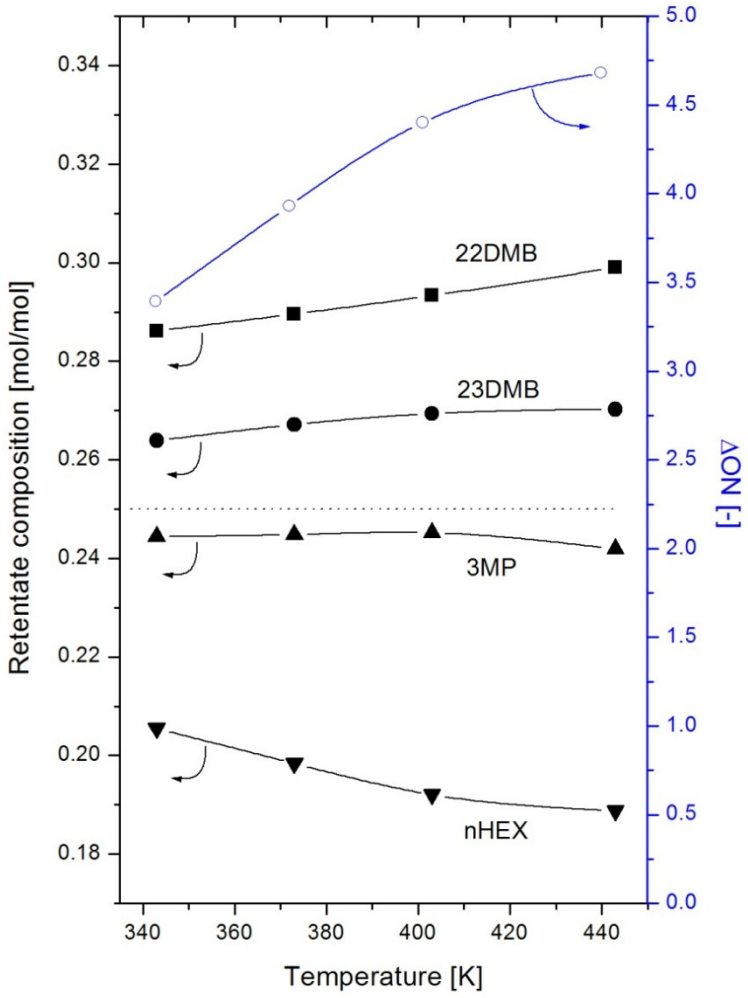


Figure 6.19. Composition of the retentate stream and octane enhancement as a function of the temperature for an equimolar mixture 22DMB, 23DMB, 3MP and nHEX through membrane MB_5. He carrier gas 50 ml/min; He sweep gas 50 ml/min; p_{mix} = 1 kPa.

Figure 6.19 shows both the composition of the retentate stream and the ON improvement as a function of the temperature for membrane MB_5. Clearly the fraction of dibranched isomers increases with the temperature as result of a faster permeation of nHEX through the zeolite film. The composition of the monobranched 3MP is not significantly influenced by the temperature change. Several authors (Sommer et al., 2003; Gora and Jansen, 2005; Funke et al., 1997) reported a significant decrease of the linear/branched selectivity as a function of the temperature for vapour permeation experiments of binary mixtures in MFI membranes. The positive selectivity/temperature relation obtained through our zeolite beta membrane gives

more flexibility for the selection of the operating conditions required to combine such a separation technology with a hydroisomerization unit. These reaction units usually operate in the temperature range 403–423 K in the case of Pt/chlorinated alumina, 453–483 K for sulphated metal oxide catalysts, and 523–553 K for Pt/zeolite based catalysts (Weyda and Köhler, 2003).

Overall, we conclude that the zeolite beta membranes exhibit a relatively low selectivity for the targeted separation. Nevertheless this work demonstrates the octane boosting by selective permeation of linear and single branched isomers from quaternary mixtures containing linear, mono- and dibranched C_6 isomers through zeolite beta membranes.

6.4 Conclusions

Three different synthesis methods and seeding techniques for producing zeolite beta membranes on tubular alumina supports have been studied. The surface of the membranes was completely covered by well intergrown crystals with a size distribution ranging from 0.2 to 2 μm in diameter; the thickness of the zeolite layers is about 5 , 2.5 and 2 μm for synthesis methods A, B and C, respectively. N_2 permeation results show that synthesis method A is the most effective procedure to obtain good quality membranes. The preparation duration was also considerably reduced compared to literature. Pervaporation experiments of a mixture ethanol/TIPB together with permporometry characterization demonstrate the low contribution of defects in most of the synthesized membranes. The vapour separation experiments at 373 K using a quaternary equimolar mixture of hexane isomers show that permeate flux increases as the branching degree decreases following the order: nHEX >> 3MP > 23DMB > 22DMB. The best quality membrane MB_5 exhibited an activated transport mechanism with a stronger temperature dependency of *n*HEX and 3MP than the dibranched hexanes. In the retentate the fraction of dibranched isomers increases

while the concentration of monobranched and normal hexane decreases compared to the feed composition. At 443 K, the octane number ON can be increased by almost five points. Comparison with literature suggest that zeolite beta performs better in the separation of mono- from dibranched C_6 isomers, while MFI membranes are more effective for the separation linear/branched C_6 isomers.

The ZEOPERM setup demonstrates a large versatility in the characterization of zeolite membranes, and is ready to be used for the study of the performance of a ZMR unit combining zeolite beta membranes with a hydroisomerization catalyst.

6.5 References

Andersson, C. Factors Affecting MFI Membrane Quality, Ph.D. Thesis, Luleå University of Technology, Sweden (2007).

Camblor, M.A.; Corma, A.; Mifsud, A.; Perez-Pariente, J.; Valencia, S. Synthesis of Nanocrystalline Zeolite Beta in the Absence of Alkali Metal Cations. *Stud. Surf. Sci. Catal.* 105, 341-348 (1997).

Caro, J.; Noack, M. Zeolite Membranes – Recent Developments and Progress. *Micropor. Mesopor. Mat.* 115, 215-233 (2008).

Ferreira, A.F.P.; Mittelmeijer-Hazeleger, M.C.; Bliek, A. Can Alkane Isomers be Separated? Adsorption Equilibrium and Kinetic Data for Hexane Isomers and their Binary Mixtures on MFI. *Adsorption* 13, 105–114 (2007).

Ferreira, A.F.P.; Mittelmeijer-Hazeleger, M.C.; Bliek, A.; Moulijn, J.A. Influence of Si/Al Ratio on Hexane Isomers Adsorption Equilibria. *Micropor. Mesopor. Mat.* 111, 171-177 (2008).

Flanders, C.L.; Tuan, V.A.; Noble, R.D.; Falconer, J.L. Separation of C_6 Isomers by Vapor Permeation and Pervaporation through ZSM-5 Membranes. *J. Membr. Sci.* 176, 43–53 (2000).

Funke, H.H.; Argo, A.M.; Falconer, J.L.; Noble, R.D. Separations of Cyclic, Branched, and Linear Hydrocarbon Mixtures through Silicalite Membranes. *Ind. Eng. Chem. Res.* 36, 137–143 (1997).

Gora, L.; Jansen, J.C. Hydroisomerization of C_6 with a Zeolite Membrane Reactor. *J. Catal.* 230, 269–281 (2005).

Jareman, F.; Hedlund, J.; Sterte, J. Effects of Aluminum Content on the Separation Properties of MFI Membranes. *Sep. Purif. Technol.* 32, 159-163 (2003).

Jareman, F.; Andersson, C.; Hedlund, J. The Influence of the Calcination Rate on Silicalite-1 Membranes. *Micropor. Mesopor. Mat*. 79, 1-5 (2005).

Lee, J.B.; Funke, H.; Noble, R.D.; Falconer, J.L. High Selectivities in Defective MFI Membranes. *J. Membr. Sci.* 321, 309-315 (2008).

Maloncy, M.L.; van den Berg, A.W.C.; Gora, L.; Jansen, J.C. Preparation of Zeolite Beta Membranes and their Pervaporation Performance in Separating di- from mono-Branched Alkanes. *Micropor. Mesopor. Mat.* 85, 96–103 (2005).

Nishiyama, N.; Ueyama, K.; Matsukata, M. Synthesis of Defect-Free Zeolite-Alumina Composite Membranes by a Vapor-Phase Transport Method. *Microporous Mater.* 7, 299-308 (1996).

Sommer, S.; Melin, T.; Falconer, J.L.; Noble, R.D. Transport of C_6 Isomers through ZSM-5 Zeolite Membranes. *J. Membr. Sci.* 224, 51–67 (2003).

Torres, M.; López, L.; Domínguez, J.M.; Mantilla, A.; Ferrat, G.; Gutierrez, M.; Maubert, M. Olefins Catalytic Oligomerization on New Composites of Beta-Zeolite Films Supported on α-Al_2O_3 Membranes. *Chem. Eng. J.* 92, 1–6 (2003).

Torres, M.; Gutiérrez, M.; López, L.; Múgica, V.; Gomez, R.; Montoya, J.A. Controlled Crystal Growth of β Zeolite Films on Alumina Supports. *Mater. Lett.* 62, 1071–1073 (2008).

Treacy, M.M.J.; Higgins, J.B. *Collection of Simulated XRD Powder Diffraction Patterns for Zeolites*, 5th revised edition. Elsevier: Amsterdam (2007).

Tuan, V.A.; Li, S.; Falconer, J.L.; Noble, R.D. In Situ Crystallization of Beta Zeolite Membranes and Their Permeation and Separation Properties. *Chem. Mater.* 14, 489-492 (2002).

Weyda, H.; Köhler, E. Modern Refining Concepts — an Update on Naphtha-Isomerization to Modern Gasoline Manufacture. *Catal. Today* 81, 51-55 (2003).

7

Separation of C_6 Isomers in Metal-Organic Frameworks

A screening study for mixtures of C_6 isomers was performed in three different metal-organic frameworks (MOFs).The first is a rigid zirconium terephthalate UiO-66, which possesses octahedric and tetrahedric cages of diameter 12 Å and 9 Å, respectively; the second one is a chromium trimesate MIL-100(Cr), which possesses a rigid structure with giant cages accessible through 5-9 Å microporous windows; and the third is the flexible $Zn_2(BDC)_2(H_2O)_2 \cdot (DMF)$ (MOF-2), in which the pore system contains 1-D large channels. Multicomponent equimolar experiments show that UiO-66 exhibits inverse shape selectivity for C_6 isomers, being the retention governed by the rotational freedom of the molecules in the small cages. In the MIL-100(Cr), the sorption hierarchy is similar to the one found in zeolite beta. Finally, MOF-2 exhibits extraordinary n/iso selectivity, by making use of an unusual guest-dependent dynamic behaviour to exclusively take up nHEX, while hindering the access of branched C_6 isomers to the pore system.

7.1 Introduction

In the last decade, a new class of synthetic porous materials, metal–organic frameworks (MOFs), has been developed into one of the most promising alternatives to zeolites for gas separations. MOFs have the potential for making a significant impact in separation processes since they offer the possibility to be tuned varying their pore size and geometry for specific applications (Férey, 2007; Yaghi et al., 2003). Numerous reviews summarize the most recent research efforts in the field (Férey, 2008; Kitagawa et al., 2004; Rowsell and Yaghi, 2004). Some of these MOFs exhibit another interesting feature which is beyond the scope of traditional adsorbents, the flexibility of the structure can be induced by external stimuli, such as pressure, temperature, and guest molecules (Noguchi et al., 2005; Serre et al., 2007a, 2007b; Trung et al., 2008). This particular property opens a window of opportunities for the development of energy saving adsorption separation processes. Review of gas selective adsorption in rigid and flexible MOFs is given by Li et al. (2009). An overview of the potential applications of MOFs in the chemical industry is presented by Czaja et al. (2009).

Since 2007, our team has been working in collaboration with leading groups on MOFs synthesis, with the goal of exploring the use of these materials, as an alternative to traditional adsorbents, such as zeolites or carbon molecular sieves, for gas and vapour separation. In the scope of these collaborations, sorption properties of C_6 isomers mixtures on three different MOFs have been measured by fixed bed adsorption at LSRE-IPB. The materials which make part of the study presented in this chapter are the following:

- the rigid MOFs UiO-66 and MIL-100(Cr), produced by the group of Prof. Gérard Férey and Prof. Christian Serre at Institut Lavoisier (CNRS/Université de Versailles, France);
- and the flexible MOF-2, synthesised by the group of Prof. Banglin Chen at the University of Texas-Pan American (Edinburg, TX, USA)[*].

[*] Presently at the Dept. of Chemistry, University of Texas at San Antonio (TX, USA).

7.2 Activation of the MOFs and Preparation of the Adsorption Column

The MOF samples have been supplied, either in their mother liquor or in powder form with occluded solvent. The first samples must be filtered and dried at moderate temperature (ca. 353 K), prior to activation. The activation procedure consists of removing the excess solvent in the micropores (remaining from the synthesis), in order to obtain crystals with permanent porosity. The evacuation of the solvent is typically performed under vacuum, at temperatures which can range up to 673 K, depending on the thermal stability of the MOF material.

In general, after the activation, the MOF sample is a very light fine powder that cannot be packed directly into an adsorption column, because the compaction of the powder would block the passage of the gas, causing a sharp increase in the pressure drop. To avoid such problem, it is recommended to create agglomerates by compressing the powder. However, some MOFs, such as for instance MOF-5, have a weak structural resistance, consequently their microcrystalline structure could collapse once exposed to external mechanical pressure (Alcañiz-Monge et al., 2009). In these cases, agglomerates can be created using a polymeric binder, for instance, Finsy et al. (2009) prepared agglomerates of MIL-53(Al) using polyvinyl alcohol as binding agent. This technique has a great potential for industrial application, but its use might not be appropriate for a first evaluation of the intrinsic adsorption properties of the MOF material. Alternatively, when either the mechanical resistance or the binder effect are unknown, adsorbing beds can be made by mixing the MOF crystals with refractory ceramic (or glass) wool. Although it does not ensure a homogeneous packing, this simple technique is adequate for preliminary lab tests.

7.3 Separation of C_6 Isomers in the Rigid MOF UiO-66

The Zr-BDC MOF (or UiO-66) was synthesized at Institut Lavoisier de Versailles (Saint-Quentin-en-Yvelines, France) by the group of Prof. G. Férey and Prof. C. Serre, and was later tested at LSRE-IPB for the separation of C_6 isomers. Details about the synthesis and characterization of the UiO-66 are given by Cavka et al. (2008).

The UiO-66 is a zirconium-based MOF with 1,4-benzene-dicarboxylate (BDC) as linker. Its rigid porous structure consists of octahedric cages of diameter 12 Å, and tetrahedric cages of diameter 9 Å, as shown in Figure 7.1. The molecules can be adsorbed in both types of cages. The cages are accessed through 5-10 Å microporous windows. MOF UiO-66 possesses a good chemical resistance toward solvents like water, acetone, benzene and dimethylformamide (DMF). Additionally, UiO-66 has an exceptional mechanical (> 10 tons/cm^2) and thermal stability (up to 773 K), which makes it a serious candidate for the industrial application (Cavka et al., 2008).

7.3.1 Experimental Procedure

The UiO-66 sample was tested in agglomerate form. The agglomerates were produced by compaction of the powder into disks in an infrared (IR) press by applying a pressure of 650 kg/cm^2. Afterwards, the disks were broken into fragments, and sieved, in order to obtain a particle size distribution ranging from 0.5 to 1.5 mm (Figure 7.2).

Prior to adsorption experiments, the agglomerates were activated under vacuum (100 mbar) at 473 K, during 12 h. A stainless steel column (L_B = 100 mm, d_B = 4.6 mm) packed with 405 mg of agglomerates was connected to the multicomponent breakthrough curve apparatus described in chapter 3. Several adsorption runs were performed with pure *n*HEX to check up on the permanent microporosity of the adsorbent. For the first runs, it was observed a successive increase in the breakthrough time; the reproducibility of the breakthrough curves being achieved from the fourth

experiment. This observation suggests that the operating conditions of the activation procedure were not completely efficient regarding the evacuation of the solvent, from the microporous structure.

Multicomponent breakthrough curves with C_6 isomers in the vapour phase were measured in the apparatus already described in chapter 3. A detailed explanation of the operating procedure can be found in chapter 3, as well.

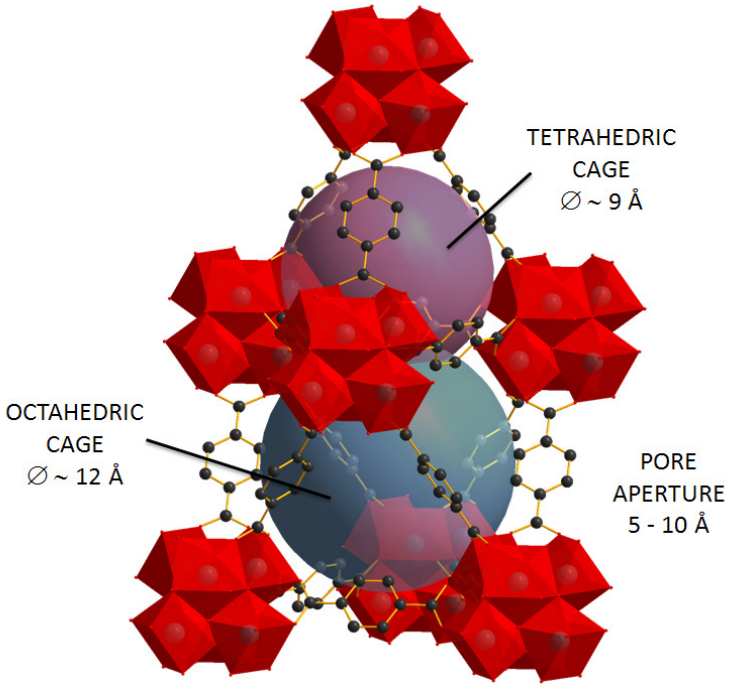


Figure 7.1. Cages in MOF UiO-66. Adapted from Chevreau (2009).

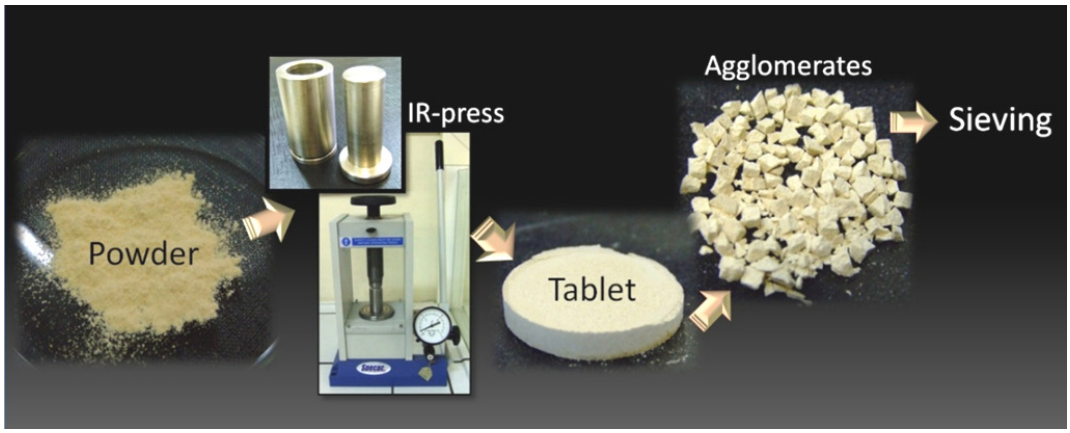


Figure 7.2. Preparation of agglomerates from a UiO-66 powder sample.

7.3.2 Adsorption of Quaternary Mixtures

To study the potential application of UiO-66 for the separation of C_6 isomers, we have performed a screening study covering four temperatures in the range 343–473 K, at low pressure (0.6 kPa) and moderate pressure (6.3 kPa). The experimental conditions, and amount adsorbed are listed in Table 7.1.

Table 7.1. Experimental conditions of the multicomponent breakthrough curves in UiO-66.

Run	T (K)	Helium flowrate (ml/min)	Hydrocarbon pressure (kPa)	Partial loading (g/100g_{ads})				Total loading (g/100g_{ads})
				22DMB	23DMB	3MP	*n*HEX	
UiO66_*1a*	343	50.0	0.6	2.81	3.04	2.64	0.87	9.35
UiO66_*2a*	373			2.63	2.76	2.01	0.53	7.92
UiO66_*3a*	423			1.95	1.92	1.02	0.29	5.18
UiO66_*4a*	473			0.61	0.57	0.40	0.20	1.78
UiO66_*1b*	343	15.0	6.3	2.84	3.35	2.95	1.75	10.89
UiO66_*2b*	373			2.97	3.26	2.70	1.46	10.39
UiO66_*3b*	423			2.97	3.06	2.19	1.12	9.34
UiO66_*4b*	473			2.41	2.34	1.63	0.80	7.19

As it can be seen from Table 7.1, the sorption capacity of UiO-66 is significantly higher than the one obtained with pellets of zeolite beta; for instance, at 423 K and hydrocarbon pressure 6.3 kPa, the total amount of C_6 isomers adsorbed in the UiO-66 is 9.3 g/100g_{ads}, while in zeolite beta this value is only of about 6.0 g/100g_{ads}. Nevertheless, it should be taken into account that the commercial pellets of zeolite beta contain 30 wt% of inert binder. Thus, considering just pure adsorbent, the difference in terms of capacity is reduced to only 8.5 wt%.

What is surprising in MOF UiO-66 is the fact that branched C_6 are more adsorbed compared to their linear isomer. Additionally, this unusual behaviour is observed in all the range of pressure and temperature herein addressed. This reversed preferential adsorption is evident from Figure 7.3, where it is shown the multicomponent

breakthrough curves for equimolar quaternary mixtures of C_6 isomers in UiO-66 (the experimental conditions are listed in Table 7.1). It is clearly seen that *n*HEX is the less retained molecule in the ranges of temperature and pressure studied. The large overshoot observed for *n*HEX, indicates a significant difference in sorption affinity compared to its branched isomers. The extension of the overshoot is more pronounced at higher pressure, and increases as the temperature decreases, i.e., the higher the coverage the higher the overshoot. Another interesting remark is the change in the adsorption hierarchy of the branched molecules at high pressure:

T = 343 K $\rightarrow$ $23DMB > 3MP > 22DMB$

T = 373 K $\rightarrow$ $23DMB > 22DMB > 3MP$

T = 423 K $\rightarrow$ $23DMB = 22DMB > 3MP$

T = 473 K $\rightarrow$ $22DMB > 23DMB > 3MP$

Similar behaviour has been observed from the adsorption of C_5/C_6 isomers in zeolite beta (see chapter 4); nevertheless, in the case mentioned, there was a displacement of the C_5 isomers breakthrough curves relatively to the C_6.

The effect of the temperature on the sorption selectivity is shown in Figure 7.4. Since we are dealing with equimolar mixtures, the selectivity can be calculated by the ratio of the amount adsorbed, q_1/q_2, being component 2 the more adsorbed. It can be seen from panel *a* of Figure 7.4, that the selectivity between *n*HEX and dibranched isomers is significant at low pressure, exhibiting a maximum of 5.2 at 373 K. Interestingly, no maximum is observed at moderate pressure (panel *b* of Figure 7.4); the selectivity between the dibranched C_6 and the linear isomers exhibits a monotonic increase with the temperature. Regarding the separation mono-/dibranched, the general trend is that the selectivity slightly increases with the temperature, and slightly decreases with the partial pressure. At the same conditions, $S_{22DMB/3MP}$ in UiO-66 is significantly lower than $S_{3MP/22DMB}$ in zeolite beta (see chapter 3); for instance, at 473 K and p_{isom} = 6.3 kPa, in UiO-66 we have $S_{22DMB/3MP}$ = 1.5, while in zeolite beta $S_{3MP/22DMB}$ = 2.7. Unlike zeolite beta, the UiO-66 does not made a significant discrimination between dibranched C_6 isomers.

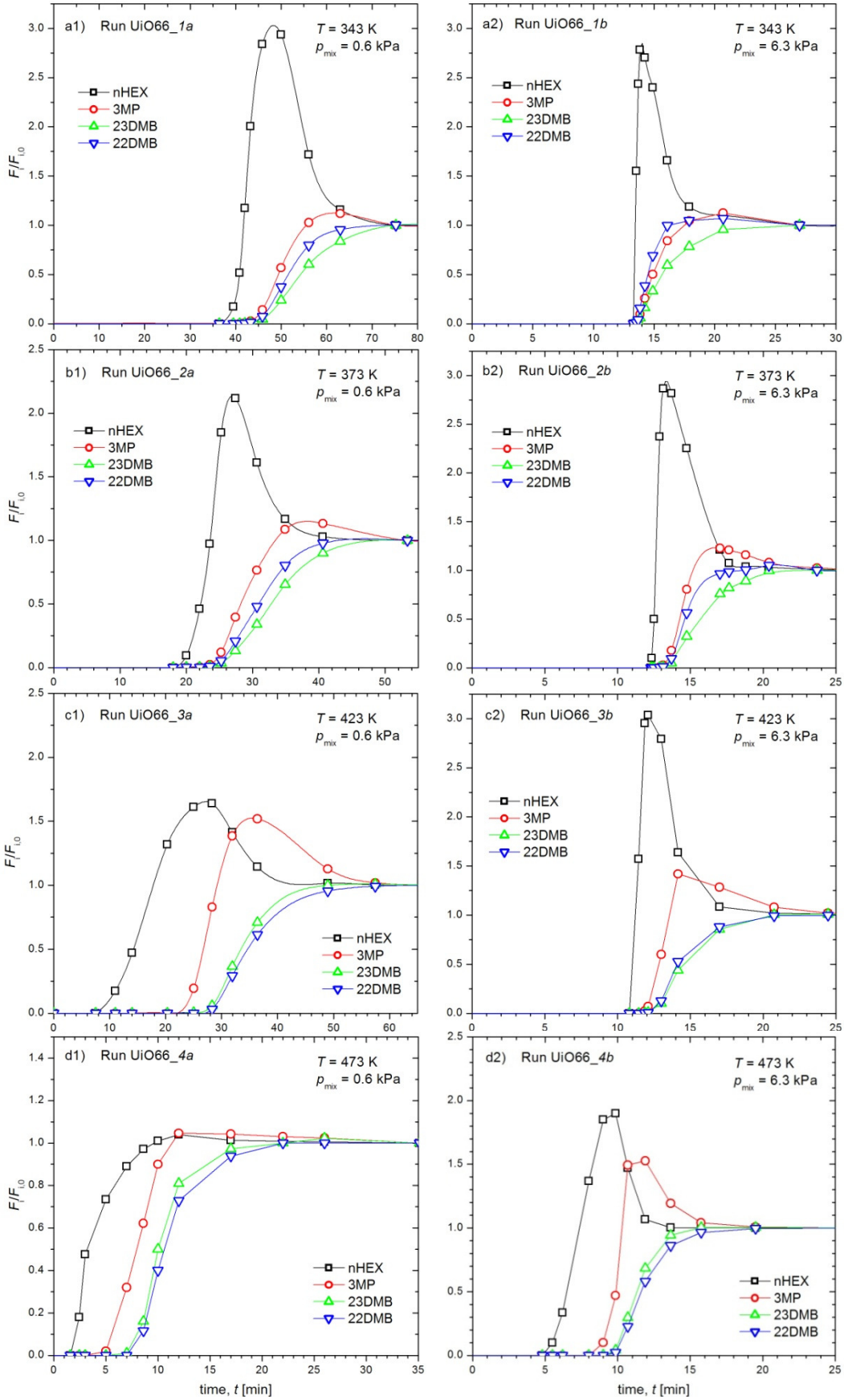


Figure 7.3. Quaternary breakthrough curves of C_6 isomers in UiO-66.

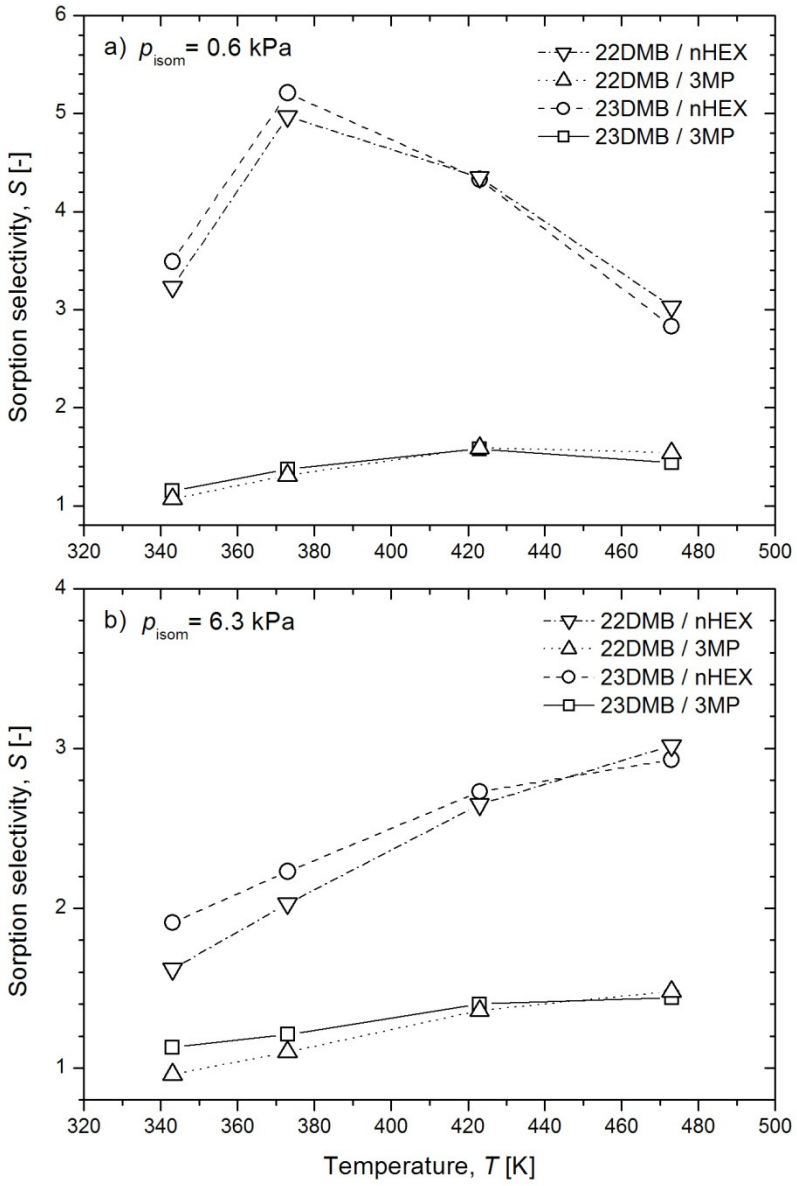


Figure 7.4. Effect of the temperature in the sorption selectivity in MOF UiO-66 at a) 0.6 kPa, and b) 6.3 kPa.

According to the classical view on adsorption, the sorption selectivity is essentially governed by interaction energy. At low coverage, an adsorbed molecule is attracted by van der Waals forces towards the pore walls; the closer the molecules approaches the pore walls, the higher the intensity of the interactions. For instance, it is well known that the *n*HEX is preferentially adsorbed over its branched homologues on most zeolites because the configuration of the linear chain maximizes the contact surface

area with the walls. The van der Waals volume is a good measure of the degree of interaction between molecules and pore walls, and its variation as a function of the branching degree of the C_6 isomers is illustrated in Figure 7.5. The values of the van der Waals volume were taken from Calixto and Raso (1982).

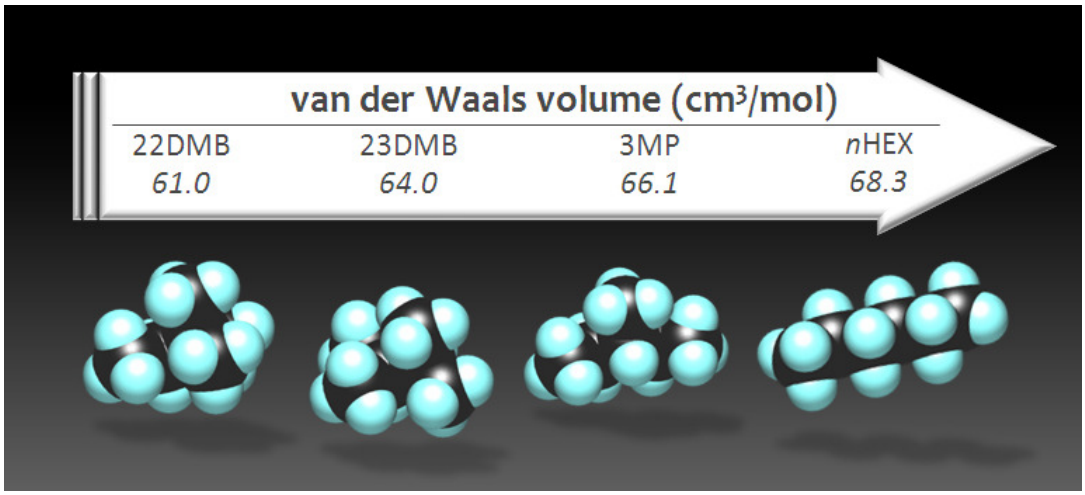


Figure 7.5. Van der Waals volume of C_6 isomers.

Unlike the general trend of typical microporous adsorbents, the UiO-66 exhibits higher capacity for bulkier molecules, i.e., molecules with lower van der Waals volume (see Figure 7.5). The preferential adsorption of branched alkanes over their linear counterparts has been experimentally observed by Santilli et al. (1993) and Denayer et al. (2004) in zeolite SAPO-5, and by Denayer et al. (2005) in zeolite MCM-22. However, as far as our knowledge goes, this is one of the first experimental demonstrations of inverse selectivity for long chain alkanes in MOF materials.

To better understand the inverse selectivity phenomena in MOF UiO-66, one should examine first, the structures SAPO-5 (AFI-type topology) and MCM-22 (MWW topology), in terms of their pore geometry. The panel *a* of Figure 7.6 shows that the pore system in SAPO-5 consists of one-dimensional, straight cylindrical channels of diameter 7.3 Å. This type of tubular pores only allows for the translational motion of the molecules. It was observed by Denayer et al. (2004) that when a mixture of

22DMB, 2MP and *n*HEX is injected in a column packed with SAPO-5, the more retained component is the 22DMB, followed by the *n*HEX and the 2MP. The preferential adsorption of the dibranched isomer is explained by the higher packing efficiency of the shorter molecules, as illustrated in panel *a* of Figure 7.6. This behaviour is also called in the literature as length entropy effect, and was extensively addressed in molecular simulation studies (Krishna et al., 2002; Krishna and van Baten, 2007; Schenk et al., 2003).

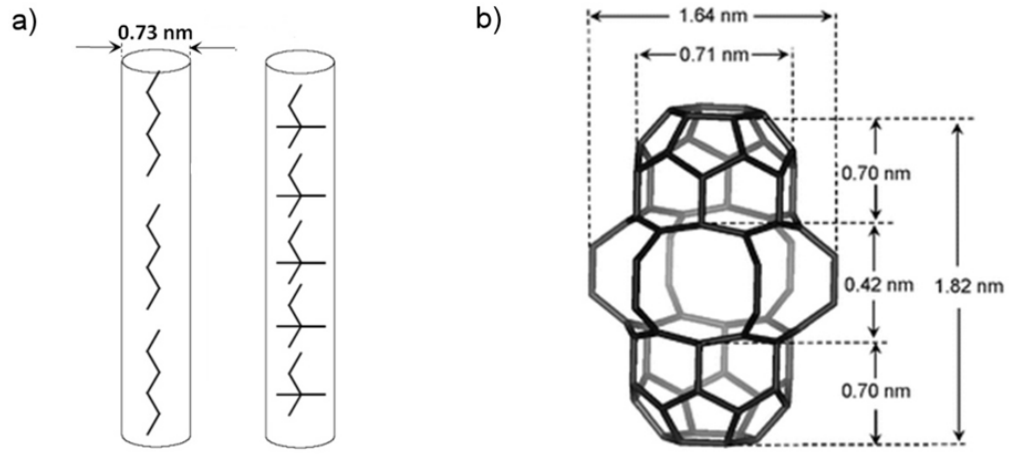


Figure 7.6. Schematic representations: a) length entropy effect during adsorption of *n*HEX, 3MP, 22DMB and 23DMB in the cylindrical channels of AFI (adapted from Smit and Krishna, 2003); b) MWW supercage (taken from Huang et al. (2009)).

Panel *b* of Figure 7.6 shows the supercage in zeolite MCM-22, which consist of a larger central cage, and two pockets located at the top and the bottom of the central cage. The supercage can be accessed through six apertures of dimensions 4.2 × 5.1 Å. In an experimental work, Denayer et al. (2005) determined that in the MCM-22, the order of the sorption hierarchy in terms of loading is 3MP > *n*HEX > 22DMB. The authors suggest that the short molecule 3MP adsorb preferentially in the pockets of the MCM-22 supercage, where they maximize energetic interaction with the zeolite. On the other hand, longer molecule *n*HEX is located in the larger central part of the supercage, because their rotational motion in the pocket is restricted. The bulkier dibranched isomer 22DMB is less adsorbed, because it cannot access to the supercages through the 4.2 × 5.1 Å apertures. In zeolite MCM-22, the preferential adsorption of

the monobranched alkane over its linear isomer is referred in the literature as a case of inverse shape selectivity based on the differences in rotational freedom in the pockets of the supercage (Denayer et al., 2004, 2005). That is to say, the shape-selectivity mechanism is due to a rotational entropy effect.

The comparison between Figure 7.1 and panel *b* of Figure 7.6 shows that the pore system of MOF UiO-66 is, in a certain way, similar to the one of MCM-22. For instance, both structures possess two different types of cages: the large cages have a diameter 12 Å and 16 Å, in UiO-66 and MCM-22, respectively; the smaller cages have a diameter of 9 Å and 7 Å, in UiO-66 and MCM-22, respectively. Such similarity might explain the inverse selectivity observed in UiO-66. The main difference, in relation to MCM-22, is that the cages can be accessed through windows with a larger pore aperture ranging from 5 to 10 Å. This particularity can explain the preferential adsorption of the bulkier dibranched C_6 isomers in UiO-66. Moreover, the distinct feature of the *n*HEX breakthrough curves shown in Figure 7.3, suggests that the linear chain is too long to fit in the small cages. On the other hand, the similarity between the breakthrough curves of monobranched and dibranched C_6 isomers indicates that these molecules are short enough to rotate freely inside the small cages.

To conclude, it was demonstrated that the retention of C_6 isomers in MOF UiO-66 could be governed by the rotational freedom of the molecules in the small cages.

7.4 Separation of C_6 Isomers in the Rigid MOF MIL-100(Cr)

The chromium hybrid solid MIL-100(Cr) (MIL = Material Institute Lavoisier) was first synthesised by Férey et al. (2004) at Institut Lavoisier de Versailles (France), and results from the combination of Cr^{3+} ions with trimesic acid (benzene-1,3,5-tricarboxylate ≡ BTC) under hydrothermal conditions. The linkage of the metal centres to the rigid carboxylate ligands generates microporous super-tetrahedral units of chemical composition $Cr_3F(H_2O)_3O[C_6H_3\text{-}(CO_2)_3]_2{\cdot}nH_2O$ ($n \approx 28$). The resulting cubic cell volume is huge (380,000 $Å^3$), with two types of mesoporous cages, as shown in Figure 7.7. After removal of the guest molecules, the free internal diameters are close to 25 Å and 29 Å. The cages are accessible through microporous windows of 5.5 Å and 8.6 Å.

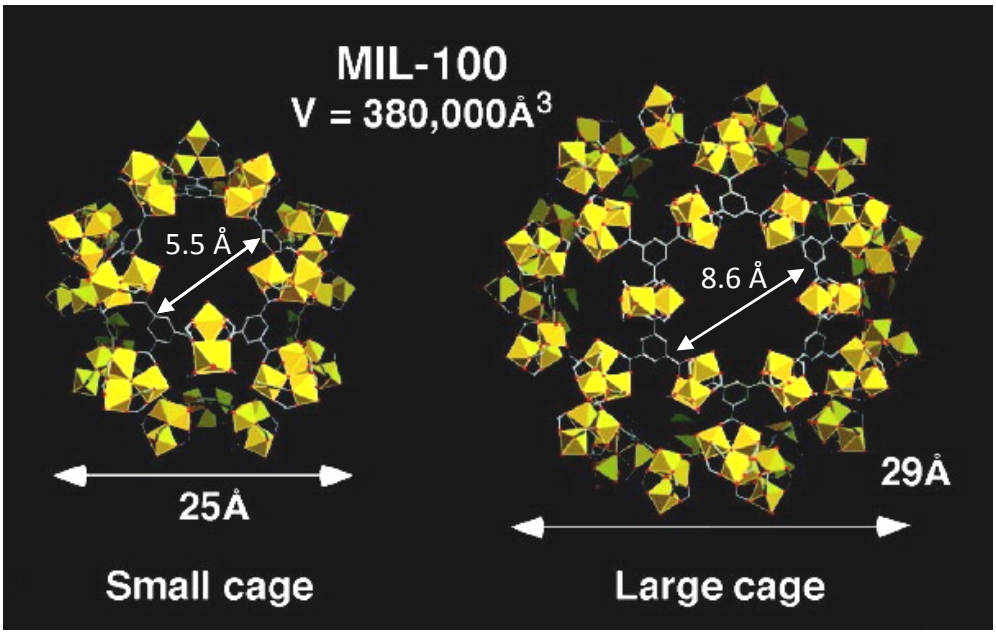


Figure 7.7. Cages of MIL-100(Cr) (Illustration taken from Llewellyn et al. (2008)).

At first sight, it seems interesting to evaluate the potential of MIL-100(Cr) for the separation of C_6 isomers, essentially because the 25 Å diameter cages (which have the potential to take up a significant amount of molecules) are accessible only through 5.5 Å windows, which in theory, might discriminate between monobranched and dibranched isomers (see kinetic diameters in Figure 2.2).

7.4.1 Experimental Procedure

The material was activated in a vacuum oven using two different procedures: under vacuum (0.1 bar) during 12 h at room temperature (Act_1), and under vacuum (0.1 bar) during 12 h at 423 K (Act_2). The first procedure was used to evacuate the non-coordinated water from the microporous structure, whereas the second results in the evacuation of the whole amount of water contained into the structure MIL-100(Cr).

There is a lack of information in the literature about the mechanical resistance of MIL-100(Cr). For that reason, the sample activated through procedure Act_2 was tested in both the powder and the agglomerate form (Figure 7.8). The agglomerates were produced by compaction of the powder into disks by applying a pressure of ca. 160 kg/cm^2, and the disks were broken into fragments and sieved (diameter ranging from 0.5 to 1.5 mm). The packing of the adsorption column, with the MIL-100(Cr) in powder form, has been done by mixing the adsorbent with a small quantity of ceramic wool.

Multicomponent breakthrough experiments in vapour phase were performed in a stainless steel column (L_B = 100 mm, d_B = 4.6 mm), following the procedure described in chapter 3.

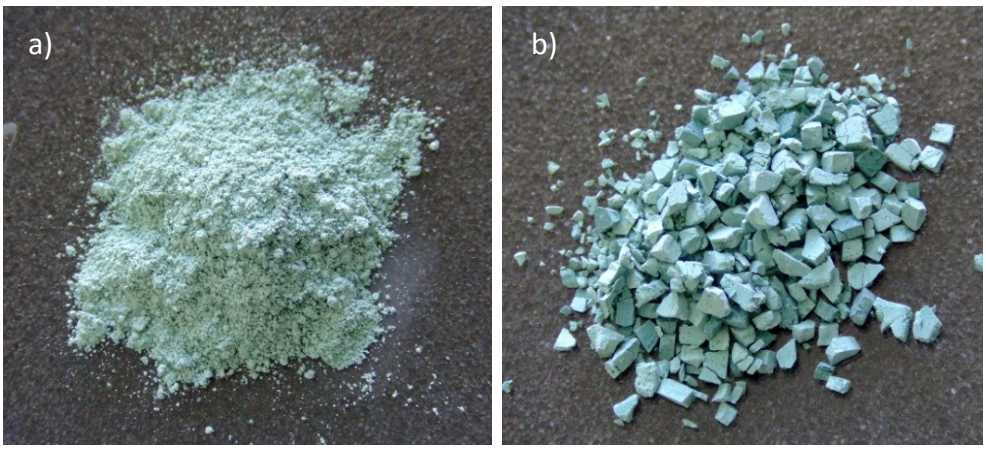


Figure 7.8. MOF MIL-100(Cr) a) in powder form, and b) in agglomerate form.

7.4.2 Influence of the Coordinated Water in the Adsorption of C_6 Isomers in MIL-100(Cr)

The influence of the coordinated water molecules in the adsorption of linear and branched hexane isomers was investigated performing a set of multicomponent breakthrough curves in samples of MIL-100(Cr) activated through method Act_1 and Act_2. About four experiments had to be performed after activation by method Act_1 in order to obtain reproducible results, indicating that activation conditions Act_1 are not totally efficient in removing the whole amount of non-coordinated water from the structure.

The experimental conditions and the amount adsorbed for each component in an equimolar mixture of 22DMB, 23DMB, 3MP, and *n*HEX are summarized in Table 7.2. At the operating conditions used in this work, if the coordinated water is present in the MIL-100(Cr), the sorption capacity is lower than those obtained with typical microporous zeolites (e.g., 6.4 g/100g_{ads} for MIL-100(Cr) against 8–12 g/100g_{ads} for zeolites such as beta, 5A or silicalite). However, the capacity is increased of 3.6 times, to a value of about 23 g/100g_{ads}, when the coordinated water is evacuated. Moreover, it is demonstrated further in the text, that capacity is even higher if the sample is used in the powder form.

Table 7.2. Experimental conditions for the equimolar quaternary breakthrough curves, and partial loadings (T= 323 K; p_{isom}= 10.0 kPa).

Activation method	Adsorbent form	Mass of adsorbent (mg)	Helium flow (ml/min)	Loading (g/100g_{ads})				Total loading (g/100g_{ads})
				22DMB	23DMB	3MP	*n*HEX	
Act_1	Agglom.	961	10.0	0.50	1.11	1.61	3.13	6.36
Act_2	Agglom.	441	10.0	3.21	5.11	5.83	8.93	23.08

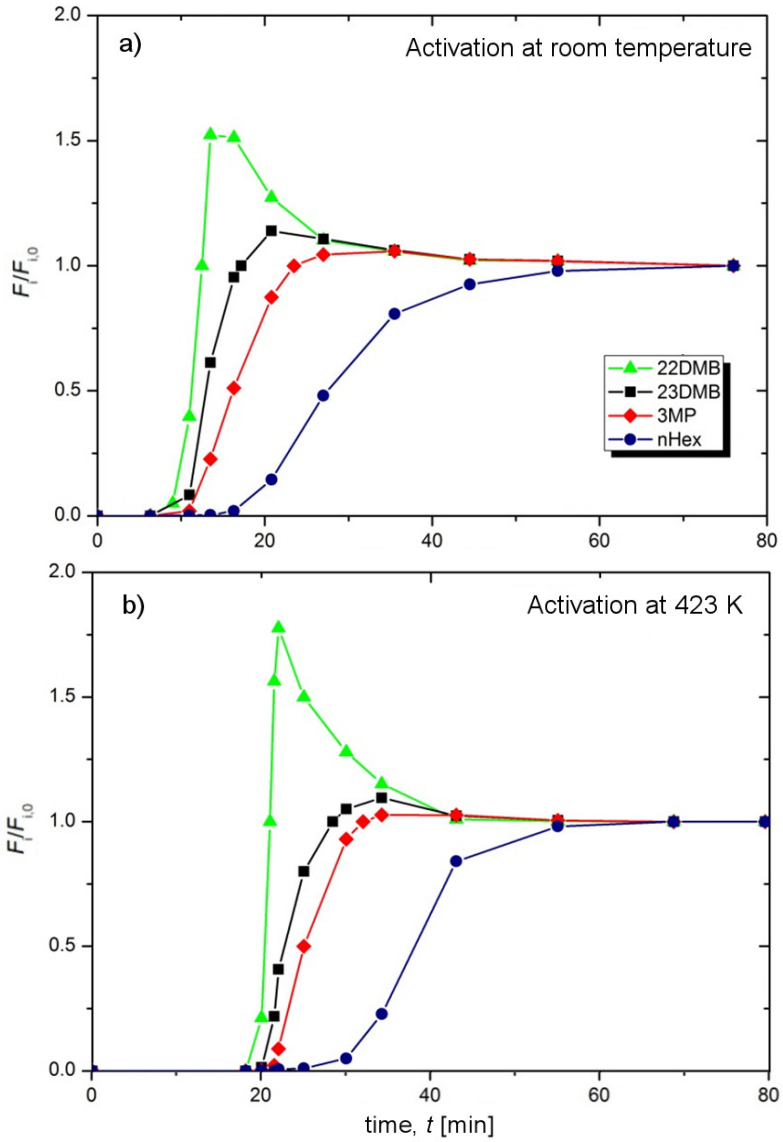


Figure 7.9. Equimolar quaternary breakthrough curves of C_6 isomers in agglomerates of MIL-100(Cr), at T= 323 K and p_{isom}= 10 kPa: a) with coordinated water (Act_1); b) without coordinated water (Act_2).

Figure 7.9 shows the quaternary equimolar breakthrough curves, obtained with samples activated through methods Act_1 (panel *a*), and Act_2 (panel *b*). It can be seen that the presence of coordinated water molecules does not influence the sorption hierarchy. Moreover, the hierarchy order is the same that the one obtained with zeolite beta and the opposite compared to MOF UiO-66. Despite the similar shape of the breakthrough curves represented in panels *a* and *b* of Figure 7.9, it is clear from

Table 7.3 that there is a significant decrease on the sorption selectivities $S_{3MP/dibranched}$ and $S_{nHEX/3MP}$ when coordinated water is evacuated.

Table 7.3. Sorption selectivity obtained from the equimolar quaternary breakthrough curves shown in Figure 7.9.

Activation method	Sorption Selectivity (-)		
	$S_{3MP/22DMB}$	$S_{3MP/23DMB}$	$S_{nHEX/3MP}$
Act_1	3.2	1.5	1.9
Act_2	1.8	1.1	1.5

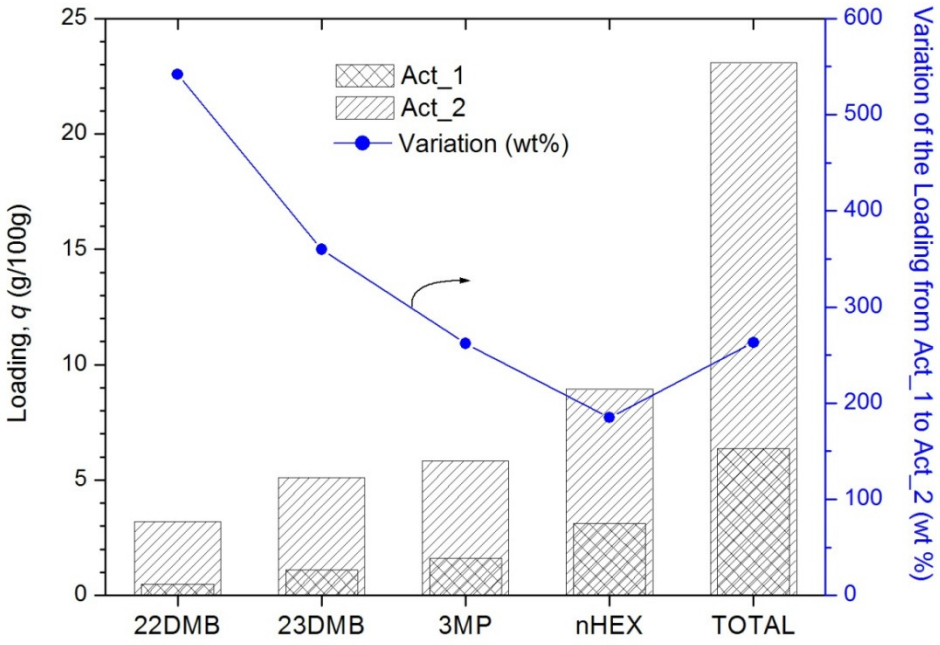


Figure 7.10. Influence of the coordinated water on the adsorption capacity of MIL-100(Cr) for an equimolar quaternary mixture.

Interesting is the influence of the coordinated water on the loading of each isomer. In Figure 7.10, it is compared the amount adsorbed of each component, with and without the presence of coordinated water in the framework MIL-100(Cr). It is

observed that the increase of the loading, resulting from the evacuation of the coordinated water, is more pronounced as the degree of branching increases. These results indicate that coordinated water molecules more significantly affect the adsorption of the bulkier molecules, suggesting also, that the water molecules could be located close to the windows, hindering in a certain way, the access of the C_6 isomers to the cages.

7.4.3 Effect of the Pressing/Shaping on the Adsorption of C_6 Isomers in the MIL-100(Cr)

In Figure 7.11, we compare the adsorption of quaternary mixtures in two samples of MIL-100(Cr); the first was used directly in powder form (panel *a* of Figure 7.11), whereas the second consists of agglomerates produced from the powder (panel *b* of Figure 7.11) following the procedure previously described in the experimental section.

Table 7.4 shows that adsorption capacity has decreased 30 wt %, on average, by applying a mechanical pressure of 160 kg/cm^2. Such effect is in part due to the reduction of the surface area in the shaped material, in comparison to the powder. However, it is seen from Table 4, that the influence of the compression is more stressed as the degree of branching increases; for instance, in the case of *n*HEX, the shaping procedure causes a reduction on the loading of 17.2 wt %, whereas for 22DMB the capacity decreases 54.9 wt %. Therefore, there is probably another phenomenon responsible for the more pronounced reduction of the loading of the 22DMB, such as for example the collapse of part of the MOF structure. However, such a conclusion should be taken with caution, because it requires a detailed X-ray diffraction study, in order to investigate the structural resistance of MIL-100(Cr) against mechanical pressures.

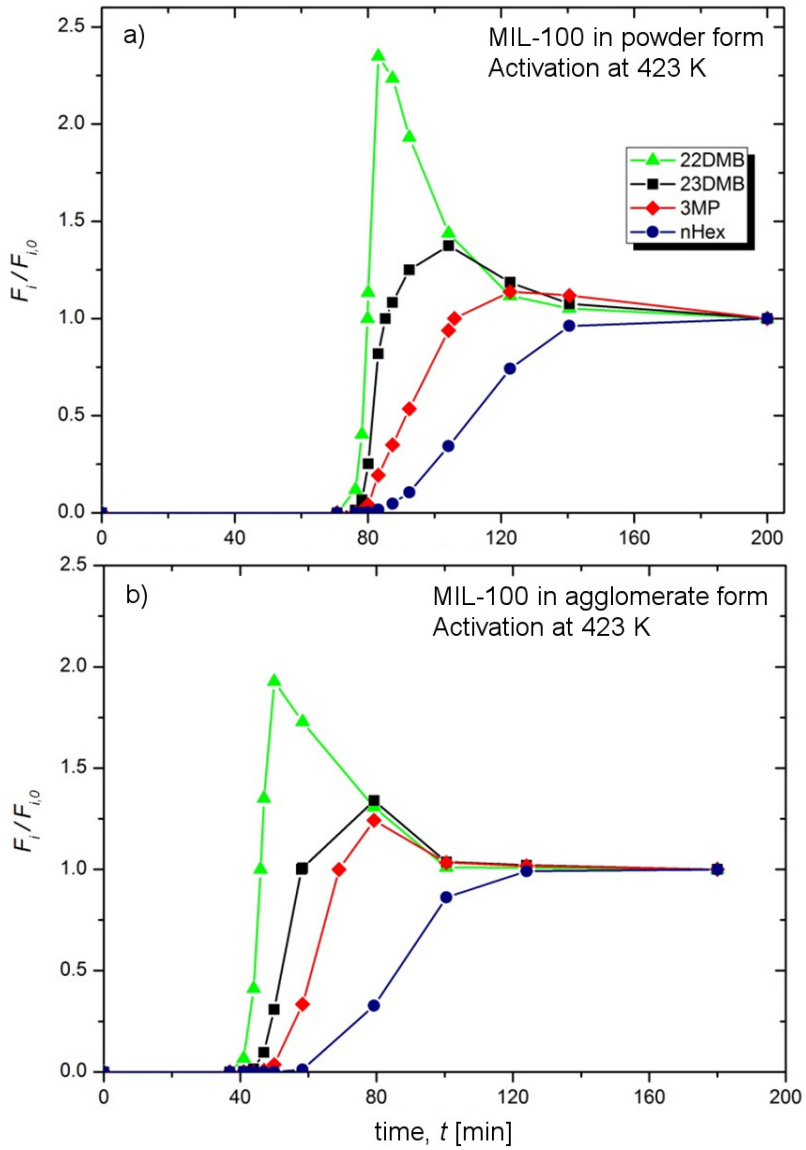


Figure 7.11. Influence of the pressing/shaping procedure on the equimolar quaternary breakthrough curves at T= 323 K and p_{isom} = 4.0 kPa: a) powder form; b) agglomerate form.

Table 7.4. Experimental conditions for the equimolar quaternary breakthrough curves shown in Figure 7.11, and partial loadings (T = 323 K; p_{isom}= 4.0 kPa).

Activation method	Adsorbent form	Mass of adsorbent (mg)	Helium flow (ml/min)	Loading (g/100g_{ads})				Total loading (g/100g_{ads})
				22DMB	23DMB	3MP	*n*HEX	
Act_2	Powder	479	10.0	4.10	5.77	7.35	9.74	26.95
Act_2	Agglom.	441	10.0	1.85	4.04	5.18	8.06	19.13
Variation (wt %)				*-54.9*	*-30.0*	*-29.5*	*-17.2*	*-29.0*

7.5 Separation of C_6 Isomers in the Flexible MOF-2

The flexible MOF-2 was prepared at the University of Texas-Pan American (Edinburg, TX, USA) by the group of Prof. Banglin Chen, and was later tested at LSRE-IPB for the separation of C_6 isomers. MOF-2 has a chemical composition Zn_2 $(BDC)_2(H_2O)_2 \cdot (DMF)$ (BDC = 1,4-benzenedicarboxylate; DMF = dimethylformamide), and results from the framework transformation of MOF-1 (Zn_2 $(BDC)_2(Dabco) \cdot 4DMF \cdot 0.5H_2O$) (Dabco = 1,4-diazabicyclo[2,2,2]octane) which was for the first time synthesised by Dybtsev et al. (2004). The structure transformation from the three-dimensional MOF-1 to the two-dimensional MOF-2 (Figure 7.12) involves the deliberation of Dabco linkers, and simultaneous bonding of water molecules. In a powder X-ray diffraction study, the group of Banglin Chen reported (Chen et al., 2009) that MOF-2 can be obtained by exposing MOF-1 in the air for 72 h. These authors suggest that the moisture (water molecules) is the driving force for this framework transformation. Interestingly, Chen et al. (2009) have also demonstrated that MOF-2 can be transformed back to MOF-1 after simple addition of Dabco in DMF at 383 K for 48 h. Thus, the framework transformation between MOF-1 and MOF-2 is completely reversible.

The representation of the X-ray single-crystal structure (Figure 7.13) shows that the as-synthesized MOF-2 possesses one-dimensional large channels of about 7.8 × 11.0 Å. However, the flexible nature of this structure, could originate unexpected behaviours, induced by the presence of adsorbates.

7.5.1 Experimental Procedure

MOF-2 was obtained from MOF-1 following the procedure herein after described. The MOF-1 sample, supplied in its mother liquor, was first filtered and dried at 353 K. The powder was then activated under vacuum (0.1 bar) during 24 h at 433 K. Finally, the powder is exposed in the air, for at least 5 days, to allow for the complete transformation of MOF-1 in MOF-2.

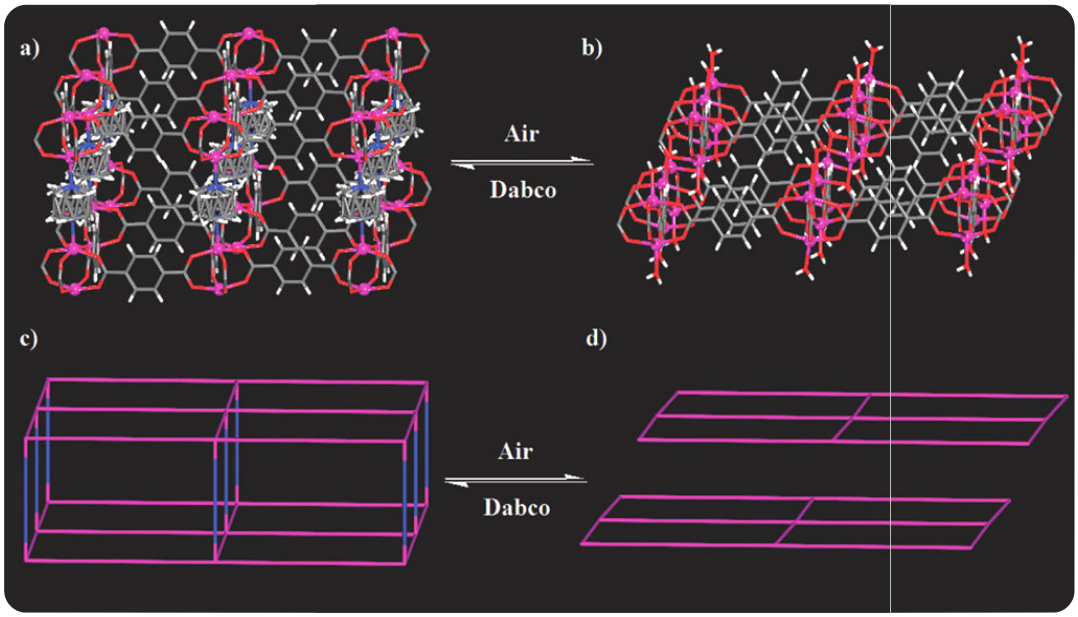


Figure 7.12. Reversible framework transformation from a) MOF-1 to b) MOF-2, and corresponding topologies c) and d), respectively (taken from Chen et al. (2009)).

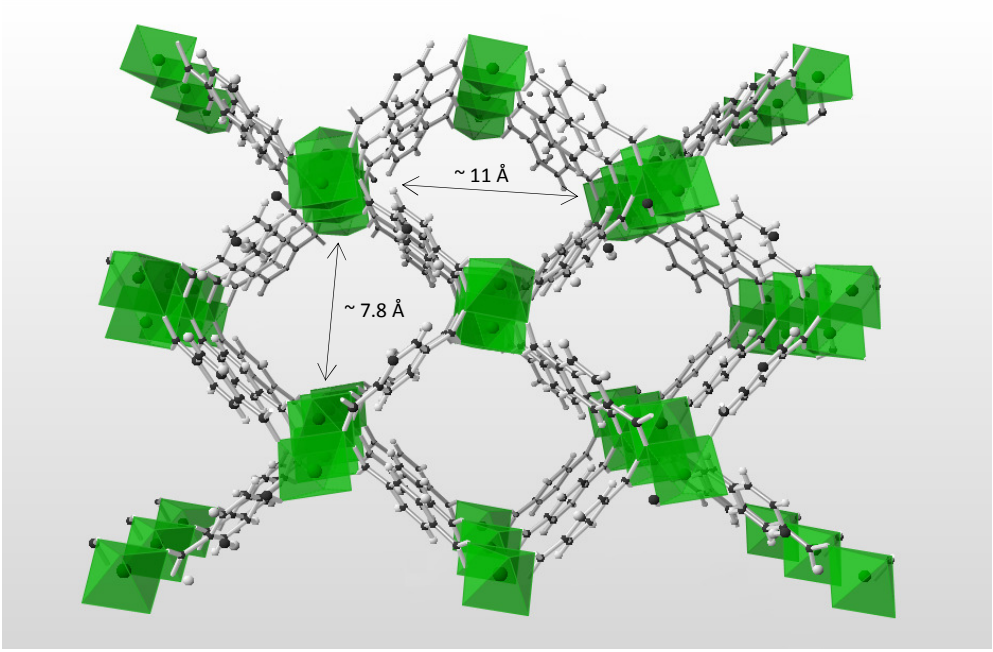


Figure 7.13. Perspective view of the channels in MOF-2. The structure was generated in CrystalMaker version 2.2.3, using the crystallographic information file (cif) given in the literature (Chen et al., 2009). The guest molecules are not shown. Zinc-oxygen clusters (green polyhedra); carbon (grey); hydrogen (white).

Since the mechanical resistance of MOF-2 is unknown, the packing of the adsorbing bed was made by scattering approximately 500 mg of MOF crystals into inert glass wool, in order to avoid channeling phenomena or large pressure drops over the column (Figure 7.14). The stainless steel column has an internal diameter of 4.6 mm with 100 mm in length.



Figure 7.14. MOF-2 powder packed with glass wool.

The adsorption properties of MOF-2 were evaluated by performing a set of breakthrough experiments of equimolar mixtures of 22DMB, 3MP and *n*HEX in the vapour phase, following the procedure described in chapter 3.

7.5.2 Pure Component Adsorption

Single-component breakthrough experiments were carried out initially to examine the feasibility and capability of MOF-2 for the separation of hexane isomers at 313 K and 343 K. As shown in Figure 7.15, their breakthrough times are quite different, from 100 s for 22DMB to 200 s for 3MP and to 800 s for *n*HEX at partial pressure near 6 kPa. When the partial pressure is increased to 28 kPa, their breakthrough times are systematically reduced to 60 s for 22DMB, to 100 s for 3MP, and to 320 s for *n*HEX, respectively. The breakthrough times of the order *n*HEX >>> 3MP > 22DMB clearly indicate that there is a distinct adsorption behaviour between the linear alkane and

the branched ones, which cannot be only attributed to the differences in van der Waals interactions with the microporous walls. The pure component breakthrough curves of *n*HEX (Figure 7.15) clearly show an inflection, which could be attributed to the flexible nature of the MOF-2 structure.

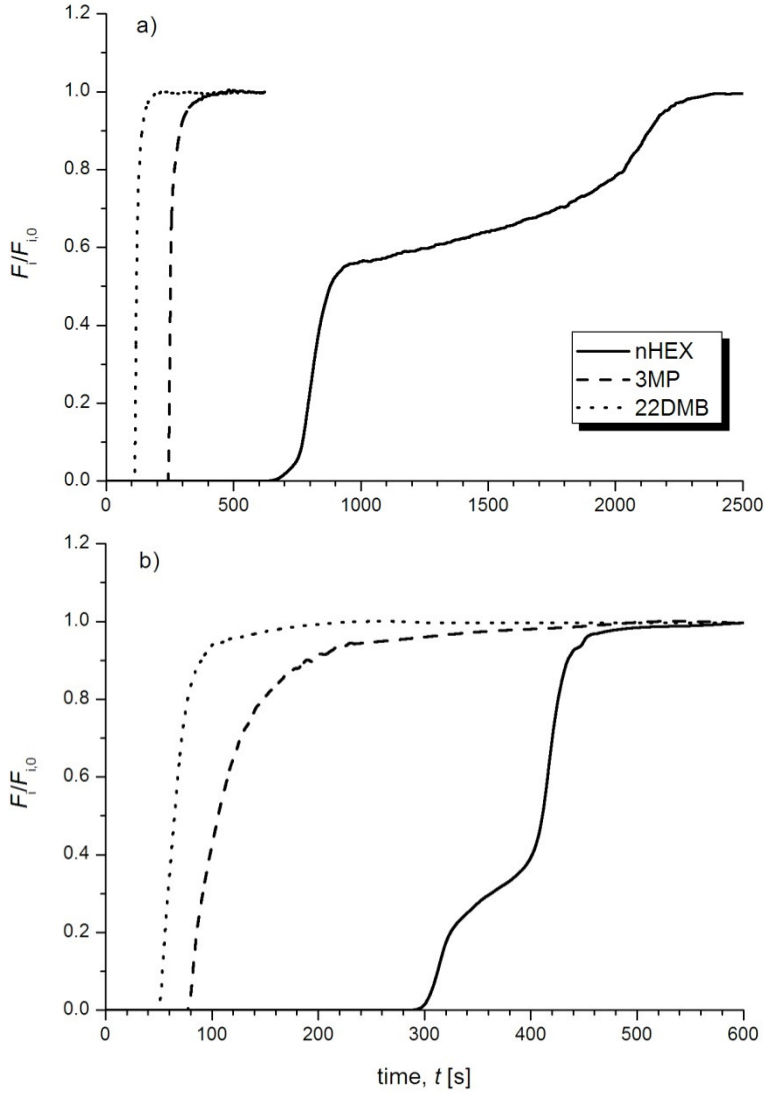


Figure 7.15. Pure component breakthrough curves for 22DMB, 3MP, and *n*HEX at T = 313 K and a) 6 kPa, and b) 28 kPa.

To figure out the separation condition with the aim to optimize and maximize the separation selectivity and capacity of MOF-2 for mixtures of hexane isomers, pure component adsorption isotherms were established from single breakthrough curves. The experimental conditions of the single breakthrough curves as well as the amount

adsorbed in each run are listed in Table 7.5. As shown in Figure 7.16, the adsorption capacities of MOF-2 for *n*HEX reach to 5.5 wt % at 313 K and 33 kPa, and 4.0 % at 343 K and 33 kPa, respectively, which are not saturated. Significantly lower is the adsorption capacities of MOF-2 for 22DMB and 3MP, less than 1.5 wt %, and 1.0 wt % at 313 K, and 343 K, respectively. Curiously, despite the large dimension of the channels in the as-synthesised MOF-2, the results show that MOF-2 is selective only towards *n*HEX.

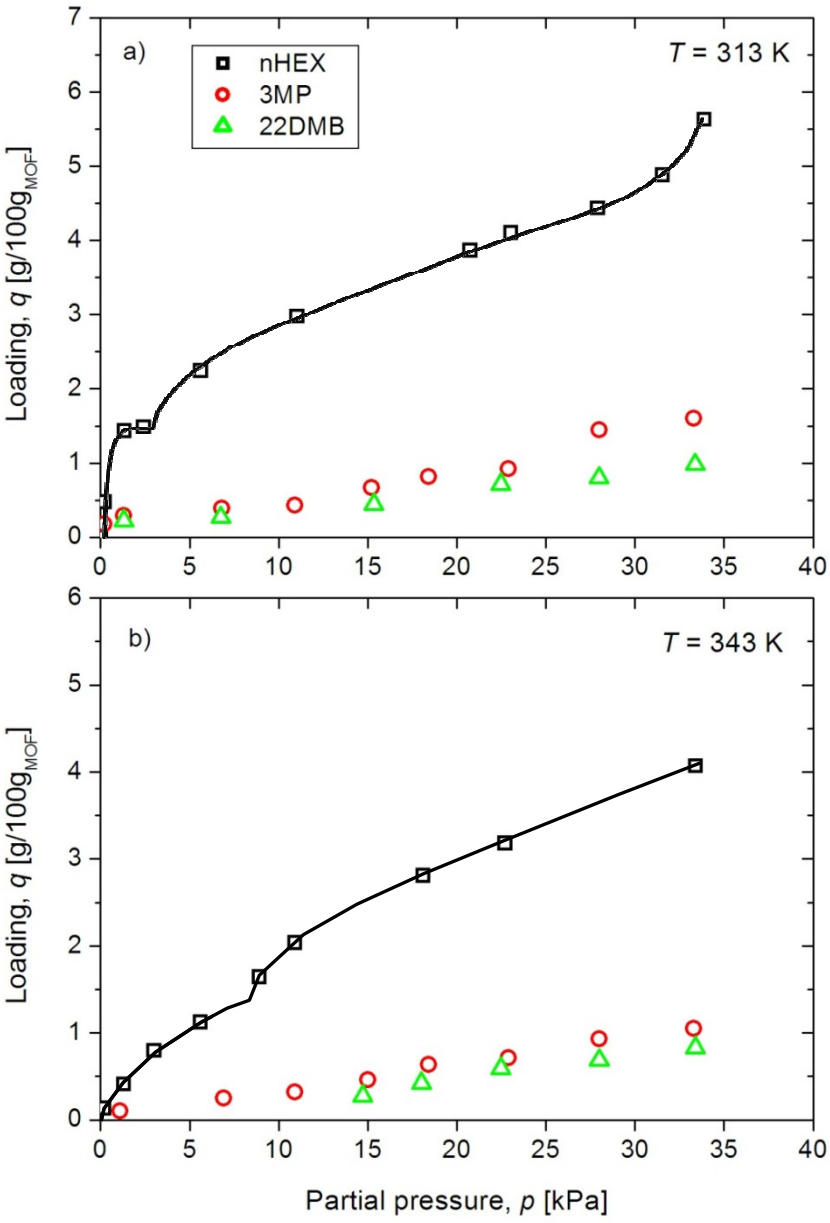


Figure 7.16. Pure component adsorption isotherms of 22DMB, 3MP, and *n*HEX at a) 313 K, and b) 343 K. Lines in *n*HEX isotherms are to aid the eyes.

Table 7.5. Experimental conditions of the single breakthrough curves in MOF-2.

Run	*T* (K)	Helium Flowrate (ml/min)	Hydrocarbon Pressure (kPa)	Mass of adsorbent (mg)	Loading ($g/100g_{ads}$)
nHEX_1	313	12.0	0.2	500	0.48
nHEX_2		5.0	1.3	516	1.43
nHEX_3		2.5	2.4	500	1.49
nHEX_4		2.5	5.5	500	2.25
nHEX_5		2.5	10.9	500	2.98
nHEX_6		2.5	20.5	500	3.87
nHEX_7		2.5	22.7	500	4.10
nHEX_8		2.5	27.5	500	4.44
nHEX_9		2.5	31.1	500	4.88
nHEX_10		2.5	33.4	500	5.63
nHEX_11	343	12.0	0.2	516	0.14
nHEX_12		5.0	1.3	516	0.41
nHEX_13		2.5	3.0	500	0.80
nHEX_14		2.5	5.6	500	1.13
nHEX_15		2.5	8.9	500	1.64
nHEX_16		2.5	10.9	500	2.04
nHEX_17		2.5	18.1	500	2.81
nHEX_18		2.5	22.7	500	3.18
nHEX_19		2.5	33.4	500	4.07
nHEX_20		2.5	42.3	500	4.80
3MP_1	313	12.0	0.2	516	0.18
3MP_2		5.0	1.3	516	0.29
3MP_3		2.5	6.8	750	0.39
3MP_4		2.5	10.9	500	0.43
3MP_5		2.5	15.2	455	0.67
3MP_6		2.5	18.4	500	0.81
3MP_7		2.5	22.9	513	0.92
3MP_8		2.5	28.0	513	1.45
3MP_9		2.5	33.3	513	1.60
3MP_10	343	3.0	1.1	750	0.23
3MP_11		2.5	6.9	500	0.25
3MP_12		2.5	10.9	500	0.32
3MP_13		2.5	15.0	500	0.46
3MP_14		2.5	18.4	500	0.63
3MP_15		2.5	22.9	513	0.71
3MP_16		2.5	28.0	513	0.93
3MP_17		2.5	33.3	513	1.05
22DMB_1	313	5.0	1.3	500	0.22
22DMB_2		2.5	6.8	500	0.27
22DMB_3		2.5	15.3	455	0.45
22DMB_4		2.5	22.5	455	0.72
22DMB_5		2.5	28.0	513	0.80
22DMB_6		2.5	33.4	513	0.98
22DMB_7	343	2.5	14.7	455	0.28
22DMB_8		2.5	18.0	500	0.42
22DMB_9		2.5	22.5	500	0.59
22DMB_10		2.5	28.0	513	0.69
22DMB_11		2.5	33.4	513	0.83

In order to understand the mechanism responsible for such a linear/branched selectivity, the effect of the partial pressure on the single breakthrough curves for 3MP and *n*HEX at 313 K was addressed. Figure 7.17 shows that the inflection of the breakthrough curves only occurs when *n*HEX is injected in the adsorption column. Although the inflection is not noticeable at 2 kPa, its effect is quite pronounced at 6 kPa, and start decreasing with a further rise in the partial pressure.

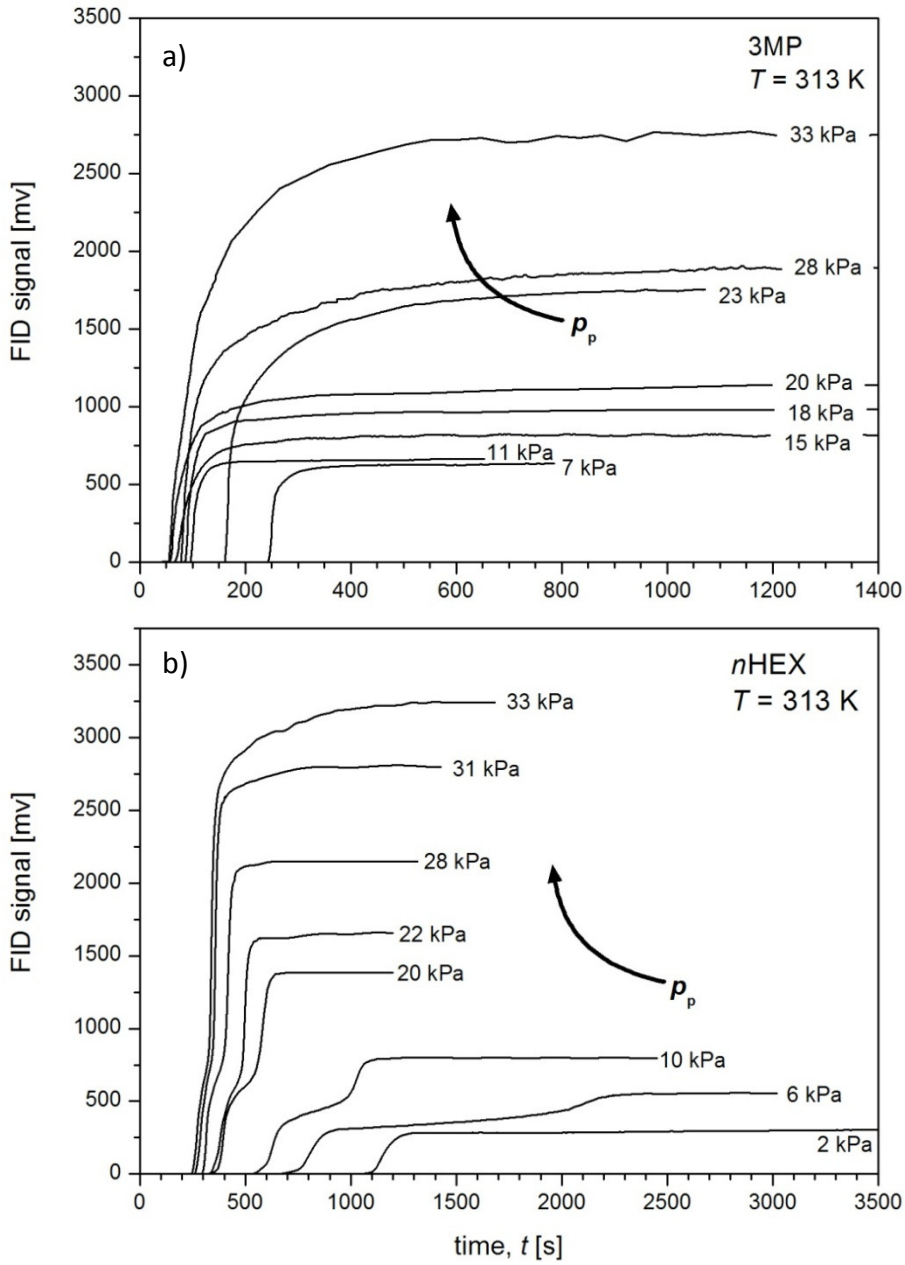


Figure 7.17. Effect of the partial pressure on the single breakthrough curves of a) 3MP, and b) *n*HEX, at 313 K.

It is also important to note that the inflections of the *n*HEX breakthrough curves starts at a FID signal of approximately 300 mV, which corresponds in its turn to a partial pressure of about 3 kPa. Figure 7.18 shows the effect of the partial pressure on the single breakthrough curves of *n*HEX at 343 K. Here, it can be seen that the inflections occurs only for a pressure equal or higher than 9 kPa. At 343 K, the inflection starts at a voltage of approximately 500 mV, which correspond to a partial pressure of about 7 kPa.

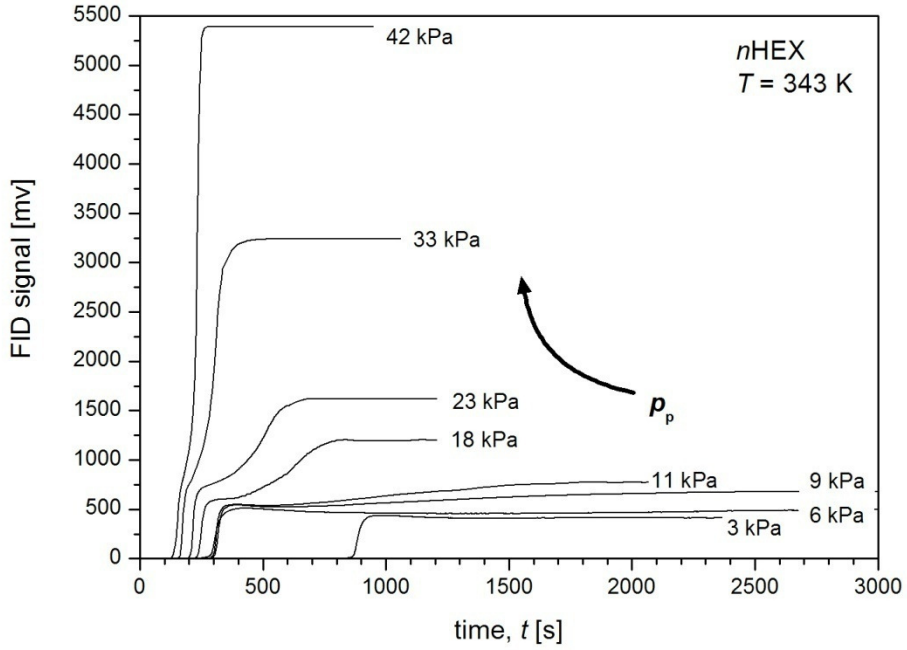


Figure 7.18. Effect of the partial pressure on the single breakthrough curves of *n*HEX at 343 K.

The lines in Figure 7.16 give an idea of the shape of the isotherms for *n*HEX, and highlight the existence of a distinct step at partial pressures around 3 kPa and 7 kPa, for temperatures of 313 K and 373 K, respectively. The panels of Figure 7.16 show a plateau at 1.4 g/100g_{ads}, independently of the temperature. This plateau is followed by a sudden rise in the adsorption capacity. An explanation can possibly be provided by two studies dealing with adsorption in MIL-53(Al, Cr), which is structurally similar to MOF-2. Indeed, a similar effect in the isotherm was found by Trung et al. (2008) for the adsorption of CO_2, and by Bourrelly et al. (2005) for the adsorption of linear alkanes. These authors found that the jump in the isotherm is due to a drastic pore volume

change – also known as “breathing” effect – induced by the inclusion of the guest molecules. Taking in to account the similarity between the MOF-2 and MIL-53(Al, Cr), the “breathing” effect offers a reasonable explanation for the adsorption behaviour in MOF-2. This mechanism is depicted in Figure 7.19, where it is shown the expanded structure, which adopts a shrinked form at pressure of *n*HEX up to the breathing pressure. At higher pressure, the structure reopens and the capacity increases.

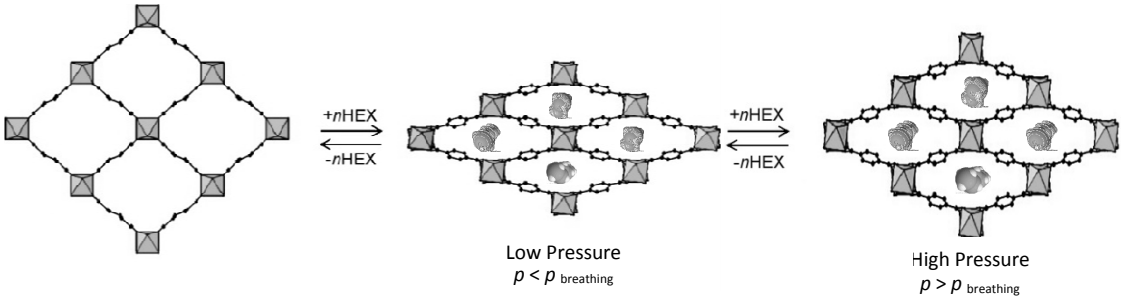


Figure 7.19. Schematic illustration of the ‘‘breathing’’ effect in MOF-2.

The inflections on the breakthrough curves of *n*HEX could be predicted based on the shape of the isotherm, through the equilibrium theory (Rodrigues, 1981). This was demonstrated, for example, by Zhang et al. (2006) for the case of isotherms with two inflection points. However, it is interesting to look at the phenomenon, which is in principle, responsible for such effect. The “breathing” phenomenon is illustrated in Figure 7.20, for the case of a linear alkane diffusing through a fixed bed. The mass front is divided in two distinct zones: the low concentration mass front (LCMF) in yellow, where MOF-2 is in the contracted form, and the high concentration mass front (HCMF) in red, where the structure is reopened. For a gas in a fixed bed adsorber, the higher the mass front concentration, the faster its propagation along the bed; however, in this particular case, the capacity of the adsorbent in the low concentration zone is lower because its structure is contracted. Consequently, the propagation velocity of the LCMF will be higher, and the distance between the LCMF and the HCMF gradually increases during the saturation of the bed. As a result, the LCMF exits the column before the HCMF, which in its turn gives rise to the second wavefront observed in Figure 7.17 (panel *b*) and Figure 7.18.

The results obtained clearly indicate that the framework dynamics is responsible for the *n*/iso selectivity of MOF-2. When MOF-2 is in the contracted form, only the linear hexane can access the channels.

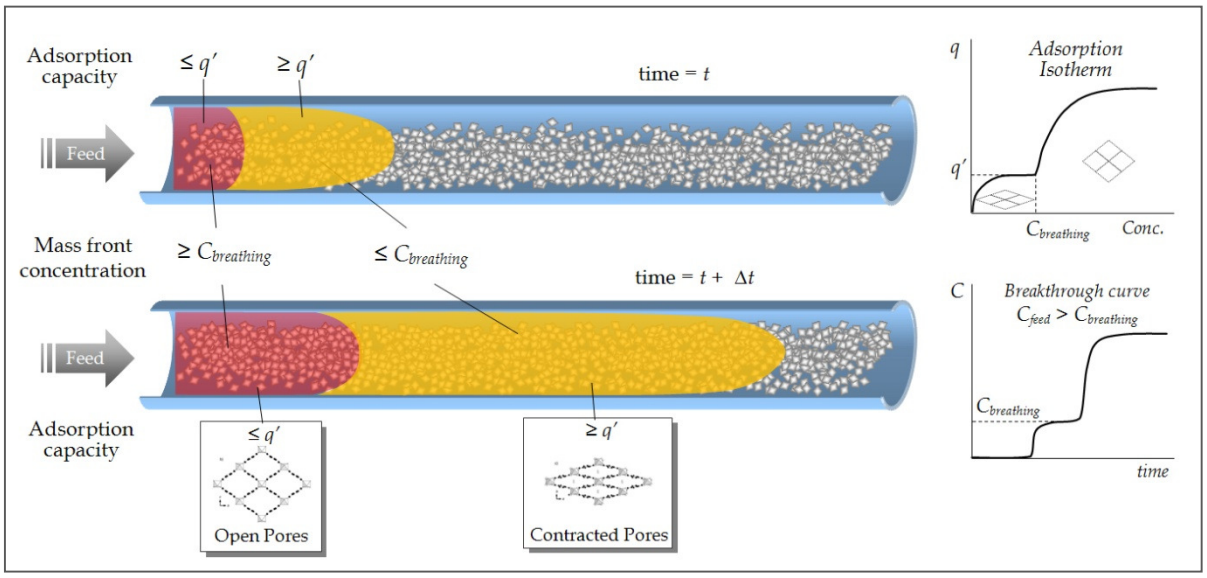


Figure 7.20. Wavefront propagation through a fixed bed packed with MOF exhibiting "breathing" effect.

7.5.3 Binary and Ternary Adsorption

The potential of MOF-2 for the separation of hexane isomers by fixed-bed adsorption was finally realized by binary and ternary breakthrough experiments. At very low partial pressure (p_{isom} = 0.7 kPa), the mixture of 22DMB and 3MP can be easily separated with breakthrough time of 500 and 1200 s, respectively (panel *a* of Figure 7.21). The separation efficiency decreases when the partial pressure increases with breakthrough time of 180 and 320 s, respectively, at 4.8 kPa (panel *b* of Figure 7.21). Since only *n*HEX can access the shrinked pore of MOF-2, the monobranched 3MP and dibranched 22DMB hexane isomers can be readily separated from linear *n*HEX isomer, as clearly shown in their binary breakthrough curves of 22DMB+*n*HEX (panel *a* of Figure 7.22) and 3MP+*n*HEX (panel *b* of Figure 7.22) with a moderate loading of *n*HEX up to 2.98 wt %. Noteworthy are the values of linear/branched selectivities for these

experiments, e.g., for the mixture 22DMB+*n*HEX, $S_{n\text{HEX/22DMB}}$ = 33, for the mixture 3MP+*n*HEX, $S_{n\text{HEX/3MP}}$ = 10.

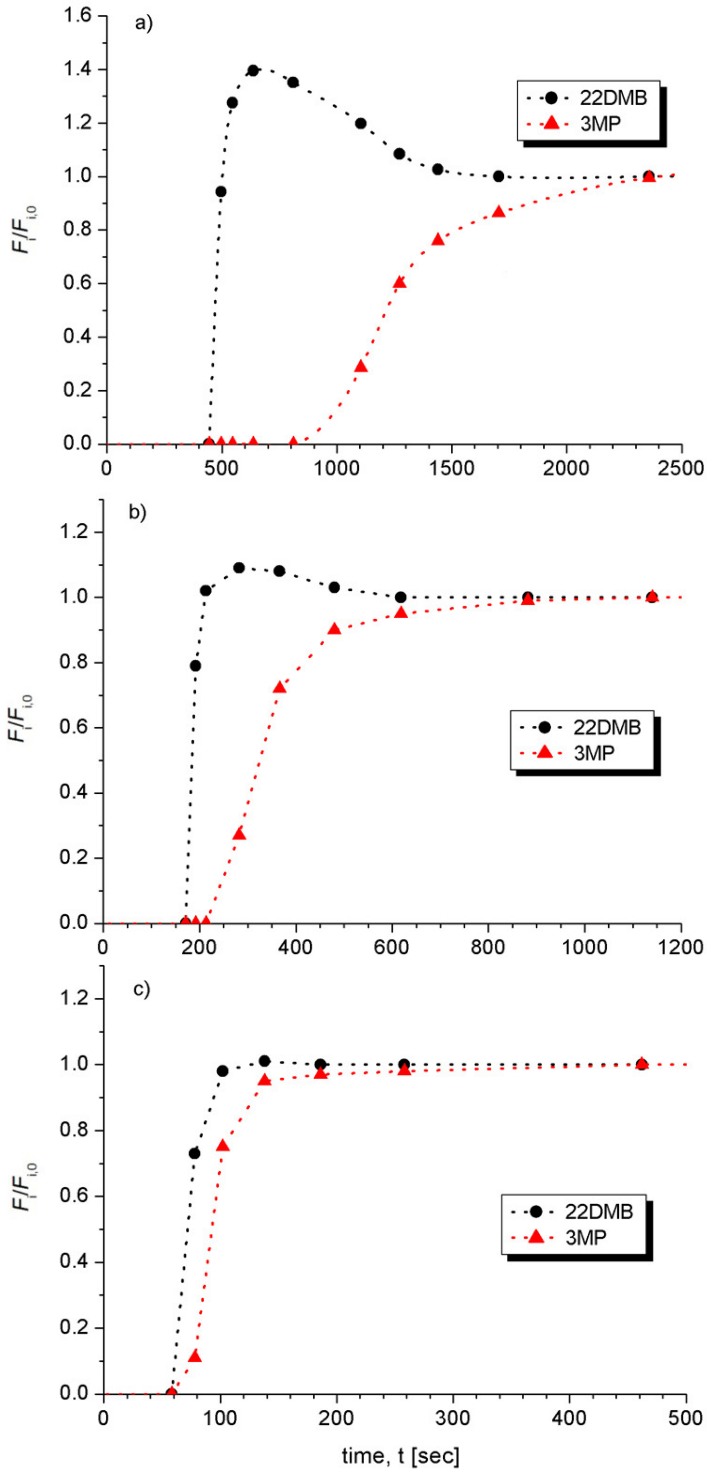


Figure 7.21. Binary breakthrough curves for equimolar mixtures of 22DMB-3MP at *T* = 313 K: a) p_{isom}= 0.7 kPa (run_ *MOF2_1*); b) p_{isom}= 4.8 kPa (run_ *MOF2_2*); c) p_{isom}= 24.0 kPa (run_ *MOF2_3*). Points are experimental data and doted lines are to aid the eyes.

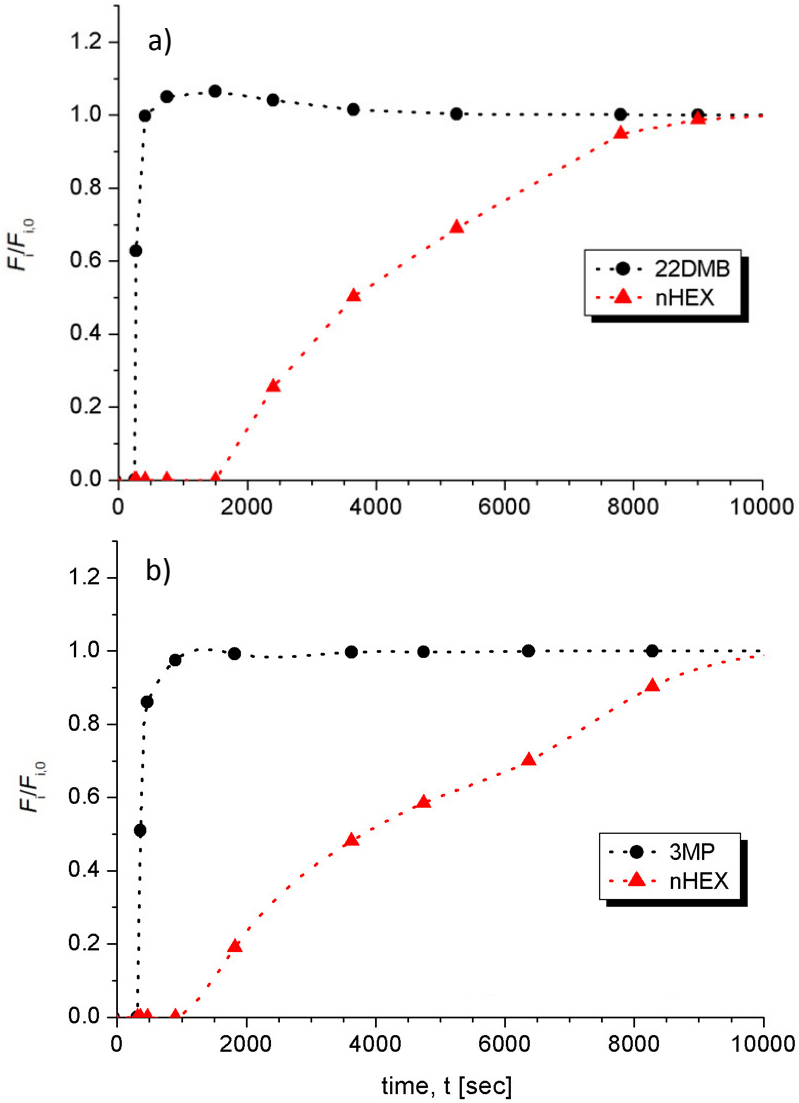


Figure 7.22. Binary breakthrough curves for equimolar mixtures of a) 22DMB-*n*HEX (run_ *MOF2_4*), and b) 3MP-*n*HEX (run_ *MOF2_5*) at T = 313 K, and p_{isom}= 4.8 kPa. Points are experimental data and doted lines are to aid the eyes.

MOF-2 is also potentially applicable to the separation of the three hexane isomers 22DMB, 3MP, and *n*HEX (Figure 7.23), although it is not as good as the well-established zeolite beta in terms of its separation efficiency for separation of dibranched 22DMB from monobranched 3MP (see chapter 3). The experimental conditions of the multicomponent breakthrough curves are listed in Table 7.6.

The most interesting feature is that MOF-2 is magnificent for its separation of linear *n*HEX from monobranched 3MP and dibranched 22DMB hexane isomers. For instance,

the sorption selectivity in a ternary mixture is, $S_{n\text{HEX/22DMB}}$ = 10, and $S_{n\text{HEX/3MP}}$ = 7. Apparently such performance is attributed to the flexible nature of MOF-2, which play the crucial roles to hinder the access of the branched isomers to the contracted pores. This superior property is very important for its potential industrial application in the recycle technologies for isomerisation process, as an alternative to the *n*/iso selective zeolite 5A.

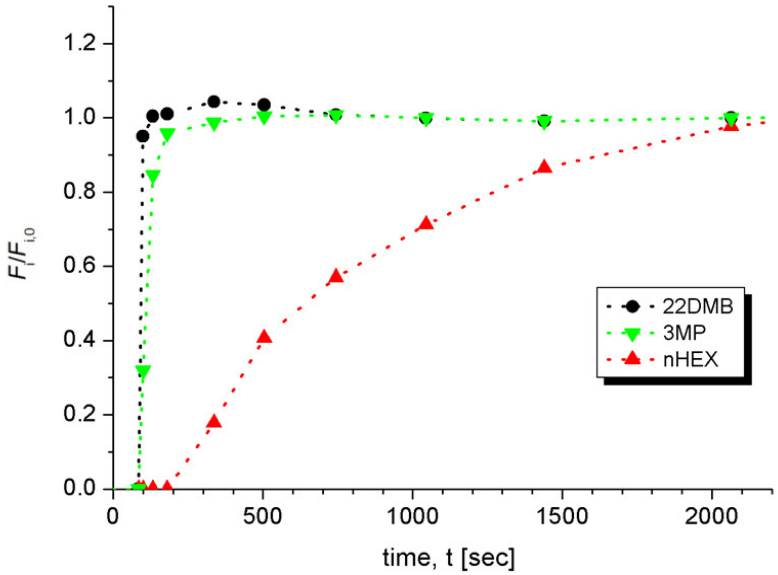


Figure 7.23. Ternary breakthrough curves for equimolar mixture of 22DMB-3MP-*n*HEX (run_ *MOF2_6*) at *T* = 313 K, and p_{isom}= 24.3 kPa. Points are experimental data and doted lines are to aid the eyes.

Table 7.6. Experimental conditions of the multicomponent breakthrough curves in MOF-2, and amount adsorbed for each run.

Run	*T* (K)	Helium Flowrate (ml/min)	Hydrocarbon Pressure (kPa)	Mass of adsorbent (mg)	Loading (g/100g_{ads})		
					22DMB	3MP	*n*HEX
Equimolar mixture 22DMB+3MP							
MOF2_1	313	3.0	0.7	688	0.023	0.123	-
MOF2_2	313	3.0	4.8	688	0.108	0.239	-
MOF2_3	313	2.5	24.0	513	0.340	0.483	-
Equimolar mixture 22DMB+nHEX							
MOF2_4	313	3.0	4.7	688	0.086	-	2.851
Equimolar mixture 3MP+nHEX							
MOF2_5	313	3.0	4.8	688	-	0.301	2.981
Equimolar mixture 22DMB+3MP+nHEX							
MOF2_6	313	2.5	24.3	513	0.198	0.309	2.027

7.6 Conclusions

In conclusion, we present the first examples of microporous MOFs for the separation of C_6 isomers by fixed bed adsorption, establishing the feasibility of the emerging microporous MOFs for their potential applications in this very important industrial process. Temperatures ranging from 313 to 473 K, and partial pressures up to 30 kPa, have been explored using three samples of MOFs with different characteristics.

Multicomponent equimolar experiments show that the sorption hierarchy in MIL-100(Cr) is, *n*HEX>>>3MP>23DMB>>22DMB. It was demonstrated that the giant pores of MIL-100(Cr) can uptake 26 wt% of C_6 isomers at 323 K when coordinated water is evacuated. However, it was found that the presence of coordinated water molecules hinder, in a certain way, the access of the bulkier C_6 isomers to the giant cages, increasing significantly the *n*HEX/22DMB selectivity.

Concerning the adsorption of C_6 isomers in the UiO-66, it was shown that the sorption hierarchy is opposite to the one of typical adsorbents: 22DMB>23DMB>>3MP>>*n*HEX. The results suggest that the retention of C_6 isomers in UiO-66 is governed by the rotational freedom of the molecules in the small cages.

The flexible MOF-2 demonstrates interesting properties for the *n*/iso separation. Its dynamic framework exhibits guest-dependent “breathing” effect, which shrinks the channels in such a way that only the linear *n*HEX is allowed to access the pores. Consequently, MOF-2 exhibits extraordinary selectivity to separate branched hexane isomers from *n*HEX. These “breathing” phenomena can open up an interesting way to efficiently control selective gas adsorption.

The results arising from this work contain essential information for the judicious choice of secondary building units (SBUs) and/or bridging organic linkers, required to design the ideal MOFs for the separation of C_6 isomers. The emerging microporous MOFs show bright promise for their practical applications on the separation of C_6 isomers.

7.7 References

Alcañiz-Monge, J.; Trautwein, G.; Pérez-Cadenas, M.; Román-Martínez; M.C. Effects of Compression on the Textural Properties of Porous Solids. *Micropor. Mesopor. Mater*. 126, 291–301 (2009).

Bourrelly, S.; Llewellyn, P.L.; Serre, C.; Millange, F.; Loiseau, T.; Férey, G. Different Adsorption Behaviors of Methane and Carbon Dioxide in the Isotypic Nanoporous Metal Terephthalates MIL-53 and MIL-47. *J. Am. Chem. Soc.* 127, 13519–13521 (2005).

Calixto, F.S.; Raso, A.G. Retention Index, Connectivity Index and Van der Waals' Volume of Alkanes (GLC). *Chromatographia* 15, 521–524 (1982).

Cavka, J.H.; Jakobsen, S.; Olsbye, U.; Guillou, N.; Lamberti, C.; Bordiga, S.; Lillerud, K.P. A New Zirconium Inorganic Building Brick Forming Metal Organic Frameworks with Exceptional Stability. *J. Am. Chem. Soc.* 130, 13850-13851 (2008).

Chen, Z.; Xiang, S.; Zhao, D.; Chen, B. Reversible Two-Dimensional−Three Dimensional Framework Transformation within a Prototype Metal−Organic Framework. *Cryst. Growth Des.* 9, 5293–5296 (2009).

Chevreau, H. *Synthèse de MOFs*; Activity Report for Institut Lavoisier (CNRS/Université de Versailles): Versailles, France (2009).

Czaja, A.U.; Trukhan, N.; Müller U. Industrial Applications of Metal–Organic Frameworks. *Chem. Soc. Rev.* 38, 1284–1293 (2009).

Denayer, J.F.M.; Ocakoglu, A.R.; Martens, J.A.; Baron G.V. Investigation of Inverse Shape Selectivity in Alkane Adsorption on SAPO-5 Zeolite using the Tracer Chromatography Technique. *J. Catal.* 226, 240–244 (2004).

Denayer, J.F.M.; Ocakoglu, R.A.; Arik, I.C.; Kirschhock, C.E.A.; Martens, J.A.; Baron G.V. Rotational Entropy Driven Separation of Alkane/Isoalkane Mixtures in Zeolite Cages. *Angew. Chem. Int. Ed.* 44, 400–403 (2005).

Dybtsev, D.N.; Chun, H.; Kim, K. Rigid and Flexible: A Highly Porous Metal–Organic Framework with Unusual Guest-Dependent Dynamic Behavior. *Angew. Chem. Int. Ed.* 43, 5033–5036 (2004).

Férey, G.; Serre, C.; Mellot-Draznieks, C.; Millange, F.; Surblé, S.; Dutour, J.; Margiolaki, I. A Hybrid Solid with Giant Pores Prepared by Combination of Targeted Chemistry, Simulation and Powder Diffraction. *Angew. Chem. Int. Ed.* 43, 6296-6301 (2004).

Férey, G. Hydrid Porous Solids, In *Introduction to Zeolite Science and Practice*; Cejka, J., van Bekkum, H., Corma, A., Schüth, F., Eds.; Studies in Surface Science and Catalysis 168; Elsevier B.V.: Amsterdam, pp 327–374 (2007).

Férey, G. Hybrid Porous Solids: Past, Present, Future. *Chem. Soc. Rev.* 37, 191–214 (2008).

Finsy, V.; Ma, L.; Alaerts, L.; De Vos, D.E.; Baron, G.V.; Denayer J.F.M. Separation of CO_2/CH_4 Mixtures with the MIL-53(Al) Metal–Organic Framework. *Micropor. Mesopor. Mater.* 120, 221–227 (2009).

Huang, S.; Finsy, V.; Persoons, J.; Telling, M.T.F.; Baron, G.V.; Denayer, J.F.M. Rotation Dynamics of 2-Methyl Butane and n-Pentane in MCM-22 Zeolite: a Molecular Dynamics Simulation Study. *Phys. Chem. Chem. Phys*. 11, 2869–2875 (2009).

Kitagawa, S.; Kitaura, R.; Noro, S. Functional Porous Coordination Polymers. *Angew. Chem. Int. Ed*. 43, 2334–2375 (2004).

Krishna, R.; Smit, B.; Calero, S. Entropy Effects during Sorption of Alkanes in Zeolites. *Chem. Soc. Rev*. 31, 185–194 (2002).

Krishna, R.; van Baten, J.M. Screening of Zeolite Adsorbents for Separation of Hexane Isomers: A Molecular Simulation Study. *Sep. Purif. Technol.* 55, 246–255 (2007).

Lawton, S.L.; Leonowicz, M.E.; Partridge, R.D.; Chu, P.; Rubin, M.K. Twelve-Ring Pockets on the External Surface of MCM-22 Crystals. *Micropor. Mesopor. Mater*. 23, 109–117 (1998).

Li, J.R.; Kuppler, R.J.; Zhou, H.C. Selective Gas Adsorption and Separation in Metal–Organic Frameworks. *Chem. Soc. Rev.* 38, 1477–1504 (2009).

Llewellyn; P.L.; Bourrelly, S.; Serre, C.; Vimont, A.; Daturi, M.; Hamon, L.; De Weireld, G.; Chang, J.S.; Hong, D.Y.; Hwang, Y.K.; Jhung, S.H.; Férey, G. High Uptakes of CO_2 and CH_4 in Mesoporous Metal–Organic Frameworks MIL-100 and MIL-101. *Langmuir* 24, 7245-7250 (2008).

Noguchi, H.; Kondoh, A.; Hattori, Y.; Kanoh, H.; Kajiro, H.; Kaneko, K. Clathrate-Formation Mediated Adsorption of Methane on Cu-Complex Crystals. *J. Phys. Chem. B* 109, 13851–13853 (2005).

Rodrigues, A.E. *Percolation Processes: Theory and Applications*. A.E. Rodrigues and D. Tondeur (eds.); Sijthoff and Noordhoff: Rockville, MD (1981).

Rowsell, J.L.C.; Yaghi, O.M. Metal-Organic Frameworks: a New Class of Porous Materials. *Micropor. Mesopor. Mater*. 73, 3–14 (2004).

Santilli, D.S.; Harris, T.V.; Zones S.I. Inverse Shape Selectivity in Molecular Sieves: Observations, Modelling, and Predictions. *Microporous. Mater.* 1, 329–341 (1993).

Schenk, M.; Calero, S.; Maesen, T.L.M.; Vlugt, T.J.H.; van Benthem, L.L.; Verbeek, M.G.; Schnell, B.; Smit, B. Shape Selectivity through Entropy. *J. Catal.* 214, 88–99 (2003).

Serre, C.; Bourrelly, S.; Vimont, A.; Ramsahye, N.A.; Maurin, G.; Llewellyn, P.; Daturi, M.; Filinchuk, Y.; Leynaud, O.; Barnes P.; Férey G. An Explanation for the Very Large Breathing Effect of a Metal-Organic Framework during CO_2 Adsorption. *Adv. Mater.* 19, 2246-2251 (2007a).

Serre, C.; Mellot-Draznieks, C.; Surblé, S.; Audebrand, N.; Filinchuk, Y.; Férey G. Role of Solvent-Host Interactions That Lead to Very Large Swelling of Hybrid Frameworks. *Science* 315, 1828–1831 (2007b).

Smit, B.; Krishna R. Molecular Simulations in Zeolitic Process Design. *Chemical Engineering Science* 58, 557–568 (2003).

Trung, T.K.; Trens, P.; Tanchoux, N.; Bourrelly, S.; Llewellyn, P.L.; Loera-Serna, S.; Serre, C.; Loiseau, T.; Fajula, F.; Férey G. Hydrocarbon Adsorption in the Flexible Metal Organic Frameworks MIL-53(Al, Cr). *J. Am. Chem. Soc.* 130, 16926–16932 (2008).

Yaghi, O.M.; O'Keeffe, M.; Ockwig, N.W.; Chae, H.K.; Eddaoudi, M.; Kim, J. Reticular Synthesis and the Design of New Materials. *Nature* 423, 705–714 (2003).

Zhang, W.; Shan, Y.; Seidel-Morgenstern, A. Breakthrough Curves and Elution Profiles of Single Solutes in Case of Adsorption Isotherms with Two Inflection Points. *J. Chromatogr. A* 1107, 216–225 (2006).

8

Conclusions and Suggestions for Future Work

The advanced recycle technologies for paraffins isomerization separate the low research octane number (RON) linear alkanes from light naphtha fractions by using zeolite 5A molecular sieves. To meet the octane quality required by modern engines, refiners use additives to artificially increase the octane quality of the gasoline. Alternatively, high octane gasoline might be produced if low RON (LRON) monobranched C_6 are separated from their high RON (HRON) dibranched isomers, but such separation is very challenging because of the similarity of their kinetic diameter. Zeolite beta is an adsorbent produced in large scale mainly for commercial applications in catalytic processes. However, it was found that its pore system has interesting properties for the separation of branched C_6 isomers. In theory, the large channels (7.6 Å) allow for a relatively fast diffusion of the paraffins inside the crystal, while the zigzag channels with an effective pore size 5.6 Å are able to discriminate between monobranched and dibranched C_6 isomers.

The development of an adsorption based separation process requires first a detailed knowledge of the equilibrium and kinetics of adsorption and their impact on the

dynamic response of an adsorption column. Although is a time consuming method, frontal chromatography was used in this work because its practical application is capable of supplying accurate information about both equilibrium and kinetic properties of either single or multicomponent systems. Accordingly, this work presents from chapter 2 to chapter 5 a complete study of the adsorption behaviour in the vapour phase of the main constituents of the light naphtha (C_5 and C_6 isomers) in a fixed bed packed with commercial sample of zeolite beta pellets.

From the single equilibrium data presented in chapter 2 it was found that the amount that can be adsorbed in zeolite beta at 423 K and at a partial pressure of 30 kPa reaches values of about 7g/100g_{ads} for all the C_6 isomers studied. However, in the low partial pressure range, the Henry's constants varies in the order, *n*HEX (125 g/(g·kPa)) > 3MP (59 g/(g·kPa)) > 23DMB (19 g/(g·kPa)) > 22DMB (14 g/(g·kPa)). Therefore, the results clearly showed that the affinity of zeolite beta towards the C_6 isomers decreases as the branching degree of the carbon chain increases. It was also demonstrated that the isosteric heats of sorption change with the coverage of the adsorbent, indicating that energetic heterogeneity on the adsorbent surface can be related with the existence of different types of adsorption sites in the zeolite beta framework. Four different models were used to fit the experimental data named: Langmuir, Dual-site-Langmuir (DSL); Multi-site-Langmuir and Toth. It is shown that the DSL, Multi-Site-Langmuir and Toth predict satisfactorily the pure component equilibrium data.

The kinetic data measured by the macroscopic zero-length chromatography (ZLC) technique indicates that macropore diffusion is clearly the controlling mechanism for *n*HEX and 3MP. However, the experiments were not conclusive about the relative importance of micropore diffusion for 23DMB and 22DMB. In order to clarify this point, experiments were performed with zeolite beta crystals with the same size used to produce the commercial pellets, but the data were not reliable due to the fast diffusion of the species leading to ZLC experiments with duration below 5 seconds.

In chapter 3 we presented a detailed study of sorption of binary, ternary and quaternary mixtures of C_6 isomers on pellets of zeolite beta. It was found that the extension of the simple models, used to correlate the single equilibrium data in chapter 2, does not give a proper prediction of the adsorption equilibrium data for ternary and quaternary mixtures. This disagreement is a clear indication of the degree of complexity of the system studied. At the same time, it was demonstrated that pure components adsorption data might not be enough to have an accurate predictive model for a real separation process. A proper correlation of the whole set of experimental data was obtained by using a Tri-site Langmuir (TSL) model which assumes that the zeolite beta framework consists of tree distinct adsorption sites, straight channels, zigzag channels, and intersections. Also, based on the effective diameter of the zigzag channels (5.6 Å), it was assumed that the access of the dibranched molecules to this site is hindered by steric constraints caused by the existence of two methyl branches linked to the carbon chain. Such hypothesis was subsequently confirmed by a preliminary molecular simulation study performed through collaboration with the Materials Computational Group of the University Pablo de Olavide (Seville, Spain).

In terms of the experimental data obtained, it was concluded from the quaternary breakthrough experiments that the separation of HRON dibranched hexanes from their LRON isomers in zeolite beta is possible at low hydrocarbon loadings (e.g., ≈ 1 $g/100g_{ads}$), and this can be achieved at high temperatures (e.g., 523 K) with sorption selectivity $S_{3MP/22DMB} \approx 4$, $S_{nHEX/22DMB} \approx 8$, and $S_{nHEX/23DMB} \approx 4$. This feature is relevant for industrial application because hydroisomerization reactor generally operates at temperature around 523 K. Moreover, reasonable selectivities achieved at low loading might contribute for a less mechanically demanding desorption stage.

The hydroisomerisation of the light naphtha mainly yield C_5 and C_6 alkanes. Therefore, a proper description of the recycle schemes for isomerisation processes requires the study of the adsorption behaviour of C_5/C_6 isomerate fractions. Such study was performed in chapter 4, where it was demonstrated that the elution order in a

C_5/C_6 light naphtha fraction can be varied by changing the operating temperature. As a result, at 583 K zeolite beta is able to separate an enriched HRON fraction composed by 22DMB, 23DMB and *i*PEN from an equimolar C_5/C_6 isomers fraction. The adsorption dynamics of a C_5/C_6 six-component fraction was properly described by a non-isothermal/non-adiabatic fixed-bed adsorption model incorporating mass, energy, and momentum balances. The model was developed using Adsim 2006.5, from Aspentech. This commercial simulator, which was introduced at LSRE for the first time during this Ph.D. work, has proven to be a powerful tool for the modelling and optimization of adsorption processes. For instance, Adsim was used to study the dynamic behaviour of feed mixtures with the composition of the hydroisomerization reactor product in a layered bed consisting of zeolite 5A and zeolite beta. The introduction of a layer of zeolite 5A in the adsorption bed has significantly enhanced the performance of the separation by avoiding the mixing of *n*PEN with the enriched high RON fraction. It was found that mono/dibranched C_6 separation can be achieved by properly tuning the operating temperature and the zeolite 5A-to-zeolite beta ratio.

The model developed in chapter 4 for the dual layer bed, was used in chapter 5 for the parametric study of an adiabatic single column with a 4-steps pressure swing adsorption (PSA) cycle. The effect of different process variables, the fraction of zeolite 5A in the bed (L_{5A}/L_B), the purge-to-feed ratio (P/F), the cycle time, the depressurization mode, and the operating temperature on the process performances were evaluated. The dynamic simulations have demonstrated that the zeolite 5A layer retains the LRON *n*PEN and *n*HEX, avoiding their penetration in the zeolite beta layer, which by its turn acts like a barrier reducing the concentration of the monobranched C_6 in the enriched fraction. This study has demonstrated that the co-current depressurization (COD) can be used to increase the adsorbent productivity and the recovery of HRON molecules, by enhancing desorption of the weak adsorptive from the zeolite beta layer. Although higher RON quality can be obtained in the dual layer PSA with countercurrent depressurization (CTD) step, the adsorbent productivity is largely reduced.

Comparing the performance of the layered bed PSA cycle operating in COD mode with the basic case of a single zeolite 5A layer PSA cycle with CTD, it was found that for L_{5A}/L_B in the range 0.67 – 0.8 and P/F ratio greater than 1.15, the product RON yield by the dual layer will be higher than the one obtained using the single layer of zeolite 5A. For instance, keeping constant the P/F ratio, it is possible to achieve octane gains of + 0.26 RON, with a reduction in the adsorbent productivity of 25 %. Further enhancement of the product RON can be achieved by finely tuning both the operating temperature and the time of feed/purge step. Higher temperatures slightly improve the octane quality of the product when the zeolite beta layer represents at least 50 % of the layered bed. Such effect results from the higher selectivity of the zeolite beta towards less branched isomers at high temperature.

In a general way, considering a maximum acceptable reduction in adsorbent productivity of about 30 %, it was demonstrated that the dual layer PSA could result in an octane gain of + 0.4 RON compared to the conventional single layer zeolite 5A. Such improvement, represents for a 10,000 BPSD hydroisomerization unit, an added value close to 400,000 US$ per year.

Nevertheless, it should be taken into account that the PSA cycles presented in this work assume that adsorber feed has the typical composition of the product resulting from the hydroisomerization in a zeolite based catalyst (Pt/H-MOR). Despite their higher resistance to deactivation by contaminants, this family of catalysts has the lowest activity, requiring an operating temperature between 250ºC and 280ºC. In this range of temperatures, the equilibrium composition of C_6 isomers is favourable to the production of more monobranched C_6 (see chapter 1). Recently, new developments have been made in the paraffins isomerisation field with the introduction of sulfated-zirconia catalysts, such as the PI-242 from UOP, or the ATIS-2L from Albemarle. This new family of isomerization catalysts possess good resistance to deactivation and are significantly more active than their zeolite analogues at temperature in the range 160-210ºC. In this range of temperatures, the isomerization reaction yield higher amounts of dibranched C_6 compared to their monobranched isomers. As a consequence, the

mass front of monobranched in the layered PSA would be less concentrated, and would travel slower along the bed than in the study presented in this work. These developments might have a significant impact in the general performance of the layered PSA cycle, by increasing both the adsorbent HRON productivity and the product RON.

Collaboration between LSRE and the Catalysis Engineering group of the Delft University of Technology allowed us to test the potential of the zeolite membranes as an alternative to PSA for the separation of C_6 isomers. Zeolite beta membranes were synthesized on ceramic supports, and characterized at DelftChemTech. A new apparatus developed during this Ph.D. thesis, the ZEOPERM unit, was designed and built at LSRE-IPB to measure N_2 permeance, TIPB pervaporation, and vapour separation. Vapour separation experiments with equimolar mixtures of C_6 isomers demonstrated that the RON of the retentate stream can be increased by almost five points compared to the feed. Comparison with literature suggests that zeolite beta performs better in the separation of mono- from dibranched C_6 isomers, while MFI membranes are more effective for the separation linear/branched C_6 isomers.

The potential application of metal-organic frameworks (MOFs) as an alternative to zeolites was addressed by performing a screening study for mixtures of C_6 isomers. The rigid MOFs UiO-66 and MIL-100(Cr) produced at CNRS/Institut Lavoisier/UVSQ (France) revealed interesting adsorption properties for vapour separation. The sorption hierarchy of C_6 isomers in MIL-100(Cr) is similar to the one found in zeolite beta; however, the sorption selectivity to separate the monobranched C_6 from its dibranched isomers is lower. Nevertheless, this material demonstrated a huge adsorption capacity (up to 26 wt %) by making use of its giant cages. Noteworthy is the inverse sorption hierarchy observed for C_6 isomers in UiO-66. Its structure, consisting of two distinct types of cages of different diameter, preferentially adsorbs bulkier dibranched hexanes over their less branched isomers. The results suggest that the retention of C_6 isomers in UiO-66 is governed by the rotational freedom of the molecules in the small cages. Unlike most MOFs, this material has a remarkable

mechanical and chemical resistance, which make it interesting for industrial applications. There are strategies to set-up a PSA-based recycle scheme in which an enriched fraction consisting of LRON components (*n*HEX and 3MP) is recycled to the isomerisation reactor, but in this case the sorption selectivity $S_{\text{di-/monobranched}}$ should be significantly greater to obtain a reasonable process performance. The third MOF material examined in this work was the flexible MOF-2, synthesised at University of Texas-Pan American. This material demonstrates interesting properties for *n*/iso-alkanes separation. Its dynamic framework exhibits guest-dependent "breathing" effect, which shrinks the channels in such a way that only the linear *n*HEX is allowed to access the pores. Consequently, MOF-2 exhibits extraordinary selectivity for nHEX, e.g., in a ternary mixture, $S_{n\text{HEX/22DMB}}$ = 10, and $S_{n\text{HEX/3MP}}$ = 7. To conclude, the work shown in chapter 7 demonstrates that the major advantage of this new class of adsorbents for gas and vapour separation, can be found in a variety of possible adsorption behaviours, arising from the large number of available pore structure configurations.

The results arising from chapter 5 of this thesis could be used now for the simulation of a multicolumn layered PSA system with pressure equilibration steps in order to obtain a more realistic representation of the real PSA operation. Additionally, the behaviour of the overall isomerisation scheme could be studied by combining an upstream hydroisomerization unit with an Aspen Adsim multicolumn PSA flowsheet using Aspen Dynamics, from the AspenOne package. This process integration will allow establishing a rigorous comparison between different isomerisation schemes.

Concerning the development of alternative technologies for paraffin isomerisation, future works should be focused on the study of the zeolite membrane reactor (ZMR) unit performance. This study can be carried out in the ZEOPERM unit built at LSRE-IPB using the zeolite beta membranes which demonstrates the best performances in term of separation. Additionally, it would be interesting to evaluate the performance of the ZMR unit with the new sulfated-zirconia catalysts.

Another interesting field of research is the development of a new generation of recycle scheme for paraffin isomerisation, by making use of the structural dynamics exhibited by some MOFs, such as the MOF-2 studied in chapter 7. The guest induced flexibility of the MOF-2 structure could be applied in a PSA system to speed-up the desorption step by simply reducing the partial pressure of *n*HEX in the gas phase. Once the "breathing" pressure is reached, the framework contracts, and ejects the linear paraffins from the porous structure. The conceptual design of this PSA cycle with rapid purge step is sketched in Figure 8.1. In terms of product RON, such process could be competitive with the conventional recycle schemes using zeolite 5A. However, the practical application of this novel concept would result in a significant reduction of the amount of purge gas necessary to clean the absorbent bed, along with strong improvement of the adsorbent productivity.

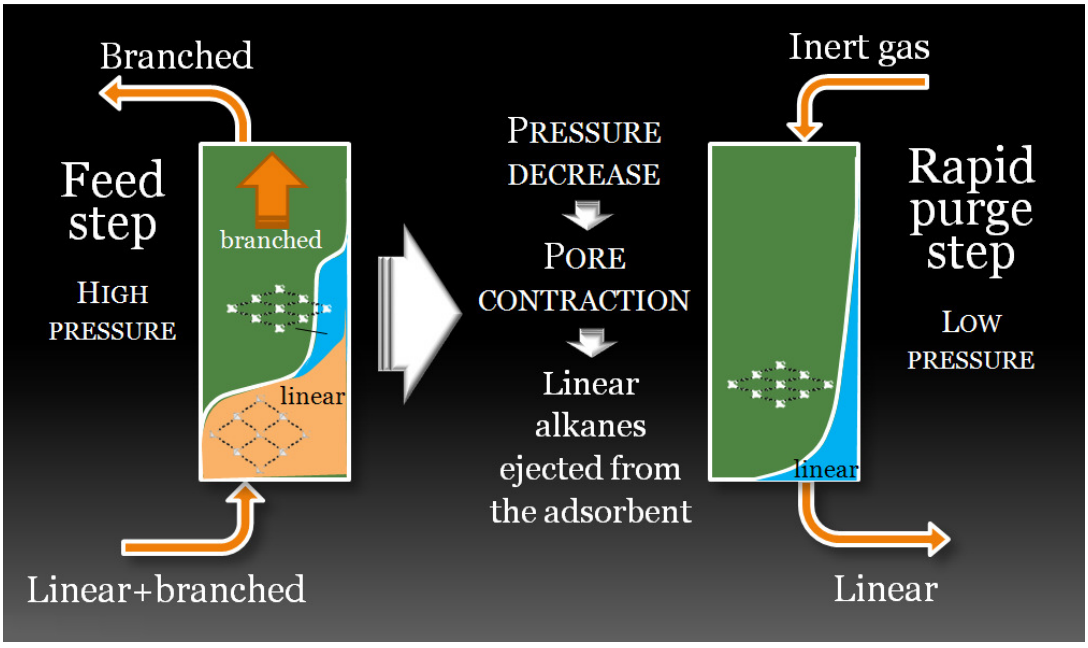


Figure 8.1. Novel concept for PSA processes with flexible MOFs: the rapid purge step.

List of Publications

Patrick S. Bárcia, José A.C. Silva, Alírio E. Rodrigues, Octane Upgrading of C_5/C_6 Light Naphtha by Layered Pressure Swing Adsorption (*submitted to Energy & Fuels,* 2010).

Patrick S. Bárcia, Daniela Guimarães, Patrícia A.P. Mendes, José A.C. Silva, Vincent Guillerm, Hubert Chevreau, Christian Serre, Alírio E. Rodrigues, Reverse Shape Selectivity in the Adsorption of Hexane and Xylene Isomers in MOF UiO-66 (*submitted to Micropor. Mesopor. Mater.,* 2010).

Elena Garcia-Perez, Patrick S. Bárcia, José A.C. Silva, Alírio E. Rodrigues, Sofia Calero, Influence of the Sodium and Calcium Non-Framework Cations on the Adsorption of Hexane Isomers in Zeolite BEA (*accepted for publication in Theor. Chem. Acc.,* 2010)

Patrick S. Bárcia, José A.C. Silva, Alírio E. Rodrigues, Adsorption Dynamics of C_5–C_6 Isomerate Fractions in Zeolite Beta for the Octane Improvement of Gasoline, *Energy Fuels* 24 (2010) 1931–1940.

Patrick S. Bárcia, Alexandre Ferreira, Jorge Gascon, Sonia Aguado, José A.C. Silva, Alírio E. Rodrigues, Freek Kapteijn, Zeolite Beta Membranes for the Separation of Hexane Isomers, *Micropor. Mesopor. Mater.* 128 (2010) 194–202.

Marco P.M. Nicolau, Patrick S. Bárcia, Jose M. Gallegos, José A.C. Silva, Alírio E. Rodrigues, Banglin Chen, Single- and Multicomponent Vapor-Phase Adsorption of Xylene Isomers and Ethylbenzene in a Microporous Metal-Organic Framework, *J. Phys Chem. C* 113 (2009) 13173-13179.

Patrick S. Bárcia, Laurent Bastin, Eric J. Hurtado, José A.C. Silva, Alírio E. Rodrigues, Banglin Chen, Single and Multicomponent Sorption of CO2, CH4 and N2 in a Microporous Metal-Organic Framework, *Separ. Sci. Technol.* 43 (2008) 3494-3521.

Laurent Bastin, Patrick S. Bárcia, Eric J. Hurtado, José A.C. Silva, Alírio E. Rodrigues, Banglin Chen, A Microporous Metal-Organic Framework for Separation of CO2/N2 and CO2/CH4 by Fixed-Bed Adsorption, *J. Phys. Chem. C* 112 (2008) 1575-1581. ("*highly cited paper"* and "*hot paper"*)

Patrick S. Bárcia, Fatima Zapata, José A.C. Silva, Alírio E. Rodrigues, Banglin Chen, Kinetic Separation of Hexane Isomers by Fixed-Bed Adsorption with a Microporous Metal-Organic Framework, *J. Phys. Chem. B* 111 (2007) 6101-6103. (*highly cited paper*)

Patrick S. Bárcia, José A.C. Silva, Alírio E. Rodrigues, Separation of Branched Hexane Isomers using Zeolite Beta for the Octane Improvement of Gasoline Pool, *Stud. Surf. Sci. Catal*. 170 (2007) 955-960.

Patrick S. Bárcia, José A.C. Silva, Alírio E. Rodrigues, Separation of Branched Hexane Isomers on Zeolite BETA, *Adsorpt. Sci. Technol.* 25 (2007) 169-183.

Patrick S. Bárcia, José A.C. Silva, Alírio E. Rodrigues, Multicomponent Sorption of Hexane Isomers in Zeolite BETA, *AIChE J*. 53 (2007) 1970-1981.

Patrick S. Bárcia, José A.C. Silva, Alírio E. Rodrigues, Separation by Fixed-Bed Adsorption of Hexane Isomers in Zeolite BETA Pellets, *Ind. Eng. Chem. Res.* 45 (2006) 4316-4328.

Grande, C.A.; Cavenati, S.; Bárcia, P.; Hammer, J.; Fritz, H. G., and Rodrigues, A.E., Adsorption of Propane and Propylene in Zeolite 4A Honeycomb Monolith, *Chem. Eng. Sci*. 61 (2006) 3053-3067.

Patrick S. Bárcia, José A.C. Silva, Alírio E. Rodrigues, Adsorption Equilibrium and Kinetics of Branched Hexane Isomers in Pellets of BETA Zeolite, *Micropor. Mesopor. Mater*. 79 (2005) 145-163.

In Preparation

Patrick S. Bárcia, Alexandre Ferreira, Jorge Gascon, Sonia Aguado, José A.C. Silva, Alírio E. Rodrigues, Freek Kapteijn, Synthesis of ITQ-17 Nanocrystals and Their Performance in the Separation of Hexane Isomers (*in preparation*).

Conference Proceedings

Patrick S. Bárcia, José A.C. Silva, Alírio E. Rodrigues, "Improvement of the recycle technologies for C5/C6 isomerization by layered PSA", Accepted for publication in the book of abstracts of 10th International Conference on Fundamental of Adsorption, Kobe (Japan): 23-28 May 2010.

Patrick S. Bárcia, José A.C. Silva, Alírio E. Rodrigues, Vincent Guillerm, Christian Serre, "Multicomponent adsorption of hexane isomers in MOFs", Accepted for publication in the book of abstracts of 10th International Conference on Fundamental of Adsorption, Kobe (Japan): 23-28 May 2010.

Patrick S. Bárcia, Marco P.M. Nicolau, José A.C. Silva, Alírio E. Rodrigues, "Upgrading of the light naphtha fraction with zeolite beta", Book of abstracts of XXXII Reunión Ibérica de Adsorción, Móstoles (Espanha): 22-24 September 2008.

Patrick Bárcia, Alírio Rodrigues, José Silva, "A Shape Selective MOF Material for the Adsorptive Separation of linear and branched hexane isomers", Book of abstracts of ChemPor 2008 - 10th International Chemical Engineering Conference, Braga (Portugal): 4-6 September, 2008.

Patrick S. Bárcia, José A.C. Silva, Alírio E. Rodrigues, "Separation of branched hexane isomers using zeolite beta for the octane improvement of gasoline pool", Book of abstracts of 15th International Zeolite Conference, Beijing (China): 12-17 August 2007.

Patrick S. Bárcia, José A.C. Silva, Alírio E. Rodrigues, "Improving Total Isomerization Processes (TIP) by separating branched hexane isomers", Book of abstracts of 9th International Conference on Fundamental of Adsorption, Giardini Naxos (Sicily): 20-25 May 2007.

Patrick S. Bárcia, Jose A. C. Silva, Alírio E. Rodrigues, "Separation of branched hexane isomers on zeolite BETA", Book of abstracts of XXXI Reunión Ibérica de Adsorción, Tarragona (Espanha): 27-29 September 2006.

Patrick S. Bárcia, José A.C. Silva, Alírio E. Rodrigues, "Separation of branched hexane isomers on zeolite BETA", Book of abstracts of ChemPor 2005 - 9th International Chemical Engineering Conference, Coimbra (Portugal): September, 2005.

Oral Presentations

Patrick S. Bárcia, José A.C. Silva, Alírio E. Rodrigues, "Improvement of the recycle technologies for C5/C6 isomerization by layered PSA", Accepted for oral presentation at the 10th International Conference on Fundamental of Adsorption, Kobe (Japan): 23-28 May 2010.

Patrick S. Bárcia, "MOFs for gas and vapor separation – Challenges in industrial application", Autumn 2009 LSRE/LCM Seminar, Porto (Portugal): 27 November 2009.

Patrick S. Bárcia, Marco P.M. Nicolau, José A.C. Silva, Alírio E. Rodrigues, "Upgrading of the light naphtha fraction with zeolite beta", XXXIII Reunión Ibérica de Adsorción, Móstoles (Espanha): 22-24 September 2008.

Patrick S. Bárcia, José A.C. Silva, Alírio E. Rodrigues, "Improving Total Isomerization Processes (TIP) by separating branched hexane isomers", 9th International Conference on Fundamental of Adsorption, Giardini Naxos (Sicily): 20-25 May 2007.

Patrick S. Bárcia, Jose A. C. Silva, Alírio E. Rodrigues, "Separation of branched hexane isomers on zeolite BETA", XXXII Reunión Ibérica de Adsorción, Tarragona (Espanha): 27-29 September 2006.

Patrick S. Bárcia, Jose A. C. Silva, Alírio E. Rodrigues, "Separation of branched hexane isomers on zeolite BETA", ChemPor 2005 - 9th International Chemical Engineering Conference, Coimbra (Portugal): 21-23 September, 2005.

Jose A. C. Silva , Patrick S. Bárcia, Alírio E. Rodrigues, "Experimental study of hexane isomers sorption on zeolite BETA pellets", in workshop "Towards new methods to design catalytic and separation processes in nanoporous materials", CECAM, Lyon (France): 5-7 September, 2005.

Poster Presentations

Patrick S. Bárcia, José A.C. Silva, Alírio E. Rodrigues, Vincent Guillerm, Christian Serre, "Multicomponent adsorption of hexane isomers in MOFs", Accepted as poster presentation at the 10th International Conference on Fundamental of Adsorption, Kobe (Japan): 23-28 May 2010.

Patrick S. Bárcia, Alexandre Ferreira, Jorge Gascon, Sonia Aguado, José A.C. Silva, Alírio E. Rodrigues, Freek Kapteijn, "Zeolite beta membranes for the separation of hexane isomers", on the occasion of the Marie Curie Training Course - Nanostructured materials and membranes for Energy, SINTEF, Oslo (Norway): 8-17 March 2009.

Patrick Bárcia, Alírio Rodrigues, José Silva, "A Shape Selective MOF Material for the Adsorptive Separation of linear and branched hexane isomers", 10th International Chemical Engineering Conference, Braga (Portugal): 4-6 September, 2008.

Patrick S. Bárcia, José A.C. Silva, Alírio E. Rodrigues, "Separation of branched hexane isomers using zeolite BETA for the octane improvement of gasoline pool", 15th International Zeolite Conference, Beijing (China): 12-17 August 2007.

Appendices

Appendix A

Single Sorption Data for *n*PEN and *i*PEN in Zeolite Beta Pellets

Single equilibrium data of C_5 isomers in pellets of zeolite beta were measured at LSRE with the apparatus described in chapter 2. The pure component isotherm is shown in Figure A1.

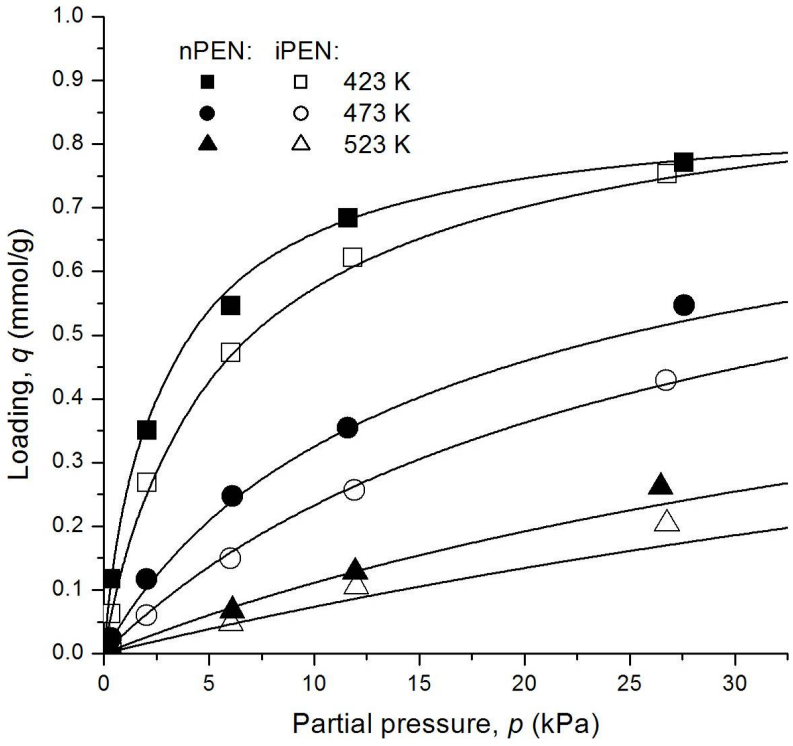


Figure A.1. Pure component adsorption equilibrium data for pentane isomers in pellets of zeolite beta. Experimental conditions are in Table A1.

In the low pressure range, the amount of *n*PEN adsorbed in pellets of zeolite beta is higher then for *i*PEN; however the experimental data at low temperature clearly shows that the difference is progressively reduced as the partial pressure increase. A similar behaviour was found in chapter 2 for the adsorption of *n*HEX and their branched

isomers on beta. An explanation for such effect is the fact that van der Waals interaction forces predominant at low coverage could be balanced at higher loading by a pore filling mechanism more favourable to the adsorption of branched isomers. Experimental conditions for the pure component breakthrough curves are presented in Table A1.

Table A.1. Experimental conditions for single component breakthrough curves and amount adsorbed for each run. †

Run	T(K)	*He* flowrate (ml/min)	p_{C5} (kPa)	q (mmol/g_{ads})
nPEN				
nP_1	423	40	0.35	0.117
nP_2		9.8	2.08	0.391
nP_3		3.5	6.04	0.546
nP_4		2.5	11.63	0.684
nP_5		1.5	27.58	0.771
nP_6	473	10	0.35	0.025
nP_7		10	2.03	0.103
nP_8		3.5	6.10	0.247
nP_9		2.5	11.60	0.354
nP_10		1.5	27.58	0.547
nP_11	523	40	0.35	0.013
nP_12		3.2	6.10	0.068
nP_13		2.3	11.95	0.128
nP_14		1.5	26.46	0.261
iPEN				
iP_1	423	40	0.34	0.063
iP_2		9.8	2.06	0.268
iP_3		3.2	6.05	0.472
iP_4		2.3	11.84	0.621
iP_5		1.5	26.80	0.753
iP_6	473	40	0.34	0.013
iP_7		9.8	2.05	0.060
iP_8		3.2	6.03	0.149
iP_9		2.3	11.90	0.256
iP_10		1.5	26.73	0.433
iP_11	523	40	0.34	0.005
iP_12		3.2	6.04	0.047
iP_14		1.5	26.77	0.231

† Runs performed on bed_1 (column properties are in Table 4.1). Total system pressure 100 kPa.

Appendix B

Derivation of the Isosteric Heat of Adsorption for TSL Model

The isosteric heat of adsorption for the TSL isotherm model was calculated from an analytical expression, being the main steps described below.

The generic expression for a Langmuir isotherm model accounting for *n* different energetic sites is defined as follows

$$q(p,b(T)) = \sum_{j=1}^{n} q_{mj} \frac{b_j p}{1 + b_j p} \tag{B.1}$$

where

$$b_j(T) = b_j^0 \exp(-E_j / RT) \tag{B.2}$$

The variation of heat of adsorption was derived decomposing first the total differentiation of the isotherm model

$$\frac{dq}{dt} = \frac{\partial q}{\partial p}\frac{dp}{dt} + \frac{\partial q}{\partial T}\frac{dT}{dt} \tag{B.3}$$

Each partial derivative of Equation B.3 is calculated separately as follows

$$\left.\frac{\partial q}{\partial p}\right|_T = \sum_{j=1}^{n} q_{mj} \frac{b_j}{(1 + b_j p)^2} \tag{B.4}$$

The differentiation of the loading with respect to the temperature at constant pressure is also decomposed

$$\left.\frac{\partial q}{\partial T}\right|_p = \frac{\partial q}{\partial b}\left.\frac{db}{dT}\right|_p \tag{B.5}$$

where

$$\left.\frac{\partial q}{\partial b}\right|_p = p\sum_{j=1}^{n} q_{mj}\frac{1}{(1+b_j p)^2} \tag{B.6}$$

and

$$\frac{db}{dT} = b\frac{-E}{RT^2} \tag{B.7}$$

From Equations B.5–B.7 we obtain

$$\left.\frac{\partial q}{\partial T}\right|_p = p\sum_{j=1}^{n} q_{mj} b_j \frac{(-E_j/RT^2)}{(1+b_j p)^2} \tag{B.8}$$

Combining Equations B.4 and Equations B.8, we can rewrite Equations B.3 as follows

$$\frac{dq}{dt} = \sum_{j=1}^{n} q_{mj}\frac{b_j}{(1+b_j p)^2}\frac{dp}{dt} + p\sum_{j=1}^{n} q_{mj} b\frac{(-E_j/RT^2)}{(1+b_j p)^2}\frac{dT}{dt} \tag{B.9}$$

Multiplying Equations B.9 by (dt),

$$dq = \sum_{j=1}^{n} q_{mj}\frac{b_j}{(1+b_j p)^2}dp + p\sum_{j=1}^{n} q_{mj} b\frac{(-E_j/RT^2)}{(1+b_j p)^2}dT \tag{B.10}$$

If (dq = 0) then,

$$-\frac{dp}{dT} = \left(p\sum_{j=1}^{n} q_{mj} b_j \frac{(-E_j/RT^2)}{(1+b_j p)^2}\right) \Big/ \left(\sum_{j=1}^{n} q_{mj}\frac{b_j}{(1+b_j p)^2}\right) \tag{B.11}$$

Since,

$$\frac{1}{p}\frac{dp}{dT} = \frac{d\ln p}{dT} \tag{B.12}$$

and considering the van't Hoff equation

$$\frac{q_{st}}{RT^2} = \left.\frac{\partial \ln p}{\partial T}\right|_q \tag{B.13}$$

Then it is possible to substitute Equations B.11 in Equations B.13, in order to obtain an analytical expression for the heat adsorption as a function of the partial pressure for a generic Langmuir isotherm model with *n* energetically different sites

$$q_{st} = \left(\sum_{j=1}^{n} q_{mj} b_j \frac{-E_j}{(1+b_j p)^2}\right) \Big/ \left(\sum_{j=1}^{n} q_{mj} \frac{b_j}{(1+b_j p)^2}\right) \tag{B.14}$$

The above equation shows the variation of the isosteric heat of adsorption with loading as the partial pressure is related to loading via Equations B.1.